Biomechanical and neural influences on locomotor gait control in mice

Zane Mitrevica

A dissertation submitted in partial fulfillment
of the requirements for the degree of
Doctor of Philosophy
of
University College London.

Sainsbury Wellcome Centre for Neural Circuits and Behaviour
University College London

January 9, 2025

I, Zane Mitrevica, confirm that the work presented in this thesis is my own. Where information has been derived from other sources, I confirm that this has been indicated in the work.

Abstract

Locomotion is one of the most fundamental behavioural outputs of the mammalian nervous system, with interlimb coordination, or gait, as a defining feature. While recent technological developments have advanced our understanding of the neural mechanisms behind various locomotor properties, the study of quadrupedal gait has been constrained by its partial dependence on speed and the difficulty to reliably evoke a variety of gaits in genetically tractable quadrupeds like mice. In addition, research on large mammals has highlighted a biomechanical component to gait control, yet experimental manipulation of body mechanics in mice has been problematic due to their small size. In my PhD work, I addressed these challenges by developing a head-fixed locomotor paradigm that decouples the speed- and leg loading-related effects on gait. Specifically, I combined unilateral optogenetic stimulation of glutamatergic neurons in the cuneiform nucleus with head height and surface slope modulation. This paradigm revealed a speed-independent shift in homolateral limb phase preference from strict alternation to a quarter-of-phase more synchronised coordination upon rearward redistribution of leg load. Conversely, hindlimb coordination was influenced by the side of optogenetic stimulation and a combination of speed, total leg load, and a posture-related variable. To explore the neural bases of these associations, I performed analogous experiments in Egr3-knockout mice that lack muscle spindle-mediated proprioception. This deficit reduced, but did not eliminate, the sensitivity of homolateral phase to changes in anteroposterior load distribution, suggesting that muscle spindle afferents contribute to the observed effect, but are not its sole mediator. In contrast, the stimulation side dependence of hindlimb coordination was largely abolished, highlighting a crucial interplay between descending and feedback influences. Altogether, my PhD research provides an entry point to behaviour-driven study of gait circuits and offers insight into the varying roles of biomechanical and neural influences on specific modules of interlimb coordination.

Impact statement

Locomotion is one of the most ubiquitous behaviours in the animal kingdom, distinguished by its rhythmicity, stereotypy, and remarkable adaptability to perturbations. Although it often appears effortless, successful locomotion in service of behavioural goals relies on precise coordination of numerous muscles within and across limbs, as well as a locomotor strategy that, through millennia of evolution, has been optimised not only for speed and trajectory, but also for the body's structure and environmental demands. How an animal's choice of interlimb coordination pattern, or gait, fits into this framework has remained unclear, partly due to a disconnect between biomechanical and neural studies.

Through design of a new experimental paradigm for mice, this thesis lays the groundwork for empirically studying quadrupedal gait as a behaviour that emerges from the interplay between environmental feedback and feedforward motor commands generated in the central nervous system. This new paradigm overcomes the limitations of earlier locomotor methodologies, providing insights that were previously unattainable due to a lack of experimental control over biomechanical constraints or the use of genetically intractable model organisms. It also opens new avenues for exploring the neural circuits at the core of locomotor gait control and offers valuable data for refining neuromechanical models, which will be crucial for achieving an integrated understanding of quadrupedal locomotion. The expanded methodological toolkit for future biomechanics and neuroscience research represents the most direct academic contribution of this work.

Beyond the specific subfield, this thesis contributes to a broader understanding of locomotion as a fundamental animal behavior with deep evolutionary roots. The mechanisms governing gait are thought to be highly conserved, with parallels observed across taxa as diverse as insects and mammals. This universality suggests that locomotion represents an optimised solution to the complex challenge of displacing the body in ways that are energy-efficient, safe, reliable, and adaptable to dynamic environments. Therefore, insights from the present work could also inform comparative studies in evolutionary biology, helping to clarify how different species have adapted their locomotor strategies to meet ecological demands.

Finally, outside of academia, insights from this thesis and future studies using the developed locomotor paradigm could contribute to innovations in robotics and treatments for gait disorders. While modern robots are already quite adept at traversing difficult terrains, understanding the principles behind animal locomotion could inspire further refinements in robot design, potentially expanding the range of their industrial applications. Similarly, an increased appreciation of the neural and biomechanical bases of interlimb coordination could inform therapeutic strategies for individuals with gait abnormalities. While the present work represents only a small step toward understanding the highly optimised system of animal locomotion, interdisciplinary collaboration has the potential to transform these findings into practical solutions that can improve lives.

Acknowledgements

It remains the fault of Icelandic horses that much of the past five years of my life were spent building tiny treadmills, playing with mice, and tinkering with data —but I would not have it any other way. This thesis marks the culmination of a disorderly journey through the highs and lows of scientific discovery that taught me lessons far beyond science and led me back to what matters most. This journey was made all the more meaningful by the support, wisdom, and enthusiasm of many people around me.

First and foremost, I wish to acknowledge **my family** for instilling in me a work ethic and values that allowed me to approach this project with utmost dedication. I am deeply grateful to my mum for her unwavering support and for being an epitome of what it takes for an educated woman to succeed in a male-dominated world. I also wish to honour the memory of my grandma, who embodied these same qualities, and my grandpa, who remains the most selfless person I have ever known. I shall always aspire to make their sacrifices worthwhile. Mīlu jūs līdz sirds dziļumiem.

Second, I wish to recognise the **remarkable colleagues** I have been fortunate to cross paths with. In particular, I am thankful to Egzona, whose friendship and inspiring presence were a major positive influence, and Fede, whose brilliance and generosity helped me transform a rather poorly defined project into something constructive. I am also sincerely appreciative of Steven for his contagious enthusiasm and altruistic sharing of his vast knowledge; of Spencer and Fred for being some of my favourite people to talk motor control with; of Edmund whose pragmatic attitude and unconventional humour helped me stay grounded; of Victoria for her warmth and companionship, and of Marta, Simon, Holly, and Shanice whose shared passion and frustrations brought much-needed camaraderie and support during a difficult time. In addition, I would like to acknowledge Rob, Marcus, Athena, Haran, and Yulin for valuable advice on my project, as well as Yiota, Klara, Karen, Eirinn, Tina, Eleni, Jamie, Jess, and Peter, who went above and beyond their job descriptions to help me navigate various technical aspects of my PhD journey. These colleagues, along with everyone I got to collaborate with in the research culture working group and symposia organising committees, greatly enriched my PhD experience. Working in a hub of invariably talented, driven, and curious individuals has been a real privilege.

Third, I wish to express my heartfelt gratitude to the **Climatematch community**, especially Mariana, Natalie, and Abigail, whose friendship has brought tremendous joy to my life over the past couple of years, and whose intelligence, kindness, and integrity have been truly inspiring. I am also sincerely thankful to Ohad, Ceyda, Jenna, Courtney, and Nick for their support, encouragement, and intellectually stimulating conversations. Thank you all for giving me a chance despite my lack of climate expertise, and for helping me rediscover a sense of purpose and rebuild my self-worth. I have learned so much from each of you and am incredibly proud of what we built together.

Last but not least, I would like to thank my **PhD advisors**: Tiago, for welcoming me to the lab, sharing his wisdom, and supporting me through the second half of my PhD, even though locomotion hardly aligned with his scientific interests; and my initial supervisor Andy, for opportunities and freedom to explore, fail, and learn. While I wish his departure had not cut so deep, it is what ultimately pushed me to explore paths beyond academia and helped me reconcile my past career aspirations with my evolving values. Everything truly does happen for a reason.

Contents

List of Figures

List of Tables

Abbreviations and Notation

AP	anteroposterior
CnF	cuneiform nucleus
CoS	centre of support
CPG	central pattern generator
DTX	diphtheria toxin
Gi	gigantocellular nucleus
GRF	ground reaction force
GTO	Golgi tendon organ
HPD	highest posterior density
IN	interneuron
LF	left forelimb
LH	left hindlimb
LPGi	lateral paragigantocellular nucleus
ML	mediolateral
MLR	mesencephalic locomotor region
MSA	muscle spindle afferents
PA	proprioceptive afferents
PC	principal component
PPN	pedunculopontine nucleus
RF	right forelimb
RH	right hindlimb
SSDO	shortest signed distance to origin
$(x, y]$	half-open interval: excludes x, includes y

Chapter 1

Introduction

Locomotion is the ability to move from one place to another, essential for the survival and adaptation of organisms across the biological spectrum. From protozoans to vertebrates, locomotion facilitates access to nutrients, evasion of threats, separation from waste, and exploration of novel habitats. To achieve these high-level objectives with maximum efficiency, locomotor capacities go hand in hand with animal lifestyles and evolved morphologies. For example, digitigrade feet and a supple spine help carnivores generate impressive speeds, whereas the distal limbs of long-distance travellers have thinner muscles to economise the effort of motion (Hildebrand, 1960). In addition, great behavioural flexibility, such as that displayed by legged animals, requires locomotion to be under elaborate, multilayered neural command (Ijspeert & Daley, 2023). To successfully escape or forage, animals must not only control their movement speed and trajectory, but also uphold a balanced posture against gravity to avoid injury. While healthy animals do this seamlessly and with little conscious effort, it is by no means an easy feat, especially when negotiating uneven terrains. Even the most capable legged robots, endowed with state-of-the-art sensing systems and biomechanically realistic internal models, are not quite as adaptable or efficient in their movement as animals (Bouman et al., 2020; Choi et al., 2023). Indeed, the natural locomotor abilities have been refined by millennia of evolution and involve precise coordination of hundreds of skeletal muscles, as well as the cardiovascular and respiratory systems.

Insight into the control principles of locomotion is important for appreciating animal behaviour more broadly, and has even been proposed as a valuable step towards the development of artificial general intelligence (Zador et al., 2023).

For centuries, locomotor capacity has fascinated and puzzled philosophers, poets, and scientists alike. While some early thinkers recognised the significance of gravity and body mechanics, conceptualising upright gait as a continually prevented fall, the initial discourse on locomotion was dominated by vitalist and physiognomic arguments (Mayer, 2020). In fact, it was not until the advent of chronophotography and experimental neurophysiology late in the nineteenth century that empirical study of locomotion became the norm. Since then, studies of comparative anatomy and biomechanics have characterised interlimb coordination patterns in numerous species (Hildebrand, 1965, 1967), identified the functional advantages conferred by various morphological adaptations (Hildebrand, 1960), and shed light on the energetics of locomotion (Hoyt & Taylor, 1981; Kram & Taylor, 1990). In parallel, neurophysiological investigations have established that the basic locomotor pattern, composed of rhythmic contractions of flexor and extensor muscles, is generated in the spinal cord and modulated by sensory feedback and descending input from the brain (Brown, 1911; Grillner, 2003). Our understanding of the neural basis of locomotion has especially accelerated over the past two decades, largely owing to the cell-type and circuit insights provided by transgenic technologies. These developments have charted the path towards a comprehensive, cellular- and systems-level view of locomotor initiation, speed, reorientation, and termination (Ferreira-Pinto et al., 2018; Kiehn, 2016; Leiras et al., 2022).

One aspect of locomotion that is comparatively less explored, especially from a neural perspective, is interlimb coordination, or gait, which is the focus of this thesis. In the first half of this introductory chapter, I provide a detailed overview of locomotor gait as a fascinating motor phenomenon, discussing its indeterminate definition as both a continuous and discrete behaviour (1.1.1, 1.1.3), its variable expression across quadrupedal animals of different body builds and lifestyles (1.1.2), as well as the internal and external factors that trigger changes in animals' choice of gait (1.1.4). In the second half of this chapter, I examine the current state of knowledge about the neural basis of gait by the three key elements of the locomotor control infrastructure: the spinal cord (1.2.1), the supraspinal circuits (1.2.2), and somatosensory feedback (1.2.3). Lastly, in section 1.3, I propose a reason for the currently limited research into locomotor gait and outline the investigation of gait presented in this thesis.

1.1 Dynamics of locomotor gait

1.1.1 Gait definition

Gait is a core characteristic of locomotion, yet its definition has been a matter of substantial debate. On the one hand, gait is a high-dimensional feature of movement, with multiple degrees of freedom at every joint of every limb. Animals can execute the same sequence of footfalls with foot trajectories and ground contact durations that vary across strides and are even more diverse across individuals (Hildebrand, 1965). An extreme example of this kinematic richness is the use of gait analysis for human identification by surveillance systems (Cresswell & Ott, 2022). On the other hand, the scientific study of gait followed centuries of horsemanship that had distinguished certain interlimb coordination patterns as discrete gaits and had given them names like 'trot' and 'gallop' ("The art of horseback riding", 1895; "Improvement in the gait of trotting horses", 1882; Wutke et al., 2016). Identifying the movement parameters that capture the fundamental nature of gait, while abstracting over the ones that reflect covariates or idiosyncrasies, has not been straightforward (Zug, 1972). Likewise, the field has not necessarily found a consensus on the best way to map the concept of discrete gaits onto an apparent continuum of limb coordination sequences, or whether such a mapping is needed at all (Gonçalves et al., 2022).

Early efforts to quantitatively characterise quadrupedal gait considered a variety of locomotor variables, including stride length, foot elevation, combinations of supporting legs, and the average number of feet in ground contact (Dagg & Vos, 1968a, 1968b; Hildebrand, 1959, 1961; Pennycuick, 1975). Today, even if the details of the analyses differ, most studies follow the minimalist approach devised by Hildebrand (1965, 1977), which specifies gait based solely on the fraction of stride each limb spends in ground contact and how its timing within a stride relates to that of other limbs. In other words, no regard is typically paid to factors like the body posture, the spacing of footfalls, or the exact trajectory of feet during swing, and the only parameters necessary for defining gait are the relative limb phases and the fraction of stride spent in stance. The only measurements required to utilise this definition are the times when each foot strikes and leaves the ground, which can be visualised using 'gait diagrams' (**Figure 1.1**).

Considering that phase and fractional durations are both continuous bounded variables, the space of possible limb coordination patterns is also continuous in principle. At the same time, a small subset of these patterns are commonly designated by specific names inherited from equine practices over the course of centuries. Thus the term 'trot' is ascribed to a mode of locomotion where the body is supported by the diagonal limbs whenever any feet are in ground contact, while the homologous limbs – that is, limbs at the same girdle – move half a stride apart. All footfall patterns that display such anti-phase homologous coordination are collectively referred to as 'symmetrical gaits', other prominent examples being pace and walk. Similar to trot, pace is a two-beat gait wherein pairs of limbs alternately strike the ground together. However, the limbs in these pairs are on the same side of the body, not diagonal. When animals accelerate using either trot or pace, ground contact durations of individual feet can change from nearly 50% to 20% and result in a suspension phase with all feet off the ground at once (Hildebrand, 1965). This is in contrast to walk that is typically seen as a slow gait with two or three legs supporting the body at any given time and the feet striking the ground in four separate beats.

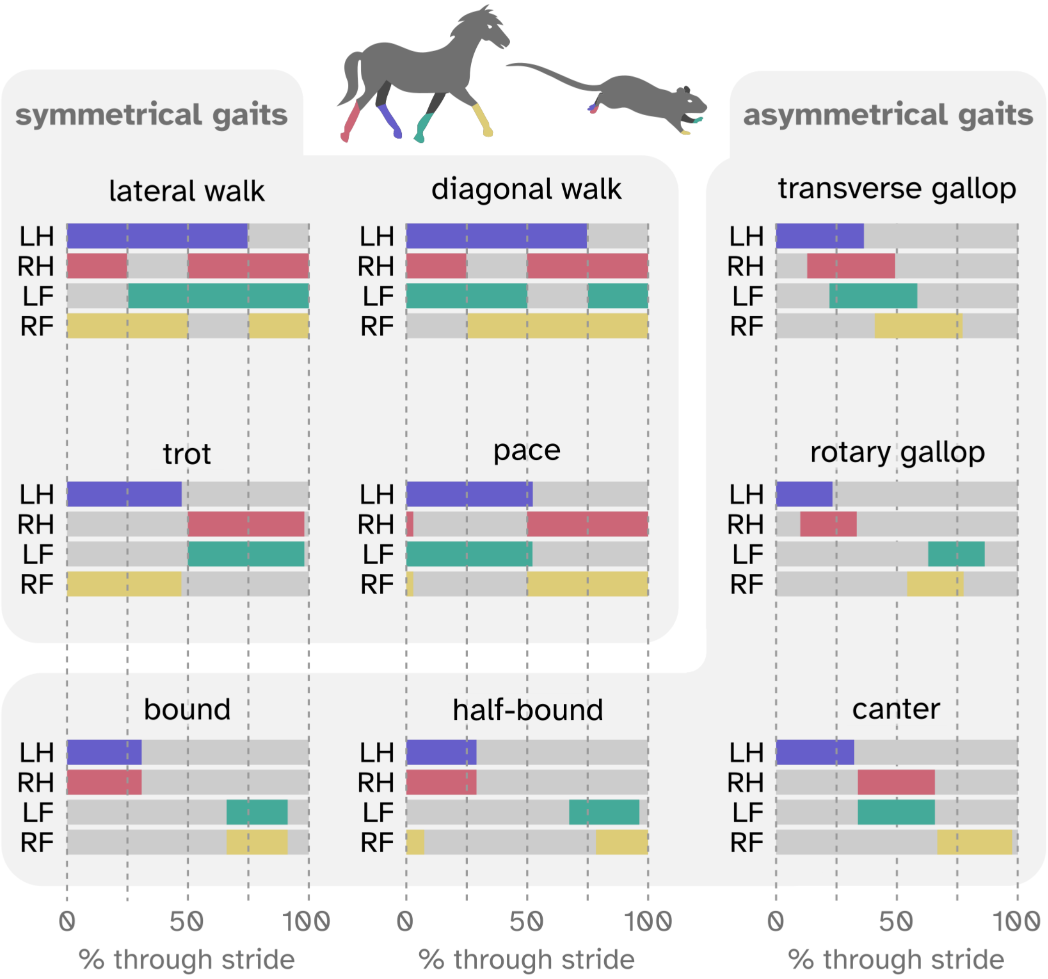

Figure 1.1: Gait diagrams for the main canonical quadruped gaits. Stance phases of left hindlimb (LH), right hindlimb (RH), left forelimb (LF), and right forelimb (RF) are shown in purple, red, teal, and yellow respectively. Swing phases are shown in gray.

Depending on whether a hindlimb step is followed by the homolateral or the diagonal forelimb, the walk is said to have a lateral or a diagonal sequence respectively. Faster symmetrical four-beat gaits include rack, running walk, and amble, but these terms are mostly applied, sometimes ambiguously, to the locomotion of certain 'gaited' horses and will therefore not be considered further in this thesis (Dagg, 1973; Hildebrand, 1965; Vincelette, 2023).

When homologous limbs are not strictly alternating, the gait is considered asymmetrical (Hildebrand, 1977). The fastest gait of this kind for most quadrupeds is gallop, characterised by four unevenly spaced footfalls and one or two suspension phases. Gallops are further categorised as transverse or rotary depending on whether the order of hindlimb footfalls is the same or the opposite as that of the forelimbs respectively. For some small animals, highest speeds can be reached by adopting a left-right synchronous gait called bound, or a variant of it known as half-bound, where only the hindlimbs move in phase. Conversely, in the lower speed range, animals might use canter, which can be seen as a three-beat version of the transverse gallop with one pair of diagonal limbs striking the ground simultaneously. Altogether these named gaits serve as qualitatively distinct examples of four-legged limb coordination patterns, but the utility of such discretisation is debatable and will be discussed in section 1.1.3 below.

1.1.2 Gait expression

With ground contact phases and durations as the variables of interest, the space of theoretically possible limb coordination patterns is vast. However, not all of it is used in practice. In fact, out of the 5040 theoretically possible quadruped footfall sequences estimated by McGhee and Jain (1972), only 21 were found to be expressed by animals based on the comprehensive locomotor surveys carried out at the time (Hildebrand, 1965, 1967; Muybridge, 2012). Hildebrand (1965) surveyed the gaits of over 150 quadrupedal genera without ever observing a symmetrical gait where forelimbs strike the ground just before the respective homolateral hindlimbs. The absence of this locomotor pattern is not well-understood, but has been proposed to arise from an undesirable hindquarter rotation around the load-bearing ipsilateral forelimb and a subsequent exacerbation of the hindleg loading (Hildebrand, 1965). Similarly, animals do not seem to use gaits with ground contact intervals that are very short, very long, or very uneven between the forelimbs and the hindlimbs (Hildebrand, 1977). This makes sense because stance phases need to be long enough to absorb the impact, but not so long or uneven that forward motion becomes discontinuous or staggered.

Besides the limitations common to all quadrupeds, the subset of gaits utilised by any particular species or breed is further constrained by its morphology and locomotor needs. The factors that govern the animal gait repertoire are thought to include stability, energy economy, speed, and avoidance of interference between legs (Hildebrand, 1980).

At low speeds, most quadrupeds use a lateral-sequence walk, with only primates and a few other arboreal and burrowing animals reported to prefer its diagonal-sequence counterpart (Hildebrand, 1965, 1967). During slow walk, when at least three feet are in ground contact throughout the stride, quadrupeds' lateral-sequence preference has been suggested to arise from its superior ability to maintain an animal's centre of gravity within the triangles formed by the supporting limbs and thus provide greater mechanical stability (Gray, 1944). Conversely, the few animals that favour diagonal-sequence walk have been proposed to ensure stability through morphological features, such as a wide stance and large feet, rendering the presumed benefit of a lateral footfall sequence unnecessary (Hildebrand, 1980). Even then, primates have sometimes been found to switch to a lateral-sequence walk, in contrast to the lateral sequence-preferring quadrupeds whose walking capacities seem to be limited to a single footfall order (Vilensky & Larson, 1989). The diagonal sequence being primates' preferred gait despite them having other options suggests that it must confer some unique advantages to these animals. Several studies have posited that this footfall order preference might have co-evolved with prehensile hindfeet (Cartmill et al., 2002; Lemelin et al., 2003) or the primates placing more than half of their body weight on their hindlimbs (Tomita, 1967). To explain the mechanical advantage of these adaptations, the diagonal sequence has been proposed to prevent backward pitching and ensure a stable base of support by placing a protracted hindlimb under the centre of mass prior to forelimb propulsion onto an untested surface (Cartmill et al., 2002; Prost, 1969).

However, these feature correlations do not hold in all primates, with several species found to use a diagonal-sequence walk despite non-grasping hindfeet or high forelimb loading (Demes et al., 1994; Hildebrand, 1980; Schmitt & Lemelin, 2004). Therefore, the relationship between foot morphology, body weight distribution, and footfall sequence is either merely correlative or part of a multiplexed control system alongside factors yet to be recognised. Either way, the primary objective quadrupeds are thought to optimise their walking gait for is stability.

To reach moderate and high speeds, almost all four-legged animals opt for symmetrical running gaits with no more than two feet in ground contact at any time during a stride (Hildebrand, 1965). A notable exception are mammals with sloping backs, such as giraffes, gnus, and spotted hyenas, who transition directly from walk to canter (Pennycuick, 1975). For the majority of quadrupeds, however, the gait of choice is trot, likely because of the mediolateral stability provided by diagonal bipod support (Hildebrand, 1980). While trot is the only symmetrical running gait available to animals with short or splayed legs or stocky build, certain dog and horse breeds have been found to reach higher speeds by switching to pace. This comparatively unstable gait is the only option for long-legged quadrupeds, like camels, who are thought to sacrifice some stability to avoid homolateral leg collisions that would occur in trot (Hildebrand, 1980). Peculiarly, pace is also the running gait of coatis despite their small size and arboreal habitat, indicating that body build is not the sole determinant of bipod gait choice (McClearn, 1992). Another benefit of pace might be energy economy thanks to a limited vertical displacement of the body (McClearn, 1992), but the apparently unique significance of this feature to an expert digger like the coati is not understood.

Finally, at their highest speeds, quadrupeds utilise asymmetrical gaits, trying to balance speed and versatility with stability and energy economy (Hildebrand, 1980, 1989). The latter are primarily associated with the transverse gallop as its footfall sequence lowers the chance of homolateral leg collisions and provides stability through greater diagonal bipod support than the rotary gallop. Transverse gallops are also thought to save energy by propelling the body forward with minimal vertical displacement, although the levelled, near-ground motion of the body is not conducive to sharp turns. Such needs are far better met by the rotary gallop, which involves two suspension phases and thus provides more opportunities for the animal to switch the leading leg and change the movement direction. This manoeuvrability is further aided by the slightly higher speeds and, hence, greater dynamic stability achieved with the rotary gallop. Unsurprisingly then, it is seen as the preferred gallop of agile predators, such as the cheetah and various racing dogs, whereas the transverse gallop is common to long-legged endurance runners like the horse (Hildebrand, 1959). Around 20% of animals are capable of executing both types of gallops at different speeds (Biancardi & Minetti, 2012), and small quadrupeds, such as rodents and rabbits, additionally display bounding gaits. These presumably help them reach high speeds even while navigating rough terrains (Hildebrand, 1980), highlighting how it is likely a combination of body build, behavioural needs, and the environment that determines animals' asymmetrical gait repertoire.

1.1.3 Gait continuum

So far, we have considered a set of discrete limb coordination patterns that reflect qualitatively distinct parts of the quadrupedal gait spectrum in line with the traditional definition of gait (Alexander, 1989). However, the strides that animals naturally display do not always fit these idealised definitions. In fact, it is reportedly rare for the diagonal limbs of a trotting animal to strike the ground at exactly the same time, with near-synchronous coordination observed instead (Hildebrand, 1989). The exact gait definitions, including the extent of deviation in limb phase and ground contact duration that is acceptable for a pattern to be categorised as a certain named gait, vary widely across studies (**Figure 1.2**). This permissible deviation would have been straightforward to derive empirically if the exhibited limb coordination patterns formed non-overlapping clusters around the idealised gaits, but that is not the case.

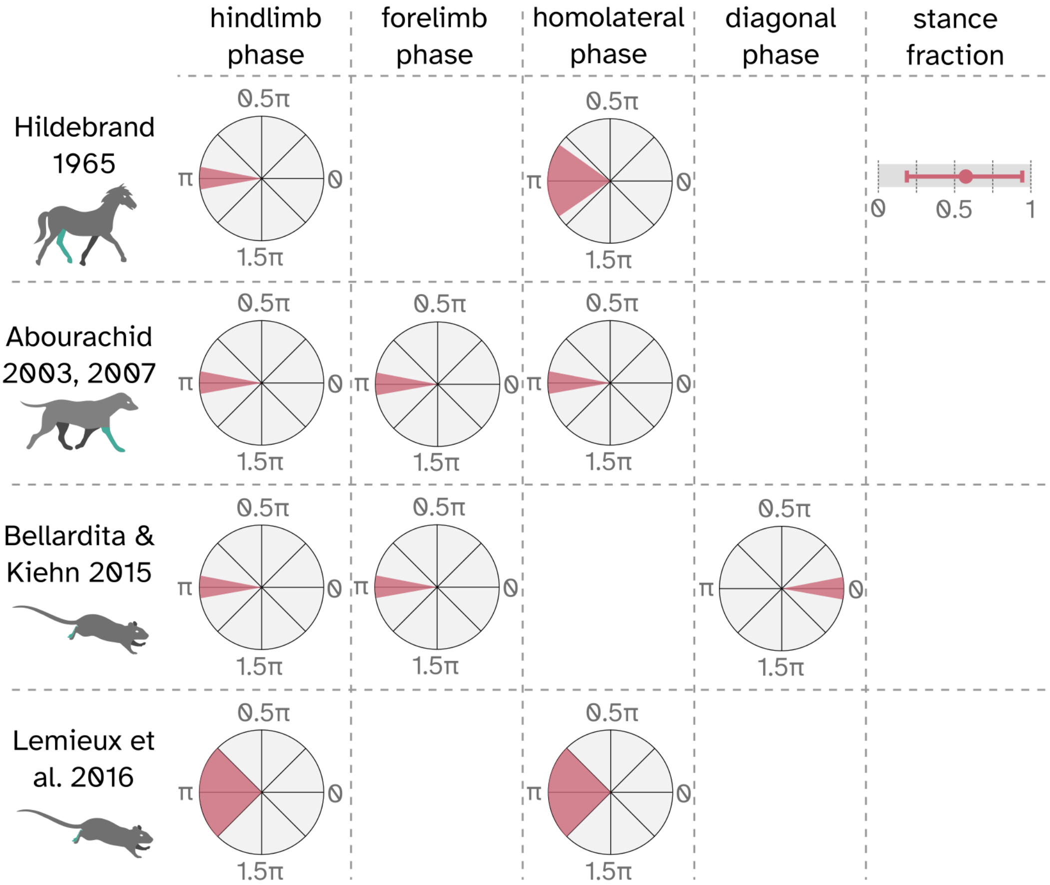

Figure 1.2: Definitions of trot differ across studies. Criteria for labelling an observed stepping pattern as trot are shown for four example empirical studies by different authors: Abourachid (2003), Abourachid et al. (2007), Bellardita and Kiehn (2015), Hildebrand (1965), and Lemieux et al. (2016). All definitions rely on some combination of limb phases and the stride fraction spent in stance, but the exact choice of parameters, their permissible ranges, and the leg used as a reference (shown in teal) vary.

On the one hand, there are numerous accounts of animals switching between canonical gaits abruptly, with few, if any, transitional strides that fit neither discrete gait category (Bellardita & Kiehn, 2015; Maes & Abourachid, 2013; Nauwelaerts et al., 2013; Pennycuick, 1975). On the other hand, studies in horses, monkeys, and other quadrupeds have noted an abundance of 'unclassifiable' footfall sequences in-between the canonical gaits, thus revealing an apparent continuum of limb coordination patterns (Cartmill et al., 2002; Hildebrand, 1980, 1989; Robilliard et al., 2007). The concept of a continuum also applies to the interface of symmetrical and asymmetrical gaits, with several quadrupeds reported to occasionally display coordination patterns that hybridise elements of the transverse gallop and either trot or pace (Eisenstein et al., 1977; Hildebrand, 1977; Robilliard et al., 2007). One such gait, named 'asymmetrical trot', was found to feature trot-like diagonal limb synchrony despite hindlimb asymmetry (Eisenstein et al., 1977). The presence of this and similar intermediate gaits indicates that there is no fundamental mechanical limitation to animals traversing the gait landscape smoothly, even if they do not always do so. In line with this view, and owing to technical advancements, it is becoming increasingly common to describe quadrupedal gait using continuous variables, rather than discrete labels with somewhat arbitrary boundaries (Gonçalves et al., 2022; Machado et al., 2015; Robilliard et al., 2007; Serra Bragança et al., 2020; Starke et al., 2009).

At the same time, there are appealing theories and some corroborating evidence that canonical gaits are biologically meaningful and not merely a simplifying heuristic. For instance, strides at the interface of symmetrical and asymmetrical gaits seem to be scarce compared to intermediate strides within a symmetry type, suggesting that the transition from trot or pace to gallop-like gaits might be discontinuous (Robilliard et al., 2007). Similarly, trot and bound have been found to stand out as the preferred limb coordination patterns of mice, accounting for over 70% of strides at certain moderate and high speed ranges respectively (Lemieux et al., 2016). This observation has led to proposals of these idealised gaits representing stable states, or attractors, that the locomoting system gravitates to over time. Such attractor-based models have been widely used on both neural and behavioural levels to mathematically describe the dynamics of natural systems (Kelso & Schöner, 1988; Khona & Fiete, 2022). In quadrupedal locomotion, this framework has been applied to gait transitions both within and across the hypothesised symmetry boundary (Buchli & Ijspeert, 2008; Schöner et al., 1990), with gait transitions modelled to occur at a critical value of another continuously changing variable, such as waist stiffness, speed, or body tilt (Aoi et al., 2013; Aoi et al., 2011; Buchli & Ijspeert, 2008). Whether any of these variables indeed serve as the trigger of biological gait transitions will be discussed in section 1.1.4. Nevertheless, dynamical systems theory has successfully reproduced several empirically observed features of locomotion, including multistability of gait in certain parts of the parameter space (Schöner et al., 1990) and the past conditions' influence on the system's response known as hysteresis (Aoi et al., 2013; Aoi et al., 2011). Thus, even if the distribution of mechanically possible footfall patterns forms a continuum, it might not be reflective of the gait generation mechanism. It should also be noted that gradual gait transitions appear to be more prevalent in studies that control the speed of the animal using a motorised treadmill and could potentially elicit locomotion at speeds that might otherwise be avoided (Eisenstein et al., 1977; Hoyt & Taylor, 1981). The ways in which experimental systems alter the natural locomotor pattern of an animal remains an open question.

1.1.4 Gait transitions

The gait repertoire of most quadrupeds features at least three canonical gaits, typically including some forms of walk and gallop, as well as trot or pace (Dagg, 1973; Pennycuick, 1975). In section 1.1.2, I considered how the range of interlimb coordination patterns a species displays is constrained by factors like body structure and lifestyle, but those cannot explain shifts between gaits within an animal. An appropriate trigger of gait transitions must show physiological variation in individual organisms and ideally explain the benefit of selecting one footfall pattern over another under specific circumstances. By itself, the evolutionary reason for a given animal to have multiple gaits is not straightforward to intuit.

A good starting point is to consider that there is a strong correlation between gait and speed, with quadrupeds transitioning from walk to trot to gallop as they accelerate (Pennycuick, 1975; Shik & Orlovsky, 1976). During overground locomotion, this relationship often manifests as an expression of different gaits in non-overlapping ranges of speed (Bellardita & Kiehn, 2015; Hoyt & Taylor, 1981). It is also exemplified by the gait transitions that accompany experimentally induced changes in speed, be it through neural stimulation or the use of a motorised treadmill (Caggiano et al., 2018; Hoyt & Taylor, 1981; Lemieux et al., 2016; Shik & Orlovsky, 1976; Wickler et al., 2003). Given that speed is a product of stride frequency and length, having the gait change alongside it is a non-trivial observation that suggests a tight coupling of speed and gait at least at the algorithmic level. At the same time, it should be noted that the association of speed and gait is not deterministic. Gait transition speeds can be very variable both within and across animals, and speeds in their vicinity are usually compatible with multiple gaits (Griffin et al., 2004; Nauwelaerts et al., 2013; Wickler et al., 2003). Moreover, some mammals, most notably horses and humans, can be trained to execute certain gaits outside of their normal speed ranges (Hoyt & Taylor, 1981; Hreljac, 1993; Wickler et al., 2003). Although these insights do not negate the possibility of speed directly controlling gait transition dynamics in line with the model of Diedrich and Warren (1995), the non-obvious benefits of the gait-speed coupling make speed itself an unlikely factor that the system optimises for.

A more widely accepted perspective on gait teleology suggests that animals alter the footfall pattern to achieve and maintain their desired speeds in an energetically optimal manner. Energy consumption of walking and trotting quadrupeds has been shown to change curvilinearly with speed such that there is a single optimum speed for a given gait (Hoyt & Taylor, 1981). Remarkably, the speeds chosen by freely moving horses appear to cluster around the energetic optima of different canonical gaits, whereas gait transitions, as expected, occur close to speeds at which multiple gaits are equally costly (Griffin et al., 2004; Hoyt & Taylor, 1981; Wickler et al., 2003). Several theories have been devised to explain how distinct interlimb coordination patterns could optimise energy expenditure at different speeds. Indeed, even with speed as the control parameter, gait transitions in the model of Diedrich and Warren (1995) were governed by an energy landscape. Other mathematical frameworks have focused on mechanisms for energy exchange, storage, and recovery that minimise muscle work in various gaits, supported by suggestive evidence of these being utilised by quadrupeds of different sizes and locomotor proficiencies (Cavagna et al., 1977; Heglund, Fedak, et al., 1982; Heglund, Cavagna, et al., 1982). As yet another alternative, distinct footfall patterns have been viewed as a means to minimise the energy loss that arises from limb-mediated redirection of body motion upon ground contact, offering an explanation for the limb desynchronisation seen in gallop and walk (Ruina et al., 2005). Although the exact mechanics of gait-mediated energy economy remain uncertain, conservation of energy is commonly accepted as the ultimate reason for animals having multiple gaits (Bertram, 2013). This hypothesis is further strengthened by the spontaneous, speed-dependent emergence of the canonical gaits in minimally constrained quadruped models designed to optimise energy expenditure (Polet & Bertram, 2019; Xi et al., 2016). Nevertheless, the capacity of animals to use gaits that are not energetically optimal, as well as the relatively slow sensing of metabolic steady states, have led to a general consensus that energetic factors cannot serve as the trigger of instantaneous gait transitions (Bertram, 2013; Farley & Taylor, 1991; Granatosky et al., 2018; Griffin et al., 2004; Wickler et al., 2003).

Among the most appealing candidates for the proximate trigger of gait transitions are mechanical factors, consistent with the fast-evolving dynamics of interlimb coordination. Rationalising gait transitions as a means to avoid injury, such potential triggers include peak bone strain and peak vertical ground reaction force (GRF) borne by the limbs. Studies in horses, dogs, and goats of various sizes have shown that these mechanical variables increase in proportion to speed within a given canonical gait and drop sharply at the transitions from trot to gallop or from trot to walk (Biewener & Taylor, 1986; Dutto et al., 2004; McLaughlin et al., 1996; Rubin & Lanyon, 1982). For example, horses carrying extra loads switch from trot to gallop at lower speeds than unloaded horses, yet it happens at the same peak vertical GRF even when the gait transition is unfavourable energetically (Farley & Taylor, 1991). A similar load-dependent shift to left-right synchronous coordination has also been reported under conditions with low frictional load (Duysens et al., 2000; Weihmann et al., 2017) and on inclines (Wickler et al., 2003). The latter is especially interesting because inclines do not affect the absolute load of the legs, but rather redistribute it towards the hindlimbs, suggesting that it might be the relative leg load that triggers changes in gait (Fukuoka et al., 2015). This hypothesis could explain some conflicting results from cats and monkeys whose gait transitions are linked with merely incremental changes in the total GRF (Demes et al., 1994), as well as results from rodents whose trot-to-gallop transition speed is not affected by changes in the absolute leg load (Iriarte-Diaz et al., 2006). It could also serve as a mechanistic basis for the dynamic similarity hypothesis, which considers the speeds of gait transitions as 'equivalent' across mammals with respect to their body size (Alexander & Jayes, 1983). This theory is rooted in reports of a remarkable scaling between numerous locomotor and mass-specific parameters, including stride frequency, stride fraction spent in stance, and metabolic cost, at least among animals of similar body builds (Alexander, 1984; Alexander & Jayes, 1983; Cavagna et al., 1977; Heglund & Taylor, 1988; Heglund et al., 1974). Mathematically, this idea is formalised through a dimensionless speed- and hip height-dependent quantity known as Froude number (F_R) such that mammals as different in size as cats and camels walk at $F_R = 0.1$, trot or pace at $F_R = 1$, and canter or gallop at $F_R > 2$ (Alexander & Jayes, 1983). Still, even if mechanical triggers of gait transitions are consistent with many empirical results and theories, some puzzling discrepancies remain. Most notably, variations in the aforementioned mechanical factors fail to explain the benefits of the reverse gallop-to-trot or walk-to-trot transitions upon deceleration and acceleration respectively, given that these gait changes are associated with a presumably undesirable increase in bone strain, leg load, or both. Therefore, even if leg loading, extension, or bone strain relate to some interlimb coordination changes, it is unlikely that any of these variables could be the sole trigger of all instantaneous gait transitions.

Another plausible trigger of gait transitions is avoidance of falls, also called gait viability, which can manifest as gait stability, evasion of leg interference, and, at least on flat surfaces, gait periodicity (Aoi et al., 2013; Griffin et al., 2004; Shafiee et al., 2024). For instance, quadrupeds have been shown to exhibit greater variability in stride duration as they approach gait transitions, suggesting avoidance of unstable states (Granatosky et al., 2018). Similarly, cats have been found to adopt an uncharacteristic pacing gait in a volatile environment, like a treadmill prone to sudden stops, as it enables longer stance durations and therefore greater stability (Blaszczyk & Loeb, 1993). The importance of gait viability has also been reinforced by recent robotics work, decisively attributing locomotor success in mechanically challenging environments to behavioural policies that prioritise viability over minimisation of energy expenditure or peak leg forces (Shafiee et al., 2024). While gait viability may well be the ultimate objective of gait transitions, with mechanical and energetic factors being of causal importance only when the risk of falls is low, it seems probable that the gait control system relies on a multitude of proximate triggers which might serve a number of cooperating or conflicting goals in different conditions (Cartmill et al., 2002; Ijspeert & Daley, 2023; McMahon, 1985). Further work is required to understand the potentially hierarchical or competing influences of speed, leg load, energy expenditure, and viability on interlimb coordination. This thesis focuses on the first two of these factors.

1.2 Neurophysiology of gait control

Locomotor control involves a complex interplay of neural circuits across different levels of organisation within the central and peripheral nervous systems (Ijspeert & Daley, 2023; Merel, Botvinick, et al., 2019; Rybak et al., 2024). At the effector end of locomotor control, rhythmic whole-body movements are orchestrated by specialised networks of neurons known as central pattern generators (CPGs) in the spinal cord (Goulding, 2009; Kiehn, 2006). Moving up the neural hierarchy, brainstem circuits set task-level variables, such as movement speed and direction, aligning them with the behavioural goals defined by forebrain regions (Ferreira-Pinto et al., 2018; Grillner & El Manira, 2019; Leiras et al., 2022). Throughout this process, sensory input from the periphery is essential for calibrating movement to environmental demands, whether through predictive anticipation or reactive adjustment (Pearson, 1995; Rossignol et al., 2006). While the exact locus of gait control within the locomotor system remains incompletely understood, it has been shown to involve circuits in the spinal cord (Kiehn, 2016), feedback from sensory inputs (Pocratsky et al., 2020), and modulation by descending signals from the brainstem (Gatto & Goulding, 2018). The established and hypothesised gait-related neural structures are illustrated in **Figure 1.3** and will be discussed in the next sections. The topic has also been comprehensively reviewed in Frigon (2017).

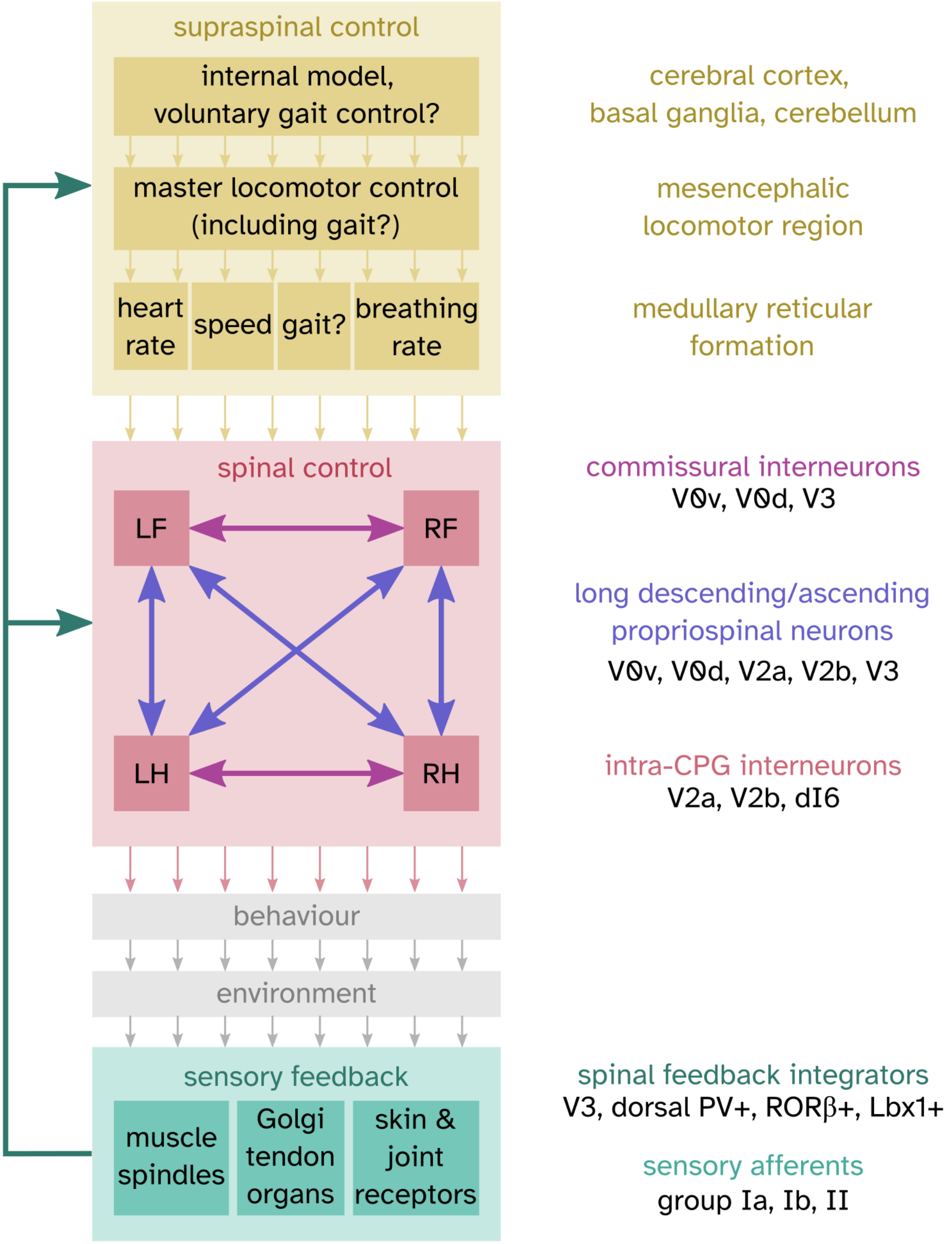

Figure 1.3: Schematic representation of the gait control system. Specific interlimb coordination patterns are generated by spinal circuits (1.2.1) that are modulated by descending commands (1.2.2) and sensory feedback (1.2.3). Spinal and peripheral neurons with established or suspected involvement in gait regulation are listed in association with their likely roles. Uncertain gait-related functions of the supraspinal circuits are flagged by a question mark.

1.2.1 Spinal circuits for gait

The fundamental rhythm and pattern of locomotor-related limb movements are generated by CPG circuits in the spinal cord. As first demonstrated by deafferentation and spinal transection experiments in cats (Brown, 1911; Grillner & Zangger, 1975, 1979), neither supraspinal input nor peripheral feedback is required for basic stepping, with the spinal cord alone capable of producing even multiple patterns of interlimb coordination. From an algorithmic perspective, it is commonly suggested that each leg is controlled by a single CPG (Grillner & Zangger, 1979; Rybak et al., 2015), and a number of theoretical frameworks have been put forward to characterise its activity. Among the most influential of these frameworks, despite its shortcomings, is the classical half-centre model that explains the alternating activity of flexor and extensor muscles trough reciprocal inhibitory connections between the respective motor neuron pools (Brown, 1911; Lundberg, 1981). Limitations of this model, including its failure to accommodate flexible motor neuron recruitment patterns or the partly independent variation of stride duration and stance phasing, have been addressed by subsequent frameworks, such as the unit burst generator and the two-level model (Grillner & El Manira, 2019; Rybak et al., 2015). The former conceptualises CPGs as a collection of partly independent, rhythmogenic, adaptable modules responsible for coordinating several joints within a leg (Grillner, 1981), whereas the latter splits the CPG into a muscle-coordinating 'pattern formation' layer and a hierarchically superior rhythm-generating layer (Rybak, Shevtsova, et al., 2006; Rybak, Stecina, et al., 2006). However, irrespective of CPG organisation, these frameworks generally agree that it is the connections between, not within, the leg CPGs that mediate generation of different gaits (Grillner, 1981; McCrea & Rybak, 2008). By abstracting over the internal CPG structure and modelling them as non-linear oscillators, computational simulations have been able to reproduce the canonical gaits either by changing the relative strength (Stafford & Barnwell, 1985; Yuasa & Ito, 1990) or polarity (Bay & Hemami, 1987) of the interlimb connections, or by modifying the amplitude or frequency of a common, or even limb-specific, external drive (Canavier et al., 1997; Collins & Richmond, 1994; Ijspeert et al., 2005). Similarly successful models of interlimb coordination have been constructed using neural networks with varying levels of biophysical detail (Buono & Golubitsky, 2001; Danner et al., 2017; Danner et al., 2016; Kimura et al., 1999), as well as networks with only weak, if any, direct coupling between leg CPGs (Bellegarda & Ijspeert, 2022; Owaki & Ishiguro, 2017). Thus, in principle, the transition from trot to bound could equally well occur through a weakening of reciprocal inhibitory signalling between the homologous legs (Stafford & Barnwell, 1985), a shift from left-right inhibition to excitation (Buono & Golubitsky, 2001), or an increase in the input from the brain or sensory periphery (Collins & Richmond, 1994). This diversity of plausible mechanisms underscores the importance of empirical insights for understanding gait generation and transitions at both biomechanical and neural level.

From a neurophysiological perspective, the locomotor CPG is composed of a wide variety of spinal interneurons (INs) defined by their laminar position, transcription factor profile, and axonal projection pattern (Goulding, 2009). Several IN subtypes, especially the V0-V3 INs in the ventral spinal cord, have been shown to contribute to interlimb coordination (Grillner & El Manira, 2019; Kiehn, 2016). Since the overall network organisation and dynamics are not agreed upon yet, it is useful to distinguish three functional classes of gait-related INs depending on the pair of limbs they modulate.

Coordination of the homologous legs is primarily attributed to excitatory and inhibitory INs that project across the spinal midline to indirectly influence muscles on the opposite side of the body (Butt & Kiehn, 2003; Lanuza et al., 2004; Quinlan & Kiehn, 2007). In particular, an excitatory subpopulation of V0 INs, called V0v, is implicated in the production of trot because global knockout of these cells has been found to selectively eliminate this highly stable gait from the mouse repertoire (Bellardita & Kiehn, 2015). Conversely, by finding that knockout of the inhibitory V0 INs abolishes left-right alternation specifically at low speeds, the major inhibitory V0 subtype, namely V0d, has been suggested to mediate walk (Talpalar et al., 2013). Both of these neuron subpopulations inhibit contralateral motor neurons either directly (V0d) or via local inhibitory premotor INs (V0v), consistent with a reciprocally suppressive role in left-right coordination (Talpalar et al., 2013). Also supportive of this hypothesis is the exclusively synchronous left-right coordination observed upon genetic ablation of all V0 INs (Bellardita & Kiehn, 2015; Talpalar et al., 2013). However, it should be noted that both V0- and V0v-deficient mice were found to gallop and bound at lower speeds than intact mice (Bellardita & Kiehn, 2015), indicating that V0 INs might additionally contribute to rhythm generation as part of a speed-dependent gait expression pathway. Another component of this pathway is thought to be a Chx10-expressing subset of excitatory, ipsilaterally projecting V2a INs whose downstream targets include the V0v INs (Crone et al., 2008). Although V2a-knockout mice are capable of trotting in general, they have been shown to transition from left-right alternating to synchronous interlimb coordination at lower speeds than their wild type littermates (Crone et al., 2009). V2a INs can therefore be inferred to support left-right alternation specifically at high speeds without necessarily restricting the expression of any gait in particular. Besides providing a neural dimension to homologous limb coordination, these findings demonstrate that gait and speed can be decoupled at least at the level of the spinal CPG.

In contrast to the strong evidence for neurons involved in bilateral alternation, the generation of left-right synchronisation remains enigmatic. A widely favoured candidate for this role is the population of V3 INs because it sends direct excitatory projections to motor neurons and INs on the contralateral side of the spinal cord (Danner et al., 2016; Kiehn, 2016; Zhang et al., 2008). A test of this hypothesis would require V3 IN perturbation at speeds (>90 cm/s) that are preferentially associated with gallop and bound in wild type mice (Lemieux et al., 2016). However, transgenic suppression of V3 IN signalling has been shown to limit the maximum locomotor speed of mice to just 35-40 cm/s (Zhang et al., 2022) consistent with their proposed role in rhythm maintenance and network gain control (Zhang et al., 2024; Zhang et al., 2008). At such low-to-moderate speeds, the animals' strong preference for trot prevents direct examination of the effects of V3 INs on left-right synchronisation, although a role in interlimb coordination has still been observed. In particular, the absence of V3 IN signalling has been found to increase the prevalence of lateral walk beyond its typical speed range, and to evoke gait instability at speeds that are normally associated with a highly stable trot (Zhang et al., 2022; Zhang et al., 2008). Interestingly, detailed network modelling suggests that the instability of trot could result from a loss of just the excitatory connections between the diagonal limb CPGs, while keeping the reciprocal excitation between the homologous limb CPGs intact (Zhang et al., 2022). Whether the latter could still support left-right synchronous gaits at high speeds, as proposed by the simulations (Zhang et al., 2022), awaits empirical investigation. Therefore, a subset of V3 INs remains a plausible mediator of synchronised homologous limb movement, but the anatomical and functional heterogeneity of V3 INs (Zhang et al., 2022; see also Borowska et al., 2015; Borowska et al., 2013) will likely make deeper insight into these neurons' gait-specific contributions conditional on further technical advancement.

Coordination of the homolateral and diagonal limb pairs is thought to be mediated by the long propriospinal neurons that connect the forelimb- and hindlimb-controlling spinal segments at cervical and lumbar levels respectively (Eidelberg et al., 1980; Miller & Van der Meche, 1976). This is a highly diverse set of neurons comprising ascending lumbo-cervical and descending cervico-lumbar subpopulations, both a mix of excitatory and inhibitory projections that are either ipsilateral or commissural (Brockett et al., 2013; Flynn et al., 2017; Ruder et al., 2016). Severing all these connections has been found to completely decouple forelimbs from hindlimbs such that their rhythm and phase become independent (Ballion et al., 2001; Eidelberg et al., 1980; Juvin et al., 2005). More subtle spatiotemporal effects on fore-hind coordination have been recently demonstrated through selective ablation of spinal V2 INs (Hayashi et al., 2023). Subsets of the ipsilaterally projecting propriospinal neuron populations have been identified as the excitatory V2a and inhibitory V2b INs (Ni et al., 2014; Ruder et al., 2016). While separate suppression of these IN subtypes affects left-right coordination (Crone et al., 2009) or flexor-extensor alternation (Britz et al., 2015), mice without both V2a and V2b neurons have been found to delay swing initiation and increase the average spacing between the homolateral limbs (Hayashi et al., 2023). Due to technological constraints, these V2 circuit perturbations were not restricted to the long propriospinal neurons that connect the forelimb and hindlimb CPGs. Nevertheless, their apparent synergistic impact on fore-hind coordination, combined with their presence among the cervico-lumbar and lumbo-cervical neuron populations, makes V2a and V2b propriospinal INs likely contributors to homolateral limb control.

Technical limitations in selectively targeting specific propriospinal neuron subtypes have also made it challenging to distinguish the diagonal connections' contributions to gait control from those of bilateral projections between the homologous legs. In fact, a computational model has been able to recapitulate speed-dependent gait transitions without any diagonal connectivity whatsoever (Danner et al., 2016). Still, left-right hindlimb alternation has been found to persist after a midsagittal transection of the lumbar spinal cord (Cowley & Schmidt, 1997), indicating an ability of the forelimb CPG to rescue homologous coordination at the other girdle. Moreover, ablation of the descending or ascending propriospinal neurons has been shown to increase the prevalence of left-right synchronisation at low speeds and in specific environmental contexts (Pocratsky et al., 2020; Ruder et al., 2016). Although these fore-hind interactions could be mediated by the ipsilaterally projecting propriospinal neurons alone, it seems more likely that the prominent excitatory contralateral projections between the cervical and lumbar spinal segments also play a role (Ruder et al., 2016). This is especially probable given that many of these neurons belong to the V0v IN subtype (Ruder et al., 2016), which is associated with controlling the diagonally synchronised trotting gait as described above (Bellardita & Kiehn, 2015). Irrespective of the exact circuitry, it is clear that the long propriospinal neurons are involved in both fore-hind and left-right coordination, reflecting a useful redundancy in the gait control system.

Also worth noting are the Dmrt3-expressing inhibitory dI6 INs that are considered part of the locomotor CPG despite residing in the dorsal spinal cord (Perry et al., 2019). A homozygotic non-sense mutation in the DMRT3 gene is strongly associated with the unique pacing ability of Icelandic horses and expression of non-standard ambling gaits in other horse breeds (Andersson et al., 2012). However, this subtle phenotype has not yet been possible to recapitulate in mice, with Dmrt3-mutant animals displaying impairments in both interlimb and intralimb coordination, as well as a dramatic reduction in locomotor speed (Andersson et al., 2012; Vallstedt & Kullander, 2013). Further experiments, such as selective dI6 IN inactivation (Kiehn, 2016), will be necessary to determine these neurons' exact contributions to the control of gait.

1.2.2 Supraspinal circuits for gait

A supraspinal structure widely recognised for coordinating task-level features of locomotion is the mesencephalic locomotor region (MLR). Over 50 years ago, seminal work in decerebrate cats demonstrated that electrical stimulation of this area can reliably trigger forward locomotion at a speed proportional to stimulus strength (Shik & Orlovsky, 1976; Shik et al., 1966). The changes in speed were accompanied by gait transitions such that cats walked at low speeds, trotted at intermediate speeds, and galloped at high speeds in line with their natural locomotor behaviour (Miller et al., 1975). These functions of the MLR are highly conserved across the vertebrate subphylum, evoking stepping in legged animals and undulation in fish (Ryczko, 2022). They are also supplemented by MLR-induced activation of respiratory and cardiovascular structures to meet the growing oxygen demands of active muscle (Chang et al., 2021; Gariépy et al., 2012; Hérent et al., 2023). Alongside its effects on speed and gait, these broad physiological capacities of the MLR position it as a master controller of locomotion (Noga & Whelan, 2022).

Anatomically, the MLR is composed of the cuneiform (CnF) and pedunculopontine (PPN) nuclei that contain spatially and genetically defined subsets of neurons with distinct effects on speed and gait (Ryczko, 2022). For instance, vGlut2-expressing CnF neurons preferentially support escape-like high-speed locomotion using left-right synchronous gaits, although bilaterally alternating stepping, as in walk and trot, can be evoked as well (Caggiano et al., 2018; Dautan et al., 2021; Josset et al., 2018; Roseberry et al., 2016). Optogenetic stimulation of these neurons elicits kinematically normal forward movement and does not impede obstacle avoidance, allowing the animal to brake and turn as necessary (Van der Zouwen et al., 2021). Conversely, glutamatergic neurons of the PPN, depending on their spatial distribution, projection targets, and transcription factor profiles, can either initiate low-speed exploratory movement with left-right alternating gaits (Caggiano et al., 2018), halt all motor output in a striking pause-and-play manner (Goñi-Erro et al., 2023), or support forelimb-mediated behaviours, such as grooming and handling (Ferreira-Pinto et al., 2021). With only about 20% of glutamatergic PPN neurons modulated by speed (Caggiano et al., 2018), their functional diversity has likely contributed to the conflicting effects on locomotion observed in studies that stimulated these neurons relatively indiscriminately (Caggiano et al., 2018; Carvalho et al., 2020; Dautan et al., 2021; Josset et al., 2018). A similar heterogeneity is suspected among the MLR neurons that express gamma-aminobutyric acid (GABA) or acetylcholine, the latter found exclusively in the PPN (Leiras et al., 2022; Roseberry et al., 2016). For the GABAergic neurons, the dominant behavioural outcome upon optogenetic activation is deceleration and locomotor cessation, presumably through suppression of their local glutamatergic counterparts (Caggiano et al., 2018; Roseberry et al., 2016). In contrast, the cholinergic PPN neurons have been variably reported to slightly boost or slow movement speed, prolong locomotor duration, and modulate the stepping pattern through stance phase extension (Josset et al., 2018; Roseberry et al., 2016; Smetana et al., 2010; Xiao et al., 2016). Acting at long latencies and unable to initiate locomotion on their own (Roseberry et al., 2016), these PPN neurons are unlikely to have a central role in moment-by-moment control of speed or gait. Overall, there is strong evidence in favour of the glutamatergic neurons of the MLR, and especially CnF, controlling locomotor speed. It is not clear whether the MLR directly hosts cells dedicated to gait control or if its apparent influence on gait reflects a secondary effect of speed modulation, mediated by gait-specific neurons in downstream brainstem regions or the spinal cord.

Candidate regions for gait control in the lower brainstem include the lateral paragigantocellular (LPGi) and gigantocellular (Gi) nucleus among other medullary regions that receive notable input from CnF (Caggiano et al., 2018; Dautan et al., 2021). The LPGi is likely part of the MLR-mediated speed control pathway, with its glutamatergic and glycinergic populations acting through bilateral spinal projections to promote and halt locomotion respectively (Capelli et al., 2017). The neighbouring Gi has been shown to trigger locomotion upon unilateral stimulation from CnF (Ferreira-Pinto et al., 2021), and to mediate braking and reorientation in response to input from other midbrain and forebrain structures (Cregg et al., 2020; Cregg et al., 2024; Usseglio et al., 2020). Although computational modelling has demonstrated the viability of separate brainstem pathways for the control of speed and gait (Ausborn et al., 2019), no gait-specific effects have been reported for either LPGi or Gi. It is possible that identification of such neurons merely requires a more nuanced neural targeting approach or a behavioural paradigm that enables dissociation of speed- and gait-related effects.

Alternatively, it might be that the MLR-induced changes in gait are implemented at the level of spinal CPGs or mechanical feedback in response to a scalar, speed-related signal from the brainstem. Multiple implementations of CPG phase oscillator models with various forms of sensory feedback have demonstrated that certain network configurations can generate and transition between the canonical interlimb coordination patterns in response to a single descending drive (Aoi et al., 2013; Fukuoka et al., 2015; Harischandra et al., 2011; Owaki & Ishiguro, 2017). At the same time, the existence of a supraspinal gait control pathway seems likely at least in humans and horses, considering these species' ability to perform certain gaits outside of their natural speed ranges (Hoyt & Taylor, 1981; Hreljac, 1993; Wickler et al., 2003).

Although the neural mechanism for these apparently voluntary aspects of gait control is unknown and even simpler quadrupeds are able to alter their interlimb coordination for obstacle avoidance (Drew & Marigold, 2015; Warren et al., 2021), larger animals have been generally proposed to employ a more model-based approach to locomotor control, with descending modulation exerting a more significant influence (Ijspeert & Daley, 2023). This difference is also reflected in the locomotor neuroanatomy such that the MLR has a notable direct projection to the upper spinal cord in monkeys and cats (Castiglioni et al., 1978; Satoda et al., 2002), but only a minor fraction of spinal neurons are targeted in mice (Caggiano et al., 2018). It is therefore plausible, if not probable, that the gait control architecture comprises varied components across species, and mechanistic insights from animals of different phylogenetic origins should be interpreted with appropriate caution.

1.2.3 Somatosensory feedback circuits for gait

As established in 1.2.1, the basic locomotor rhythm can be generated by central mechanisms alone. However, sensory input is crucial for calibrating these central commands to the specific body and environment, enabling smooth and stable movement in a dynamically changing world (Rossignol et al., 2006). Although recent work has highlighted the locomotor contributions of the vestibular system and begun to incorporate visual input in models of locomotion (Akay & Murray, 2021; Gay et al., 2013; Shafiee et al., 2024), the most prominent source of sensory feedback for gait control remains the musculoskeletal system. This system provides information on key biomechanical features, such as joint position, body orientation, and leg load, which have all been linked to the generation of different gaits (Farley and Taylor, 1991; Fukuoka et al., 2015; Owaki and Ishiguro, 2017; Owaki et al., 2013; Shafiee et al., 2024; Shao et al., 2021; Yu et al., 2023, see also 1.1.4) and can exert their influence through at least three routes. First, cutaneous stimulation during locomotion has been found to evoke reflex responses in all four legs, indicating the possibility of direct interlimb modulation by somatosensory feedback (Hurteau et al., 2018). Second, biomechanical information can influence interlimb coordination through local intralimb adjustment, such that leg loading and hip extension modulate stance duration and thus affect the relative timing of swing onsets across the limbs (Duysens & Pearson, 1980; Hiebert et al., 1996). Finally, a third likely route for biomechanical feedback to affect gait is via long feedback loops that involve ascending pathways to the brain (Bosco & Poppele, 2001; Ijspeert & Daley, 2023), but this indirect influence, ultimately reflected in descending signals, will not be considered further here.

At the level of sensory transduction, biomechanical feedback is encoded by muscle spindles, Golgi tendon organs (GTOs), as well as low-threshold mechanoreceptors in joints and skin. For a thorough review of their anatomical and functional properties, see Duysens et al., 2000; Proske and Gandevia, 2012; Rossignol et al., 2006. In brief, muscle spindles are stretch-sensitive proprioceptors in skeletal muscle, innervated by large-diameter primary (group Ia) and small-diameter secondary (group II) afferent fibres that relay information to the spinal cord. By responding to changes in muscle length and the rate of this change, muscle spindles provide an indirect measurement of joint angles (Akay & Murray, 2021; Wei et al., 1986), serve as accessory detectors of load (Duysens et al., 2000), and thus contribute to the swing-to-stance and stance-to-swing transitions (Akay et al., 2014; McVea et al., 2005). Although these intralimb actions have plausible consequences on interlimb coordination, genetic knockout of muscle spindle afferents gives rise to a broadly ataxic phenotype that makes interlimb-specific impairments difficult to observe in traditional locomotor settings (Akay et al., 2014). Nonetheless, through clever experiments in variable leg-load conditions, it has been found that an absence of muscle spindle afferents can be partly compensated by intact GTO signalling. GTOs are tension-sensitive proprioceptors located at the muscle-tendon interface and connected to the central nervous system by large-diameter group Ib afferents. They are considered the primary receptors of gravitational, frictional, and inertial load (Duysens & Pearson, 1980), yet their individual contributions to gait control remain unclear due to the current technical challenges in selectively perturbing these receptors. At the same time, concurrent loss of both GTO and muscle spindle afferents produces a pronounced ataxia such that animals are dragging their feet and can no longer reach high movement speeds (Takeoka & Arber, 2019). Besides complicating empirical investigation of gait-specific effects, the severity of this proprioceptor-deficient phenotype suggests that the locomotor-related role of joint and skin receptors is comparatively minimal. Indeed, selective removal of low-threshold cutaneous feedback has been found to produce relatively minor changes in joint movements that become easily noticeable only in demanding locomotor conditions, and gradually recover in the presence of supraspinal input (Bouyer & Rossignol, 2003a, 2003b). Whether these receptors contribute specifically to gait control is yet to be determined.

Downstream of the sensory afferents, proprioceptive and cutaneous feedback is integrated with central gait control circuits, including those described in 1.2.1. For example, V3 INs have been reported to receive direct proprioceptive input and undergo selective activation during weight-bearing locomotion (Borowska et al., 2013; Laflamme et al., 2023). For a more subtle effect, reversible silencing of the long ascending propriospinal neurons has been found to make homologous coordination context-dependent such that left-right alternation dominates only in attention-demanding locomotor settings, specifically a slippery surface and nose-down 'exploratory' movement (Pocratsky et al., 2020). On the one hand, these tasks have been hypothesised to engage greater supraspinal control (Pocratsky et al., 2020). On the other hand, they are associated with higher frictional load and gravitational hindlimb load, suggesting that the long ascending propriospinal neurons might promote left-right alternation in a leg load-dependent manner. A recent theoretical study potentially reconciles these ideas by proposing that generation of slow, exploratory locomotion requires extra-spinal modulation due to a non-oscillatory operational regime of spinal networks, and either supraspinal or peripheral input can suffice (Rybak et al., 2024). Further evidence for load-dependent support of bilaterally alternating gaits comes from inducing a specific population of normally ipsilateral dorsal premotor neurons downstream of proprioceptive afferents to develop aberrant contralateral projections (Satoh et al., 2016). Such rerouting of leg load-related information was shown to abolish left-right alternating coordination, except under weight-bearing conditions (Satoh et al., 2016). A slightly different effect, namely an expanded speed range for left-right alternating gaits, has been reported after selective ablation of inhibitory, parvalbumin-expressing deep dorsal horn INs that integrate proprioceptive and cutaneous input (Gradwell et al., 2024). In addition to somatosensory feedback, these neurons receive input from another class of inhibitory dorsal INs, ones expressing RORβ, which have been shown to control the gain of locomotor-related somatosensory afferent transmission through pre-synaptic inhibition (Koch et al., 2017). This kind of central gating of proprioceptive and cutaneous feedback highlights the interdependent nature of the gait control system and underscores the importance of integrative approaches in its exploration.

1.3 Summary and research overview

In this chapter, I have summarised a substantial body of evidence showing that locomotor gait is controlled by not only central mechanisms, but biomechanical factors as well. However, the enhanced access to neural circuits over the past few decades has led the field to primarily focus on a few genetically manipulable species and the conventional locomotor paradigms designed for them. These approaches often neglect the biomechanical aspects of movement and fail to capture the full range of movement speeds and patterns characteristic of the studied species. Consequently, locomotor features likely influenced by the body biomechanics, such as gait, have been explored notably less than, for example, motion speed or redirection. To glean insight into the computational logic of gait and its neural implementation, it is important to consider both the close association between gait and supraspinally defined locomotor features, such as speed, and its dependence on somatosensory feedback.

In this thesis, I describe a novel locomotor paradigm that enables independent modulation of speed and body biomechanics in mice (Chapters 2 and 3) and use it to explore the descending and feedback influences on interlimb coordination (Chapter 4). After identifying notable leg load-related influences on homolateral and hindlimb phase preferences, I probe the causal involvement of proprioceptive feedback in these relationships by testing proprioceptive afferent-deficient mice on the same experimental setup (Chapter 5). Finally, I conclude with a general discussion (Chapter 6) on how this work lays the foundation for further investigation of the neural basis of gait in a behaviour-driven manner.

Chapter 2

Materials and methods

2.1 Experimental procedures

2.1.1 Animals

All experiments were performed under the Animals (Scientific Procedures) Act of 1986 (PPL PE4FA53CB) following local ethical approval. Male and female mice were housed on a reversed 12 hour light-dark cycle with experiments carried out during the dark phase. Animals were group-housed when possible and had ad-libitum access to food pellets and water. Surgeries were performed on 7-9 weeks old mice. Passive treadmill and load sensor experiments described in Chapters 3 and 4 were done with 10-20 weeks old Vglut2-ires-Cre mice (Jackson Laboratory stock #016963). Motorised treadmill experiments in Chapter 4 involved 6-9 weeks old Vglut2-ires-Cre and C57BL/6J wild type (Charles River 027) mice. All experiments in Chapter 5 used 10-15 weeks old Egr3-knockout mice (Tourtellotte & Milbrandt, 1998), PV-Cre;Avil-iDTR mice (derived from Jackson Laboratory stock #008069 and Stantcheva et al. (2016) following Takeoka and Arber (2019)), and littermate controls. Animals were weighed at least once a week during all behavioural procedures.

2.1.2 Neural manipulation and tissue processing

2.1.2.1 Viruses

For optogenetic triggering of locomotion in vGlut2-Cre mice, 23 nL of AAV1-EF1a-DIO-hChR2(H134R)-EYFP (titre 1.0×10^{13}, Sainsbury Wellcome Centre Viral Vector Core, henceforth SWC VVC, from Addgene plasmid #20289) were injected unilaterally into CnF at AP -5.0, ML 1.2, DV -3.0 mm from bregma. Control mice received the same injection but were of the C57BL/6J phenotype. These mice had no perceptible reaction to the optical stimulus and were not used for data acquisition.

In Egr3-knockout, PV-Cre;Avil-iDTR mice, and their littermates optogenetic initiation of locomotion was achieved by injection of 200 nL AAV1-CaMKIIa-hChR2(H134R)-EYFP (titre 1.8×10^{14}, SWC VVC from Addgene plasmid #26969) into CnF.

A subset of vGlut2-Cre and wild type mice used in the motorised treadmill experiments had received a bilateral CnF injection of 23 nL AAV2-EF1a-DIO-iChloc-2A-dsRed (titre 1.1×10^{14}, SWC VVC from Addgene plasmid #70762) for a separate experiment. These mice showed no discernible reaction to the optical stimulus, did not differ from intact mice in their locomotor performance (one-way ANOVA, $p = 0.29$), and were therefore pooled for analysis. Data from these mice was used as a control specifically for analysis of homolateral phase presented in 4.2.1. The motorised treadmill results presented in 4.2.2, specifically Figures 4.8 and 4.11, are based on mice with unilateral CnF surgeries as described above.

2.1.2.2 Surgical procedures

Mice were anaesthetised with 4% isoflurane and maintained under anaesthesia for the duration of the surgery with 1.5-2.5% isoflurane (both in oxygen

1 L/min). Analgesia was provided through subcutaneous administration of meloxicam (5 mg/kg).

Viral vectors were delivered via pulled 3.5” glass pipettes (Drummond scientific) at a speed of 23 nL/s with a Nanoject II injector (Drummond scientific) coupled to a stereotaxic frame (Kopf model 902). Optic fibre cannulae (New Doon, FOC-C-1.25-200-7.0-0.37) and stainless steel headplates were affixed to the skull using a combination of light-cured (RelyX Unicem 2, 3M) and self-curing (Superbond, C&B) dental cement.

2.1.2.3 Diphtheria toxin delivery

Three weeks after surgery, PV-Cre;Avil-iDTR mice and their littermates received intraperitoneal injections of up to 100 μg/kg diphtheria toxin (DTX; Sigma D0564). Experimental testing started 5 days after DTX injection.

2.1.2.4 Histological processing

At the end of all behavioural experiments (2.1.3), mice were anaesthetised with intraperitoneally injected pentobarbital (Euthatal or Dolethal 30 μg/kg) and transcardially perfused with 10-15 mL of 0.01 M phosphate buffered saline (PBS) followed by 4% paraformaldehyde solution in PBS. Brains were post-fixed at room temperature overnight and cut into 50 μm coronal sections on a vibratome (Leica VT1000 S).

To locate the boundary between the target region (CnF) and its neighbouring PPN, brain slices were immunohistochemically stained for choline acetyltransferase (ChAT). Sections were first permeabilised and blocked in a solution containing 1% bovine serum albumin (BSA, Cambridge Bioscience) and 0.3% Triton X (VWR International Ltd) in 0.01 M PBS for 1.5 hours at room temperature, on a shaker. In parallel, goat anti-ChAT (Millipore AB144P, 0.1

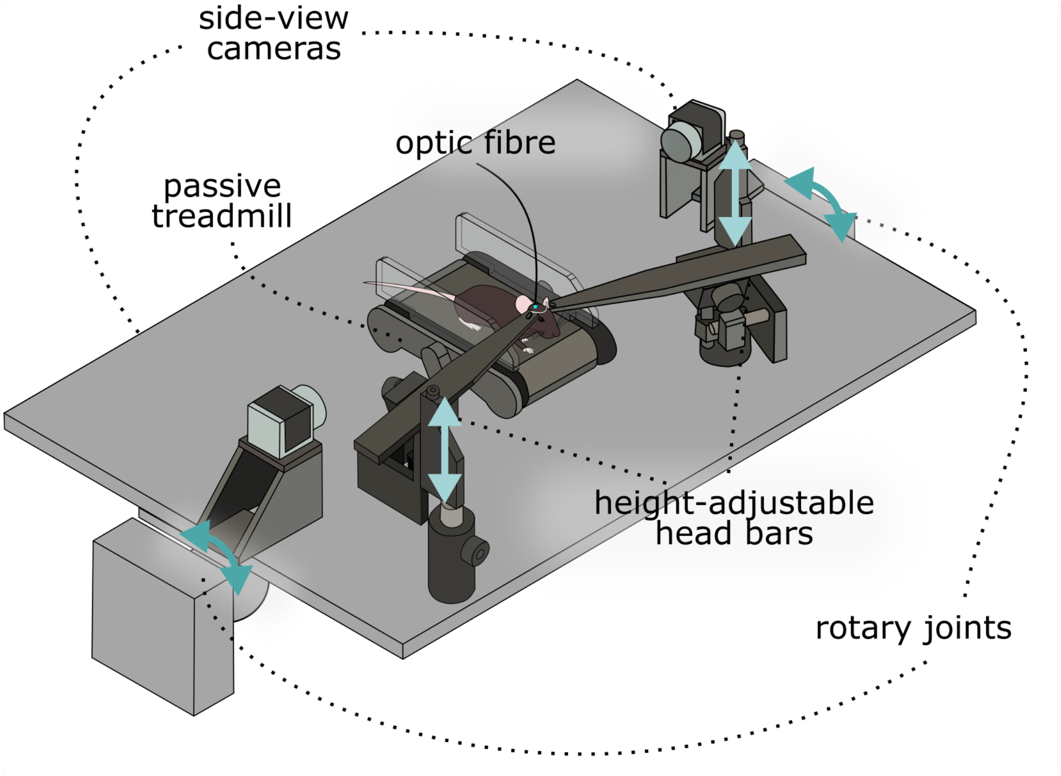

Figure 2.1: Passive treadmill setup. A schematic representation of the passive treadmill setup that allows modulation of mouse head height (lighter arrows) and surface slope (darker arrows), while evoking forward locomotion through optogenetic stimulation of glutamatergic neurons in the cuneiform nucleus.

mg/mL, 1:100 dilution) was pre-incubated with an anti-goat Fab fragment (Jackson Immunoresearch AF594, 1.6 mg/mL) in a solution containing 1% BSA and 0.1% Triton in 0.01 M PBS for 1.5 hours at 37°C The sections were subsequently incubated in this primary antibody solution for 3 days at 37°C on a shaker. This was followed by three 30-minute washes with the 1% BSA, 0.1% Triton PBS solution and a final 30-minute wash with PBS. Finally, the sections were counterstained and mounted with DAPI Fluoromount-G (Southern Biotech), and imaged at 1.3 μm/px resolution on an epifluorescent microscope (Zeiss Axio Imager 2). A selection of slices was also imaged at 270 nm/px resolution on a confocal microscope (Leica SP8).

2.1.3 Behavioural procedures

Ahead of any behavioural procedure or habituation period, mice were handled for 15 minutes on two consecutive days to acclimatise to the experimental room and the experimenter.

2.1.3.1 Passive treadmill locomotion

After recovering from surgery, mice underwent a 10-day habituation period on the passive treadmill setup, adapting to head fixation, blue light flashes, and manipulations of head height and surface slope (**Figure 2.1**). Daily habituation sessions gradually increased in duration from 15 to 50 minutes. In each session, head-fixed mice sat unperturbed on a low-friction non-motorised treadmill, custom-made using the documentation and source code released by the Janelia Research Campus (Jackson et al., 2018). Head height, surface slope, or both were changed several times during each session, depending on the type of experiment the mice were going to engage in. Drops of condensed milk were delivered at randomised intervals to mitigate stress. In the last three habituation sessions, animals were exposed to low-intensity overhead flashes of blue light to acclimate to the visual component of the optogenetic stimulus.

Following the habituation period, 5-second optical stimuli (10-50 Hz, 10 mW at fibre tip) were delivered with a 473 nm laser (Shanghai Laser & Optics Century) for 20-25 trials daily to induce locomotion. Only the mice that showed reliable locomotor responses to the stimulation were used in the experiments. Videos of the left and right side views were recorded at 400 frames per second using a pair of cameras (Basler acA1920-150um). Data acquisition, camera trigger, and optogenetic stimulation were synchronised through a PCIe-6351 board (National Instruments) and controlled using Bonsai (Lopes et al., 2015).

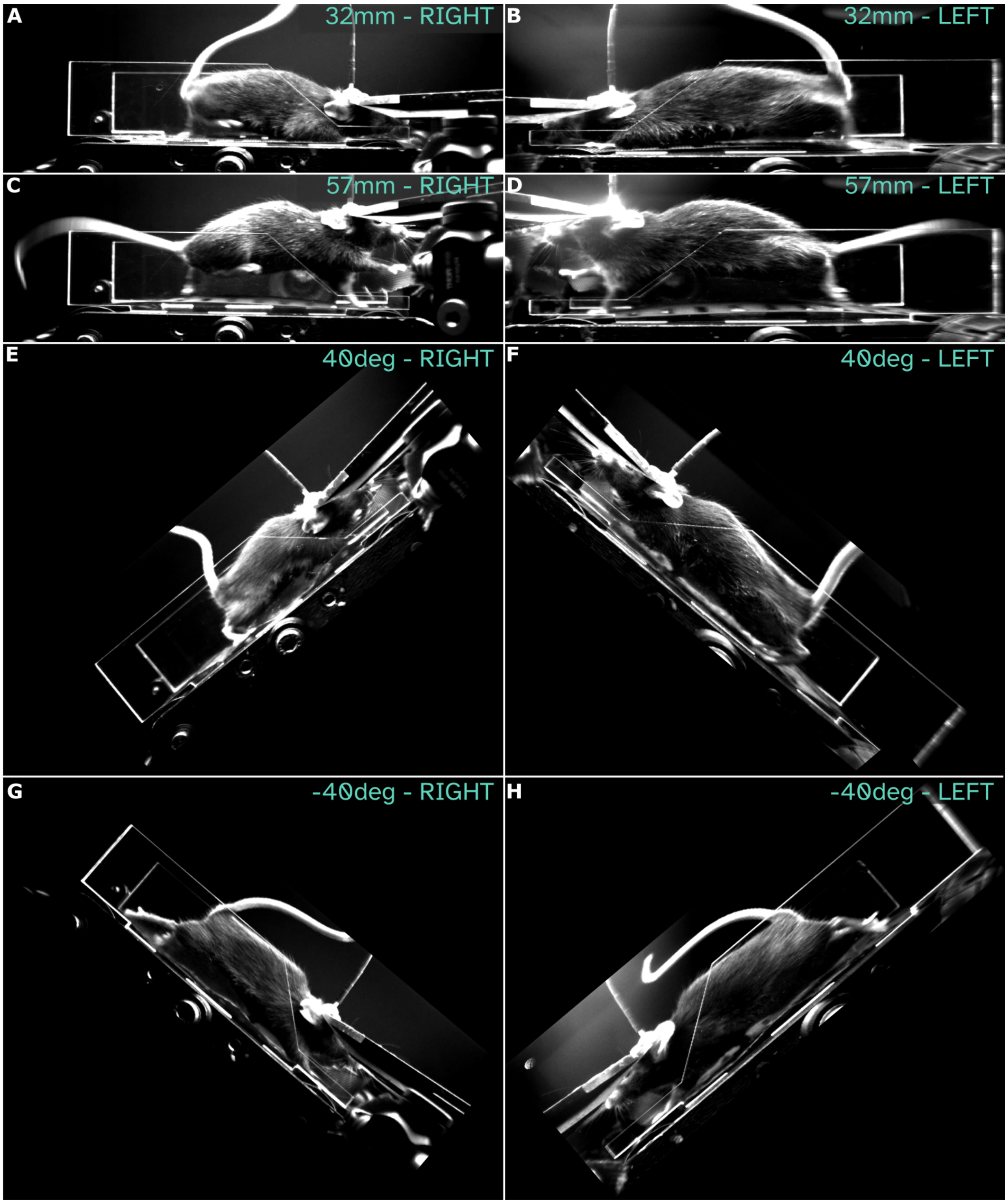

Figure 2.2: Trial configurations on the passive treadmill setup. **(A-H)** Video frames of a representative mouse, illustrating the extreme configurations of head height (A-D) and surface slope manipulations (E-H), filmed from right (A, C, E, G) and left (B, D, F, H) sides.

Somatosensory feedback to the animal was manipulated with two types of trials. In head height trials, the height of the head fixation apparatus was controlled over a range of 32-57 mm above ground with ±0.1 mm precision and without any change in head rotation. Surface grade was fixed at 0 degrees. In surface slope trials, the grade of the treadmill, the head fixation apparatus, and the cameras were jointly changed in 5±1 deg increments over a [-40, 40] degree range, while keeping the head fixed at 44 mm above ground. The same ranges of head heights and surface slopes were used during habituation and experiments. **Figure 2.2** shows the extremes of these ranges.

2.1.3.2 Leg load measurements

Headplated vGlut2-Cre mice were head-fixed on a set of four aluminium single point load cells (Tedea Huntleigh, dimensions: 11 x 3.3 x 1 cm) such that each cell supported exactly one foot, similar to the configuration described in Morina, 2023. Analogous to the passive treadmill experiments, this force sensor setup allowed independent manipulation of head height and surface slope (**Figure 2.3**). One set of trials was performed modifying animal head height over a range of 32-57 mm above ground with ±0.1 mm precision. In another set of trials, setup grade was changed between -40 and 40 degrees with the head fixed at 37 and 44 mm above ground. Two different head heights were used in this experiment to characterise the impact of head height on slope-dependent changes in load distribution (see 2.2.2.3).

Load cells were calibrated ahead of each recording session. Load measurements were amplified 250000x and high-pass filtered at 100 Hz (pre-amplifier MA103S and amplifier MA102S, both custom-built in the Neuroscience Electronics Lab, University of Cologne), digitised at 1428 Hz (Cambridge Electronic Design Power1401), and recorded in Spike2 software (Cambridge Electronic Design). In parallel, videos with the right side view of the mouse were acquired at 100 Hz using Bonsai (Lopes et al., 2015). Only trials with mice standing still for at least 5 seconds were included in analysis. Individual force components could not be measured with this setup.

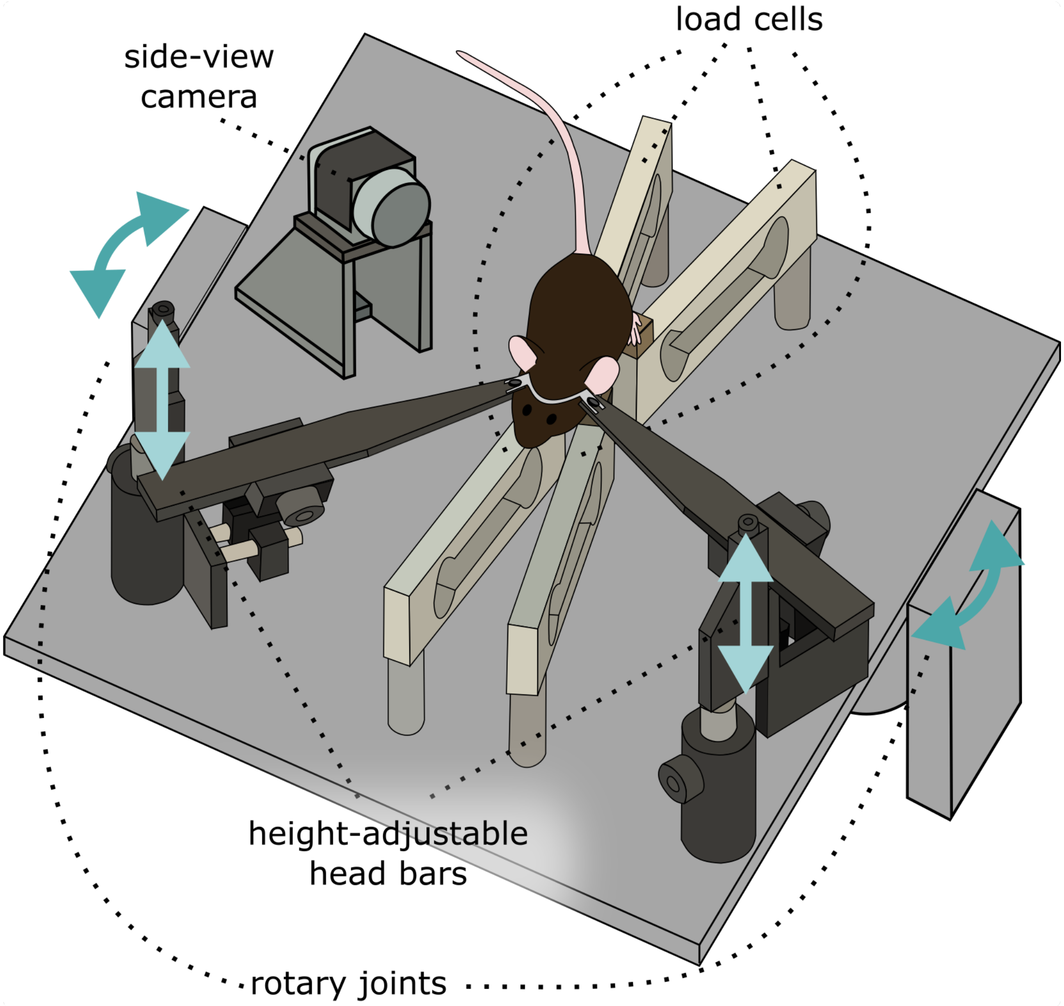

Figure 2.3: Force sensor setup.
A schematic representation of the force sensor setup that allows precise measurement of the load borne by each leg during modulation of mouse head height (lighter arrows) and surface slope (darker arrows).

2.1.3.3 Motorised treadmill locomotion

Experiments began with a 15-minute habituation session that allowed mice to freely explore the motorised treadmill setup (model 009, custom-built in the Neuroscience Electronics Lab, University of Cologne) and experience three 30-second episodes of treadmill movement at 5 cm/s. Afterwards, animals were trained on the treadmill for up to 10 consecutive days. During this period, non-restrained mice underwent 8-12 locomotor trials per day, each lasting 15 seconds. The maximum treadmill speed, ranging from 15 to 150 cm/s, was gradually increased over days based on animal performance using Spike 2 software (Cambridge Electronics Design). Treadmill speed output was used to trigger video data acquisition in a closed-loop manner through a PCIe-6351 board (National Instruments) and Bonsai (Lopes et al., 2015). Videos from both right and left sides were recorded at 400 frames per second using two cameras (Basler acA1920-150um).

2.1.3.4 Open field locomotion

An open field arena was constructed from a transparent acrylic platform (35 x 35 cm) with 30 cm tall opaque walls. Animal behaviour was recorded from below at 100 frames per second using an industrial camera (Basler acA1920-150um). Starting two weeks after surgery, mice were placed in the arena for 3 minutes per day, 9 sessions in total. A 5-second optical stimulus (10-50 Hz, 10 mW at fibre tip) was delivered with a 473 nm laser (Shanghai Laser & Optics Century) in the middle of each session.

2.1.3.5 Sound-triggered escape locomotion

To observe natural high-speed locomotion, a shelter was placed along the short wall of an elevated 20 x 60 cm open field arena, analogous to the arena described above (2.1.3.4), and mice were exposed to threatening auditory stimuli to evoke escape responses. In particular, prior to experiments, wild-type mice were single-housed to increase their baseline stress level. During each experimental session, the mice were first allowed to explore the arena unperturbed for 7 minutes. Subsequently, when the mice entered a threat area located ∼10 cm from the wall opposite the shelter, they were pseudorandomly exposed to an aversive auditory stimulus composed of three consecutive upsweeps from 17 to 20 kHz over 3 s (Evans et al., 2018). Each session lasted up to an hour but was terminated earlier if the animals did not leave the shelter for 20 minutes.

2.1.3.6 Ataxia scoring

Egr3-knockout mice and DTX-injected PV-Cre;Avil-iDTR mice are ataxic (Takeoka & Arber, 2019; Tourtellotte & Milbrandt, 1998). To characterise the ataxic phenotype and maintain high standard of animal care, mice were assessed every 1-3 days using a dedicated rubric (**Table 2.1**) developed in consultation with the Named Veterinary Surgeon. Before Egr3-knockout mice reached 7-8 weeks of age, this assessment was carried out by the Neurobiological Research Facility at the institute.

2.2 Quantification and statistical analysis

2.2.1 Pose estimation from videos

Tracking of the four feet, snout, tail base, and either hump (side view) or body centre (bottom view) was performed using DeepLabCut (versions 2.1.10.4 and 2.3.8, Lauer et al., 2022; Mathis et al., 2018; Nath et al., 2019; **Figure 2.4**). Twenty frames were labelled in each video, with 95% of those used for training. Most neural networks were trained for 650000 iterations in single-animal mode using ResNet-101 as a starting point. The only exception was the open field model that was trained for 30000 iterations in multi-animal mode based on DLCRNet. In all cases, default training parameters were used and the networks were validated with 10 shuffles. Video dimensions and number, as well as the corresponding train and test errors for each model are shown in **Table 2.2**.

In the passive and motorised treadmill experiments, further analysis included only those trials where at least 90% of the predicted ‘snout’ and ‘hump’ labels and at least 80% of the predicted ‘left hindlimb’ (primary reference limb)

Table 2.1: Rubric for assessment of ataxic phenotype. If the phenotype matched any criteria in the red-coloured cells, the animal was humanely euthanised.

Observation	Score 0	Score 1	Score 2	Score 3	Score 4	Score 5
Forelimb dragging	No dragging	Limited motion of one or both legs	Occasional dragging	Constant dragging	Attempts to move without success	Does not attempt to move
Hindlimb dragging	No dragging	Limited motion of one or both legs	Occasional dragging	Constant dragging	Attempts to move without success	Does not attempt to move
Forelimb splaying	No splaying	Brief splaying, single incidents within motion episode	Repeated splaying within motion episode, but can move in straight line	Constant splaying with limited coordination	Attempts to move without success	Does not attempt to move
Hindlimb splaying	No splaying	Brief splaying, single incidents within motion episode	Repeated splaying within motion episode, straight line motion possible	Constant splaying with limited coordination	Attempts to move without success	Does not attempt to move
Wobbling	No wobbling	Wobbles while moving or still	Both wobbles and falls	Falls from side to side whenever moving	Falls onto side and cannot get up	N/A
Head posture	Normal posture	Head slightly down	Head down, not corrected when approached	N/A	N/A	N/A
Trunk posture	Normal posture	Slightly lower walking posture	Belly dragged when moving	N/A	N/A	N/A

labels had a tracking likelihood equal to, or greater than, 0.95. The predicted body part coordinates were processed with custom Python scripts to estimate postural and kinematic variables, including snout-hump angle, speed, and in-

Table 2.2: Training set composition and performance metrics of DeepLabCut networks used for pose estimation on the experimental setups described in 2.1.3. Separate networks were used for videos of ataxic mice to capture their distinct motor phenotype. Due to changes in setup appearance over time, different models were also trained for the three load sensor experiments. Standard deviations are shown for train and test errors. Mouse size refers to snout-to-tail-base length and torso height (side view) or width (bottom view) irrespective of leg extension.

Experimental setup	**Mouse size in video (mm)**	**Number of training videos**	**Train error (mm)**	**Test error (mm)**
Passive treadmill, right side view	65 x 21	72	0.34 ± 0.01	1.97 ± 0.20
Passive treadmill, left side view	64 x 21	72	0.26 ± 0.02	1.73 ± 0.22
Passive treadmill (ataxic), right side view	64 x 22	27	0.25 ± 0.02	1.58 ± 0.30
Passive treadmill (ataxic), left side view	64 x 22	20	0.17 ± 0.01	1.75 ± 0.26
Motorised treadmill, right side view	65 x 24	50	0.56 ± 0.02	1.55 ± 0.13
Motorised treadmill, left side view	64 x 22	50	0.48 ± 0.02	1.49 ± 0.16
Load sensor head height trials	67 x 23	48	0.55 ± 0.05	0.80 ± 0.16
Load sensor slope trials	64 x 23	27	0.28 ± 0.02	0.65 ± 0.07
Load sensor Egr3 knockout	66 x 23	15	0.30 ± 0.01	0.97 ± 0.20
Open field, bottom view	65 x 22	15	0.84 ± 0.02	2.18 ± 0.61

terlimb phase (2.2.3.1).

2.2.2 Quantification of variables related to posture and leg load

2.2.2.1 Computing body weight distribution in head-fixed mice

The distribution of body weight at different head heights and surface slopes was derived from body weight measurements and load cell recordings of stationary mice (2.1.3.2) based on the weight calibration of load cells. Body weights were measured within no more than 3 days before and after load cell recordings and interpolated accordingly. Without head fixation, the total weight recorded by the four load cells would be expected to match animal body weight. In the presence of head fixation, there can be a difference between the two measures due to the tensile or reactive force arising from the animal's interaction with the head fixation apparatus.

A detected load less than the body weight indicated that the mouse had transferred some of its weight onto the head fixation apparatus. Conversely, when the detected load exceeded the body weight, it likely reflected a combination of body weight and reactive force due to the mouse actively pushing against the headbars.

In surface slope trials, it was possible to measure the distribution of a fraction of body weight equal to $\cos(\theta) \cdot weight$ where θ is the incline or decline angle. This was taken into account when computing the fraction of body weight transferred onto the head fixation apparatus. Since the same scaling applied to the readings of all four load cells, slopes did not affect the fractional weight distribution across limbs.

2.2.2.2 Computing centre of support

Centre of support (CoS) was approximated along the anteroposterior and mediolateral body axes based on the fraction of total recorded weight w_i placed on each foot i:

$$CoS_{AP} := w_{RF} + w_{LF} - (w_{RH} + w_{LH})$$

$$CoS_{ML} = w_{RF} + w_{RH} - (w_{LF} + w_{LH})$$

Interactions with the head fixation apparatus were ignored for this metric.

2.2.2.3 Computing weight-adjusted head height

A given absolute head fixation height likely results in different body weight distributions depending on animal size. To account for these size-related differences, a dimensionless variable called *weight-adjusted head height* was derived

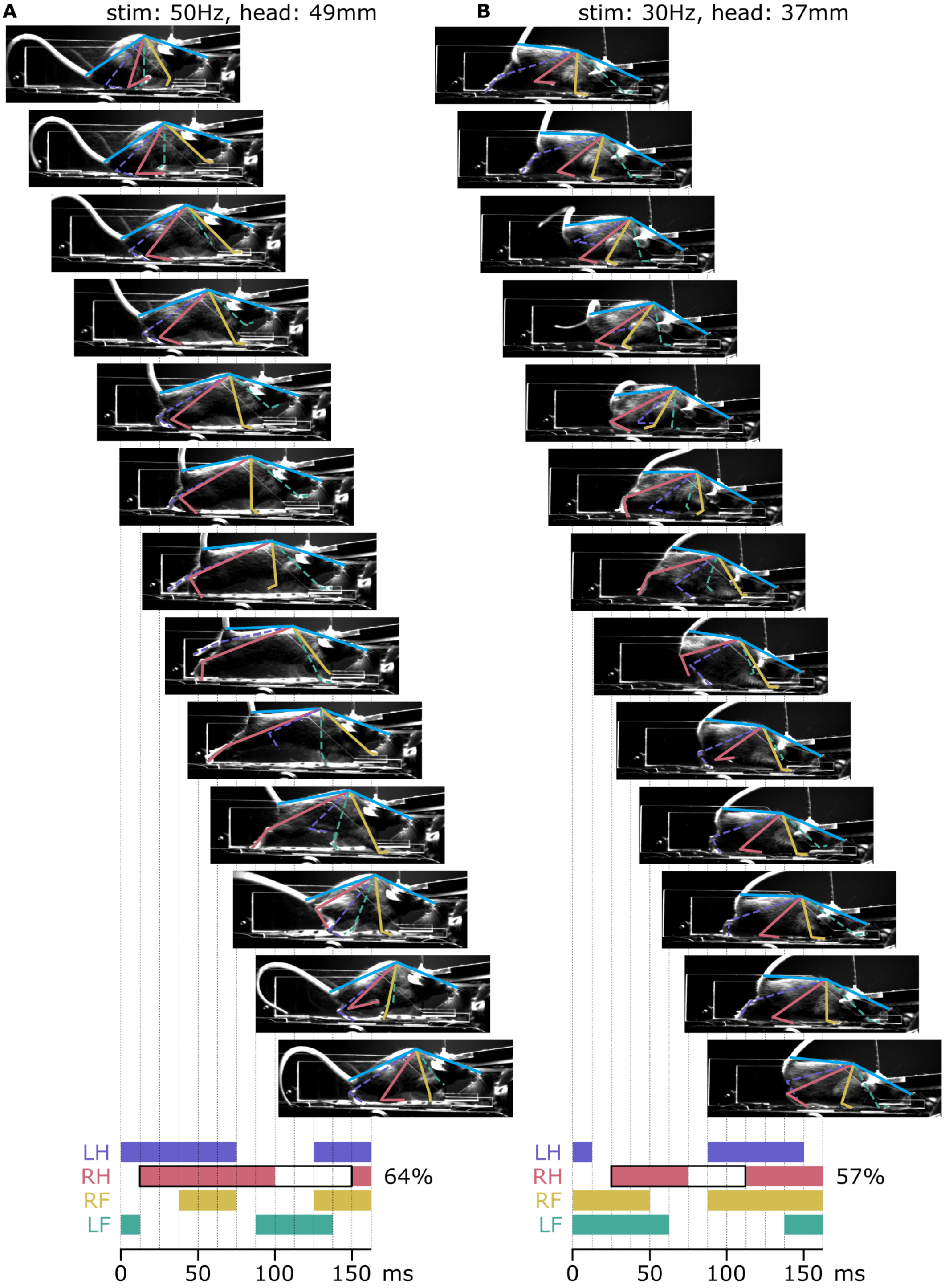

Figure 2.4: Tracking of body parts and stride parameters on the passive treadmill.
(A-B) A sequence of non-consecutive video frames from the right side-view camera, spanning a 162.5 ms window from two example trials on the passive treadmill. The displayed snapshots are five frames apart, with the tracked skeleton superimposed. The corresponding gait diagrams at the bottom highlight a single right hindlimb stride and its duty factor. Note that the trajectories of the left hindlimb and forelimb were tracked using the left side-view camera, so their respective skeletons are shown by dashed lines.

using body weight as a proxy for mouse size. In particular, it was assumed that there is a linear relationship between body weight and the maximum comfortable head height, namely the maximum height at which the forefeet of a mouse were in full contact with the ground. This relationship was estimated empirically by manipulating head height in 1 mm increments and observing forefeet contact with the ground (n=8 mice; **Figure 2.5 A**). The following relationship was derived:

$$\text{Maximum comfortable head height} = 24.5 + 1.25 \times \text{Weight}$$

Thus, the maximum comfortable head heights of 22 and 27 g mice were estimated to be 52 and 57 mm above ground respectively.

Using the above equation, weight-adjusted head heights were computed by first calculating the animal weight for which a given absolute head fixation height would be the maximum comfortable head height, and then dividing it by the actual animal weight.

$$\text{Weight-adjusted head height} = \frac{\text{Physical head height} - 24.5}{1.25 \times \text{Weight}}$$

Thus, a weight-adjusted head height value of 1 corresponded to the maximum height at which the forefeet of a typical mouse of a certain weight were in full contact with the ground.

Surface slope trials were performed with all mice head-fixed at 44 mm above the ground, which was near the middle of the comfortable head height range. For animals of different sizes, this absolute head height translated to weight-adjusted head heights between 0.62 and 0.68. Considering the statistically significant associations between weight-adjusted head height and the load-related variables measured in the surface slope trials (see Figures 3.1 and 3.2 in section

3.2.1), fixing the head at the same absolute height can be expected to result in different baseline weight distributions across mice. To test this expectation, I fit a linear mixed-effects regression model with the anteroposterior CoS as the dependent variable, surface slope as the independent variable, and a random intercept for mouse identity:

$$CoS_{AP} \sim \text{slope} + (1|\text{mouse ID})$$

The random intercepts of this regression reflect the anteroposterior CoS on a levelled surface for individual mice. Except for one animal whose CoS was positioned far more anteriorly than expected based on its size, this measure of weight distribution was moderately correlated with body weight (Pearson correlation coefficient: 0.49; **Figure 2.5 B**). To further explore the impact of head height on surface slope, the experiment was repeated with a 7 mm lower head height. The previous mixed-effects regression model was extended to include the absolute head height as both a fixed effect and a random slope:

$$CoS_{AP} \sim \text{slope} + \text{head height} + (\text{head height}|\text{mouse ID})$$

Since the relationships between weight-adjusted head height and the load-related variables of interest are non-linear (see 3.2.1), the effect of a 7 mm change in the absolute head height can be expected to depend on body weight, being smaller for heavier animals. This measure is reflected by the absolute values of the random slope coefficients that were indeed found to display a moderate negative correlation with animal weight (Pearson correlation coefficient: -0.67; **Figure 2.5 C**).

Overall, these observations confirm that using the same absolute head height for all mice contributed to the observed variability in leg load recordings across animals. Adjusting head height individually based on body weight would have likely reduced this variability. Nonetheless, this experimental caveat is not expected to significantly impact the general conclusions, given that the variability in weight-adjusted head height across mice was relatively small (coefficient of variation: 3% and 11% on force sensors and treadmill respectively; **Figure 2.5 D**) and the variability in leg load was comparable in head height and slope trials (p=0.68, *t-test*; see Figures 3.1, 3.2, 3.4). Additionally, instead of head height, the majority of analyses relied on the snout-hump angle, which served as a weight-independent proxy for animal posture.

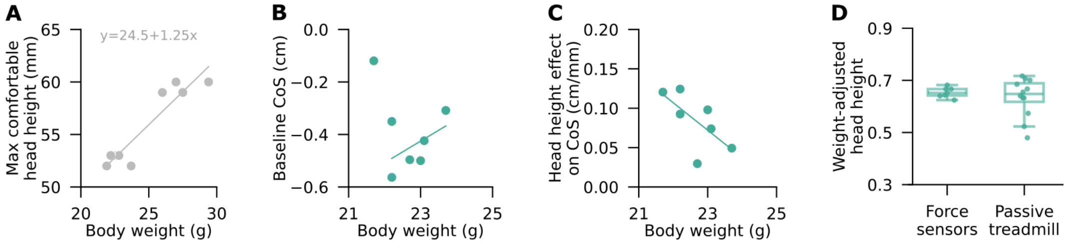

Figure 2.5: Body weight-related variability in maximum comfortable head height or leg load distribution at a single head height.
(A) Maximum head height at which the forefeet are in full contact with the ground plotted as a function of body weight, along with the line of best fit. Its equation was used to estimate weight-adjusted head height. **(B-C)** Baseline CoS (B) and effect size of a 7 mm change in head height on CoS (C) plotted as a function of body weight. Data points represent individual mice. Lines of best fit are shown, not including the outlier in the top left corner of panel (B). **(D)** Distribution of weight-adjusted head heights in slope trials on the force sensors and the passive treadmill.

2.2.2.4 Comparing animal posture across setups

Animal posture was characterised using a set of pose-related features, specifically snout-hump angle, head pitch angle, hump-tailbase angle, and the height of the body and tailbase relative to the right hindfoot. Postural differences across experimental setups were first quantified on a per-feature basis using Cohen's d. For a more comprehensive analysis across multiple features, the data were balanced with respect to experimental setup, split into train (75%) and test (25%) sets, standardised, and subjected to principal component analysis to extract the primary vectors of variance. A support vector classifier was then trained on the top two principal components to classify postural data according to the experimental setup it was acquired on. Classifier accuracy was evaluated using 5-fold cross-validation, and the receiver operating characteristic (ROC) curve was used to analyse its discriminative ability. Note that head pitch angle was excluded from the cross-feature analysis, as it remained constant at 10.75 deg in head-fixed experiments.

2.2.2.5 Linear regression analysis of non-circular variables

Linear relationships between two non-circular variables were characterised by fitting three types of simple or multiple linear regression models: a fixed-effects model ($y \sim x$), a random intercept model ($y \sim x + (1|mouse)$), and a random slope and intercept model ($y \sim x + (x|mouse)$). These models were implemented using the *lm* function from the base R package (version 4.1.2) and the *lmer* function from the $lme4$ package (version 1.1.28, Bates et al., 2014). Inclusion of random effects allowed for capturing potential heterogeneity in the relationship between the examined variables across individual mice. Model residuals were examined to assess model fit and check for potential violations of the model assumptions, such as non-normality or homoscedasticity. Model selection was based on the lowest Akaike Information Criterion value, which indicated a better trade-off between model complexity and goodness of fit. Tables 2.3, 2.4, 2.5, and 2.6 below show regression parameters for the linear relationships reported in the following chapters. The significance of fixed-effects predictors in mixed-effects models was assessed through Student's t-tests with Satterthwaite's degrees of freedom method, as implemented in the $lmerTest$ package (version 3.1.3). To study linear relationships between more than two variables while accounting for group-level variability, the approach described above was extended to multiple linear mixed-effects regression.

Table 2.3: Parameters of simple linear regression models $y = A + Bx$. Asterisks (*) mark the models that are related to the named figures, but excluded for brevity.

Figure	y	x	A	B
3.4B	Forelimb weight fraction	Surface slope	0.36	-0.003
3.4B	Hindlimb weight fraction	Surface slope	0.60	0.007
3.4D	Total leg load	Surface slope	96.8 %	0.4 %/deg
4.4*	Stride length	Surface slope	-8.7 cm	0.003 cm/deg
4.4*	Stride length	Snout-hump angle	4.5 cm	0.08 cm/deg

2.2.2.6 Exponential regression analysis of non-circular variables

When the relationship between two linear variables displayed saturation behaviour, it was characterised with an exponential decay model:

$$y = A - Be^{-kx}$$

where y is the dependent variable, x is the independent variable, A is the asymptote, B is the scale factor, and k is the rate constant.

Initial parameter estimates were derived as follows: A was estimated as the maximum observed value of the dependent variable, B was estimated as the difference between the initial value and the estimated asymptote, and k was estimated as the inverse of the mean of the independent variable values.

Curve fitting was performed using the $curve\_fit$ function from the $scipy.optimize$ library in Python. This function uses non-linear least squares to fit the model to the data. The fitted parameters were obtained along with their standard errors and covariance matrix. Statistical significance of the fitted parameters was assessed using Student's t-tests. Independent samples were compared with the log likelihood ratio test by evaluating whether a combined regression model provides a significantly better fit than separate models.

Table 2.4: Parameters of simple linear random intercept models $y = A + Bx + (1|mouse)$. Asterisks (*) mark the models that are related to the named figures, but excluded for brevity.

Figure	y	x	A	B
3.1C	Hindlimb weight fraction	Weight-adjusted head height	0.54	-0.05
3.4C	Anteroposterior CoS	Surface slope	-0.23 cm	-0.01 cm/deg
3.5C	Snout-hump angle (load sensors)	Surface slope	162	-0.18
3.5C	Snout-hump angle (passive treadmill, stationary)	Surface slope	151	0.08
3.5D	RH foot position (load sensors)	Surface slope	8.2 cm	0.02 cm/deg
3.5D	RH foot position (passive treadmill, stationary)	Surface slope	9.3 cm	-0.02 cm/deg
3.7A	Mean speed	Stimulation frequency	39 cm/s	0.46 $\mathrm{cm \cdot s^{-1}Hz^{-1}}$
3.7A	Max speed	Stimulation frequency	115 cm/s	0.71 $\mathrm{cm \cdot s^{-1}Hz^{-1}}$
3.8Ai	Stride length	Speed	4.4 cm	0.017 s
3.8Aii	Stride frequency	Speed	7.3 Hz	0.04 $\mathrm{Hz \cdot s^{-1}cm^{-1}}$
3.8Aiii	Hindlimb duty factor	Speed	0.70	-0.002 s/cm
4.6A	Snout-hump angle (passive treadmill, locomoting)	Surface slope	160	0.08
4.6A	Snout-hump angle (motorised treadmill)	Surface slope	155	0.06
4.6B	RH foot position (passive treadmill, locomoting)	Surface slope	7.6 cm	-0.02 cm/deg
4.6B	RH foot position (motorised treadmill)	Surface slope	-1.26 cm/deg	-0.01 cm/deg
5.4D	Hindlimb weight fraction (MSA-deficient)	Weight-adjusted head height	0.009	-0.11
5.4F	Anteroposterior CoS (MSA-deficient)	Weight-adjusted head height	-0.01 cm	-1.15 cm
5.4I	Anteroposterior CoS (MSA-deficient)	Snout-hump angle	0 cm	-0.05 cm/deg

Table 2.5: Parameters of simple linear random slope and intercept models $y = A + Bx + (x|mouse)$.

Figure	y	x	A	B
3.2B	Mediolateral CoS	Weight-adjusted head height	0.10 cm	0.24 cm
3.3B	Anteroposterior CoS	Snout-hump angle	-0.26 cm	-0.05 cm/deg
3.3B	Mediolateral CoS	Snout-hump angle	0.08 cm	0.01 cm/deg

2.2.3 Quantitative analysis of interlimb coordination

2.2.3.1 Quantifying interlimb phase

Interlimb coordination was characterised by estimating the phases of limb movement relative to a reference limb. Throughout this thesis, limb phase is defined relative to the step cycle of the left or right hindlimb. The only exception is the computation of homologous phase at the pectoral girdle, for which the left forelimb is used as the reference. Irrespective of reference limb identity, the quantification of phase was based on the time series of tracked foot positions (see 2.2.1), specifically focusing on the time periods where the speed of the self-paced or motorised treadmill belt exceeded 1 cm/s indicative of locomotion. The reference foot time series was segmented into strides by applying a peak detection algorithm to the respective horizontal coordinate time series given that peaks and troughs marked swing and stance onsets respectively. Strides were defined as the intervals between consecutive stance onsets (**Figure 2.6 A**). Next, to compute the relative phase of each non-reference limb, its horizontal coordinate time series was cross-correlated with that of the reference limb for every stride of duration d over delays in range $[\frac{-d}{2}, \frac{d}{2}]$. The peak of this time series cross-correlation corresponded to the interlimb phase difference and was subsequently normalised by stride duration to yield a value in interval $[-0.5, 0.5]$ or $[-\pi, \pi]$ in polar coordinates (**Figure 2.6 B**). If the phase values of two independently tracked points on the same foot differed

Table 2.6: Equations for multiple linear mixed-effects regression models fitted on passive treadmill data, and the significance of their coefficients. Fixed effect predictors are highlighted in bold; p values in brackets represent the results of two-sided t-tests.

Fig 4.4E: Shift in PC3 ~ **speed** * **snout-hump angle** * **slope** + **trial type** + (snout-hump angle + slope |mouseID)
intercept: n.s. (0.93), **speed**: n.s. (0.31), **angle**: *** (6×10^{-7}), **slope**: n.s. (0.59), **trial type**: n.s. (0.07), **speed x angle**: *** (1×10^{-41}), **speed x slope**: n.s. (0.08), **angle x slope**: *** (0.0001), **speed x angle x slope**: n.s. (0.99)
Fig 4.4F: Shift in PC4 ~ **speed** * **snout-hump angle** * **slope** + **trial type** + (snout-hump angle + slope |mouseID)
intercept: n.s. (0.66), **speed**: *** (7×10^{-76}), **angle**: n.s. (0.19), **slope**: n.s. (0.44), **trial type**: n.s. (0.92), **speed x angle**: n.s. (0.08), **speed x slope**: n.s. (0.68), **angle x slope**: ** (0.009), **speed x angle x slope**: n.s. (0.69)
Fig 4.4G: PC3 ~ **sine of homolateral phase** + **cosine of homolateral phase** + **trial type** + (sine + cosine |mouseID)
intercept: *** (7×10^{-6}), **sine**: n.s. (0.29), **cosine**: *** (3×10^{-6}), **trial type**: n.s. (0.25)
Fig 4.4H: PC4 ~ **sine of homolateral phase** + **cosine of homolateral phase** + **trial type** + (sine + cosine |mouseID)
intercept: *** (9×10^{-5}), **sine**: * (0.006), **cosine**: *** (9×10^{-5}), **trial type**: n.s. (0.55)
Fig 4.7C,E: PC3 ~ **speed** * **snout-hump angle** * **slope** * **trial type** + (snout-hump angle + slope |mouseID)
intercept: n.s. (0.11), **speed**: *** ($\sigma 0$), **angle**: ** (0.002), **slope**: *** (0.0003), **trial type**: * (0.02), **speed x angle**: *** (1×10^{-67}), **speed x slope**: *** (1×10^{-32}), **angle x slope**: *** (1×10^{-7}), **speed x angle x slope**: *** (3×10^{-17}), **trial type x angle**: n.s. (0.84)
Fig 4.7D,F: PC4 ~ **speed** * **snout-hump angle** * **slope** * **trial type** + (snout-hump angle + slope |mouseID)
intercept: ** (0.001), **speed**: *** ($\sigma 0$), **angle**: *** (2×10^{-7}), **slope**: n.s. (0.07), **trial type**: *** (9×10^{-7}), **speed x angle**: *** (4×10^{-22}), **speed x slope**: *** (9×10^{-25}), **angle x slope**: n.s. (0.08), **speed x angle x slope**: *** (3×10^{-16}), **trial type x angle**: n.s. (0.36)
Fig 5.6A: PC3 ~ **speed** * **snout-hump angle** * **strain** + (snout-hump angle |mouseID)
intercept: n.s. (0.17), **speed**: *** (2×10^{-41}), **angle**: *** (7×10^{-8}), **strain**: n.s. (0.85), **speed x angle**: *** (2×10^{-18}), **speed x strain**: *** (6×10^{-81}), **angle x strain**: n.s. (0.3), **speed x angle x strain**: *** (3×10^{-12})
Fig 5.6B: PC4 ~ **speed** * **snout-hump angle** * **strain** + (snout-hump angle |mouseID)
intercept: n.s. (0.25), **speed**: *** (2×10^{-19}), **angle**: n.s. (0.07), **strain**: n.s. (0.15), **speed x angle**: n.s. (0.09), **speed x strain**: *** (2×10^{-6}), **angle x strain**: n.s. (0.86), **speed x angle x strain**: n.s. (0.13)
Fig 5.6C: PC3 ~ **sine of homolateral phase** + **cosine of homolateral phase** + **strain** + (sine + cosine |mouseID)
intercept: *** (3×10^{-8}), **sine**: n.s. (0.74), **cosine**: *** (8×10^{-9}), **strain**: * (0.02)
Fig 5.6D: PC4 ~ **sine of homolateral phase** + **cosine of homolateral phase** + **strain** + (sine + cosine |mouseID)
intercept: *** (5×10^{-9}), **sine**: n.s. (0.41), **cosine**: *** (4×10^{-9}), **strain**: * (0.04)

Table 2.7: Parameters of exponential regression models $y = A - Be^{-kx}$

Figure	**y**	**x**	**A**	**B**	**k**
3.1C	Forelimb weight fraction	Weight-adjusted head height	0.224	-1.602	3.878
3.1D	Total detected leg load	Weight-adjusted head height	58.052 %	-128.670 %	2.094 %
3.2B	Anteroposterior CoS	Weight-adjusted head height	-1.15 cm	-2.25 cm	1.68 cm
3.3A, 3.5B	Snout-hump angle (load sensors)	Weight-adjusted head height	180.090 deg	47.885 deg	1.253 deg
3.5B	Snout-hump angle (treadmill)	Weight-adjusted head height	176.621 deg	38.693 deg	1.238 deg
5.4D	Forelimb weight fraction (MSA-deficient)	Weight-adjusted head height	0.075	-0.567	2.105
5.4E	Total detected leg load (MSA-deficient)	Weight-adjusted head height	41.173 %	-75.449 %	1.989 %
5.4H	Snout-hump angle (MSA-deficient)	Weight-adjusted head height	181.646 deg	19.445 deg	1.432 deg

by more than 0.05, the particular stride was excluded from analysis.

Given the frequent absence of clear boundaries between the observed combinations of limb phases, especially during treadmill locomotion (Gonçalves et al., 2022), the analysis refrained from assigning discrete gait labels to individual strides. Instead, the focus remained on relative phase distributions of homologous, homolateral, and diagonal limb pairs. These distributions across snout-hump angle or surface slope categories were visualised using density plots, excluding data from mice that performed fewer than 20 strides in the respective category. Data from mice that performed fewer than 1000 strides across all experimental conditions were excluded from analysis altogether.

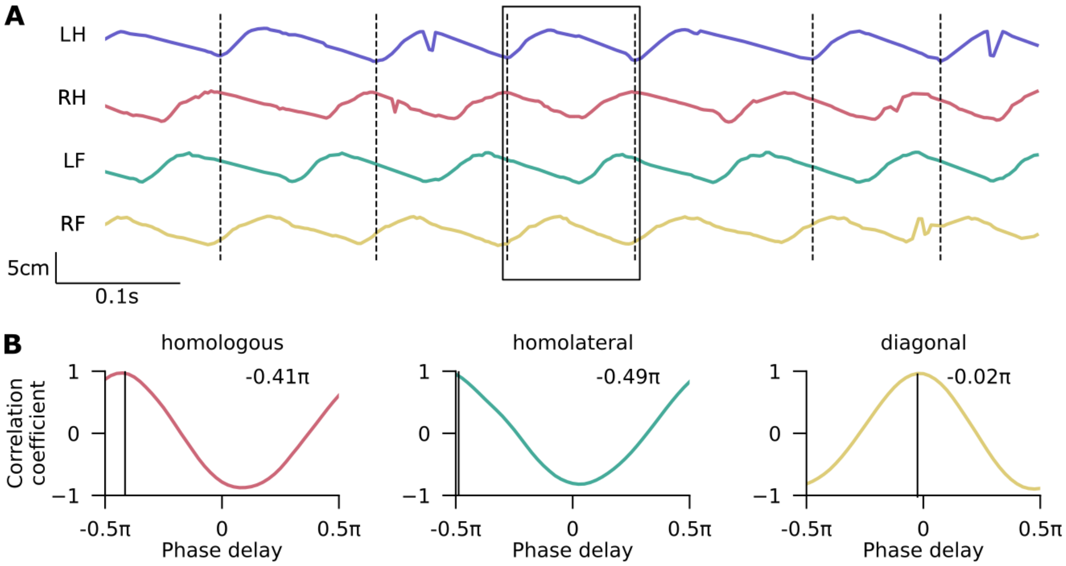

Figure 2.6: Example quantification of interlimb phases.
(A) Example horizontal coordinate traces of the four limbs tracked by DeepLabCut during a 50 Hz optogenetic stimulus. Vertical dashed lines correspond to swing onsets of the reference limb (LH), marking stride boundaries. The rectangular box highlights the stride shown in panel (B). **(B)** Cross-correlation of the reference limb and homologous (*left*), homolateral (*middle*), diagonal (*right*) limb time series at different phase delays. Vertical lines mark the peak of the cross-correlation, indicating the relative phase of the respective limb pair.

2.2.3.2 Computing CoS-equivalent shifts in limb phase

To compare the shifts in relative limb phase observed in surface slope and head height trials, a given change in snout-hump angle or slope on the passive treadmill was assumed to result in the same average weight redistribution as directly measured on the load sensors. Thus, by matching slopes and snout-hump angles across the passive treadmill and load sensor setups, it was possible to relate shifts in limb phase to certain changes in the anteroposterior CoS position.

These CoS-equivalent phase shifts were computed on a per-mouse basis using two data sources: (1) individual animal data from the treadmill experiments, since the same set of mice performed both head height and surface slope trials, and (2) population-averaged load sensor data, as these experiments were conducted on a different cohort of animal. Therefore, another assumption is that the average relationships between CoS and surface slope or snout-hump angle are representative of typical mouse behavior.

2.2.3.3 Circular mixture model analysis of limb phase data

The distribution of relative limb phases, including its modality, was characterised for subsets of data, such as specific ranges of snout-hump angles, using univariate Von Mises mixture models implemented in the BAMBI R library (Chakraborty & Wong, 2021). In particular, I iteratively fit models with 1-4 components and selected the optimal number of components based on a combination of the Watanabe-Akaike information criterion (WAIC) and a Z-test applied to the difference in expected log predictive density between models. All models were fit with three Markov chains, 5000 burn-in iterations, and 5000 sampling iterations.

The circular-linear regression analysis described in section 2.2.3.4 assumes a unimodal normal distribution of the circular data. Data from a given mouse was included in the analysis only if the corresponding optimal Von Mises mixture model met one of the following criteria: (1) it had a single component, (2) the dominant component represented at least 80% of the model, or (3) the modes of two components that jointly represented at least 80% of the model differed by less than 0.2π.

2.2.3.4 Circular-linear regression analysis of limb phase data

To quantify the relationships between limb phase and a range of kinematic (speed), postural (snout-hump angle, weight-adjusted head height), and environmental (surface slope) variables, along with the impact of variability across mice, I used a Bayesian mixed-effects regression framework for circular data developed by Cremers and Klugkist (2018) and Cremers et al. (2018) in R (*bpnreg* package, version 2.0.2). The basic process of modelling limb phase data as a function of linear variables is depicted in Figure 2.7. All models were fitted using 100 burn-in iterations, 1000 output iterations, and a lag of 3. Predictors with variance inflation factor above 5 were excluded to avoid multicollinearity. Due to limited computational resources, some regression models were based on a random sample representing 30-60% of the data. Regression convergence was verified with traceplots for all fixed-effects predictors. The significance of individual fixed-effects predictors was assessed using the highest posterior density (HPD) interval of the signed shortest distance to origin (SSDO) as described in Cremers et al., 2018. Predictors were considered significant if the HPD_{SSDO} interval did not include the origin (zero). Models of different complexities were compared using WAIC.

2.2.3.5 Exploring lateralisation effects of unilateral optogenetic stimulation

To determine whether interlimb coordination was affected by the side of unilateral optogenetic stimulation, binary classification was performed similarly to the approach described in section 2.2.2.4. Here, the side of optogenetic stimulation was treated as the binary outcome variable, while the sine and cosine components of the relative phase from one or multiple limb pairs were used as predictors. The training data were balanced with respect to both the outcome variable and mouse identity.

2.2.4 Histological quantification

Brain sections were registered to the Allen Mouse Brain Common Coordinate Framework (CCFv3, Wang et al., 2020) using the ABBA plugin in

ImageJ (BioImaging And Optics Platform, Ecole Polytechnique Federale de Lausanne). The positions of virally labelled cells and optic fibre implants were subsequently determined in Qupath (Bankhead et al., 2017) using its cell detection and manual annotation tools respectively. Finally, the data were visualised in 3D with Brainrender (Claudi et al., 2021).

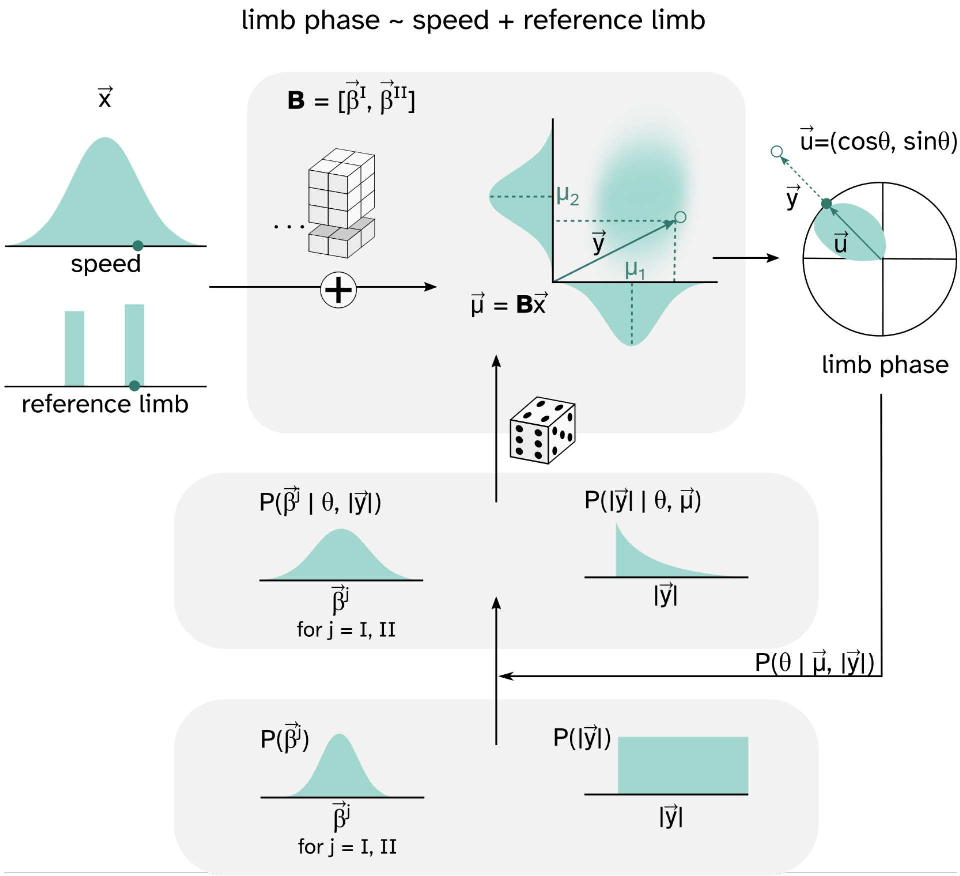

Figure 2.7: Schematic of the Bayesian regression framework to model circular data as a function of linear variable.
Circular data $\vec{u} = (cos\theta, sin\theta)$, where θ is limb phase in range $[0, 2\pi]$ radians, are embedded in a bivariate linear space, assuming a symmetric, unimodal distribution. The magnitude of the embedded vectors, $|\vec{y}|$, is estimated from an exponential posterior distribution using a uniform prior, with the inference performed through Markov Chain Monte Carlo (MCMC) sampling. A regression model of linear predictors, such as speed and reference limb, is then fitted on the mean of the bivariate distribution, with the matrix of model coefficients B inferred through a Bayesian MCMC approach using a diffuse normal prior. For details about the model, consult Cremers and Klugkist, 2018; Cremers et al., 2018.

Table 2.8: Equations for circular-linear mixed-effects regression models fitted on passive treadmill data, and the HPD_{SSDO} of their predictors. Fixed effect predictors are highlighted in bold. Asterisks (*) mark the models that are related to the named figures, but excluded for brevity.

Fig 4.1D: LF phase ∼ **speed** * **snout-hump angle** + (snout-hump angle |mouseID)

speed: * (-0.76,-0.63), **angle**: * (0.60,0.74), **speed x angle**: n.s. (-0.66,0.91)

Fig 4.1E-F: Homolateral phase ∼ **speed** * **snout-hump angle** + **ref limb** + (snout-hump angle |mouseID)

speed: * (-0.82,-0.64), **angle**: * (0.67,0.85), **speed x angle**: n.s. (-0.81,0.81), **ref limb**: n.s. (-0.04,0.08)

Fig 4.2D: LF phase ∼ **speed** * **snout-hump angle** * **slope** + (snout-hump angle + slope |mouseID)

speed: * (-0.88,-0.65), **angle**: * (0.63,0.88), **slope**: * (0.64,0.88), **speed x angle**: n.s. (-0.84,0.87), **speed x slope**: * (0.63,0.87), **angle x slope**: * (-0.88,0.79), **speed x angle x slope**: n.s. (-0.84,0.87)

Fig 4.2E-G, 4.3B: Homolateral phase ∼ **speed** * **snout-hump angle** * **slope** + **ref limb** + (snout-hump angle + slope |mouseID)

speed: * (-0.84,-0.64), **angle**: * (0.64,0.82), **slope**: * (0.64,0.83), **speed x angle**: n.s. (-0.74,0.84), **speed x slope**: * (0.64,0.83), **angle x slope**: * (-0.83,-0.63), **speed x angle x slope**: n.s. (-0.83,0.78), **ref limb**: n.s. (0,0.12)

Fig 4.2*: Homolateral phase ∼ **speed** + **snout-hump angle** * **slope** + (snout-hump angle + slope |mouseID)

speed: * (-0.82,-0.63), **angle**: * (0.63,0.82), **slope**: * (0.63,0.82), **angle x slope**: * (-0.82,-0.62)

Fig 4.3A: LF phase ∼ **speed** * **snout-hump angle** * **slope** + trial type + (snout-hump angle + slope |mouseID)

speed: * (-0.80,-0.63), **angle**: * (0.62,0.79), **slope**: * (0.61,0.80), **speed x angle**: n.s. (-0.66,0.83), **speed x slope**: n.s. (-0.79,0.77), **angle x slope**: * (-0.81,-0.64), **speed x angle x slope**: n.s. (-0.77,0.79), **trial type**: n.s. (-0.02,0.11)

Fig 4.3C: Homolateral phase ∼ **speed** + **snout-hump angle** * **slope** + weight + (snout-hump angle + slope |mouseID)

speed: * (-0.81,-0.64), **angle**: * (0.63,0.80), **slope**: * (0.64,0.81), **weight**: * (-0.84,-0.63), **angle x slope**: * (-0.81,-0.64)

Fig 4.4A: LF phase ∼ **duty factor ratio** * **snout-hump angle** * **slope** + **trial type** + (snout-hump angle + slope |mouseID)

DF ratio: n.s. (-1.19,1.18), **angle**: * (0.60,0.79), **slope**: * (0.60,0.80), **DF ratio x angle**: n.s. (-0.73,0.76), **DF ratio x slope**: n.s. (-0.78,0.71), **angle x slope**: n.s. (-0.76,0.75), **DF ratio x angle x slope**: * (-0.77,-0.59)

Fig 4.4B: Homolateral phase ∼ **duty factor ratio** * **snout-hump angle** * **stride length** + **ref limb** + (snout-hump angle |mouseID)

DF ratio: * (0.78,0.93), **angle**: * (0.58,0.73), **stride length**: * (-0.69,-0.55), **DF ratio x angle**: * (-0.73,-0.59), **DF ratio x stride length**: n.s. (-0.66,0.72), **angle x stride length**: * (0.60,0.74), **DF ratio x angle x stride length**: n.s. (-0.71,0.74), **ref limb**: n.s. (-0.14,0)

Fig 4.4C: Homolateral phase ∼ **duty factor ratio** * **snout-hump angle** * **slope** * **stride length** + **ref limb** + (snout-hump angle + slope |mouseID)

DF ratio: n.s. (-0.94,0.97), **angle**: * (0.63,0.81), **slope**: * (0.62,0.81), **stride length**: n.s. (-0.83,0.79), **DF ratio x angle**: n.s. (-0.76,0.77), **DF ratio x slope**: n.s. (-0.82,0.75), **DF ratio x stride length**: * (-0.80,-0.61), **angle x slope**: * (-0.85,-0.59), **angle x stride length**: n.s. (-0.80,0.80), **slope x stride length**: * (0.62,0.81), **DF ratio x angle x slope**: n.s. (-0.80,0.79), **DF ratio x angle x stride length**: n.s. (-0.81,0.80), **DF ratio x slope x stride length**: n.s. (-0.79,0.80), **angle x slope x stride length**: * (-0.80,-0.61), **DF ratio x angle x slope x stride length**: * (0.61,0.82), **ref limb**: n.s. (-0.04,0.07)

Continued from previous page.

Fig 4.4*: LF phase ∼ **stride length** * **snout-hump angle** * **slope** + **trial type** + (snout-hump angle + slope |mouseID)
stride length: n.s. (-0.70,0.69), **angle**: * (0.57,0.74), **slope**: * (0.59,0.72), **stride length x angle**: * (0.59,0.73), **stride length x slope**: * (0.58,0.73), **angle x slope**: * (-0.73,-0.57), **stride length x angle x slope**: n.s. (-0.73,0.66), **trial type**: * (0.01,0.16)
Fig 4.6D: LF phase ∼ **speed** * **snout-hump angle** + (snout-hump angle |mouseID) using only strides with strict left-right alternation
speed: n.s. (-1.27, 1.24), **angle**: * (1.05, 1.18), **speed x angle**: * (1.12, 1.26)
Fig 4.9D-E: RH phase ∼ **speed** * **snout-hump angle** + (snout-hump angle |mouseID)
speed: * (0.46,0.70), **angle**: * (0.39,0.62), **speed x angle**: * (0.46,0.69)
Fig 4.10E-F: RH phase ∼ **speed** * **snout-hump angle** * **slope** + (snout-hump angle + slope |mouseID)
speed: * (0.64,1.23), **angle**: n.s. (-1.13,1.09), **slope**: n.s. (-1.19,1.07), **speed x angle**: * (-1.19,-0.68), **speed x slope**: * (0.68,1.19), **angle x slope**: * (-1.19,-0.68), **speed x angle x slope**: n.s. (-1.15,1.17)
Fig 4.10G-H: RH phase ∼ **speed** * **head height** * **snout-hump angle residuals** + (head height + angle residuals |mouseID)
speed: n.s. (-0.92,1.09), **head height**: n.s. (-2.74,3.01), **angle residuals**: * (0.41,1.16), **speed x head height**: n.s. (-1.05,0.97), **speed x angle residuals**: * (0.38,1.06), **head height x angle residuals**: * (0.48,1.21), **speed x head height x angle residuals**: * (0.39,1.08)
Fig 5.5C: LF phase (MSA-deficient) ∼ **speed** * **snout-hump angle** + (snout-hump angle |mouseID)
speed: * (0.53,0.83), **angle**: * (0.52,0.82), **speed x angle**: n.s. (-0.73,0.83)
Fig 5.5F: LF phase (MSA littermates) ∼ **speed** * **snout-hump angle** + (snout-hump angle |mouseID)
speed: * (-0.84,-0.58), **angle**: * (0.56,0.84), **speed x angle**: n.s. (-0.59,0.58)
Fig 5.9F: LF phase (MSA littermates) ∼ **speed** * **snout-hump angle** + (snout-hump angle |mouseID)
speed: * (-0.84,-0.58), **angle**: * (0.56,0.84), **speed x angle**: n.s. (-0.59,0.58)
Fig 5.9C-E: Hindlimb phase (MSA-deficient vs. MSA littermates) ∼ **speed** * **snout-hump angle** * **strain** + (snout-hump angle |mouseID)
speed: n.s. (-1.00,0.64), **angle**: n.s. (-0.73,1.02), **strain**: n.s. (-0.58,0.08), **speed x angle**: * (0.42,1.03), **speed x strain**: n.s. (-0.75,0.81), **angle x strain**: n.s. (-0.82,0.40), **speed x angle x strain**: * (-0.82,0.56)
Fig 5.9D: Hindlimb phase (MSA littermates vs. vGlut2-Cre) ∼ **speed** * **snout-hump angle** * **strain** + (snout-hump angle |mouseID)
speed: * (0.54,0.92), **angle**: n.s. (-0.89,0.89), **strain**: n.s. (-0.25,0.24), **speed x angle**: * (-0.91,-0.53), **speed x strain**: * (-0.94,-0.49), **angle x strain**: n.s. (-0.92,0.83), **speed x angle x strain**: * (-0.84,0.91)
Fig 5.9F-G: RH phase ∼ **speed** * **head height** * **snout-hump angle residuals** + (head height + angle residuals |mouseID)
speed: * (-1.00,-0.51), **head height**: n.s. (-1.24,1.66), **angle residuals**: * (0.20,1.32), **speed x head height**: n.s. (-0.87,1.02), **speed x angle residuals**: * (0.52,1.00), **head height x angle residuals**: n.s. (-0.86,0.73), **speed x head height x angle residuals**: * (-1.12,-0.41)

Table 2.9: Equations for circular-linear mixed-effects regression models fitted on motorised treadmill data, and the HPD_{SSDO} of their predictors. Fixed effect predictors are highlighted in bold.

<table>
<tr><td>Fig 4.5C: LF phase ∼ speed * snout-hump angle + (snout-hump angle |mouseID)</td></tr>
<tr><td>speed: * (-2.44,2.14), angle: * (2.12,2.40), speed x angle: n.s. (-2.42,2.40)</td></tr>
<tr><td>Fig 4.5F: Homolateral phase ∼ speed * snout-hump angle + ref limb + (snout-hump angle |mouseID)</td></tr>
<tr><td>speed: * (-2.42,-2.14), angle: * (2.10,2.38), speed x angle: * (2.13,2.41), ref limb: n.s. (-0.03,0.07)</td></tr>
<tr><td>Fig 4.5D,E: LF phase ∼ speed * snout-hump angle * slope + (snout-hump angle + slope |mouseID)</td></tr>
<tr><td>speed: * (-2.61,-2.28), angle: * (2.25,2.56), slope: * (2.26,2.59), speed x angle: * (2.26,2.59), speed x slope: n.s. (-2.59,2.45), angle x slope: n.s. (-2.51,2.59), speed x angle x slope: * (-2.59,-2.24)</td></tr>
<tr><td>Fig 4.5G: Homolateral phase ∼ speed * snout-hump angle * slope + ref limb + (snout-hump angle + slope |mouseID)</td></tr>
<tr><td>speed: * (-2.03,-1.75), angle: * (1.73,2.00), slope: * (1.74,2.02), speed x angle: n.s. (-2.01,1.99), speed x slope: * (-2.11,-1.64), angle x slope: n.s. (-2.02,1.96), speed x angle x slope: n.s. (-2.02,1.93), ref limb: n.s (0,0.05)</td></tr>
<tr><td>Fig 4.5*: Homolateral phase ∼ speed + snout-hump angle * slope + ref limb + (snout-hump angle + slope |mouseID)</td></tr>
<tr><td>speed: * (-2.25,-1.96), angle: * (1.92,2.20), slope: * (1.95,2.24), angle x slope: n.s (-2.19,2.23), ref limb: * (0.02,0.05)</td></tr>
<tr><td>Fig 4.5H: LF phase ∼ speed * snout-hump angle * slope + trial type + (snout-hump angle + slope |mouseID)</td></tr>
<tr><td>speed: * (-2.34,-2.09), angle: * (2.06,2.30), slope: * (2.06,2.34), speed x angle: n.s. (-2.28,2.33), speed x slope: * (-2.43,-2.02), angle x slope: n.s. (-2.22,2.35), speed x angle x slope: n.s. (-2.28,2.33), trial type: * (0.06,0.24)</td></tr>
<tr><td>Fig 4.11A: RH phase ∼ speed * snout-hump angle + (snout-hump angle |mouseID)</td></tr>
<tr><td>speed: n.s. (-2.70,2.63), angle: n.s. (-2.58,2.64), speed x angle: * (-2.70,-2.33)</td></tr>
<tr><td>Fig 4.11B-C: RH phase ∼ speed * snout-hump angle * slope + (snout-hump angle + slope |mouseID)</td></tr>
<tr><td>speed: * (-2.45,-1.90), angle: n.s. (-2.35,2.36), slope: n.s. (-2.34,2.39), speed x angle: * (-2.44,-1.89), speed x slope: n.s. (-2.40,2.33), angle x slope: n.s. (-2.14,2.44), speed x angle x slope: * (1.86,2.43)</td></tr>
<tr><td>Fig 5.7B: LF phase (MSA-deficient) ∼ speed * snout-hump angle + (snout-hump angle |mouseID)</td></tr>
<tr><td>speed: * (-1.87,-1.54), angle: * (1.52,1.84), speed x angle: * (1.53,1.85)</td></tr>
<tr><td>Fig 5.7B: LF phase (MSA littermates) ∼ speed * snout-hump angle + (snout-hump angle |mouseID)</td></tr>
<tr><td>speed: * (-2.55,-2.27), angle: * (2.21,2.50), speed x angle: * (2.24,2.52)</td></tr>
<tr><td>Fig 5.7C: Homolateral phase (MSA-deficient vs. MSA littermates) ∼ speed * snout-hump angle * strain + (snout-hump angle |mouseID)</td></tr>
<tr><td>speed: * (-2.03,-1.68), angle: * (1.68,2.04), strain: * (-0.48,-0.26), speed x angle: * (1.67,2.02), speed x strain: * (-2.03,-1.68), angle x strain: n.s. (-1.98,1.98), speed x angle x strain: * (-2.06,-1.64)</td></tr>
<tr><td>Fig 5.7C: Homolateral phase (MSA littermates vs. vGlut2-Cre) ∼ speed * snout-hump angle * strain + (snout-hump angle |mouseID)</td></tr>
<tr><td>speed: * (-2.89,-2.60), angle: * (2.51,2.78), strain: n.s. (-0.04,0.16), speed x angle: * (2.56,2.85), speed x strain: * (2.53,2.82), angle x strain: n.s. (-2.83,2.85), speed x angle x strain: * (-2.85,-2.56)</td></tr>
<tr><td>Fig 5.10A: RH phase ∼ speed * snout-hump angle + (snout-hump angle |mouseID)</td></tr>
<tr><td>speed: n.s. (-1.87,1.98), angle: n.s. (-1.97,1.90), speed x angle: n.s. (-1.88,1.97)</td></tr>
</table>

Chapter 3

A paradigm to decouple the descending and feedback influences on gait

3.1 Introduction

The gait displayed by a locomoting animal depends on the behavioural demand for speed, as well as the mechanical constraints imposed by the body and the environment (Frigon, 2017). For example, a rodent escaping down a hill needs high speed to evade a predator, but using a highly propulsive gait, such as bound, increases the risk of toppling over on a downward slope (Smith et al., 1998). The interplay between such volitional and biomechanical factors has generated considerable interest in theoretical work on gait and other aspects of locomotion (Fukuoka et al., 2015; Ijspeert & Daley, 2023; Rybak et al., 2024; Shafiee et al., 2024). However, in empirical research, a slight disconnect exists between studies on the feedforward and feedback control of gait. This gap arises from the difficulty of combining causal neural perturbations with experimental manipulation of mechanical dynamics within the same species. On the one hand, one of the most effective ways to modify leg load and its distribution is weight application to animals' backs, but this approach has only been feasible in large mammals, such as horses and dogs (Farley & Taylor, 1991; Lee et al., 1999; Lee et al., 2004), whose neural circuits remain largely inaccessible. On the other hand, the unparalleled access to neural circuits provided by transgenic technologies have given the mouse a lot of untapped potential as a model system for locomotion, (Arber & Costa, 2022; Kiehn, 2016; Leiras et al., 2022), but their small bodies are not well-suited for the majority of mechanical manipulations available to larger quadrupeds. Alternative ways to control leg load, such as the use of sloped and low-friction surfaces (Dutto et al., 2004; Lammers et al., 2006; Lee et al., 2008; Pocratsky et al., 2020), have not been common in mouse research so far.

In fact, a typical experimental pipeline in behaving mice relies entirely on neural perturbations to reveal effects on interlimb coordination because the standard behavioural paradigms they use, such as overground or motorised treadmill locomotion, have little power to do so on their own (Bellardita & Kiehn, 2015; Capelli et al., 2017; Crone et al., 2008). With this approach, changes in gait are rarely so striking that they can be readily dissociated from speed-related effects on locomotion (Bellardita & Kiehn, 2015; Talpalar et al., 2013). More often, neural perturbations shift the range of speeds compatible with a given gait, but it is not clear whether this change reflects a primary effect on interlimb coordination or a secondary effect of a speed disturbance, especially given that the maximum speed the animal can reach is frequently reduced as well (Crone et al., 2009; Pocratsky et al., 2020; Ruder et al., 2016). To uncover gait-specific effects even when they are relatively subtle, it is pertinent to use a behavioural paradigm that can dissociate gait from speed (Batka et al., 2014).

Nonetheless, the standard behavioural setups do offer certain advantages. For example, overground experiments maintain natural locomotor kinematics and allow easy integration of environmental features, such as air puffs or burrows, to simulate escape or exploratory locomotion respectively (Caggiano et al., 2018; Tello et al., 2024). Conversely, a motorised treadmill offers the benefit of partial control over animal speed, which has been effective in eliciting a wide range of gaits in horses (Farley & Taylor, 1991; Hoyt & Taylor, 1981). However, in laboratory mice, reliably evoking sustained high-speed locomotion and gaits other than walk and trot has proven challenging. Few mice are able to reach speeds high enough for gallop and bound to become prevalent, especially without negative reinforcement (Crone et al., 2009; Lemieux et al., 2016). To glean insight into gait beyond left-right alternation, the experimental paradigm must be able to consistently elicit interlimb coordination patterns from the entire mouse repertoire.

In this chapter, I introduce a novel locomotor paradigm that addresses the aforementioned challenges by combining biomechanical and transgenic techniques in mice. In particular, it decouples gait from speed through head height and surface slope modulation, leveraging mouse amenability to head fixation (3.2.1). The paradigm also takes advantage of a series of recent discoveries about the supraspinal locomotor circuitry (Caggiano et al., 2018; Dautan et al., 2021; Josset et al., 2018) to routinely evoke a wide range of interlimb coordination patterns through unilateral optogenetic stimulation of glutamatergic CnF neurons (3.2.2).

3.2 Results

3.2.1 Modulating leg load and its distribution

3.2.1.1 Head height manipulation

Evidence from theoretical and cross-species empirical research suggests that the interlimb coordination pattern of a quadrupedal animal is influenced by the absolute or relative load borne by its legs (Farley & Taylor, 1991; Fukuoka et al., 2015; Iriarte-Diaz et al., 2006; Pocratsky et al., 2020; Shafiee et al., 2024; Wickler et al., 2003). To leverage these insights for a behaviour-driven investigation of gait selection, I sought to design a locomotor paradigm that enables modulation of the anteroposterior leg load distribution in mice by altering their head height. Specifically, I utilised the head fixation techniques developed for this species, expecting higher head positions to shift body weight towards the hindlimbs. To verify this hypothesis, I head-fixed mice above four single-point load cells and measured the vertical GRF borne by each foot of stationary mice as their head height was changed over a 25 mm range (**Figure 3.1 A**, see also 2.3). Leg load data from five trials of a representative mouse at a low and high head position are shown in **Figure 3.1 B**. As expected, forelimbs were more loaded when the head was positioned close to the ground, and this relationship was highly conserved across all mice (**Figure 3.1 C**). In contrast, the observed change in the absolute hindleg load with increased head height was comparatively minimal (p=0.009, *t-test*). Instead, the total detected load decreased as a function of head height, indicating that animal body weight was primarily redistributed between the forelimbs ($p<1 \times 10^{-16}$, *t-test*) and the head fixation apparatus ($p<1 \times 10^{-16}$, *t-test*; **Figure 3.1 D**). Specifically, the mice were pushing against the head bars at low head positions and transferred part of their forelimb load onto the head fixation apparatus as the head height was increased. These relationships were faithfully captured by models of exponential decay, indicating that the weight fractions borne by the forelimbs and the head fixation apparatus both approached stable values as the head position rose towards the maximum height compatible with a quadrupedal stance. At this height, forelimbs, hindlimbs, and the head bars bore approximately 20%, 45%, and 35% of mouse weight respectively.

Transfer of weight between the mice and the head fixation apparatus re-

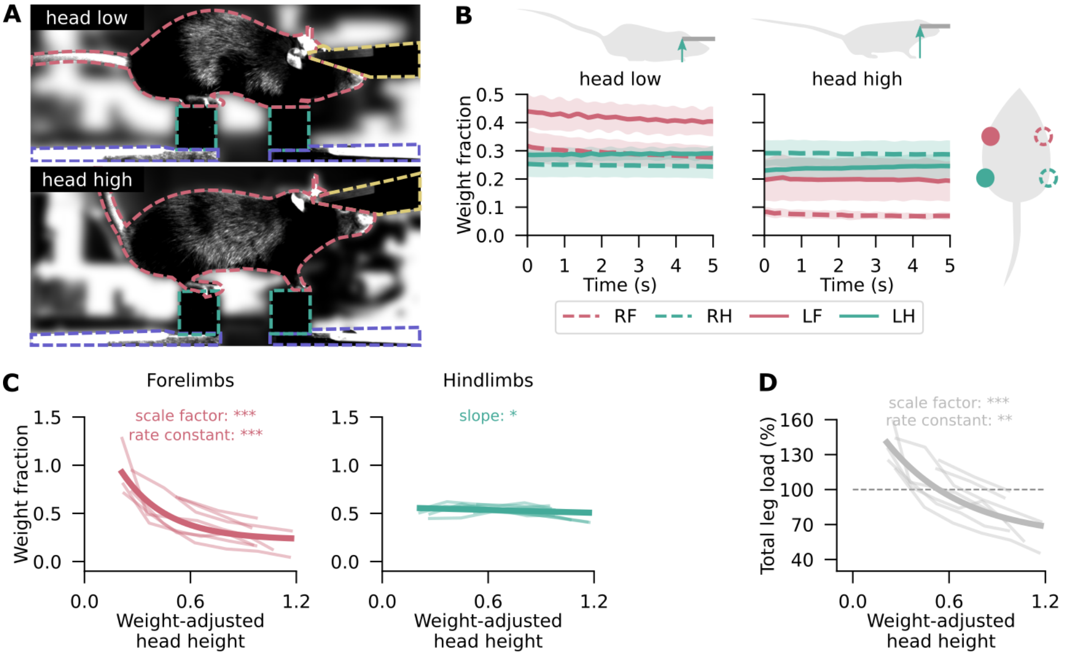

Figure 3.1: Head height manipulation modulates leg load. **(A)** Video frames of a mouse standing still on the force sensor setup at low and high head positions. Background has been blurred in post-processing for ease of visualisation. **(B)** The average fraction of body weight placed on each of the four limbs by a representative mouse during five-second standstills at two head heights 15 mm apart. The shaded areas show 95% confidence intervals across trials. **(C)** The fraction of body weight placed on forelimbs (*left*) and hindlimbs (*right*) as a function of weight-adjusted head height (see 2.2.2.3 for a definition of this metric). Shown are trial averages of individual mice (n=7; thin lines), and a function to characterise the relationship between the variables (thick lines). This was exponential decay for forelimb weight fractions and linear fit for hindlimb weight fraction. **(D)** Same as (C), but showing the total detected load as a percentage of body weight.
All regression model parameters are given in 2.2.2.6. Statistical significance thresholds: * $p < 0.05$, ** $p < 0.01$, *** $p < 0.001$.

flected a significant deviation from the animals' natural, unrestrained condition. Nonetheless, as required, the paradigm enabled manipulation of body weight distribution across the legs, which was conveniently captured in a single variable called centre of support (CoS; see 2.2.2.2 for details of its quantification). In line with the initial expectation, an increase in head height was associated with a CoS shift towards the hindlimbs (Figure 3.2 A). Specifically, a 25 mm rise in head position shifted CoS posteriorly by 1.1 ± 0.2 cm on average (p<1×10^{-16}, *t-test*), and this relationship was well-approximated by an exponential decay function (Figure 3.2 B). No significant shift in CoS was observed along the mediolateral body axis (p=0.1, *t-test*).

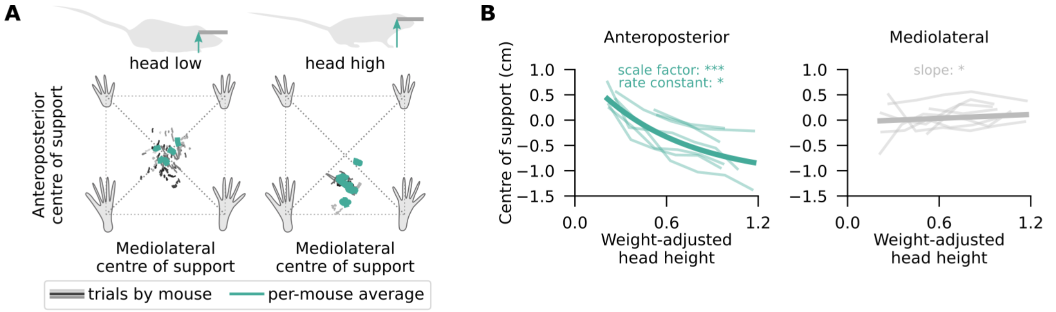

Figure 3.2: Higher head positions redistribute load towards the hindlimbs. **(A)** CoS along the anteroposterior and mediolateral body axes at a low (*left*) and high (*right*) head position. Grey traces show individual trials with shade indicative of mouse identity (n=7). Within-mouse means are shown in teal. **(B)** Anteroposterior (*left*) and mediolateral (*right*) CoS over five-second standstills as a function of weight-adjusted head height. Zero CoS reflects equal weight placed on forelimbs and hindlimbs. Shown are trial averages of individual mice (thin lines), and a function to characterise the relationship between the variables (thick lines). This was exponential decay for the anteroposterior CoS, and linear fit for the mediolateral CoS. For regression parameters, see 2.2.2.6.
Statistical significance thresholds: * $p < 0.05$, ** $p < 0.01$, *** $p < 0.001$.

The results so far have confirmed that manipulating head height in head-fixed mice is an effective way to modulate total leg load, forelimb load, and weight distribution across the legs. However, animals are still able to redistribute their body weight through changes in posture that head height as a metric cannot capture. Assuming that major postural adjustments are reflected in the curvature of the back, I quantified the obtuse angle formed between the vector from the hump of the back to the fixed snout and a line parallel to the ground (inset in **Figure 3.3 A**). Similar to forelimb load and the anteroposterior CoS, this snout-hump angle was found to vary curvilinearly with head height, with lower head positions corresponding to more hunched postures (p=1.4×10^{-9}, *t-test*). Notably, while no effect on CoS was seen along the mediolateral body axis (p=0.05, *t-test*), the relationship between snout-hump angle and the anteroposterior CoS was linear such that the CoS shifted by 0.5 ± 0.2 mm/deg and by 1.1 ± 0.1 cm over the entire range of observed snout-hump angles ($p=3.9 \times 10^{-52}$, *t-test*; **Figure 3.3 B**). Taking advantage of this linear association, I use snout-hump angle as a proxy for the anteroposterior CoS in subsequent analyses of locomotion (Chapters 4 and 5).

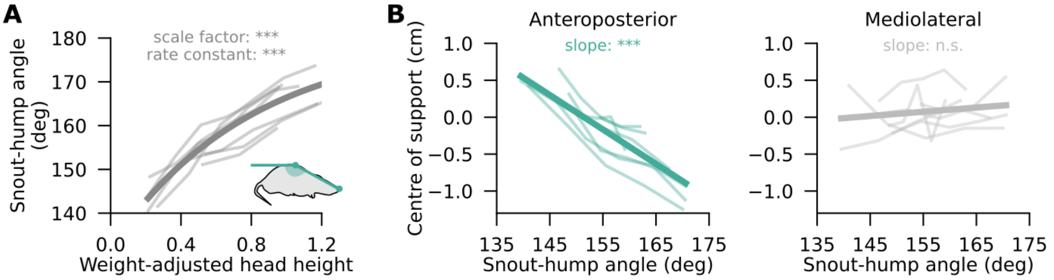

Figure 3.3: Snout-hump angle can serve as a proxy for anteroposterior centre of support.
(A) The obtuse angle between the hump-snout vector and the treadmill surface (*inset*) plotted as a function of weight-adjusted head height of individual mice across trials (thin lines). This relationship is approximated by an exponential decay model (thick lines; see regression parameters in 2.2.2.6). **(B)** Anteroposterior (*left*) and mediolateral (*right*) CoS over five-second standstills as a function of snout-hump angle. Zero CoS reflects equal weight placed on forelimbs and hindlimbs. Shown are trial averages of individual mice (thin lines), along with a linear mixed-effects regression line (thick lines).
Statistical significance thresholds: * $p < 0.05$, ** $p < 0.01$, *** $p < 0.001$.

3.2.1.2 Surface slope manipulation

Head height-related variation in both total leg load and the anteroposterior CoS represents a shortcoming of head height manipulation as an approach to leg load modulation. For example, if a locomotor variable was influenced by head height or snout-hump angle, it would be difficult to distinguish whether it was due to changes in the absolute or relative leg load. To better discriminate between these mechanical factors, I further sought to modulate the anteroposterior CoS by changing the slope of the limb support surface while keeping the head at a fixed medium height. Based on previous work in horses, goats, and opossums (Dutto et al., 2004; Lammers et al., 2006; Lee et al., 2008), I hypothesised that inclines would shift CoS posteriorly through a redistribution of load from forelimbs to hindlimbs.

Indeed, changing the surface slope from a decline to an incline by 80 de-

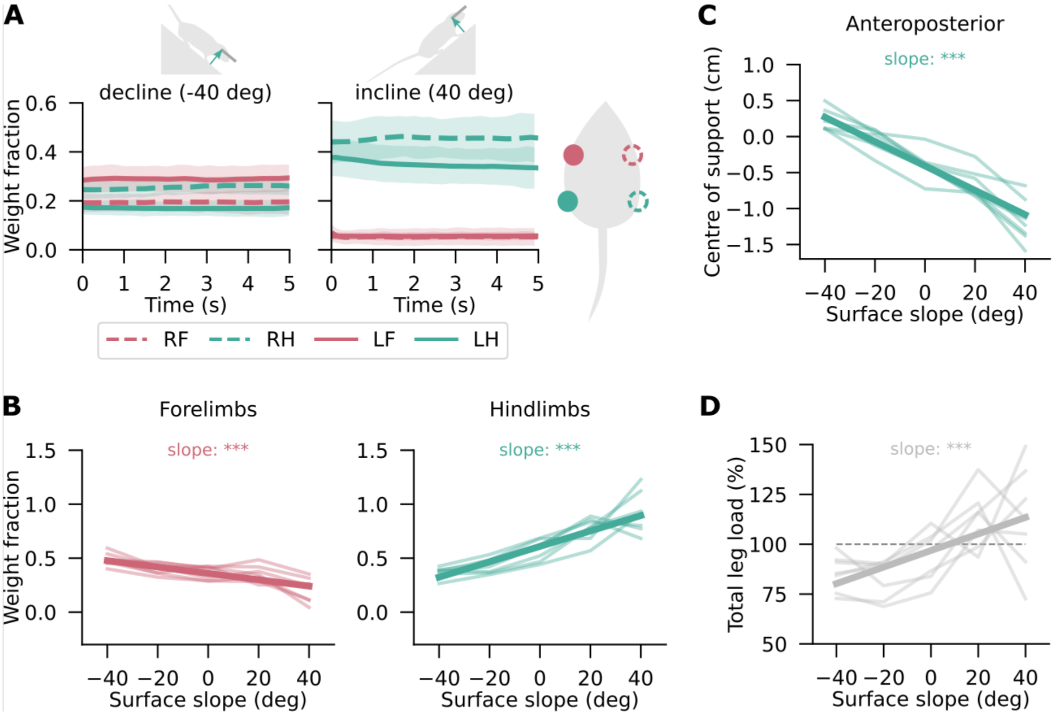

Figure 3.4: Inclines redistribute load towards the hindlimbs.
(A) The average fraction of body weight placed on each of the four limbs by a representative mouse during five-second standstills on a decline (-40 deg) and an incline (40 deg). The shaded areas show 95% confidence intervals across trials. **(B)** The fraction of body weight placed on forelimbs (*left*) and hindlimbs (*right*) as a function of surface slope. Shown are trial averages of individual mice (n=7; thin lines) along with linear regression fit (thick lines) that best approximate the relationships between variables. **(C)** Same as (B), but showing the anteroposterior CoS where zero CoS reflects equal weight placed on forelimbs and hindlimbs. **(D)** Same as (B), but showing the total detected load as a percentage of body weight.
Parameters of all regression models are given in 2.2.2.5. Statistical significance thresholds: * $p < 0.05$, ** $p < 0.01$, *** $p < 0.001$.

grees increased the fraction of weight borne by the hindlimbs from 0.37 ± 0.02 to 0.92 ± 0.07 (p=7.6×10^{-37}, *t-test*) while the forelimb load decreased from 0.49 ± 0.02 to 0.21 ± 0.04 (p=4.2×10^{-15}, *t-test*; **Figure 3.4 A, B**). Evidently, unlike head height manipulation, changes in slope resulted in a transfer of load between the forelimbs and hindlimbs. This was also reflected in a linear posteriorward CoS shift by 1.42 ± 0.09 cm upon an 80 degree increase in slope (p<1×10^{-16}, *t-test*; **Figure 3.3 C**) without a significant change along the mediolateral axis (p=0.13). Still, the total detected leg load also varied with slope (p=1.6×10^{-11}, *t-test*; **Figure 3.3 D**). In particular, on a -40 deg decline, mice transferred $15 \pm 3\%$ of their weight onto the head fixation apparatus, whereas on a 40 deg incline, $13 \pm 9\%$ of the detected load was attributed to animals exerting force on the head bars. Notably, the correspondence between the total detected load and the direction of load redistribution along the anteroposterior body axis during slope manipulation was the inverse of that observed upon changes in head height. A posteriorward CoS shift during head height manipulation and an anteriorward CoS shift during modulation of slope both correlated with a propensity to transfer weight onto the head fixation apparatus. This difference indicates that the effects of total load and its distribution can be distinguished by combining the two load manipulation approaches.

3.2.1.3 Applicability of load data across experimental setups

Ultimately, the goal was to modulate leg load on a flat treadmill belt rather than a set of cube-shaped force sensors with gaps in between. The passive treadmill setup and its key features, including head fixation, head height manipulation, and slope modulation, are shown in **Figure 2.1**. Since direct load measurement on the treadmill was not technically feasible, I sought indirect ways to compare body mechanics across the two experimental setups. Using postural variables as a surrogate measure, I found no setup-dependence in the relationship between snout-hump angle and weight-adjusted head height ($p=0.15$, *log-likelihood ratio test*; **Figure 3.5 A**). Thus, a given head position on the treadmill can be assumed to reflect the same load and its distribution as was recorded on the force sensors.

In contrast, slope modulation led to distinct postural adaptations on the two setups (angle $p<1 \times 10^{-16}$, position $p<1 \times 10^{-16}$, *log-likelihood ratio tests*). On the force sensors, mice countered the incline-induced posteriorward shift in CoS by adopting more hunched postures ($p<1 \times 10^{-16}$) and positioning their feet more anteriorly ($p<1 \times 10^{-16}$; **Figure 3.5 B, C**). These adjustments likely improved the animals' stability on the limited surface area provided by the load cells. However, on the treadmill, mice tended to assume slightly more upward oriented postures ($p<1\times10^{-16}$) as the slope increased, and placed their feet more posteriorly ($p<1 \times 10^{-16}$; **Figure 3.5 B, C**). Since these postural adaptations support uphill movement, it is plausible that the different reactions to slope modulation reflect the mobile nature of the treadmill surface and the potential for movement it provides.

Two conclusions can be drawn from these results. First, the observed adaptive strategies indicate that force sensor recordings might underestimate the true relationship between slope and CoS. Second, the difference in adaptive strategy between the two setups suggests that the association between CoS and slope quantified from force sensor recordings might not be directly applicable to the treadmill. Therefore, while manipulating both head height and slope provides a direct experimental approach to modulating body mechanics, inferences about slope-related biomechanics based on comparisons across the two setups should be treated with caution.

3.2.2 Consistently evoking a variety of gaits

The other major challenge of studying gait in mice has been the difficulty to consistently elicit left-right synchronous coordination patterns, such as gallop and bound. To address this, locomotion in head-fixed mice on the passive treadmill was evoked through optogenetic stimulation of the glutamatergic CnF neurons known to induce forward movement at a speed that scales with stimulation intensity (Caggiano et al., 2018; Dautan et al., 2021; Josset et al., 2018; Shik and Orlovsky, 1976; **Figures 3.6 A-D**). CnF stimulation at 10-50 Hz reliably triggered locomotion at short latencies (<150 ms in 88% trials) such that the mean and maximum speeds were linearly related to stimulation

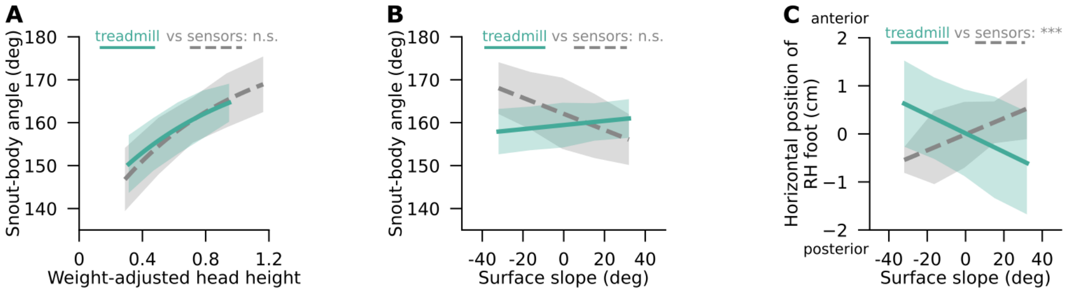

Figure 3.5: Different postural adaptations to slope on force sensors and treadmill.
(A-B) Snout-hump angle as a function of weight-adjusted head height (A) and surface slope (B) on the passive treadmill (solid teal line) and the force sensors (dashed grey line), approximated by exponential decay (A) or linear (B) functions. The shaded regions show 95% confidence intervals. For the passive treadmill, only data from stationary pre-stimulation periods are included. Statistical significance is assessed using a likelihood ratio test. **(C)** Same as (A), but showing the relative position of right hindfoot as a function of surface slope.
Parameters of all regression models are given in 2.2.2.5. Statistical significance thresholds: * $p < 0.05$, ** $p < 0.01$, *** $p < 0.001$.

frequency (mean speed p=1.6×10^{-19}, max speed p=2.7×10^{-15}, *t-test*; **Figure 3.7 A**). Importantly, optogenetically induced locomotion comprised a variety of limb coordination patterns, including 16-25% of strides with hindlimb alternation and 35-41% of strides with synchronised hindlimb movement at low and moderate speeds (<80 cm/s). As the speed increased, the proportion of left-right synchronous strides grew to 57±5% with sizeable proportions of right-leading (24±5%) and left-leading (12±2%) out-of-phase movement (**Figures 3.7 B**). This was contrary to locomotion on a motorised treadmill where left-right alternation dominated (68-86% of strides) in all speed bands and synchronised hindlimb coordination constituted only 5±2% of strides even in the highest speed quintile (89-169 cm/s; **Figures 3.7 C**). In a freely-moving sound-triggered escape paradigm (see 2.1.3.5), relatively similar proportions of anti-phase (18-28%), out-of-phase (46-50%), and synchronised (25-30%) hindlimb movements were observed at least during the first two strides after the aversive stimulus (**Figures 3.7 D**). However, with the exception of homolateral coordination, limb phase was more concentrated during escape than on the passive treadmill, as indicated by a higher mean resultant length (**Figures 3.7 E-F**). In addition, the use of an escape paradigm for the study of gait would be impractical due to sensitisation to the stimulus and reduced likelihood of exiting the shelter after a few stimulus exposures. Indeed, while mice performed 5±1 escapes during the first 1-hour session in the open field, the probabilities of escape and shelter departure in the second experimental session dropped by 35% and 83% respectively, highlighting the challenges of sensitisation and reduced engagement over time. Overall, these findings demonstrate the advantages of optogenetically induced locomotion on a passive treadmill over two more traditional locomotor paradigms, specifically its ability to consistently and efficiently elicit a variety of limb coordination patterns.

Head fixation and optogenetic stimulation are significant perturbations that might alter the natural locomotion of animals. To assess the extent of such potential alterations, I compared the kinematics of optogenetically evoked head-fixed locomotion on the passive treadmill with head-free, self-generated locomotion on a motorised treadmill. Examining left-right synchronous and alternating gaits separately, stride length, stride frequency, and duty factor changed monotonically with speed on both setups (all $p<1 \times 10^{-16}$; **Figures 3.8 A-i, ii, iii**), suggesting generally normal locomotor kinematics with respect to motion velocity. In fact, there were no significant differences in the absolute values of stride length on the two setups irrespective of left-right coordination pattern and speed (p between 0.21 and 0.99, *pairwise t-tests*; **Figure 3.8 A-i**. However, notable differences on the passive treadmill included a slightly higher stride frequency at low speeds ($p=0.004$ and $p=0.0002$, *pairwise t-tests*; **Figures 3.8 A-ii**), a longer fraction of stride spent in ground contact (p between 0.001 and 3.3×10^{-16}, *pairwise t-tests*; **Figures 3.8 A-iii**), and an increase in four- and three-feet support patterns across all speeds (**Figures 3.8 B**). These discrepancies likely arose due to constraints on the vertical body displacement

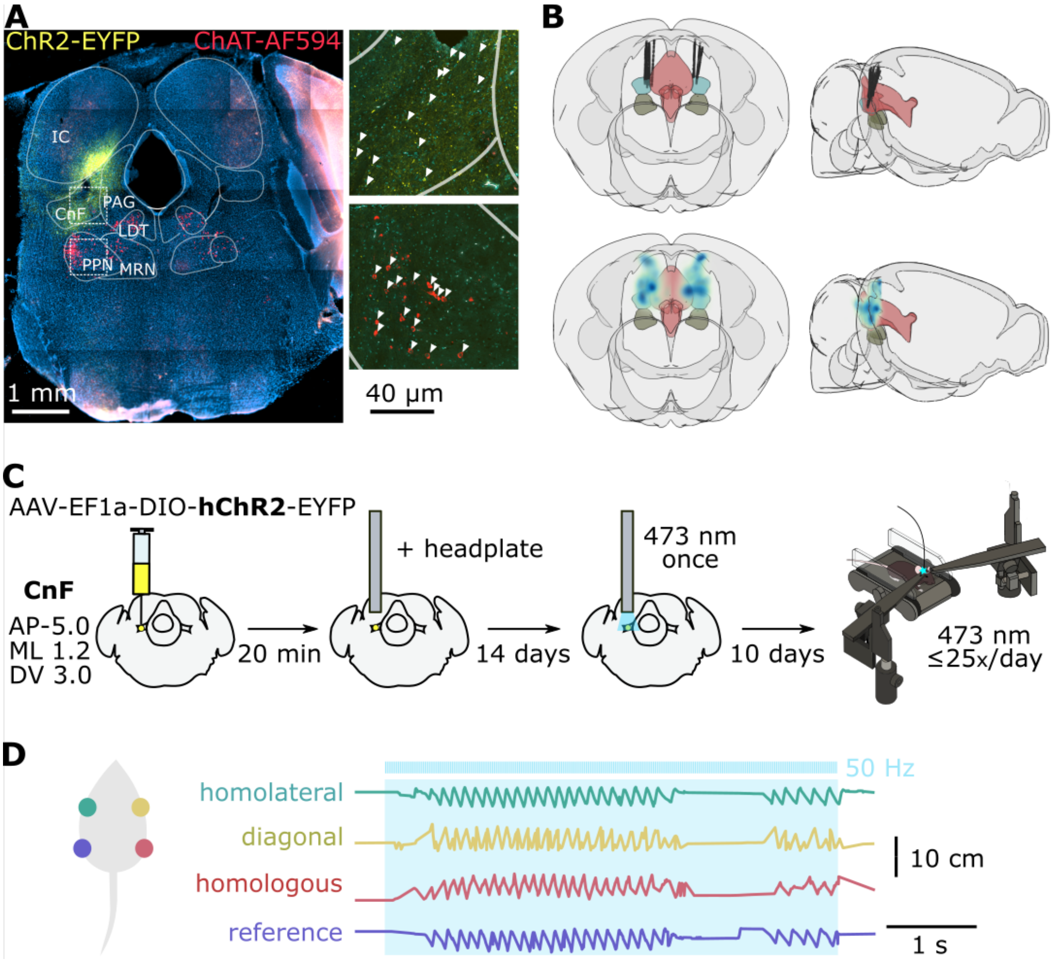

Figure 3.6: Experimental approach for triggering locomotion in head-fixed mice.
(A) An example coronal section at the virus injection and optic fibre implantation site, visualised by epifluorescence (*left*) and confocal (*right: two insets*) microscopy. The images show enhanced yellow fluorescent protein (YFP) labelling in the opsin-expressing cells (yellow), choline acetyltransferase (ChAT) antibody staining (red), and DAPI staining (blue). CnF, cuneiform nucleus; PPN, pedunculopontine nucleus; MRN, mesencephalic reticular nucleus; PAG, periaqueductal grey; IC, inferior colliculus; LDT, laterodorsal tegmental nnucleus. **(B)** Traced positions of optic fibre implants (*top*) and density distributions of virally labelled cells (*bottom*) viewed in coronal (*left*) and sagittal (*right*) planes. CnF, PPN, and PAG are shown in blue, dark grey, and red respectively. **(C)** Experimental strategy and timeline. **(D)** Example x-coordinate traces of the four limbs tracked by DeepLabCut during a 50 Hz optogenetic stimulus (blue shaded region; light pulses shown by the blue bars above).

during head-fixed locomotion (p between 0.01 and 3.1×10^{-10}, *pairwise t-tests*; **Figures 3.8 A-iv**) and indicate a significant deviation from natural movement. Head fixation, specifically at low heights, could also explain the

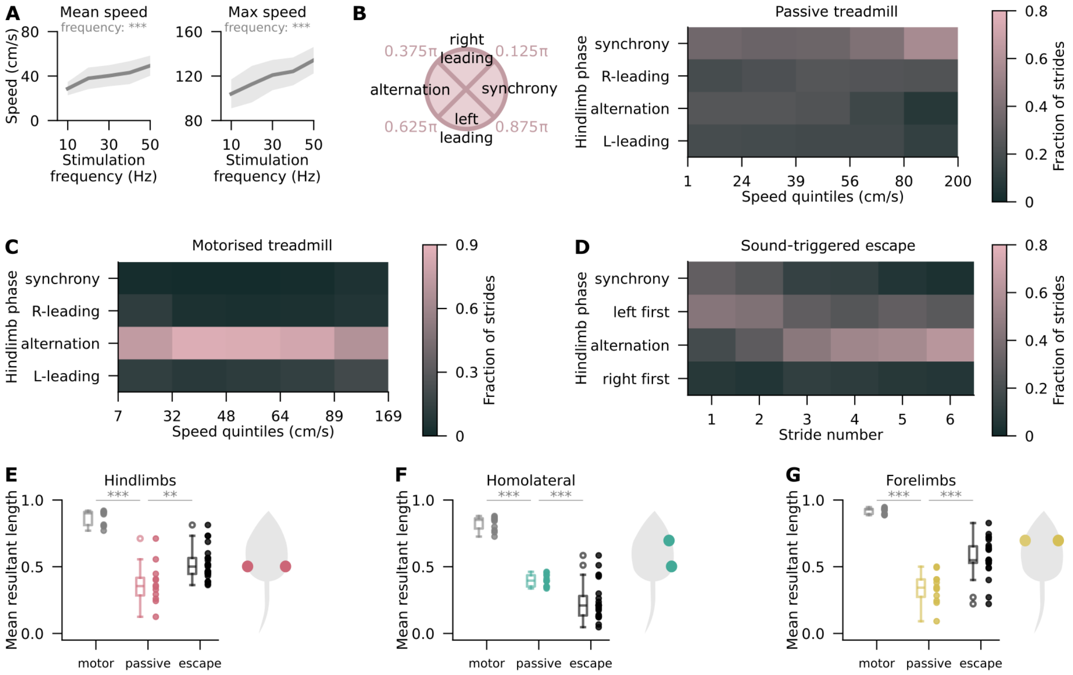

Figure 3.7: Optogenetic CnF stimulation consistently evokes a variety of gaits. **(A)** Median (*left*) and maximum (*right*) speed of optogenetically evoked head-fixed locomotion as a function of optical stimulation frequency, averaged across a range of head fixation heights. Shown are means with 95% confidence intervals. The statistics refer to the slope coefficient in a linear regression (see 2.2.2.5). **(B-C)** Fraction of strides with synchronous, alternating (anti-phase), and left- or right-leading out of phase hindlimb coordination patterns in speed quintiles on the passive treadmill (B) and motorised treadmill (C). **(D)** Same as (B) but for consecutive strides in an escape bout. **(E-G)** Mean resultant length of hindlimb (E), homolateral limb (F), and forelimb (G) phase distributions in motorised treadmill, passive treadmill, and escape paradigms. For reference, mean resultant length is an inverse measure of variability that varies between 0 and 1, with these extremes representing a uniform and a degenerate distribution respectively.
Statistical significance thresholds: * $p < 0.05$, ** $p < 0.01$, *** $p < 0.001$.

slightly reduced forelimb swing amplitude on the passive treadmill (p between 0.02 and 0.0002, *pairwise t-tests*; **Figures 3.8 A-v**), whereas hindlimb swing at low speeds was marginally more pronounced on the passive treadmill at low speeds (p=0.0002 and p=0.005, *pairwise t-tests*; **Figures 3.8 A-vi**). Other differences in limb support, such as a greater prevalence of low-speed single- and two- non-diagonal limb support patterns on the passive treadmill (**Figures 3.8 D**), reflect the increased variety of interlimb coordination patterns on this setup, which was a desirable feature of the novel locomotor paradigm.

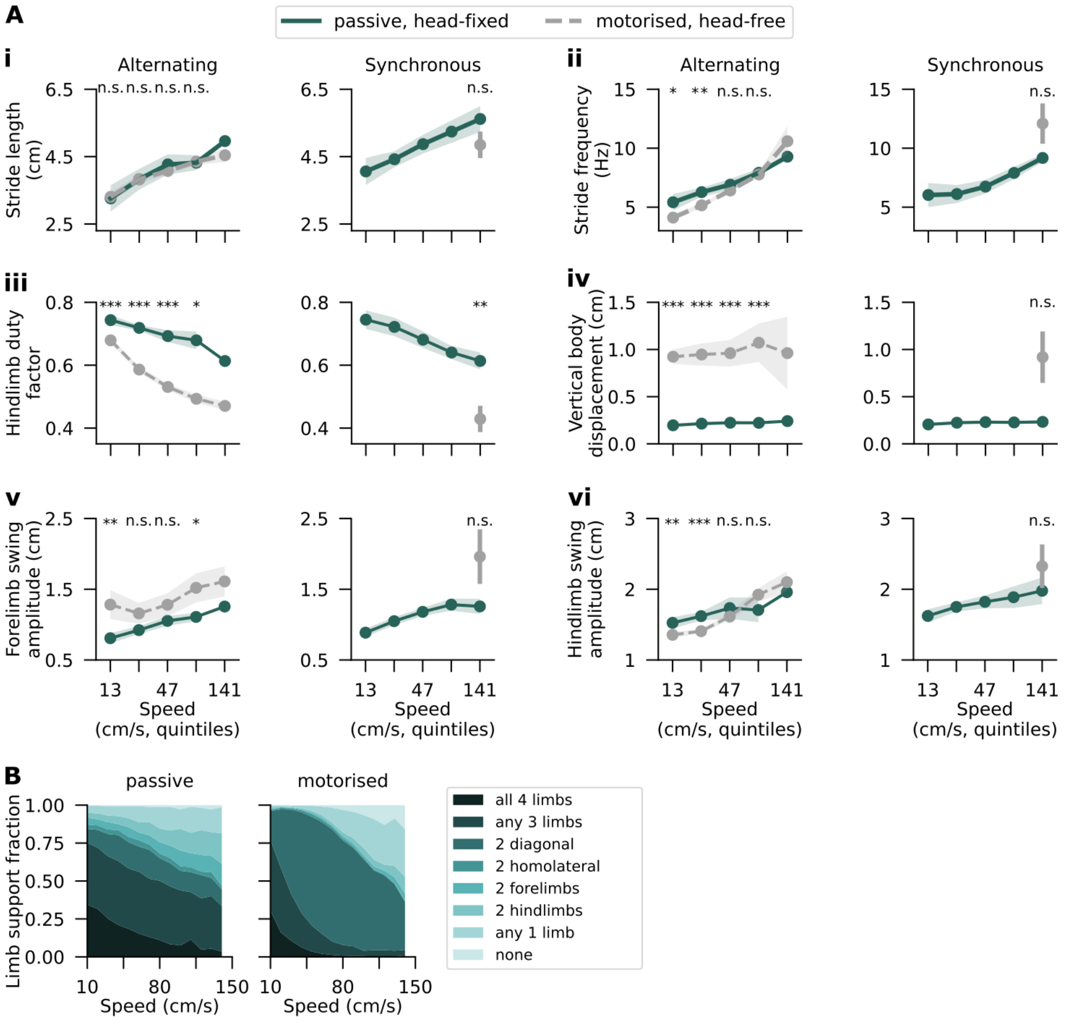

Figure 3.8: Comparative kinematics of head-fixed and head-free locomotion. **(A)** Average stride length (A-i), stride frequency (A-ii), hindlimb duty factor (A-iii), vertical body displacement (A-iv), vertical amplitude of forelimb motion (A-v), and vertical amplitude of hindlimb motion (A-vi) during left-right alternating (*left*) and synchronous (*right*) locomotion on the passive (solid teal line) and motorised treadmill (dashed grey line), plotted for speed quintiles in the passive treadmill data. A plot of forelimb duty factor is not shown as this parameter was not significantly different from the hindlimb duty factor shown in (A-iii; p=0.99). **(B)** Area plot of average foot support types as a fraction of stride cycle across speeds for passive treadmill (*left*) and motorised treadmill (*right*), based on one thousand randomly selected strides per mouse and inspired by (Machado et al., 2015).
Statistical significance thresholds before Bonferroni corrections: * $p < 0.05$, ** $p < 0.01$, *** $p < 0.001$.

In addition to kinematics, head fixation and its height manipulation influenced the postures mice adopted while locomoting on the passive treadmill. For instance, the snout-hump angles at high head fixation positions were markedly different from those seen during non-restrained locomotion on the motorised treadmill (Cohen's d: 2.1, $p < 1 \times 10^{-16}$; **Figures 3.9 A**). In fact, only the lowest tercile of head fixation positions was associated with snout-hump angles that were replicated during head-free locomotion (Cohen's d: 0.2, $p = 5 \times 10^{-5}$). However, while the head was always fixed parallel to the ground on the passive treadmill, the absence head restraint on the motorised treadmill allowed mice to vary the pitch of their head over a ∼95 deg range and assume a 27 deg downward head tilt on average (**Figures 3.9 B**). Even though the two variables were highly correlated (Pearson coefficient: 0.91), every 1-degree change in snout-hump angle corresponded to an average 8 degree variability in head pitch (**Figures 3.9 C, D**). Due to this variability in head pitch, snout-hump angles measured on the two setups did not necessarily correspond to the same degree of back curvature or leg load distribution. Further postural differences during head height manipulation on the passive treadmill were a ∼0.8 cm higher average body position (Cohen's d: 2.0, $p < 1 \times 10^{-16}$), a ∼0.3 cm higher average tailbase position (Cohen's d: 0.4, $p = 4 \times 10^{-15}$), and a marginally wider angle between the body-tailbase vector and the ground (Cohen's d: 0.2, $p = 1 \times 10^{-4}$). A binary classifier trained on the first two principal components of these features distinguished between the two setups with 83.6±0.3% accuracy, significantly outperforming chance (**Figures 3.9 E, F**). Similar postural differences between the two setups were observed during slope trials (classifier accuracy: 95.4±0.2%). Taken together with locomotor data, these results suggest that optogenetic stimulation induced kinematically normal limb movement, but the mechanical constraints imposed by the head fixation apparatus, along with its use for head height manipulation, altered several aspects of intralimb coordination and posture. These factors will need to be considered when examining interlimb coordination in Chapters 4 and 5.

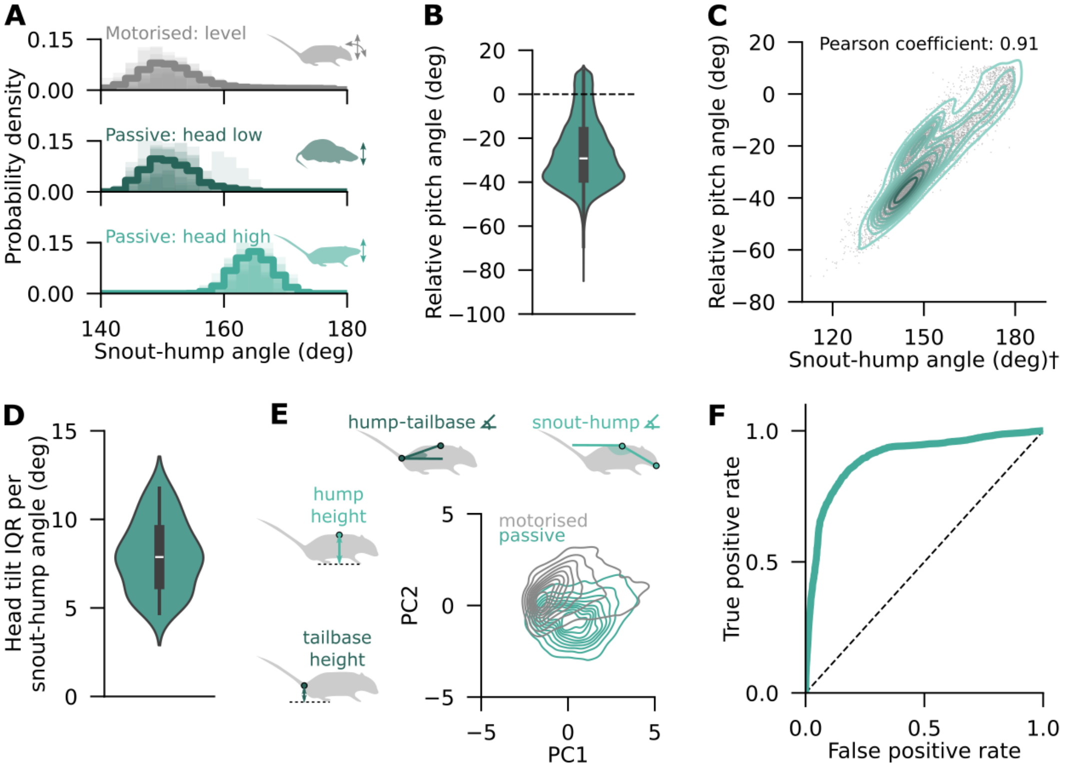

Figure 3.9: Postural comparison of head-fixed and head-free locomotion. **(A)** Histograms of snout-hump angles observed during non-restrained locomotion on the motorised treadmill (*top*) and during head-fixed locomotion on the passive treadmill at the lowest (*middle*) and highest (*bottom*) tercile of weight-adjusted head height. Shaded histograms represent individual mice, the thick line is the average. **(B)** Distribution of head pitch angles recorded during non-restrained locomotion relative to the head tilt during head fixation. **(C)** Correlation between snout-hump angle and head pitch angle during non-restrained locomotion. A kernel density estimate plot is overlaid such that darker colours indicate regions of higher data density. **(D)** Distribution of head pitch variability observed for each 1-degree increment in snout-hump angles, quantified as the interquartile range. **(E)** Kernel density smoothed distributions of the first two principal components capturing variation across the four postural features shown above the plot during motorised and passive treadmill locomotion. **(F)** Receiver operating characteristic curve of a binary classifier trained on the data shown in (E). The dashed diagonal line represents chance-level performance.
† indicates that snout-hump angle is measured in non-restrained conditions and is not necessarily directly comparable to the snout-hump angle from head-fixed experiments

3.3 Discussion

In this chapter, I have introduced a novel locomotor paradigm for studying the biomechanical and neural underpinnings of quadrupedal gait. This paradigm combines optogenetic induction of locomotion and markerless tracking of body parts with head height and surface slope modulation in head-fixed mice. Thus, it provides experimental control over the total gravitational load and its anteroposterior distribution across the entire spectrum of mouse interlimb coordination patterns, while preserving major kinematic features of locomotion.

Compared to traditional approaches to studying locomotion, the present paradigm confers a unique set of advantages that make it well-suited for a systematic and comprehensive investigation of gait. First, its use of environmental modulation creates favourable conditions for observing speed-independent effects on gait, thus enabling a behavioural decoupling of these correlated locomotor features. Even if reductionist in some ways, this method follows the view that a detailed understanding of behavioural components must precede investigation of neural implementation (Krakauer et al., 2017), sharing this property with weight-bearing paradigms applied to large mammals (Farley & Taylor, 1991; Lee et al., 1999; Lee et al., 2004), freely moving slope experiments (Dutto et al., 2004; Lammers et al., 2006; Lee et al., 2008), and swim tests that render leg loading feedback irrelevant (Akay et al., 2014; Gruner & Altman, 1980; Pocratsky et al., 2020). This contrasts with the most common approach in rodent locomotor research that relies on a loss-of-function neural intervention to reveal gait-specific effects in uncontrolled or speed-controlled environmental conditions (Bellardita & Kiehn, 2015; Crone et al., 2009; Ruder et al., 2016).

Second, by using a combination of head height and slope modulation, the new locomotor paradigm can distinguish the influence of total gravitational load from that of load distribution. Previous research in weight-bearing horses on flat and inclined surfaces has generated conflicting results regarding the relevant trigger for gait transition (Wickler et al., 2003). Owing to animal interaction with the head-fixation apparatus, the environmental manipulations used in this thesis generate opposite effects on the total leg load and the centre of leg support (see Figures 3.1, 3.2, 3.4), effectively dissociating the two. In larger quadrupeds, equivalent inferential power could be achieved by combinatorially varying the magnitude and placement of weights carried by the animal. However, most approaches to biomechanical modulation, such as changing the size or position of the load, altering surface slope or texture, or using swim tests or airstepping, provide control over only one of the two hypothesised triggers.

Third, the use of optogenetic CnF stimulation allows the locomotor paradigm to sample the space of natural mouse gaits more evenly and reliably than motorised treadmill, escape, or overground locomotion in this species (see Figure 3.7; Crone et al., 2009; Lemieux et al., 2016; Machado et al., 2015). This feature expands the range of questions that can be addressed in mice, enabling efficient investigation of high-speed gaits and transitions between left-right alternating and synchronised limb coordination patterns. Consequently, it makes locomotor research in mice comparable in behavioural scope to work in quadrupeds of cursorial body build, most notably horses and cats (Hoyt & Taylor, 1981; Miller et al., 1975), whose gait repertoire can be adequately exposed even with the traditional locomotor paradigms.

Finally, the present locomotor paradigm is designed for mice, providing access to neural circuits unparalleled in most other species used for locomotor research. In Chapter 5 of this thesis, I begin this neural-level investigation by perturbing the sensory feedback pathways mediated by proprioceptive afferents, but potential applications of this paradigm in studies of neural implementation are vast. For example, it could enable empirical research into the interplay between the descending speed-related inputs and somatosensory feedback in relation to gait control, which has so far been explored primarily in theoretical work (Ijspeert & Daley, 2023; Shafiee et al., 2024). The ability to decouple gait from speed could also facilitate the search for 'gait control neurons', possibly exhibiting activity that jointly correlates with interlimb phase and biomechanical variables irrespective of movement speed. Thus, the introduced behavioural paradigm has notable potential for advancing future research into the biomechanical and neural control of locomotor gait.

However, there is also a trade-off between the experimental control provided by the locomotor paradigm and preservation of natural locomotor kinematics. Most notably, head fixation prevents rotational head movement, eliminates the possibility of fall, and limits the vertical body oscillation seen in normal locomotion. To assess how head-fixed locomotion compares with more natural, non-restrained movement, this thesis primarily uses the motorised treadmill as a control, favouring it over overground paradigms for its effectiveness in evoking locomotion at varying speeds. Through this comparison, the passive treadmill paradigm was shown to increase the fraction of stride spent in stance and the prevalence of four- and three-feet support (see Figure 3.8), likely reflecting the mechanical constraints of head fixation. At the same time, it should be noted that motorised treadmill locomotion is not an entirely faithful representation of natural locomotion either, with animals known to display longer strides and an extended stance phase compared to overground locomotion (Blaszczyk & Loeb, 1993; Buchner et al., 1994). It also likely differs from CnF-induced locomotion by being relatively more reliant on sensory feedback for interlimb control (Barbeau & Rossignol, 1987; Forssberg et al., 1980; Takeoka et al., 2014). These differences limit the utility of the motorised treadmill as a control paradigm for non-stimulated head-free locomotion as used in this thesis.

In addition, the absence of head rotation on the passive treadmill also means that a given snout-hump angle recorded with this paradigm represents a slightly greater curvature of the back than under head-free conditions. Thus, while snout-hump angle remains a convenient, mouse size-independent, and internally consistent proxy for animal posture, cross-setup comparisons of locomotor data on the basis of snout-hump angle requires appropriate care. This limitation is especially important in the present study given that body tilt and head pitch are key postural instruments quadrupeds use to adapt to changing locomotor conditions, such as slope-induced load redistribution and potentially destabilising rotational moments during acceleration (see Figure 3.5, also Gottschall and Nichols, 2007; Lee et al., 1999).

Another aspect of the paradigm that prioritises experimental control over natural locomotion is its reliance on optogenetic stimulation for locomotor initiation. Although the optical stimulus has been shown to convert into naturally expressed locomotor rhythm (Caggiano et al., 2018), the stimulated population of glutamatergic CnF neurons is likely more heterogeneous than currently understood, with various potential implications for the experimental paradigm.

A technical, rather than fundamental, shortcoming of the behavioural paradigm is its inability to measure leg loads directly on the treadmill. Given that mice use different postural adaptations on the force sensors and the passive treadmill, extrapolation of load-related information to treadmill locomotion should be approached with caution. Integrating force sensors into the treadmill design would be a useful refinement of the paradigm in the future.

In summary, I have described a novel locomotor paradigm for studying gait control that combines the benefits of biomechanics-centred research approaches used in large mammals with the advantages conferred by transgenic techniques in mice. While this enhanced experimental control comes at the expense of some aspects of natural locomotor kinematics, the paradigm provides a unique opportunity to empirically investigate the interaction between the descending and feedback influences on interlimb coordinatinon. I pursue this research question at a behavioural level in the following chapter.

Chapter 4

Dissecting the influences of leg loading feedback and top-down modulation on interlimb coordination

4.1 Introduction

As outlined in 1.1.4, extensive evidence suggests that leg loading feedback affects locomotor gait, but several important aspects of this influence remain unresolved. These include the precise effect of leg load on interlimb coordination, the extent to which it varies with speed, and whether the critical factor is the magnitude of the load or its distribution. The novel locomotor paradigm introduced in Chapter 3 holds promise for clarifying such inconsistencies, so it is worth exploring these points of contention in greater detail. Note that the following paragraphs describe changes in limb phase relative to the step cycle of a hindleg, which is the default approach in this thesis (see 2.2.3.1).

Trotting quadrupeds have generally been reported to change their homolateral limb phase in response to load redistribution along the antero-posterior body axis, but the nature of this change has varied across studies. For example, locomotor simulations by Fukuoka and colleagues (2015) have predicted that nose-down locomotion and the associated increase in relative foreleg load will trigger a transition from trot to diagonal-sequence walk. This effect has been rationalised by a delay in forelimb swing onset relative to the diagonal hindlimb, which is consistent with the widely observed increase in the duty factor of loaded legs (Biewener, 1983; Lee, 2011; Lee et al., 2004) and is expected to widen the phase difference of homolateral limbs (Fukuoka et al., 2015). Reinforcing these results, an increase in hindlimb duty factor in anticipation of sudden treadmill stops has been linked to a reduction in homolateral phase difference and even emergence of pace in cats (Blaszczyk & Loeb, 1993). However, a number of studies, including empirical work on sloped surfaces and load-bearing experiments, have reported the opposite effect. Specifically, a more synchronised homolateral coordination has been associated with a forelimb-biased load distribution due to a delayed hindleg touchdown (Lammers et al., 2006; Lee, 2011; Lee et al., 2004; Owaki et al., 2013), such that the resulting stepping sequence resembles lateral walk at low speeds and could reflect a shift towards transverse gallop at high speeds. In agreement with these findings, mammals with a marked forelimb bias in their load distribution, such as hyenas and giraffes, do not display symmetrical two-beat gaits like trot and pace, and instead transition directly from walk to canter (Basu et al., 2019; Pennycuick, 1975). Given this conflicting evidence, it is apparent that the relationship between biomechanical feedback and homolateral coordination warrants further investigation.

Leg loading feedback has also been associated with more pronounced changes in gait, such as the transition from trot to gallop, which involves a phase shift in both homolateral and homologous limb pairs. For example, switching to gallop has been described to decrease the hindlimb duty factor less than that of the forelimbs, suggesting a posteriorward shift in relative support (Biewener, 1983). Another pair of studies has found a lowering of the trot-to-gallop transition speed after an increase in the total leg load (Farley & Taylor, 1991) or its redistribution towards the hindlegs (Wickler et al., 2003). While these reports disagree on the load-related variable relevant for gait transition, they highlight a speed-independent influence of biomechanical feedback on interlimb coordination. At the same time, a substantial body of work has proposed that the locomotor impact of leg load does depend on speed, becoming more significant during slow movement (Full & Koditschek, 1999; Ijspeert & Daley, 2023; Owaki et al., 2013; Pocratsky et al., 2020; Rybak et al., 2024). In particular, at low speeds and in demanding contexts, such as a slippery surface or exploratory locomotion, the spinal pattern-generator system has been suggested to operate in a "state-machine" mode, relying on continuous coordinating input from an extraspinal source, be it mechanical feedback, descending control, or a combination of both. In contrast, at moderate and high speeds, as well as on less challenging terrains, the control system is thought to operate in a spinal-autonomous feed-forward regime, dominated by intrinsic network oscillations. Although supraspinal input and load-related feedback are still considered important under those circumstances, their roles are thought to be limited to providing high-level guidance and supporting responses to perturbations, respectively (Rybak et al., 2024). It is further worth noting that the speed-dependence of biomechanical signals reflects a form of interaction between feedback and top-down locomotor control systems, given that the speed command is widely accepted to be conveyed through descending inputs from the MLR. As summarised in 1.2.2, changes in speed are associated with largely predictable, albeit probabilistic and often discontinuous, transitions between canonical gaits. Therefore, it is also interesting to consider the possibility of speed-dependent mechanical signals serving as mediators in the relationship between speed and gait.

In this chapter, I use the locomotor paradigm presented in Chapter 3 to investigate the role of leg loading feedback in interlimb coordination and its interaction with movement speed. It seems reasonable to hypothesise that modulation of load or its distribution will affect at least the homolateral phase, but I will also explore the impact of these variables on hindlimb coordination. It will be interesting to place the results in the context of the conflicting prior research described above, especially considering that biomechanical influences on locomotion have primarily been studied in large mammals with body builds and baseline weight distributions distinct from those of mice. Part of this work has been uploaded to a preprint server (Mitrevica & Murray, 2023).

4.2 Results

4.2.1 Speed-independent influence of load distribution on homolateral limb coordination

4.2.1.1 Manipulation of posture and slope in head-fixed locomotion suggests homolateral phase dependence on leg load distribution

Having established the snout-hump angle as a mouse size-invariant proxy for leg load and its anteroposterior distribution, I set out to explore the relationship between snout-hump angle and homolateral coordination. Over a period of two weeks, mice (n=20) were optogenetically induced to locomote on the passive treadmill while their head was fixed at different heights over a 25 mm range, as described in 2.1.3.1. Across experimental conditions, the observed homolateral phase varied from trot-like anti-phase coordination ($\sim \pi$ rad) to out-of-phase movements resembling gallop, with $\sim$1% average phase variation stride to stride (**Figure 4.1 A**). Notably, regardless of locomotor speed, there was a striking prevalence of strict homolateral alternation at hunched postures (mean±sd: $1.06 \pm 0.11\ \pi$ rad) and a quarter-of-phase more synchronised coordination at upward oriented snout-hump tilts ($0.54 \pm 0.13\ \pi$ rad; **Figure 4.1 B**). In addition, at either end of the observed snout-hump angle range, a minority of mice displayed a bimodal phase distribution (**Figure 4.1 C**). At more hunched postures, the homolateral phase distribution of 20% of mice peaked at $1.01 \pm 0.01\ \pi$ rad and $1.32 \pm 0.09\ \pi$ rad. Conversely, when the hump-snout vector was more upward directed, the phase distributions of another 15% of mice peaked at $0.49 \pm 0.02\ \pi$ rad and $0.91 \pm 0.09\ \pi$ rad. These mice were excluded from further analyses due to the unimodality assumption as described in 2.2.3.3.

To better discern the relative effects of posture and speed on homolateral coordination, I performed a circular-linear mixed-effect regression analysis, modelling homolateral phase as a linear function of speed, snout-hump angle, and reference leg with random effects to account for individual differences among mice (see 2.2.3.4 for details). The results confirmed snout-hump angle as a strong predictor of homolateral limb phase (*highest posterior density interval* HPD_{SSDO} = (0.58,0.75)), associating upward reorientation of the hump-snout vector with a phase transition that followed an approximately inverse sigmoidal pattern (**Figure 4.1 D**). This effect was bilaterally symmetrical (reference limb HPD_{SSDO} = (-0.04,0.08)) and highly conserved across animals (mean resultant length: 0.98, slope standard deviation: 4×10^{-4} rad/deg; **Figure 4.1 D, E**). In contrast, the effect of locomotor speed, while statistically significant (HPD_{SSDO} = (-0.82,-0.63)), was relatively minor, with higher speeds delaying forelimb stance onset by just $<0.1\ \pi$ rad over the range of observed speeds (**Figure 4.1 F**). Crucially, the influence of snout-hump angle was independent of speed, as indicated by the non-significant speed-angle interaction term (HPD_{SSDO} = (-0.81,0.80)). Therefore, these findings support the existence of a sensory-driven gait modulation mechanism that operates separately from the established speed-related pathway from the midbrain. However, considering that snout-hump angle in a head-fixed setting is associated with changes in both the absolute and relative leg load (see Figures 3.1, 3.4), the current results alone cannot determine whether the partial synchronisation of homolateral movements resulted from a reduction in the total load, its posteriorward redistribution, or upward arching of the back irrespective of leg load.

In order to differentiate between these possibilities, the same mice performed analogous trials on surfaces of various slopes, while their head was fixed at a single height. If homolateral limb phase was primarily influenced by the total leg load, declines would likely lead to more synchronised homolateral movement due to partial transfer of weight onto the head fixation apparatus, similar to upward oriented hump-snout vectors in head height trials. Conversely, if the relevant variable was the anteroposterior distribution of load, declines would be expected to increase the homolateral forelimb phase lag, akin to the effect of hunched postures in head height trials. Lastly, if leg load had no impact on homolateral phase and the previously observed effects were due solely to postural changes, homolateral coordination would remain unaffected by surface slope. Notably, slope trials revealed a shift in homolateral phase preference from nearly anti-phase coordination on steep declines (0.96 ± 0.14 π rad) to more synchronised movement on steep inclines (0.64 ± 0.17 π rad), supporting leg load distribution as a relevant factor in homolateral coordination (**Figure 4.2 A, B**). A few mice exhibited bimodal phase distributions, with one animal (8%) on declines and two others (17%) on inclines showing peaks at both 0.51-0.55 π and 0.95-1.25 π rad (**Figure 4.2 C**). At the same time, the phase modulation by surface slope was ∼57% more subtle than that by snout-hump angle in the head height trials, as well as slightly more varied

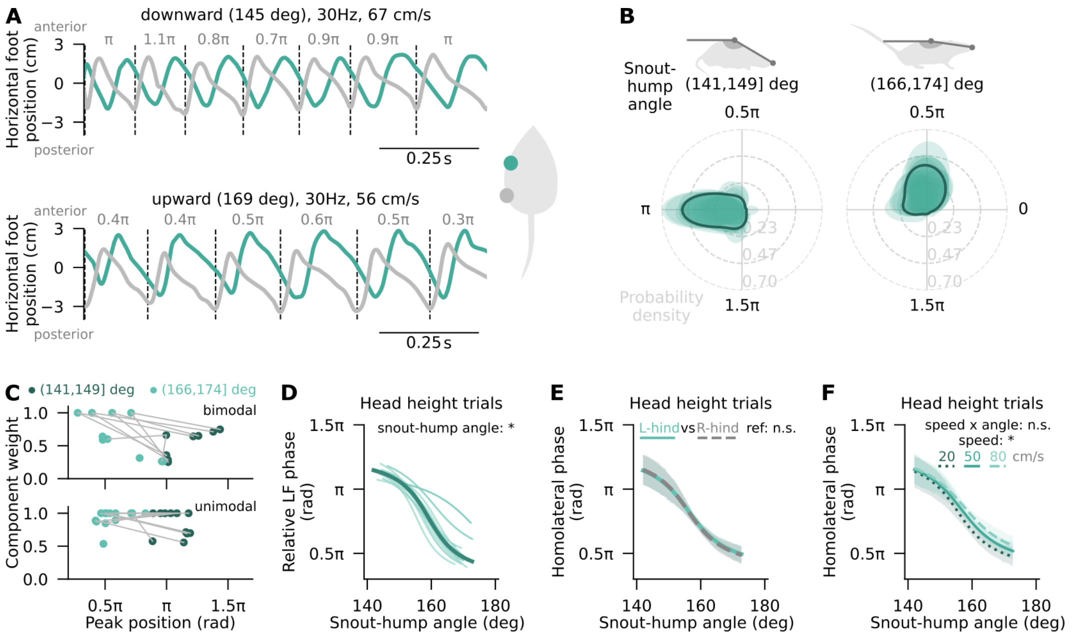

Figure 4.1: Homolateral limb phase correlates with snout-hump angle regardless of speed.
(A) Example time series showing the horizontal coordinate of the left hindlimb (LH; *grey*) and the left forelimb (LF; *teal*) during locomotion with a downward (*left*) and upward (*right*) oriented hump-snout vector. Speeds and snout-hump angles are averaged across strides. Vertical dashed lines partition the time series into strides based on LH swing onsets. Homolateral limb phases are printed above the traces. Optogenetic stimulation frequency is 30 Hz in both examples. **(B)** Kernel density smoothed distributions of LF phase relative to LH in two intervals of snout-hump angles, shown for individual mice (shaded regions; n=12 mice) and as averages across mice (solid outlines). Limb phase values of 0 and π rad reflect limb synchrony and alternation respectively. Data from mice with fewer than 40 strides per category were excluded from the respective plot. **(C)** Component weights from optimal Von Mises mixture model fits to the homolateral phase data in two snout-hump angle intervals, plotted against the phase corresponding to the peak of the respective component's probability distribution. Points are colour-coded by snout-hump angle interval, with each point representing an individual mouse. Points for the same mouse are connected by grey lines. Note that peak position is a circular variable presented on a linear scale for convenience. Components with weights under 0.2 are considered negligible and not shown (see 2.2.3.3). **(D)** Relative LF phase as a function of snout-hump angle with LH as the reference limb at median speed. Shown are circular-linear mixed-effects regression fits to single mouse data (random effects; light traces; n=12 mice) from head height trials and the average (fixed effect; dark trace). See Table 2.8 for model equation and statistics. **(E)** Homolateral phase as a function of snout-hump angle with both LH (solid teal traces) and right hindlimb (RH; dashed grey traces) used as the reference leg. Shown are the fixed effects from circular-linear mixed-effects regression on data from surface slope trials. Shaded regions represent 95% highest posterior density intervals. **(F)** Same as (E) but for three representative speeds. Statistical significance criterion: * HPD_{SSDO} interval does not include zero, n.s. otherwise.

across animals (mean resultant length: 0.96, slope standard deviation: 3×10^{-3} rad/deg; **Figure 4.2 D**).

Further insight into various influences on homolateral coordination was again gleaned through circular-linear mixed-effect regression analysis, using a linear function of all the previous predictors, as well as surface slope, to model changes in homolateral phase. Like in the head height trials, homolateral coordination was confirmed as bilaterally symmetrical ($HPD_{SSDO} =$ (0,0.12); **Figure 4.2 E**), and the effect of speed was found to be relatively minor (0.05±0.06 π rad; **Figure 4.2 F**). The speed-slope interaction, although statistically significant, contributed a phase difference of just ∼0.01 π rad over an 80 deg change in slope, suggesting that the apparent interdependence of speed and slope might bear no practical relevance. This conjecture was further supported by an improvement in model fit after excluding the speed-slope interaction term from the regression equation (Table 2.8). Conversely, snout-hump angle was again found to have a pronounced effect on homolateral phase ($HPD_{SSDO} =$ (0.63,0.88)). Over the comparatively narrow 11±1 deg range of snout-hump angles allowed by the fixed absolute head height, homolateral phase shifted by 0.45±0.05 π rad towards more synchronised coordination at more upward snout-hump orientations, reflecting a slightly smaller incremental effect of posture than in the head height trials (**Figure 4.2 G**). If the observed changes in homolateral phase were truly explained by leg load distribution, the difference in effect attributed to snout-hump angle in head height and slope trials would be expected to be entirely captured by the effect of slope. Indeed, performing joint regression analysis on data from both head height and slope trials revealed no significant effect of trial type (**Figure 4.3 A**), supporting the hypothesis of load distribution-dependent homolateral coordination.

This interpretation of the relationship between homolateral phase and leg load distribution is strengthened by three further arguments. First, the ef-

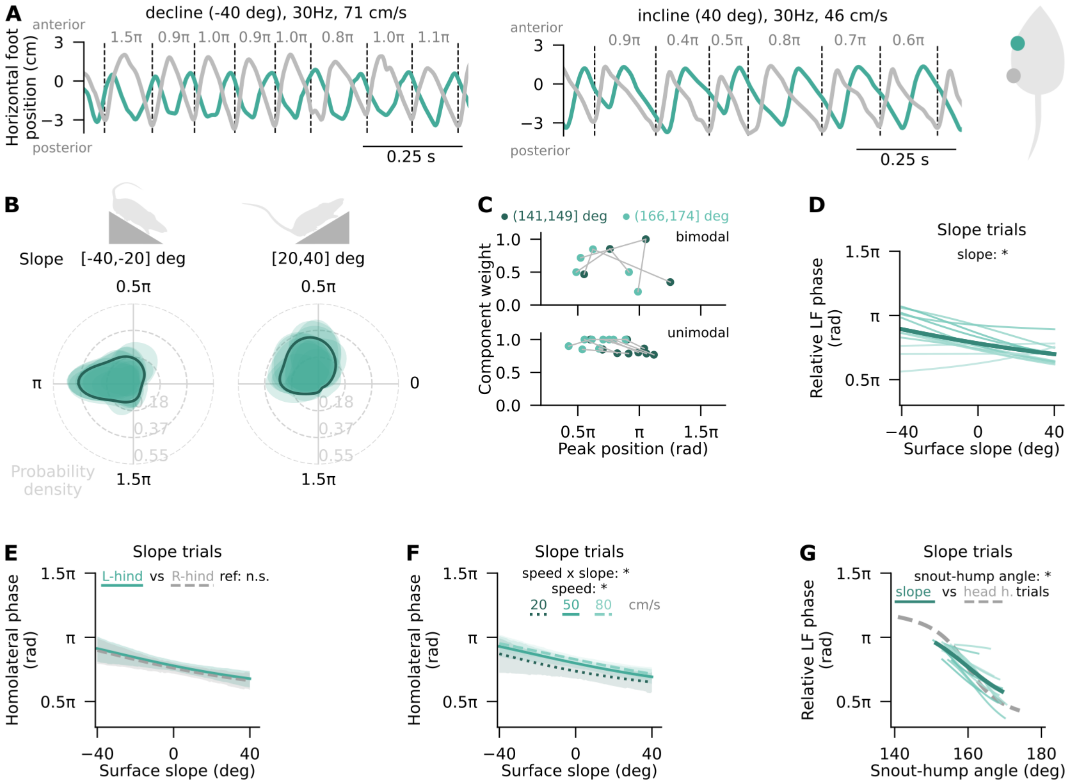

Figure 4.2: Homolateral limb phase correlates with surface slope regardless of speed.
(A) Example time series of LH (*grey*) and LF (*teal*) horizontal coordinates during locomotion on a 40 degree decline (*left*) and incline (*right*). Speeds are stride-averaged. Vertical dashed lines mark LH swing onsets, with homolateral limb phases indicated above. Optogenetic stimulation frequency: 30 Hz. **(B)** Kernel density smoothed distributions of LF phase relative to LH in two surface slope intervals, shown for individual mice (shaded regions; n=12 mice) and as averages across mice (solid outlines). Phases of 0 and π rad reflect limb synchrony and alternation respectively. Data from mice with fewer than 40 strides per category were excluded. **(C)** Component weights from optimal Von Mises mixture model fits to the homolateral phase data in two surface slope intervals, plotted against the phase corresponding to the peak of the respective component's probability distribution. Points are colour-coded by slope interval, with each point representing an individual mouse. Points for the same mouse are connected by grey lines. Note that peak position is a circular variable presented on a linear scale for convenience. Components with weights under 0.2 are considered negligible and not shown (see 2.2.3.3). **(D)** Relative LF phase as a function of surface slope with LH as the reference limb at median speed and snout-hump angle. Shown are circular-linear mixed-effects regression fits to single mouse data (random effects; light traces) from head height trials and the average (fixed effect; dark trace). See Table 2.8 for model equation and statistics. **(E)** Homolateral phase as a function of surface slope with both LH (solid teal traces) and RH (dashed grey traces) used as the reference leg. Shown are the fixed effects from circular-linear mixed-effects regression on data from surface slope trials. Shaded regions represent 95% highest posterior density intervals. **(F)** Same as (E) but for three representative speeds. **(G)** Same as (D) but as a function of snout-hump angle. The analogous fixed effect of snout-hump angle in head height trials is shown by the dashed grey trace.
Statistical significance criterion: * HPD_{SSDO} interval does not include zero, n.s. otherwise.

fects of snout-hump angle and slope were interdependent, with each variable exerting a stronger influence on homolateral phase when the other variable was associated with relatively greater forelimb loading (angle-slope interaction HPD_{SSDO} = (-0.83,-0.63); **Figure 4.3 B**). This interaction suggests that the effects of the two perturbations might be mediated through a common mechanism, such as the anteroposterior load distribution. It is also worth noting that the most forelimb-biased load distribution achieved by the passive treadmill paradigm placed CoS just slightly anterior to the geometric centre of the body, whereas the most hindlimb-biased load distribution was considerably more asymmetrical (see Figures 3.3 B, 3.4 C). This skew in experimental design raises the possibility that the reduced sensitivity of homolateral phase to changes in snout-hump angle observed on extreme inclines, as well as its lower sensitivity to changes in surface slope at most upward oriented postures, could indicate a saturation effect.

Second, including body weight as a predictor in regression analysis revealed a propensity of greater weight to delay the phase of the homolateral forelimb (HPD_{SSDO} = (-0.83,-0.63); **Figure 4.3 C**). Since heavier mice require a greater redistribution of body mass to shift the CoS over a given distance, this finding is consistent with load distribution contributing to homolateral phase modulation. Finally, having load sensor and locomotor data for both types of trials allowed me to translate changes in snout-hump angle and slope into shifts in anteroposterior CoS. This in turn provided an opportunity to investigate whether the relationship between homolateral coordination and CoS was consistent across biomechanical manipulations. The analysis confirmed that the shift in homolateral phase associated with changes in anteroposterior load distribution was not significantly different between head height and slope trials (p=0.1, *t-test*; **Figure 4.3 D**). In particular, a posteriorward ~0.4 cm shift in the CoS was associated with a quarter-of-phase more synchronised homolateral coordination regardless of the approach used to manipulate CoS. Altogether, these results are consistent with the hypothesis that anteroposterior leg load distribution contributes to interlimb coordination by specifically influencing homolateral limb phase, and does so in a manner independent of locomotor speed (**Figure 4.3 E**).

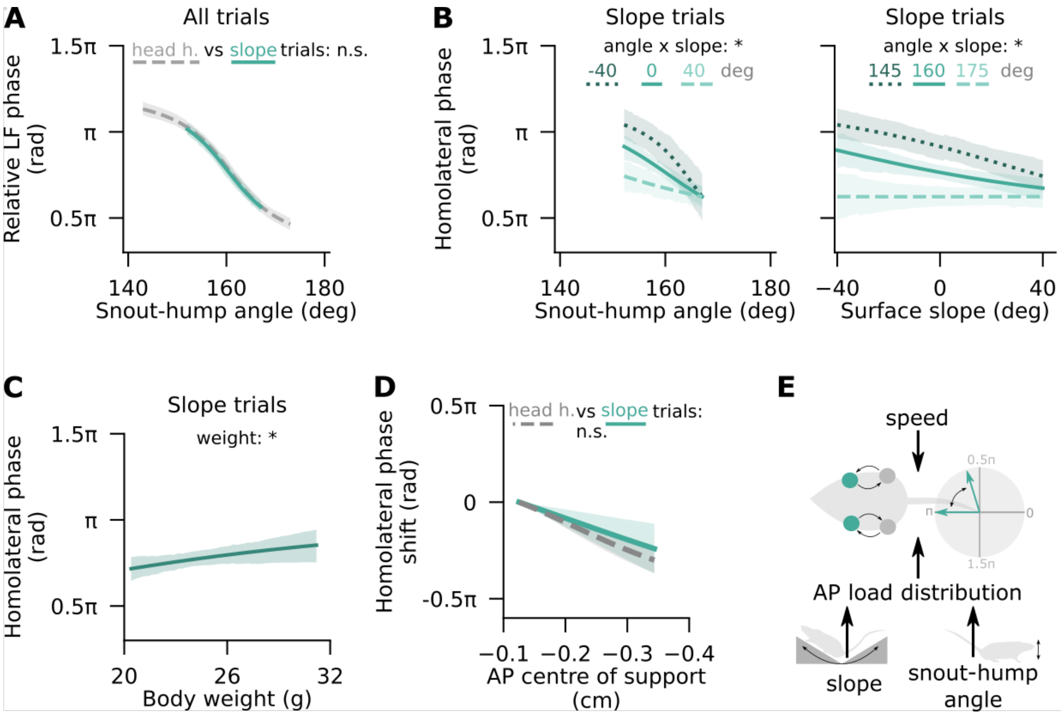

Figure 4.3: Anterposterior leg load distribution is a plausible modulator of homolateral phase.
(A) Relative LF phase as a function of snout-hump angle with LH as the reference limb at median speed and surface slope. Shown are circular-linear mixed-effects regression fits to data from head height and slope trials with trial type as a predictor. Shaded regions are 95% highest posterior density intervals. See Table 2.8 for model equation and statistics. **(B)** Homolateral phase as a function of snout-hump angle (*left*) and surface slope (*right*) in slope trials at median speed, showing the slope-angle interaction effect determined through circular-linear mixed-effects regression. **(C)** Same as (B) but as a function of animal body weight. **(D)** Homolateral phase shift as a function of the anteroposterior CoS position in surface slope (teal) and head height (grey) trials, analysed over the range of CoS positions observed in all mice in response to changes in either slope or snout-hump angle. This range was constrained by the snout-hump angles seen in slope trials. **(E)** Schematic representation of the working hypothesis.
Statistical significance criterion (A-D): * HPD_{SSDO} interval does not include zero, n.s. otherwise. Statistical significance thresholds (E): * $p < 0.05$, ** $p < 0.01$, *** $p < 0.001$.

4.2.1.2 Load-related phase transitions modulate limb support distribution with minimal influence from stride length or stance duration

Based on the evidence considered so far, the relationship between anteroposterior CoS and homolateral phase cannot be considered causal and the mechanism linking these variables is not necessarily straightforward to intuit. While the former caveat will be addressed in Chapter 5, the latter can be explored by considering the biomechanical consequences of increased and unevenly distributed leg load. For example, an increase in the absolute load borne by a leg could result in strain-related injury. To prevent this scenario, mice might counteract the associated rise in peak muscle forces by spreading the total force over a longer period of time or a greater number of effectors. Alternatively, mice might adopt more synchronised homolateral coordination to lower the chance of limb collision, especially if the posteriorward redistribution of load had increased hindlimb stride length. Thus, it is worth examining if the relationship between load distribution and homolateral phase could be mediated by changes in stance duration or stride length of the loaded leg.

If the association between homolateral phase and anteroposterior load distribution was mediated by load-dependent changes in stance duration, proxy measures of load, like snout-hump angle and surface slope, should correlate with the ratio between hindlimb and forelimb duty factors. Furthermore, including this ratio in circular-linear regression analyses would be expected to weaken or eliminate the effects on homolateral phase attributed to snout-hump angle and slope. Notably, neither of these predictions were supported by the data. The duty factor ratio was not correlated with the load-related variables (absolute Pearson coefficient values: <0.1), and its effect on homolateral phase was not significant in either head height or slope trials ($HPD_{SSDO} =$

(-1.19,1.18); **Figure 4.4 A**). Still, this variable showed significant interaction effects with both snout-hump angle and slope such that greater hindleg-bias in stance phase duration made homolateral phase 18-25% less sensitive to changes in snout-hump angle or slope over the observed range of duty factor ratios (**Figure 4.4 B, C**). These results suggest that the balance between forelimb and hindlimb duty factors might influence the relationship between load distribution and homolateral phase, but is not its sole mediator.

The role of stride length was found to be similar. A set of regression analyses showed that stride length had no main effect on homolateral phase (HPD_{SSDO} = (-0.70,0.69)) and accounted for only 6-18% of the variance in surface slope and snout-hump angle. Although its interaction with load-related variables was statistically significant, it produced a phase difference of less than 0.1π over the entire observed range of stride lengths. Thus, stride length is also unlikely to be a primary mediator of the striking shift in homolateral phase preference upon posteriorward redistribution of leg load.

Notably, the relationship between anteroposterior CoS and homolateral phase in itself could potentially be rationalised as an injury prevention mechanism. By engaging the support from the homolateral forelimb earlier in the step cycle, mice can distribute load over a greater number of legs or swap the diagonally synchronised trotting gait for an energetically favourable footfall pattern with distributed contacts (Usherwood, 2020). To assess the viability of this hypothesis, I examined the primary axes of limb support variance during passive treadmill locomotion and studied their association with snout-hump angle, slope, and anteroposterior centre of support. The first four principal components (PCs) collectively explained 90% of variance (**Figure 4.4 D**). The first PC (33% of variance) distinguished between three- and four-limb support, the second (27%) captured a broad shift from higher levels of limb support to one- and two-limb support, the third (23%) emphasised changes in diagonal support, whereas the fourth (8%) reflected an increase in single leg support at the expense of homologous leg support. A support pattern that results from a leg load-related change in homolateral phase would be expected to have a consistent, and significant, relationship with anteroposterior centre of support across head height and slope trials. These criteria were met only by the third and fourth PCs, with their projected values suggesting that diagonal and, to a lesser extent, homologous leg support decreased in favour of single-leg support as load was redistributed towards the hindlimbs (p between 5×10^{-9} and 3×10^{-13}; **Figure 4.4 E, F**). Data projected along the other major axes of limb support variance either displayed conflicting influences of snout-hump angle and slope (PC1) or had different effects of snout-hump angle depending on trial type (PC2). Regressing the projected values of the third PC against speed, snout-hump angle, and slope revealed a significant main effect of snout-hump angle and interaction effects between snout-hump angle ($p=6 \times 10^{-7}$) and each of the other two predictors (angle-speed: $p=1 \times 10^{-41}$, angle-slope: $p=1 \times 10^{-4}$). Analogous analysis of the fourth PC indicated a significant main effect of speed ($p=7 \times 10^{-76}$) and an interaction between snout-hump angle and slope (p=0.01). Since no effect of snout-hump angle was found in head height trials with fixed slope, variation in single-leg support likely relates to, but is not primarily driven by, leg load-related variables. Given that homolateral phase was independently influenced by both speed and leg load-related variables, these results are consistent with the interpretation that changes in the prevalence of diagonal and single-leg support within each stride are a secondary effect of load-related changes in homolateral coordination.

To further explore the roles of diagonal and distributed support, I directly regressed data projected along the third and fourth PCs of limb support variance against homolateral phase, split into sine and cosine components. If more synchronised homolateral coordination promoted an increase in single-leg support at the expense of diagonal support, the projected values of PC3 and PC4 would be expected to show a significant association with at least one of the circular phase components (sine or cosine), reaching a minimum and maximum respectively near a homolateral phase of 0. Moreover, trial type should have no bearing on this relationship. Fully consistent with this prediction, the data projection along PC3 peaked near strict homolateral alternation (0.9π) and reached a minimum at the point of homolateral synchrony (**Figure 4.4 G**). The opposite pattern was seen for the same data projected along PC4, with a minimum between 0.9 and 1.1 π (**Figure 4.4 H**). Both PCs showed a significant correlation with homolateral phase (cosine p between 9×10^{-5} and 3×10^{-6}), independent of trial type (p between 0.2 and 0.6). Overall, these results support a hypothesis that the change in homolateral phase in response to a load redistribution is itself a strategy for lowering mechanical strain and energy costs.

4.2.1.3 Homolateral coordination in non-restrained locomotion is consistent with load distribution-dependent modulation

So far, I have demonstrated a significant shift in homolateral limb coordination in response to changes in snout-hump angle or surface slope during optogenetically induced, head-fixed locomotion. To investigate whether these effects are present during non-restrained self-initiated movement, I recorded mouse locomotion on a level (n=12 mice) and sloped (n=10) motorised treadmill without head fixation or optogenetic stimulation. Just as observed on the passive treadmill, upward reorientation of the hump-snout vector correlated with a homolateral phase shift towards synchronisation, reflected by a phase change from 0.92±0.07 π rad to 0.79±0.11 π rad as the snout-hump angle increased by 25 deg (**Figure 4.5 A**). Similarly, an 80 deg change in surface slope was associated with a shift in homolateral phase from 0.85±0.08 π rad

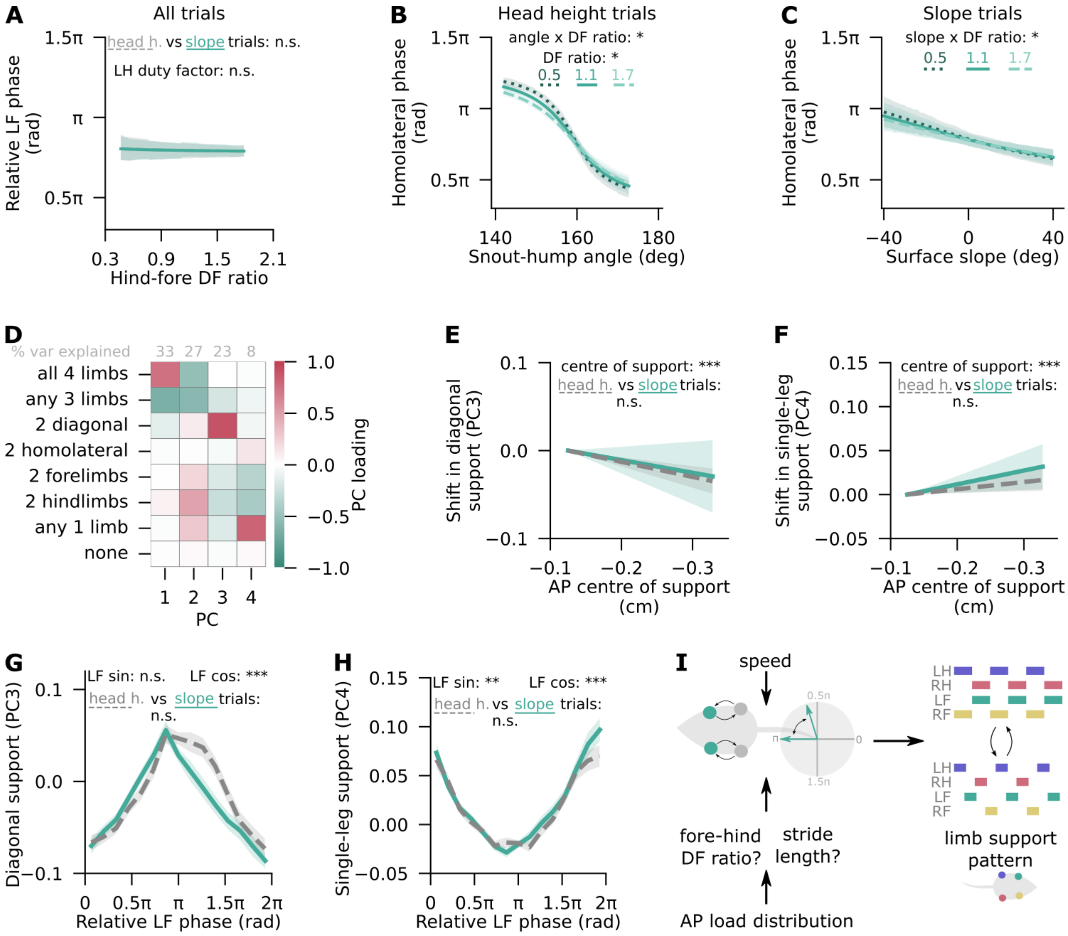

Figure 4.4: Load-related phase transitions modulate limb support distribution with minimal influence from stride length or stance duration.
(A) Relative LF phase as a function of hindlimb-forelimb duty factor ratio, with LH as the reference limb. Shown are the fixed effects from circular-linear mixed-effects regression on data from head height and slope trials with trial type as a predictor. Shaded regions are 95% highest posterior density intervals. See Table 2.8 for model equation and statistics. **(B-C)** Homolateral phase as a function of snout-hump angle (B) and surface slope (C) at three duty factor ratios that span the range of observed values. Shown are the fixed effects from circular-linear mixed-effects regression analysis. Shaded regions represent 95% highest posterior density intervals. **(D)** Loadings of the first four principal components representing variance in limb support fractions. The variance explained by each component is shown above the heatmap. **(E-F)** Shift in limb support data projected along PC3 (E) and PC4 (F) as a function of anteroposterior centre of support in head height and slope trials. Statistical significance was assessed through linear mixed-effects regression (see 2.2.2.5). **(G-H)** Projections of limb support data along PC3 (G) and PC4 (H) as a function of left forelimb phase relative to left hindlimb phase in head height and slope trials. The horizontal axis presents a circular variable on a linear scale for convenience. **(I)** Schematic representation of the working hypothesis updated in light of the results of section 4.2.1.2.
Statistical significance criteria: (A-C) * HPD_{SSDO} interval does not include zero, n.s. otherwise. Statistical significance thresholds (E-H): * $p < 0.05$, ** $p < 0.01$, *** $p < 0.001$.

on steep declines to 0.78±0.06 π rad on steep inclines (**Figure 4.5 B**). As before, the relationships between these variables, as well as the influence of speed and reference leg identity, were quantified using circular-linear mixed-effects regression. This analysis confirmed that the effects of snout-hump angle and surface slope were statistically significant, bilaterally symmetrical, and consistent across mice (mean resultant length: 0.98; see Table 2.9 for other statistics; **Figure 4.5 C-E**). The influence of speed was more pronounced than during head-fixed stepping, consistent with the idea of motorised treadmill locomotion requiring substantial supraspinal oversight (Pocratsky et al., 2020; **Figure 4.5 F, G**). This also implies that the optogenetic CnF stimulation used to trigger locomotion on the passive treadmill might be a comparatively crude approach to speed control, despite the correlation between speed and stimulation frequency (see Figure 3.7). In addition, speed appeared to interact significantly with both snout-hump angle and surface slope, although the interaction effects were minimal at just 0.02 rad/deg and less than 0.01 rad/deg respectively (**Figure 4.5 F, G**). Since removing the interaction terms improved model fit (Table 2.9), the influence of these variables can be considered practically independent of speed, as on the passive treadmill.

The most notable difference compared to the passive treadmill experiments is that the effects related to variations in snout-hump angle and slope during non-restrained locomotion were comparatively small, amounting to just 22-24% of the phase shift seen previously. Moreover, within the observed range of snout-hump angles, there was no indication of a steep sigmoid-like change in homolateral phase, as seen near 160 degrees on the passive treadmill (compare Figures 4.1 D and 4.5 C). This apparent decrease in homolateral phase modulation is likely explained by a combination of factors. Firstly, during non-restrained locomotion, mice were unable to manipulate their total leg load through interaction with the head fixation apparatus, which presumably re-

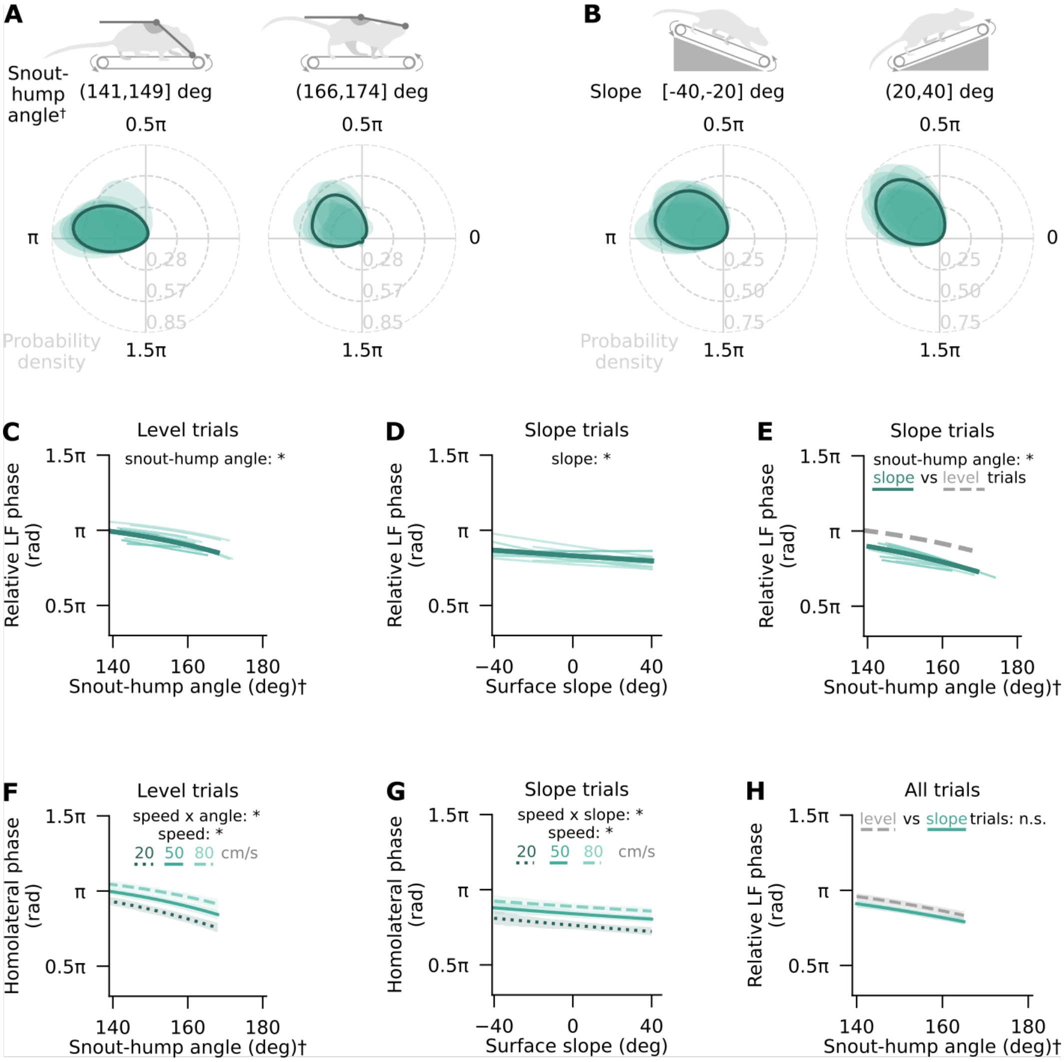

Figure 4.5: Homolateral coordination in non-restrained locomotion is consistent with load distribution-dependent modulation.
(A-B) Kernel density smoothed distributions of LF phase relative to LH in two intervals of snout-hump angles (A) and surface slopes (B) recorded on the motorised treadmill. Shown are data for individual mice (shaded regions; n=12 mice) and their averages (solid outlines). Phase values of 0 and π rad reflect limb synchrony and alternation respectively. Data from mice with fewer than 40 strides per category were excluded. **(C-E)** Relative LF phase as a function of snout-hump angle (C, E) and surface slope (D) with LH as the reference limb at median speed, using data from level (C) and slope (D-E) trials. Shown are circular-linear mixed-effects regression fits to single mouse data (random effects; light traces) and the average (fixed effect; dark trace). See Table 2.9 for model equation and statistics. In (E), the mean effect from level trials is also shown (*grey, dashed*). **(F-G)** Homolateral phase as a function of snout-hump angle (F) and surface slope (G) at three representative speeds, using data from level (F) and slope (G) trials. Shown are the fixed effects from circular-linear mixed-effects regression analysis. Shaded regions represent 95% highest posterior density intervals. **(H)** LF phase as a function of snout-hump angle with LH as the reference limb, using data from level (*grey, dashed*) and slope (*teal, solid*) trials. Shown are the fixed effects from circular-linear mixed-effects regression analysis with trial type as a predictor. Statistics refer to regression terms that capture the interaction between trial type and snout-hump angle, not the categorical main effect of trial type.
† indicates that snout-hump angle is measured in non-restrained conditions and is not necessarily directly comparable to the snout-hump angle from head-fixed experiments. Statistical significance criterion: * HPD_{SSDO} interval does not include zero, n.s. otherwise.

duced the redistribution of load they experienced. Secondly, mice countered increases in surface slope by both adopting more hunched postures and positioning their feet more anteriorly (**Figure 4.6 A, B**). This dual adaptive strategy can be expected to minimise the posteriorward load redistribution imposed by inclined surfaces to a greater degree than the adaptations mice used on the passive treadmill. Finally, due to the variability in head pitch angle during head-free locomotion, the snout-hump angles recorded in those conditions do not directly correspond to the snout-hump angles observed while the mice were head-fixed (see Figure 3.9). This discrepancy can be expected to dilute the phase modulation effect attributed to snout-hump angle, just as it likely obscures the correlation between snout-hump angle and foot position seen on the passive treadmill (**Figure 4.6 C**). Furthermore, it complicates efforts to relate the observed changes in homolateral phase to leg load distribution. In fact, given that mice adopted a downward head tilt on average, it is plausible that their load distribution was anterior-biased enough to restrict homolateral phase to the saturation region characteristic of low snout-hump angle values on the passive treadmill. Additionally, non-restrained mice exhibited a 12% lower body height in slope trials compared to locomotion on a level surface, which might explain the significant categorical effect of trial type on homolateral phase that remained even after accounting for snout-hump angle and slope (HPD_{SSDO} = (0.06,0.24)). Still, trial type did not affect the relationship between homolateral phase and snout-hump angle, as indicated by a non-significant interaction between these predictors (HPD_{SSDO} = (-1.9,1.9); **Figure 4.5 H**).

Another major difference between the two treadmill setups is the substantially greater propensity by the passive treadmill paradigm to elicit a variety of left-right coordination patterns, in contrast to the dominance of trot on the motorised treadmill (see Figure 3.7). Given inter-CPG connectivity, it would

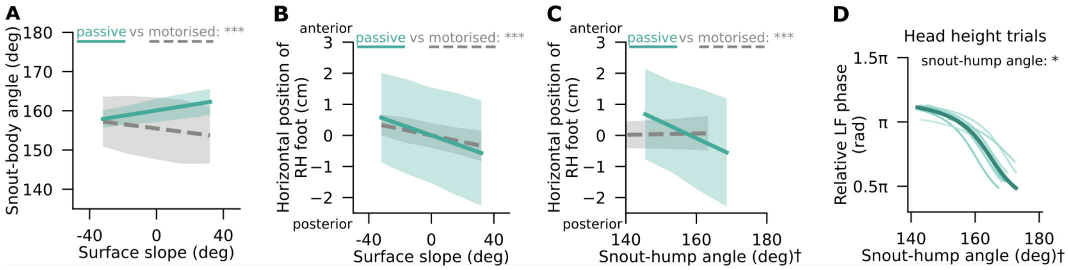

Figure 4.6: Motorised and passive treadmill data differ partly due to distinct postural adaptations to slope, with no clear link to differences in left-right coordination.
(A-C) Snout-hump angle (A) and the relative position of the right hindfoot (B-C) as a function of surface slope (A-B) and snout-hump angle (C) during locomotion on the passive treadmill (solid teal line) and motorised treadmill (dashed grey line), approximated by linear regression. The shaded regions show 95% confidence intervals. Statistical significance is assessed using a likelihood ratio test. **(D)** Relative LF phase as a function of snout-hump angle in strides when left-right phase was $1 \pm 0.2\ \pi$. LH is used as the reference limb. Shown are circular-linear mixed-effects regression fits to single mouse data (random effects; light traces) from head height trials on the passive treadmill and the average (fixed effect; dark trace), all at median speed. See Table 2.8 for model equation and statistics.
† indicates that snout-hump angle is measured in non-restrained conditions and is not necessarily directly comparable to the snout-hump angle from head-fixed experiments
Statistical significance thresholds (A-C): * $p < 0.05$, ** $p < 0.01$, *** $p < 0.001$. Statistical significance criterion (D): * HPD_{SSDO} interval does not include zero, n.s. otherwise.

seem trivial for a strong coupling between the homologous limbs, as seen on the motorised treadmill, to limit the space of viable coordination patterns for the homolateral legs. However, even when considering only the passive treadmill strides with strict left-right alternation ($1.0 \pm 0.2\ \pi$ rad), changes in snout-hump angle correlate with a pronounced shift in homolateral phase (**Figure 4.6 D**). Thus, differences in homologous coordination are unlikely to significantly contribute to the decrease in homolateral phase modulation seen on the motorised treadmill.

It is also worth noting that, like on the passive treadmill, changes in snout-hump angle or slope were not correlated with hindlimb-forelimb duty factor ratio (absolute Pearson coefficient values: <0.05). Although this kinematic variable had a significant main effect on homolateral phase (level trials:

HPD_{SSDO}=(-2.00,-1.74); slope trials: HPD_{SSDO}=(-1.92,-1.64)), its inclusion in the regression analyses did not diminish the effects attributed to snout-hump angle or surface slope. In fact, its influence was minor in comparison, amounting to just a 0.01-0.02 π rad change in homolateral phase over the entire range of observed duty factor ratios (**Figure 4.7 A, B**). Thus, consistent with the passive treadmill experiments, the hypothesised relationship between antero-posterior leg load distribution and homolateral phase may be modulated, but is not mediated, by changes in the relative ground contact duration of the legs.

At the same time, projecting data onto the primary limb support axes of variance identified in 4.2.1.2 revealed strong associations between snout-hump angle and the prevalence of both diagonal ($p=0.002$) and single-leg ($p=2\times10^{-7}$) support patterns, captured by PC3 and PC4 respectively (**Figure 4.7 C, D**). Consistent with head-fixed locomotion, the within-stride fraction of diagonal support declined, while that of single-leg support increased as the hump-snout vector assumed a more upward orientation. Likewise, the use of diagonal support decreased on upsloping surfaces especially when the snout-hump angle promoted more anterior load distribution ($p=1 \times 10^{-7}$; **Figure 4.7 E**). Notably, these relationships were preserved on the motorised treadmill despite the overall dominance of trot-like diagonal support (see Figure 3.9). Only the slope-dependence of single-leg support deviated from that seen during head-fixed locomotion, failing to reach statistical significance ($p=0.07$) and tending to decrease on inclined surfaces ($p=0.08$; **Figure 4.7 E**). Since this tendency was more pronounced when the snout-hump angle encouraged a posteriorward shift in load distribution, the observed discrepancy in slope dependence across trial types might reflect the postural counter-adjustments to changes in slope described previously (see Figure 4.6). Still, speed was a highly significant predictor of both examined support patterns ($p<1 \times 10^{-16}$). Altogether these results reinforce the hypothesis that modulation of limb sup-

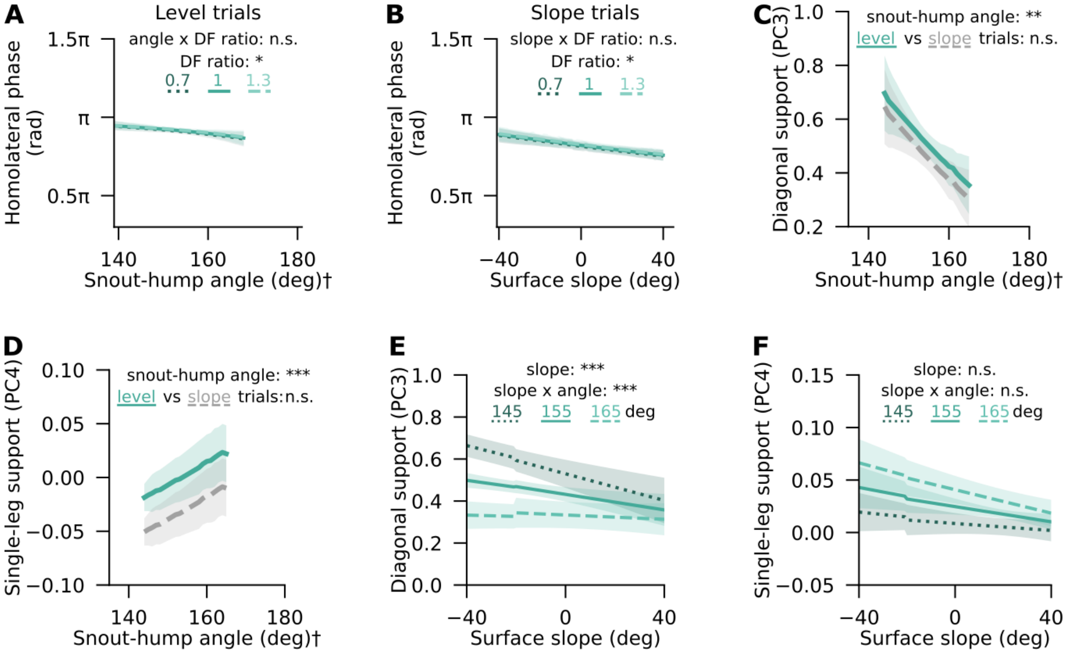

Figure 4.7: Roles of limb support patterns and duty factor ratio are consistent during non-restrained and head-fixed locomotion.
(A-B) Homolateral phase as a function of snout-hump angle (A) and surface slope (B) at three duty factor ratios that span the range of observed values. Shown are the fixed effects from circular-linear mixed-effects regression analysis. Shaded regions represent 95% highest posterior density intervals. **(C-D)** Projections of limb support data along PC3 (C) and PC4 (D) as a function of snout-hump angle in level (*teal, solid*) and slope (*grey, dashed*) trials. Shaded regions show 95% confidence intervals. Statistics refer to the effects attributed to snout-hump angle and its interaction with trial type in linear mixed-effects regression. **(E-F)** Same and (C) and (D) but projections of limb support data have been plotted as a function of surface slope at three representative snout-hump angle values.
† indicates that snout-hump angle is measured in non-restrained conditions and is not necessarily directly comparable to the snout-hump angle from head-fixed experiments.
Statistical significance criterion (A-B): * HPD_{SSDO} interval does not include zero, n.s. otherwise. Statistical significance thresholds (C-F): * $p < 0.05$, ** $p < 0.01$, *** $p < 0.001$.

port patterns is a speed-dependent downstream effect of load-driven shifts in homolateral phase.

Overall, without direct load measurement on the motorised treadmill, it is challenging to connect the observed changes in homolateral phase to leg load distribution or explain the differences in the results obtained during optogenetically stimulated head-fixed locomotion on the passive treadmill and non-restrained self-driven locomotion on the motorised treadmill. Nonetheless, the results on the two setups are broadly consistent in that conditions associated with posteriorward load redistribution tend to reduce the relative phase of the homolateral forelimb, thereby shifting homolateral coordination towards synchrony. This suggests that the proposed role of anteroposterior load distribution in homolateral coordination is not an artifact of the novel locomotor paradigm, but rather a fundamental feature of quadrupedal gait control that the passive treadmill paradigm has helped uncover.

4.2.2 Dominance of descending influences in homologous limb coordination

4.2.2.1 Asymmetries in homologous limb coordination relate to descending inputs

Although homolateral coordination was hypothesised to be the primary target of leg load-related modulation, the novel locomotor paradigm presented an exciting opportunity to explore how descending and biomechanical inputs influence left-right coordination as well. At both pelvic and shoulder girdles, homologous limb phase displayed a notable lateral bias such that gallop-like out-of-phase coordination was preferentially right-leading in mice with optogenetic stimulation in the right cuneiform nucleus (CnF), and predominantly left-leading in those stimulated on the left side (hindlimb $p=9 \times 10^{-8}$, forelimb $p=2 \times 10^{-5}$, *t-test*; **Figure 4.8 A**). In other words, whenever homologous coordination was neither strictly alternating nor synchronous, descending activation, on average, promoted a stepping sequence in which the ipsilateral leg touched the ground more anteriorly and generated the final push-off force for propulsion. This pattern was not observed during motorised treadmill locomotion without stimulation (**Figure 4.8 B**), where stepping order preference was inconsistent across the two girdles and showed no significant difference between mice with right and left CnF surgeries (hindlimb p=0.41, forelimb p=0.37). These results suggest a significant role for descending stimulation in modulating left-right phase preference.

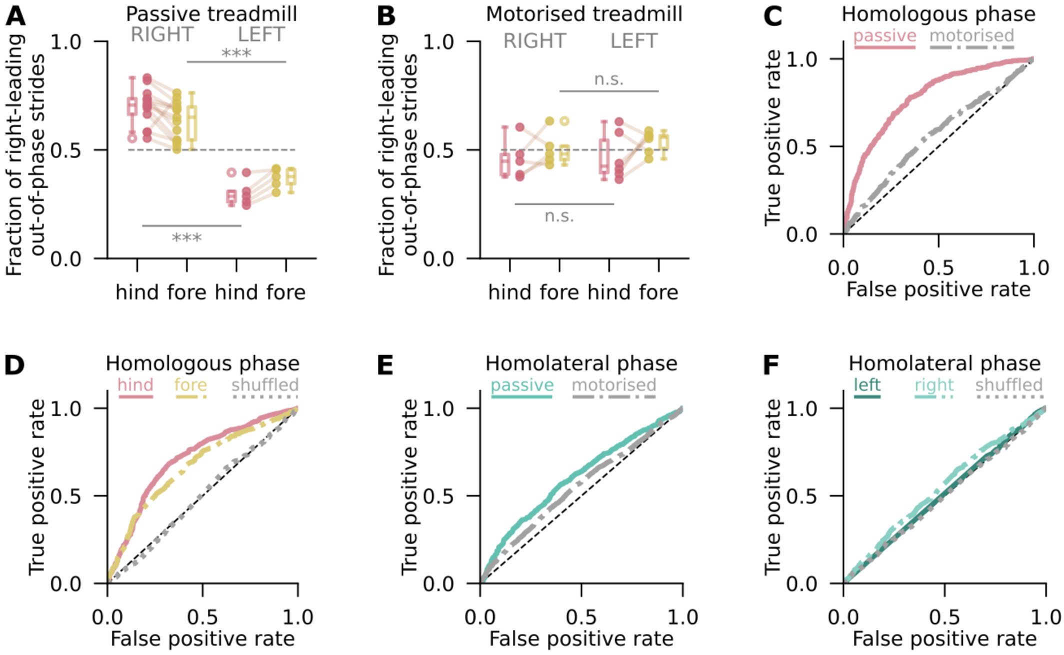

Figure 4.8: Motorised and passive treadmill data differ partly due to distinct postural adaptations to slope, with no clear link to differences in left-right coordination.

(A-B) The fraction of right-leading steps between hindlimbs (*pink*) and forelimbs (*yellow*) during optogenetically induced locomotion on the passive treadmill (A) and motorised treadmill (B). Dots represent individual mice, connected by lines and plotted separately depending on the side of optogenetic stimulation. Near-alternating (1±0.2 π rad) or near-synchronised (0±0.2 π rad) steps are excluded. **(C-F)** Receiver operating characteristic curve of a binary classifier trained to predict the side of virus injection and optic fibre implantation. In (C), the classifier was trained on a combination of hindlimb and forelimb homologous phase data during stimulated locomotion on the passive treadmill (*pink, solid*) and non-stimulated locomotion on the motorised treadmill (*grey, dash-dot*). In (D), it was trained on hindlimb (*pink, solid*) and forelimb (*yellow, dash-dot*) homologous phase data separately. In (E), the classifier trained on a combination of left and right homolateral phase data during stimulated locomotion on the passive treadmill (*teal, solid*) and non-stimulated locomotion on the motorised treadmill (*grey, dash-dot*). In (F), it was trained on left (*dark teal, solid*) and right (*light blue, dash-dot*) homolateral phase data. In (D) and (F), also shown is the performance of a binary classifier trained on homologous phase data with shuffled outcome labels (*grey, dotted*).

Statistical significance thresholds: * $p < 0.05$, ** $p < 0.01$, *** $p < 0.001$.

To further investigate this hypothesis, I extended the analysis beyond per-mouse averages by exploring the capacity of a binary classifier to predict the side of optogenetic stimulation from limb phase data. The classifier achieved an accuracy of 70.2±1.5% when trained on homologous phase data from both forelimbs and hindlimbs, performing well above chance (**Figure 4.8 C**). This performance surpassed classifiers trained on either hindlimb or forelimb phase data alone, although those were still able to predict stimulation side with 67.7±0.5% or 62.7±2.0% accuracy respectively (**Figure 4.8 D**). Notably, even in the absence of stimulation, combined limb phase data from both girdles yielded a prediction accuracy of 54.3±1.3%, slightly exceeding chance. This outcome suggests that unilateral tissue damage from virus injection and optic fibre implantation might have introduced subtle biases in homologous coordination. A similar, slightly above-chance accuracy of 56.1±0.9% was also achieved by a classifier trained on optogenetically induced homolateral phase data (**Figure 4.8 E**). However, this non-random performance likely reflects the interdependence between homolateral and homologous limb pairs, considering that classifiers trained on data from only the left or right homolateral pair performed at chance level (**Figure 4.8 F**). Altogether, these findings highlight a substantial capacity of bilaterally asymmetrical descending inputs from the CnF to influence homologous coordination.

4.2.2.2 Hindlimb coordination is influenced by snout-hump angle and total leg load in a speed-dependent manner

Data from head height and slope trials presented in 4.2.1 provides a valuable basis for exploring the influences of body biomechanics and speed on homologous leg coordination. Owing to the optogenetic CnF stimulation used in the novel locomotor paradigm, both left-right alternating and synchronous steps were consistently observed (**Figure 4.9 A**). Given the phase bias associated with the side of optogenetic stimulation (see 4.2.2.1), further analyses were conducted by reflecting the phase data from left-injected mice across the origin. These analyses focus solely on hindlimb coordination because of its critical role in rodent propulsion and because the phase of the fourth limb pair (the forelimbs in this case) is inherently constrained by the coordination of the other three limb pairs.

In head height trials, near-synchronous hindleg coordination dominated across experimental conditions, the mean phase being $0.06\pm0.36\ \pi$ rad at hunched postures and $0.25\pm0.11\ \pi$ rad when the hump-snout vector was more upward oriented (**Figure 4.9 B**). A minority of mice (11-17%) displayed significantly bimodal phase distributions at one or both ends of the observed snout-hump angle range, with the secondary peak at less synchronised phases (0.45-1.00π rad; **Figure 4.9 C**). Thus, hindleg coordination did not seem to change systematically with snout-hump angle.

These observations were reinforced by circular-linear regression analysis that showed no significant main effect of snout-hump angle (HPD_{SSDO} = (-0.91,0.81)) and a slightly greater phase variability across mice than seen for homolateral phase (mean resultant length: 0.94; **Figure 4.9 D**). Still, there was a significant interaction effect between snout-hump angle and speed such that lower speeds promoted hindleg desynchronisation by up to $\sim0.9\ \pi$ rad specifically when the hump-snout vector was pointed more steeply downward (HPD_{SSDO} = (-0.92,-0.44); **Figure 4.9 E**). In head-fixed conditions, this posture corresponded to a more foreleg-biased load distribution and a greater total leg load (see Figure 3.1), suggesting that the sensitivity of speed-dependent hindlimb phase modulation might be influenced by a leg load-related variable. If this was the case, the effect of speed on hindleg phase should also depend on surface slope. In particular, if the relevant biomechanical variable was the anteroposterior leg load distribution, one would expect declines to enhance hindleg phase sensitivity to speed. Conversely, if the effect was tied to changes in the total leg load, greater hindleg phase modulation would be expected on inclines. In either scenario, surface slope should not have a main effect on its

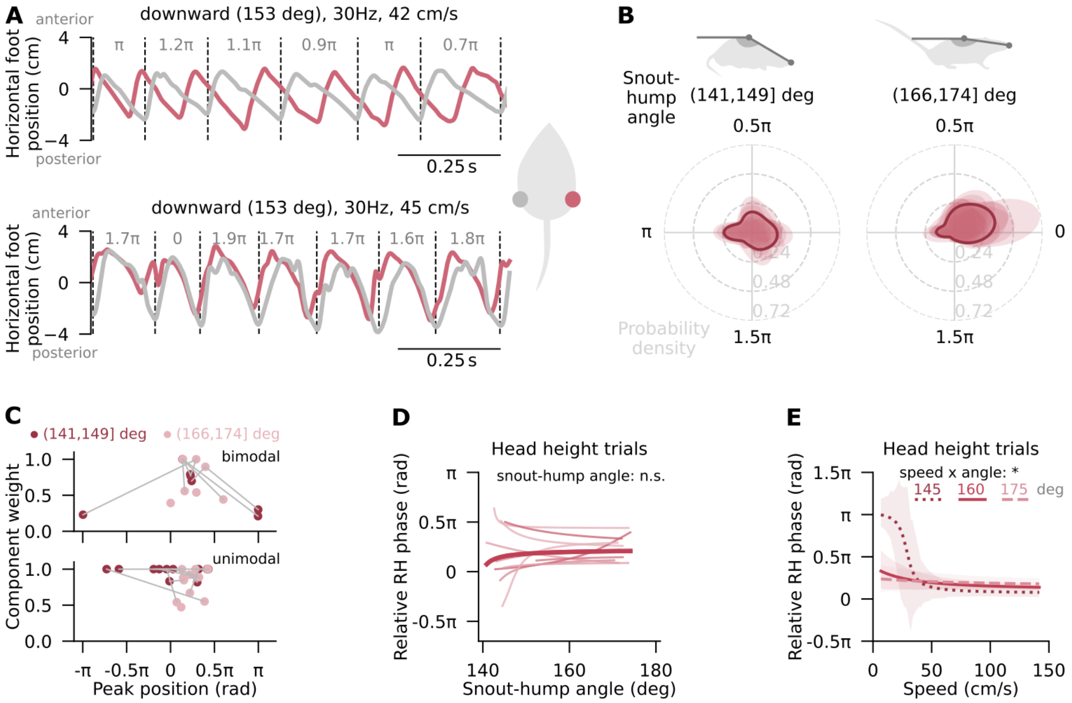

Figure 4.9: Speed and snout-hump angle have interdependent effects on hindlimb phase in head-fixed locomotion.
(A) Example time series of LH (*grey*) and RH (*red*) horizontal coordinates during alternating (*top*) and synchronised (*bottom*) movement at similar snout-hump angles and speeds. Vertical dashed lines partition the time series into strides based on LH swing onsets. Homolateral limb phases are printed above the traces. Optogenetic stimulation frequency is 30 Hz in both examples. **(B)** Kernel density smoothed distributions of RH phase relative to the LH in two snout-hump angle intervals, shown for individual mice (shaded regions; n=12 mice) and as averages across mice (solid outlines). Limb phase values of 0 and π rad reflect limb synchrony and alternation respectively. Data from mice with bimodal distributions (as defined in 2.2.3.3) or fewer than 40 strides per category were excluded. **(C)** Component weights from optimal Von Mises mixture model fits to homologous hindleg phase data in two snout-hump angle intervals, plotted against the phase corresponding to the peak of the respective component's probability distribution. Points are colour-coded by snout-hump angle interval, with each point representing an individual mouse. Points for the same mouse are connected by grey lines. Note that peak position is a circular variable presented on a linear scale for convenience. Components with weights under 0.2 are considered negligible and not shown (see 2.2.3.3). **(D)** Relative RH phase as a function of snout-hump angle with left hindlimb as the reference limb at median speed. Shown are circular-linear mixed-effects regression fits to single mouse data (random effects; light traces; n=12 mice) from head height trials and the average (fixed effect; dark trace). **(E)** Same as (D) but showing the fixed effect of speed for three snout-hump angles. Shaded regions are 95% highest posterior density intervals.
Statistical significance criterion: * HPD_{SSDO} interval does not include zero, n.s. otherwise.

own.

Data from the slope trials can be used to test these predictions given that the locomotor paradigm allowed for expression of various hindlimb coordination patterns (**Figure 4.10 A**). As expected, hindleg phase was not affected by surface slope, with a minor 0.23-0.25 π rad left-right phase lag dominating across all tested slopes (HPD_{SSDO} = (-0.98,0.96); **Figure 4.10 B-D**). At the same time, there was a significant interaction effect between slope and speed, with low speeds encouraging ~0.4 π rad greater hindleg desynchronisation on steep inclines (HPD_{SSDO} = (0.69,1.04); **Figure 4.10 E**). Therefore, hindlimb phase sensitivity to speed was likely influenced by the total leg load, not by its distribution, such that higher total loads required higher speeds for hindlimb synchronisation. This interpretation was further supported by significant interaction effects between speed and snout-hump angle, as well as between snout-hump angle and slope, consistent with these variables acting through a shared mechanism (HPD_{SSDO} = (-1.04,-0.69)).

However, the interdependent effects of speed and snout-hump angle were qualitatively distinct from those observed in the head height trials (**Figure 4.10 F**). Whereas in the head height trials, the primary effect of increasing snout-hump angle from 145 to 175 deg appeared to be a reduction in hindlimb phase sensitivity to speed modulation, a much smaller snout-hump variation (153-165 deg) in the the slope trials was associated with a complete reversal of the speed-related influence on hindlimb coordination. Specifically, when the snout-hump angle was small, hindlimb coordination became up to ~0.6 π rad more synchronised as the speed increased, but it was low speeds that promoted hindlimb synchronisation when the snout-hump angle was large. These results suggest that snout-hump angle might have a speed-dependent effect on hindlimb phase that cannot be accounted for solely by changes in the total leg load.

To explore this hypothesis, I performed two further circular-linear regression analyses with hindlimb phase as the dependent variable. First, I repeated its regression against speed, snout-hump angle, and slope on combined data from both head height and slope trials with trial type as an additional predictor. If the effect of snout-hump angle reflected only the role of the total leg load, one would expect the trial type-specific differences in the interaction between speed and snout-hump angle to be explained by the influence of surface slope without any effect attributed to trial type per se. However, this regression analysis revealed a significant effect of trial type (HPD_{SSDO} = (-0.28,-0.14)), implying that variation in the total leg load was unable to fully explain the speed-dependent effects of snout-hump angle on hindlimb phase. To identify this additional influence of snout-hump angle, one can leverage head height trial data, where, by design, leg load-related variation in snout-hump angle is also captured by changes in the absolute head fixation height (see Figures 3.1D, 3.3A, 3.5A). Therefore, in the second regression analysis, I included speed, weight-adjusted head height, and the residuals of snout-hump angle regression against head height as predictors, expecting the latter to at least partly capture any effect of snout-hump angle that was not related to the total leg load. Notably, this analysis attributed significant speed-dependent effects on hindleg phase to both head height (three-way interaction: HPD_{SSDO} = (0.39,1.08)) and snout-hump angle residuals (HPD_{SSDO} = (0.38,1.06)), but these effects differed considerably. The speed-dependent influence of snout-hump angle residuals was qualitatively similar to that attributed to speed-angle interaction in the slope trials, such that hindlimb phase increased with speed specifically at larger-than-predicted snout-hump angles, represented by positive residuals, while negative residuals tended to have the opposite effect (**Figure 4.10 G**). Conversely, head height primarily affected hindlimb phase sensitivity to speed modulation (**Figure 4.10 H**), consistent with the influence of slope in the slope trials. Altogether, these results suggest that hindlimb coordination in the passive treadmill paradigm is modulated by both total leg load and snout-hump posture, each with distinct speed-dependent effects.

Finally, I used motorised treadmill data to explore the validity of these conclusions in a freely moving locomotor setting. Without head fixation, the influences of speed, snout-hump angle, and slope on hindlimb phase can be expected to differ from those seen on the passive treadmill in two key ways. First, surface slope should have no effect on hindlimb phase or its sensitivity to speed modulation, as the non-restrained locomotor conditions eliminate the possibility of changes in the total leg load. Second, the effects of snout-hump angle are likely to be more diffuse or shifted because head rotations in the freely moving setting introduce additional variability in the relationship between snout-hump angle and overall posture. Nevertheless, there should be a speed-dependent influence of snout-hump angle on hindlimb phase that at least qualitatively resembles the effect seen during head-fixed locomotion.

Indeed, circular-linear regression of hindlimb phase against speed, snout-hump angle, and slope revealed a significant speed-dependent effect of snout-hump angle in both level (HPD_{SSDO} = (-2.70,-2.33)) and slope trials (HPD_{SSDO} = (-2.44,-1.89)), with no significant difference between the two trial types (HPD_{SSDO} = (-0.05,0.11)). As during head-fixed locomotion, small snout-hump angles promoted a 0.4% reduction in hindleg phase lag with every 10 cm/s increase in speed, and this relationship was reversed at larger snout-hump angles (**Figure 4.11 A, B**). Importantly, owing to the dominance of strict left-right alternation on the motorised treadmill (mean phase 1 ± 0.04 π rad; see also Figure 3.7), it becomes evident that the target of speed- and posture-interdependent modulation was really the hindlimb phase lag, rather than the balance between hindlimb synchronisation and alternation. On the passive treadmill, where hindlimb coordination was just slightly out of phase on aver-

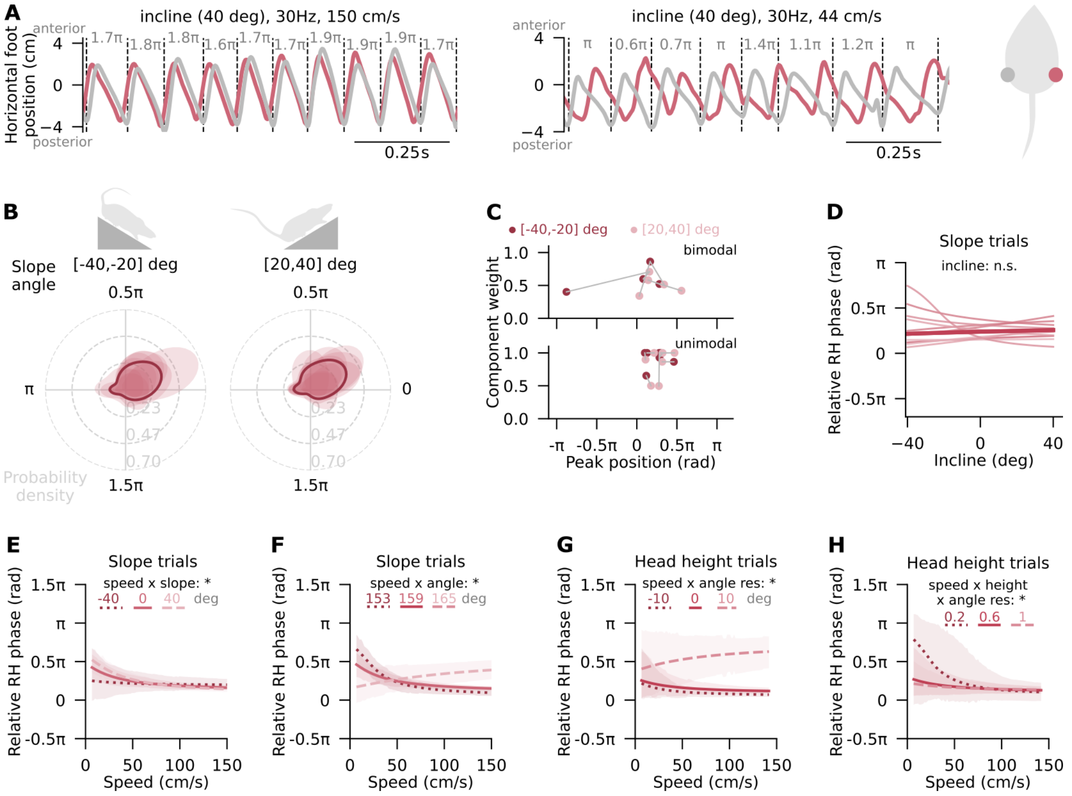

Figure 4.10: Hindlimb phase in head-fixed locomotion is modulated by total leg load and posture in a speed-dependent manner.
(A) Example time series of LH (*grey*) and RH (*red*) horizontal coordinates during synchronised (*top*) and alternating (*bottom*) movement on steep inclines. Vertical dashed lines partition strides based on LH swing onsets. Relative limb phases are printed above the traces. **(B)** Kernel density smoothed distributions of relative hindlimb phase in two surface slope intervals, shown for individual mice (shaded regions; n=12 mice) and as averages across mice (solid outlines). Limb phase values of 0 and π rad reflect limb synchrony and alternation respectively. Data from mice with bimodal distributions (as defined in 2.2.3.3) or fewer than 40 strides per category were excluded. **(C)** Component weights from optimal Von Mises mixture model fits to hindlimb phase data in two surface slope intervals, plotted against the phase corresponding to the peak of the respective component's probability distribution. Points are colour-coded by slope interval, with connections for the same mouse in grey. Peak position is a circular variable presented on a linear scale for convenience. Components with weights under 0.2 are not displayed (see 2.2.3.3). **(D)** RH phase as a function of surface slope with LH as the reference limb at median speed. Shown are circular-linear mixed-effects regression fits to single mouse data from head height trials (light traces; n=12 mice) and the average (dark trace). **(E-H)** Hindlimb phase as a function of speed at three representative slopes (E), snout-hump angles (F), levels of residuals from snout-hump angle regression against the weight-adjusted head height (G), and weight-adjusted head heights (H). Shown are the fixed effects from circular-linear mixed-effects regression. Shaded regions are 95% highest posterior density intervals. In (F) and (H), 159 deg and 0.6 approximate conditions with natural total load respectively. In (G), positive residuals reflect snout-hump angles that exceed the angles predicted by the weight-adjusted head height.
Statistical significance criterion: * HPD_{SSDO} interval does not include zero, n.s. otherwise.

age, both hypotheses had been consistent with the data. Lastly, as expected, there was no significant effect of surface slope (HPD_{SSDO} = (-2.40,2.33); **Figure 4.11 C**), supporting the earlier interpretation that the speed-dependent effect of slope on the passive treadmill was related to the total leg load. Overall, these results suggest that total leg load and an unspecified posture-related variable regulate the speed-dependence of hindlimb coordination (**Figure 4.11 D**).

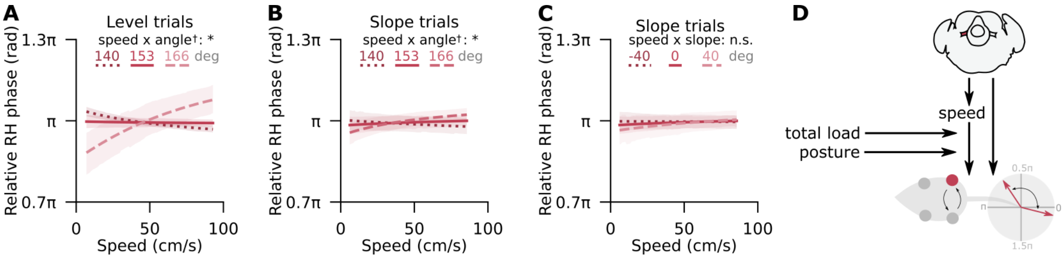

Figure 4.11: Hindlimb coordination in non-restrained locomotion is influenced by snout-hump angle in a speed-dependent manner.
(A-C) Relative RH phase as a function of speed at three representative snout-hump angles (A-B) and slopes (C) during level (A) and surface slope (B-C) trials on the motorised treadmill, with LH as the reference leg. Shown are the fixed effects from circular-linear mixed-effects regression analysis. Shaded regions represent 95% highest posterior density intervals. **(D)** Schematic representation of the working hypothesis on the roles of CnF stimulation, total load, and an unspecified posture-related variable in hindlimb coordination.
Statistical significance criterion: * HPD_{SSDO} interval does not include zero, n.s. otherwise.

4.3 Discussion

In this chapter, I have shown that distribution of leg load along the anteroposterior body axis primarily affects homolateral coordination, supporting my initial hypothesis. Specifically, I have uncovered a strong correlation between increased relative loading of the hindlimbs and a speed-independent shift in homolateral phase preference from strict alternation to up to a quarter-of-phase more synchronised coordination. In contrast, I have found that homologous coordination shows a notable association with the side of optogenetic stimulation and that hindlimb phase in particular can be modulated at low speeds by the interplay of total leg load and an upper body posture-related variable.

The observed association between leg load distribution and homolateral coordination is consistent with previous research in several ways. For instance, the baseline weight distribution of mice, which corresponds to a CoS of approximately -0.1 cm (Morina, 2023), is compatible with strict homolateral alternation, characteristic of a trotting gait. The same applies to most studied quadrupeds as long as their baseline weight distribution is not as extremely fore- or hind-biased as that of giraffes or ring-tailed lemurs, which bypass two-beat gaits by switching directly from walk to canter (Demes et al., 1994; O'Neill & Schmitt, 2012; Pennycuick, 1975). In addition, the size of the observed homolateral phase shift in response to a given change in surface slope is comparable with a previous study in opossums that saw a $\sim 0.16\ \pi$ phase difference between 30 degree inclines and declines (Lammers et al., 2006). In general, these findings are consistent with prior knowledge and reasonable expectations. While the diagonal limb support pattern of trot is associated with high mechanical stability, quadrupeds rely on limb repositioning and anteroposterior load redistribution to maintain this gait (Lee et al., 1999). Highly uneven load distributions, whether at baseline like in giraffes or due to environmental perturbations as in the present work, likely impose a severe constraint on the range of adjustment available to the animal, making transitions to three- or four-beat gaits mechanically inevitable. Still, it is worth noting that this shift in interlimb coordination occurred regardless of the phase adopted by homologous limbs and even during head-fixed locomotion, when the risk of falling along the pitch axis was eliminated. Therefore, the biomechanical advantages conferred by the observed changes in homolateral phase likely extend beyond balance, with the temporally distributed footfalls potentially contributing to a lower mechanical cost of transport (Lee, 2011; Ruina et al., 2005).

However, the direction of the observed leg load-related change in homolateral coordination, namely a reduction in phase lag upon a posteriorward load redistribution, contradicts a number of empirical studies in both opossums and dogs (Bertram et al., 2000; Lammers et al., 2006; Lee, 2011; Lee et al., 2004). In these studies, reductions in homolateral phase lag have been associated with conditions reflecting increasingly fore-biased load distributions, be it declines or additional load at the pectoral girdle. Differences in these animals' baseline load distributions could help explain this discrepancy as well. The majority of quadrupeds, including dogs and opossums, have a forelimb-heavy baseline distribution of load, whereas mice place a greater fraction of body weight on their hindlimbs (Demes et al., 1994; Morina, 2023). In fact, the posteriormost load distributions examined previously in dogs (Bertram et al., 2000; Lee et al., 2004) closely resemble the most front-heavy conditions experienced by mice in the present work, where ∼63% of total load was on the forelimbs. Intriguingly, in both species, these conditions have been linked to a slight increase in homolateral phase lag beyond strict alternation (1.02-1.10 π rad). Similarly, it is in more forelimb-loaded conditions of front-heavy animals and more hindlimb-loaded conditions of hind-heavy animals that the homolateral phase lag is reduced. This raises the possibility of homolateral coordination being determined not by the absolute leg load distribution, but by the direction of its deviation from the animal's baseline (**Figure 4.12**).

What might be the advantage for a dog or a mouse to narrow, rather than expand, the homolateral phase gap in fore- or hind-biased conditions respectively? On the one hand, more synchronised homolateral coordination has often been associated with a reduced risk of leg collisions in longer-legged animals or with increased stride lengths (Blaszczyk & Loeb, 1993; Hildebrand, 1980), but it is not clear how changes in stride length might relate to variations in leg load. On the other hand, many quadrupeds, including load-bearing dogs

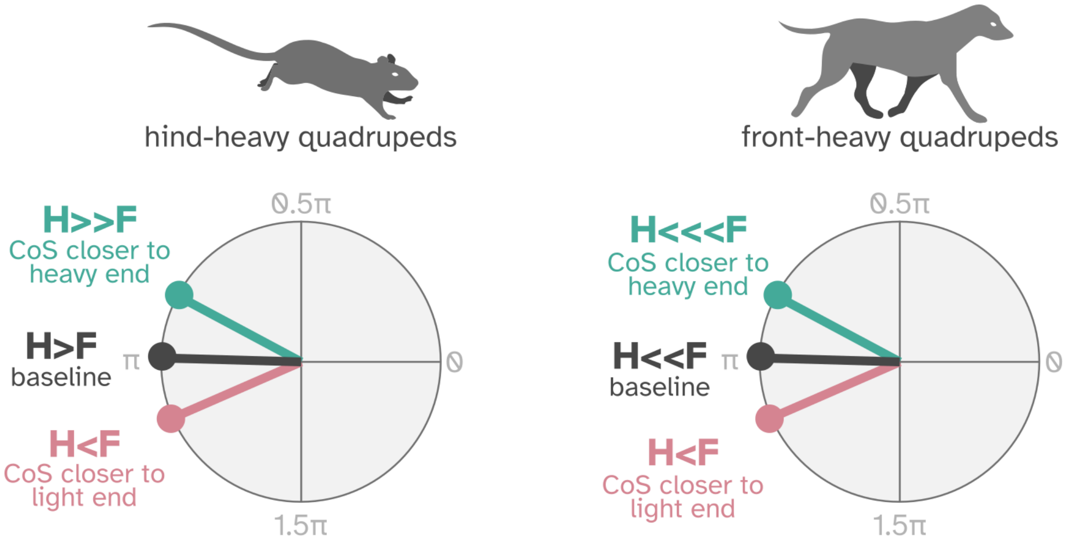

Figure 4.12: Hypothesised relationship between anteroposterior leg load distribution and homolateral phase.
Quadrupeds' homolateral coordination might be determined by deviations in leg load distribution from baseline, not by the absolute load. Hindlimb phase lag decreases as the centre of support (CoS) shifts towards the end that is more loaded at rest (hind in mice, front in dogs), and extends beyond π when CoS shifts towards the lighter end (front in mice, hind in dogs).

(Lee et al., 2004), have been found to adapt to increased load by prolonging the duty factor of the loaded legs (Biewener, 1983), thereby distributing the increased load over a longer period and protecting against strain. However, the mechanism potentially linking this kinematic adjustment to gait is not well understood (Bertram et al., 2000), and changes in neither stride length nor duty factors could explain the homolateral phase shift observed in the present work. Without clear kinematic correlates, it remains plausible that animals adjust homolateral phase as a direct protective strategy to redistribute load between the more heavily loaded limb (hind or fore) and its homolateral counterpart. Testing this hypothesis would, at minimum, require direct load recordings during locomotion, and would benefit from more detailed measurement of joint kinematics.

The other avenue of interlimb coordination explored in this thesis concerns the homologous limbs, specifically the hindlimbs. Recent work in mice has demonstrated mediolateral asymmetry in the temporal pattern of spinal cord activation upon unilateral stimulation of glutamatergic neurons in medullary reticular formation (Hsu et al., 2023). These neurons have been shown to receive excitatory input from both ipsi- and contralateral CnF, with the former a slightly more prevalent source (Capelli et al., 2017). Even though the frequency of descending CnF stimulation does not directly translate into stepping frequency, the spatial and temporal asymmetries in the wiring and dynamics of descending locomotor circuits likely contribute to the stimulation-related hindlimb phase bias observed in the present work.

Earlier research in horses has also identified a link between the trot-to-gallop transition speed and leg load-related variables, though it remains debated whether it is the absolute leg load or its anteroposterior distribution that drives this speed-dependent change in limb phase. At first glance, the current work appears to support the former hypothesis, showing that the speed of hindlimb phase transitions can be influenced by the total load, but bears no correlation with anteroposterior load distribution. However, whereas Farley and Taylor (1991) have observed a lowering of the trot-gallop transition speed with increasing load, the present experiments in mice associate greater load with hindlimb desynchronisation. This discrepancy might be attributable to differences in experimental design, including the use of unilateral optogenetic stimulation to trigger locomotion and the distinct range of explored loads. While the 23% increase in total load borne by horses in Farley and Taylor (1991) is comparable to the maximum load experienced by mice here, peak locomotory stress has been estimated to scale with animal mass with a slight positive allometry (Biewener, 1983). Thus, it seems plausible for hindlimb coordination of mice to remain compatible with trot-like alternation across the range of observed loads if not for the descending drive towards near-synchronous, gallop-like phasing. In fact, the increased propensity for hindlimb alternation at higher total loads might represent a load-dependent enhancement in the capacity of somatosensory feedback to counteract the descending influence. In a similar vein, and consistent with the results presented here, a series of theoretical studies have predicted sensory feedback to have more impact on interlimb coordination at low speeds, when top-down control is less dominant (Full & Koditschek, 1999; Ijspeert & Daley, 2023; Owaki et al., 2013; Rybak et al., 2024). Future development of a non-stimulated head-fixed locomotor paradigm or the use of more varied stimulation intensities could offer further insight into how homologous coordination is shaped by the interacting effects of speed and total load, as well as the interplay between descending and feedback input.

Finally, it is worth noting that varying load distribution along the anteroposterior body axis might have predisposed the gait control system to homolateral modulation, similar to how left-right differences in optogenetic stimulation biased homologous phase. Consequently, while the current results suggest distinct capacities of feedback and descending signals to influence homolateral and homologous coordination, the limb pair specificity of these effects might be an artifact of experimental design. Moreover, despite efforts to approach the problem from multiple complementary angles, the relationships between leg load-related variables and interlimb coordination presented in this chapter remain correlational. One cannot dissociate whether the key sensory variable for homolateral coordination is the anteroposterior CoS position or leg load distribution itself, nor is it possible to rule out potential contributions from other sensory sources, such as neck proprioceptors or the vestibular system (Akay & Murray, 2021; Shafiee et al., 2024). The fixed head orientation relative to the gravity vector likely minimised vestibular influence in the head height trials, but it could offer an alternative explanation for the slightly smaller effect attributed to snout-hump angle in the slope trials. Such exteroceptive signals might also account for the comparatively modest change in homolateral coordination seen during non-restrained locomotion. In fact, head pitch manipulation experiments have previously likened the muscle activation patterns of nose-up movement with those of decline locomotion (Gottschall & Nichols, 2007). These findings contrast with the incline-like shift in homolateral phase seen at more upward oriented snout-hump angles in head-fixed, no-pitch-change conditions, suggesting that pitch modulation might naturally oppose the effects of load distribution. I will investigate the neural origins of the behavioral results presented here by conducting experiments with proprioceptive afferent-deficient mice in Chapter 5.

Chapter 5

The role of proprioception in leg load-dependent interlimb coordination

5.1 Introduction

The behavioural data presented in Chapter 4 point to an intriguing association between homolateral coordination and a load-related biomechanical variable, specifically the leg load distribution or CoS position along the anteroposterior body axis. These findings raise questions about the underlying neural control mechanisms and offer a behaviour-driven framework for exploring them. Assuming load to be the relevant variable, the most prominent candidate sensors for feedback-dependent interlimb phase modulation are the tension-sensitive GTOs whose signals are relayed to the central nervous system via type Ib afferent fibres (for review, see Duysens and Pearson (1980) and Proske and Gandevia (2012), also 1.2.3). During sloped locomotion, the firing of these afferents has been found to scale with the loading of the respective leg, acting to elevate muscle activity through positive feedback (Conway et al., 1987; Donelan et al., 2009; Gregor et al., 2006; Prochazka et al., 1997). Besides GTOs, correlates of load have been identified in the signalling of cutaneous mechanoreceptors at the sole of the foot and even the primarily stretch-sensitive type Ia afferents that relay muscle spindle input (Blum et al., 2017; Duysens & Stein, 1978; Duysens et al., 2000). Although it remains to be determined whether all of these findings generalise to actively contracting muscle, this likely redundancy in the processing of load-related information has obscured attribution of specific functions to individual receptors.

Furthermore, during natural locomotion, changes in leg load are often accompanied by variations in other biomechanical and postural variables that might contribute to gait control as well. For example, downhill locomotion has been shown to involve not only an anteriorward redistribution of load, but also a more anterior foot placement and greater joint flexion compared to level or inclined surfaces (Carlson-Kuhta et al., 1998; Gregor et al., 2006; Lammers et al., 2006; Smith et al., 1998). In fact, as shown in Chapter 4, a more anterior range of foot motion coincides with greater forelimb loading even in head height trials (see Figure 4.6), potentially making the relative foot position a relevant factor in feedback-dependent homolateral coordination. Other plausible contributors include neck proprioceptive and vestibular signals that are thought to represent head orientation relative to the body or the gravity vector respectively (Akay & Murray, 2021). These two inputs have been shown to elicit opposing responses at least in vestibular nuclei, and have even been proposed to act in opposition to explain the transient nature of muscle activation in response to head pitch modulation (Gottschall & Nichols, 2007; Kasper et al., 1988). It has also been suggested that vestibular input might be particularly important at low speeds, whereas the impact of whole-body proprioceptive information might grow with speed (Akay & Murray, 2021). In the present locomotor paradigm, snout-hump angle might serve as a proxy for neck proprioceptor activation across experimental conditions. Conversely, substantial vestibular modulation is likely limited to slope trials, as head height trials involve no change in head orientation relative to gravity.

The ability to manipulate the body biomechanics of locomoting mice offers an opportunity for targeted neural interventions that are not feasible in most subjects of locomotor studies. A common approach to probing the function of muscle spindles is through transgenic knockout of early growth response protein 3 (Egr3), a zinc-finger transcription factor expressed in intrafusal muscle fibres (Tourtellotte & Milbrandt, 1998). Due to degeneration of muscle spindles and type Ia afferents shortly after birth, Egr3-deficient (*Egr3-/-*) mice display mild gait ataxia with altered timing and amplitude of intra- and interlimb coordination (Santuz et al., 2019; Takeoka et al., 2014; Tourtellotte et al., 2001). These defects become more pronounced during swimming, when activity of the intact GTOs is diminished due to buoyant support and unable to provide any compensation (Akay et al., 2014). While a transgenic method for selective GTO ablation is yet to be developed, insight into GTO-specific function can be gleaned by leveraging the intersectional expression of parvalbumin (PV) and advillin (Avil) in proprioceptive afferents (PA; Takeoka and Arber, 2019). Diphtheria toxin injection in *PV-Cre;Avil-iDTR* mice results in degeneration of both muscle spindle and GTO afferents, producing a pronounced locomotor ataxia with uncoordinated limb movements and a severe reduction in the maximum attainable speed (Santuz et al., 2022; Takeoka & Arber, 2019). While these detrimental effects can be attenuated in models with spatially restricted PA ablation, it is interesting that systematically greater homolateral and homologous synchronisation has only been observed in mice with PA loss limited to forelimbs or hindlimbs (Takeoka & Arber, 2019).

In this chapter, I study *Egr3-/-* and *PV-Cre;Avil-iDTR* mice in the novel locomotor paradigm to probe the role of muscle spindle and GTO inputs in mediating the biomechanical effects on interlimb coordination reported in Chapter 4. Given the redundancy of direct and indirect load detection mechanisms within the nervous system, it seems reasonable to expect neither of these circuit manipulations to completely eliminate the correlation between anteroposterior load distribution and homolateral phase. However, based on the current knowledge, the possibility of this relationship being mediated by a particular afferent pathway rather than generalised load information cannot be ruled out and merits investigation. In addition, even if the neural perturbations presented here might be both too crude and too narrowly focused to yield definitive conclusions, they can still provide valuable insights to guide future studies.

5.2 Results

5.2.1 Ataxia restricts mouse compatibility with the novel locomotor paradigm

To test whether the observed correlations between interlimb phases and leg load-related variables represent causal relationships, I sought to perform analogous experiments with mice that have reduced proprioception, specifically the muscle spindle afferent (MSA) deficient *Egr3-/-* mice (Tourtellotte & Milbrandt, 1998) and the *PV-Cre;Avil-iDTR* mice that irreversibly lose both MS and GTO afferents after DTX injection (Takeoka & Arber, 2019). To gain a comprehensive understanding of these animals' motor deficits, I qualitatively scored their ataxic phenotype from weaning until the end of data collection period. MSA-deficient mice displayed a stable mild ataxia with limited motion and brief splaying of the hindlimbs and occasional wobbling of gait ($p<0.001$, *one-sample t-tests*; **Figure 5.1 A-B, E**). Forelimb movements and the posture of head and trunk remained normal on average ($p>0.05$; **Figure 5.1 C-D, F-G**). Still, MSA-deficient mice had 3-4 g lower body mass than their non-ataxic (*Egr3+/-* or *Egr3+/+*) littermates (adult p between 0.002 and 9×10^{-42}, *independent t-tests*; **Figure 5.1 H-I**). In the context of passive treadmill experiments, it suggests that MSA-deficient mice will require a lesser absolute redistribution of body weight to shift their CoS a given distance.

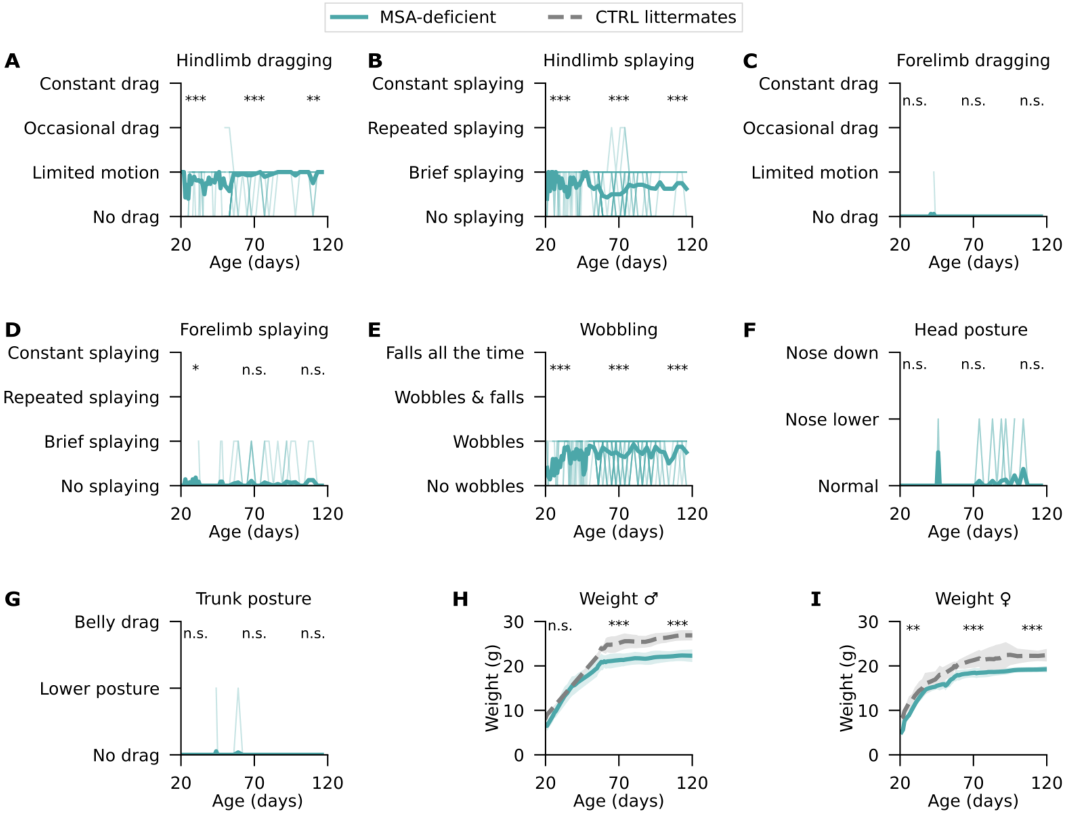

Figure 5.1: MSA-deficient mice display stable, mild ataxia.
(A-G) Qualitative assessment of the extent of hindlimb dragging (A), hindlimb splaying (B), forelimb dragging (C), forelimb splaying (D), wobbling (E), head posture (F), and trunk posture (G) in MSA-deficient (Egr3-/-) mice between weaning and the end of experiments. **(H-I)** Weight of male (H) and female (I) MSA-deficient mice (*teal, solid*) and littermate controls (*grey, dashed*).
Statistical significance is assessed for ±2 day periods around 30, 70, and 110 days of age, using thresholds: * $p < 0.05$, ** $p < 0.01$, *** $p < 0.001$.

The ataxia developed by DTX-injected *PV-Cre;Avil-iDTR* mice was considerably more pronounced and displayed partial dose-dependence. Within 3-5 days of DTX administration, animals injected with the highest tested DTX dose (100 μg/kg) showed a continuously wobbly gait, hindlimb dragging and splaying, loss of postural integrity, and occasional deficits in forelimb movement (**Figure 5.2 A-G**). The ataxic phenotype in these mice was significantly more intense and developed slightly sooner after DTX injection than in animals receiving a 2-50 fold lower DTX dose (p between 1×10^{-5} and 3×10^{-73}). This contrast was also evident in body weight such that mice experienced up to a 15% greater drop in weight after receiving the maximum tested dose compared to the lower doses (**Figure 5.2 H-I**). Conversely, there was no systematic difference between most aspects of ataxia induced by the lower DTX doses (p: 0.06-0.48), with animals showing occasional hindlimb dragging, repeated hindlimb splaying, and a lower trunk posture. The only dose-dependent effect in the 2-50 μg/kg DTX dose range was a 5-6 day delay in the development of lowered head posture when the amount of injected toxin was lower (p=0.001; **Figure 5.1 F**). These results suggest that, within the tested dose range, DTX might regulate the extent of PA ablation in a biphasic manner, while still producing stronger ataxic effects than MSA ablation alone.

Testing the two proprioceptively impaired mouse lines in an open field arena revealed a significantly reduced locomotor capacity even in the presence of optogenetic CnF stimulation (**Figure 5.3 A**). Despite no change in response latency, the peak speed reached by PA- and MSA-deficient mice was just 53±13 and 69±7 cm/s respectively ($p=4\times10^{-4}$), in contrast to the >80 cm/s achieved by their non-ataxic littermates (p<0.003; **Figure 5.3 B**). The difference in speed between ataxic and control animals increased to 20-45 cm/s late in the stimulus, indicating a reduced ability of MSA- and especially PA-deficient mice to sustain high locomotor speed despite ongoing descending stimulation. This was also reflected in a lower distance coverage ($p<1 \times 10^{-5}$; **Figure 5.3 C**) and was primarily due to an increased number of brief (0.6±0.2 s) mid-stimulus interruptions to the ataxic animals' forward motion (PA: $p=4\times10^{-4}$, MSA: p=0.01; **Figure 5.3 D**). Representing episodes of more variable, and likely inefficient, limb movement than seen during the rare stops of control an-

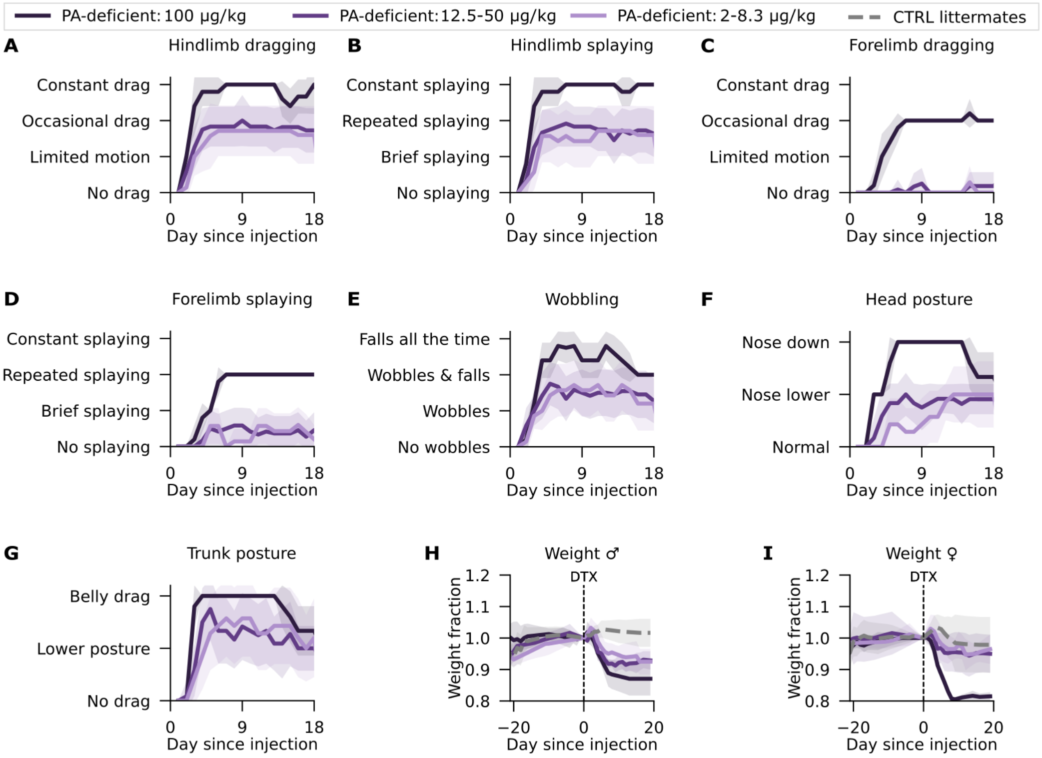

Figure 5.2: DTX-inducible PA-deficient mice display moderate ataxia with limited DTX dose dependence.
(A-G) Qualitative assessment of the extent of hindlimb dragging (A), hindlimb splaying (B), forelimb dragging (C), forelimb splaying (D), wobbling (E), head posture (F), and trunk posture (G) in DTX-inducible PA-deficient (PV-Cre;Avil-iDTR) mice following DTX injection at varying doses. **(H-I)** Weight of male (H) and female (I) DTX-inducible PA-deficient mice (*purple, solid*) and littermate controls (*grey, dashed*).
Statistical significance is assessed for the period 8-12 days post-injection, using thresholds: * $p < 0.05$, ** $p < 0.01$, *** $p < 0.001$.

imals (p=0.04), these interruptions to locomotion reduced the fraction of time PA- and MSA-deficient mice spent locomoting by 24% and 9% respectively. Nevertheless, binary classifiers trained on the relative limb phases during successful forward locomotion performed only marginally better than chance (PA: 62±1% accuracy, MSA: 60±4%), suggesting that PA- and MSA-deficient mice maintained nearly normal limb phasing (**Figure 5.3 E**).

The locomotor deficits of proprioceptively impaired mice were exacerbated in the novel locomotor paradigm. While the peak optogenetically evoked speed of the control animals increased to 104-134 cm/s, likely reflecting the lack of physical barriers in their path, the maximum speed of PA- and MSA-deficient mice dropped to just 33±13 and 47±11 cm/s respectively (**Figure 5.3 F**). Importantly, although this peak speed was comparable for the two ataxic cohorts (p=0.68, *t-test*), the distance covered by PA-deficient mice was significantly lower ($p=8 \times 10^{-8}$; **Figure 5.3 G**). This was largely due to a 24% decrease in the fraction of time spent locomoting ($p=3 \times 10^{-6}$) and a three-fold reduction in the number of strides executed per 5-second stimulus (3±1 strides total; $p=3 \times 10^{-8}$; **Figure 5.3 H**). Thus, the moderate ataxia of PA-deficient mice seemed to pose a significant barrier to collecting enough stride data on the passive treadmill for meaningful analysis of gait. Conversely, the mildly ataxic phenotype of MSA-deficient mice enabled a similar distance coverage (p=0.05) and time spent locomoting (p=0.85) as seen in littermate controls (**Figures 5.3 G**). Despite a slightly lower number of optogenetically evoked strides (9±1 vs. 12±2 strides; p=0.004; **Figures 5.3 H**), this was sufficient to proceed with analysis of interlimb coordination in the novel locomotor paradigm.

5.2.2 Posture-dependence of weight distribution is altered in MSA-deficient mice

To assess the relationship between postural variables and body weight distribution in head-fixed MSA-deficient mice, the vertical GRFs borne by these animals' feet were measured on the force sensor setup over a 9-18 mm range of head heights. This range was smaller than that used for non-ataxic mice due to a limited ability of MSA-deficient animals to maintain muscle tone and stand still, especially at higher head positions (**Figure 5.4 A**). Reflecting this comparative instability, the CoS position of MSA-deficient mice shifted during apparent standstills significantly more than for control animals both within and across 5-second periods at a given head height (**Figure 5.4 B, C**, see Figure 3.2 for control data). Moreover, although an increase in head height

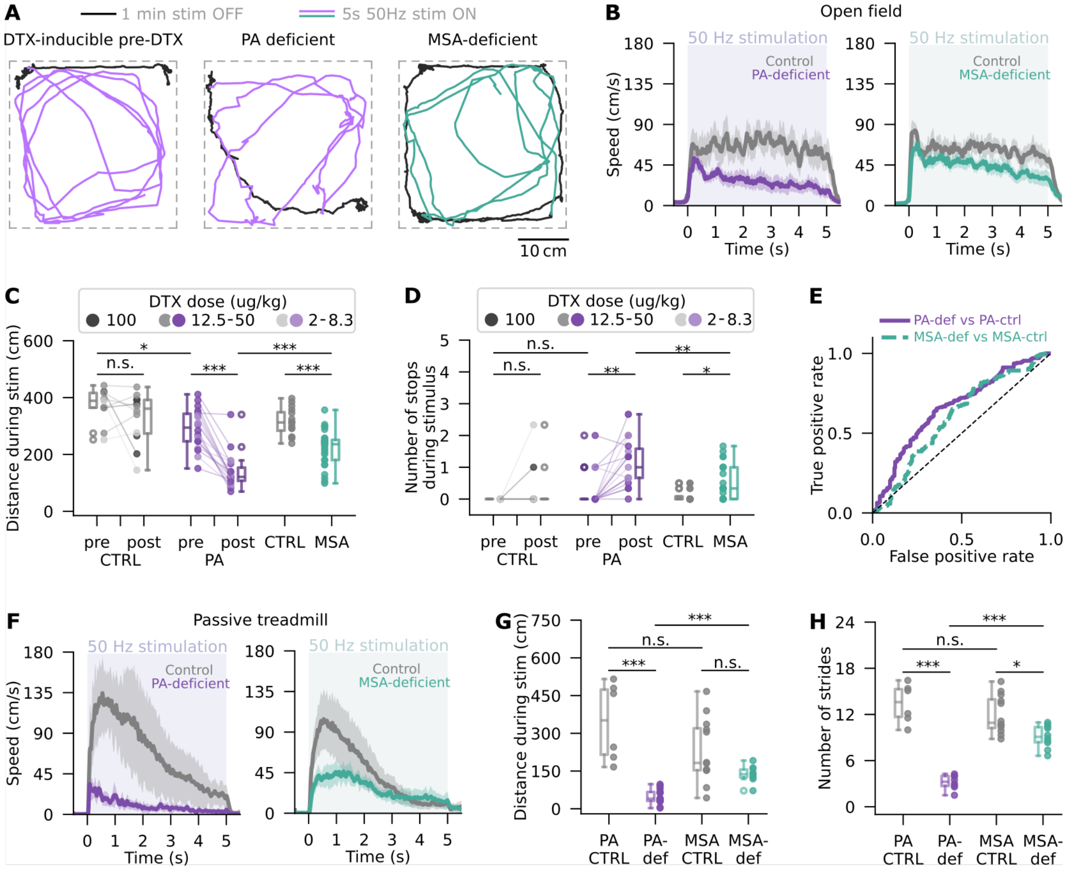

Figure 5.3: PA-deficient mice are too ataxic to test on the new paradigm. **(A)** Trajectories of a representative DTX-inducible PA-deficient mouse (*left, middle*) and MSA-deficient mouse (*right*) in the open field before (*black*) and during (*purple, teal*) 50 Hz optogenetic stimulation. The PA-deficient mouse is shown one day before (*left*) and seven days after (*right*) DTX injection. **(B)** Locomotor speed of PA-deficient (n=19; *purple, left*) and MSA-deficient (n=28; *teal, right*) mice and their littermate controls (PA-CTRL: n=12, MSA-CTRL: n=16; *grey*) during 50 Hz optogenetic CnF stimulation in the open field. Average trace across mice is shown along with a 95% confidence interval (shaded). **(C-D)** Distance covered (C) and the number of stopping episodes (D) during 50Hz optogenetic stimulus by PA-deficient mice and their littermates pre and post DTX injection, and by MSA-deficient mice and their littermates. Stopping episodes were defined as movement slower than <5 cm/s for at least 100 ms. **(E)** Receiver operating characteristic curve of a binary classifier trained to predict animal genotype based on the first two principal components of the relative phases between homologous, homolateral, and diagonal limbs. Separate classifiers were trained to distinguish between PA-deficient mice and their DTX-injected littermates (*purple, solid*) and between MSA-deficient mice and their littermates (*teal, dashed*). **(F)** Same as (B), but on the passive treadmill (PA-CTRL: n=6 mice, PA: n=17, MSA-CTRL: n=12, MSA: n=10). **(G-H)** Distance covered (G) and the number of strides (H) by PA- and MSA-deficient mice and their littermates during 50Hz optogenetic stimulus.
All panels include only those DTX-inducible PA-deficient (PV-Cre;Avil-iDTX) mice that received up to half of the maximum tested DTX dose (2-50 μg/kg). Where not stated otherwise, data from these animals and their littermates pertains only to the period following DTX injection.
Statistical significance thresholds: * $p < 0.05$, ** $p < 0.01$, *** $p < 0.001$.

consistently reduced forelimb loading ($p=2 \times 10^{-84}$), this change in forelimb load was 92% less pronounced than in non-ataxic animals ($p=1 \times 10^{-7}$), with the fraction of forelimb load decreasing by just 0.36±0.03 over the testable head height range (**Figure 5.4 D**). As in control mice, this shift in forelimb load was almost entirely due to a transfer of weight onto the head fixation apparatus ($p=7 \times 10^{-91}$; **Figure 5.4 E**). At the same time, the total leg load of MSA-deficient mice was consistently lower than that of control animals ($p=5 \times 10^{-6}$), only rarely exceeding 100% in line with a reduced muscle tone and limited force generation capacity.

The relationship between head height and anteroposterior CoS position was best described by a linear function with a slope similar to that of non-ataxic mice ($p=0.5$; **Figure 5.4 F**). However, the intercepts were different such that MSA-deficient mice showed a 0.2±0.2 cm more posterior weight distribution for any given head height ($p=9 \times 10^{-4}$). Some of this discrepancy might be explained by these mice having an approximately 0.5 cm lower body height than control animals ($p=1 \times 10^{-15}$; **Figure 5.4 G**). Consequently, the obtuse angles formed by the hump-snout vector of MSA-deficient mice and the horizontal axis were 15-20 degrees wider than that of non-ataxic mice, reflecting more upward body orientations across the studied head heights ($p=3 \times 10^{-15}$; **Figure 5.4 H**). However, even at comparable snout-hump angles, the body weight distributions of MSA-deficient and control mice differed, being more fore-biased in the former cohort ($p=1 \times 10^{-6}$; **Figure 5.4 I**). Therefore, while these results confirm a linear relationship between anterposterior weight distribution and snout-hump angle, there are fundamental differences in how MSA-deficient mice distribute their body weight between limbs in a given posture.

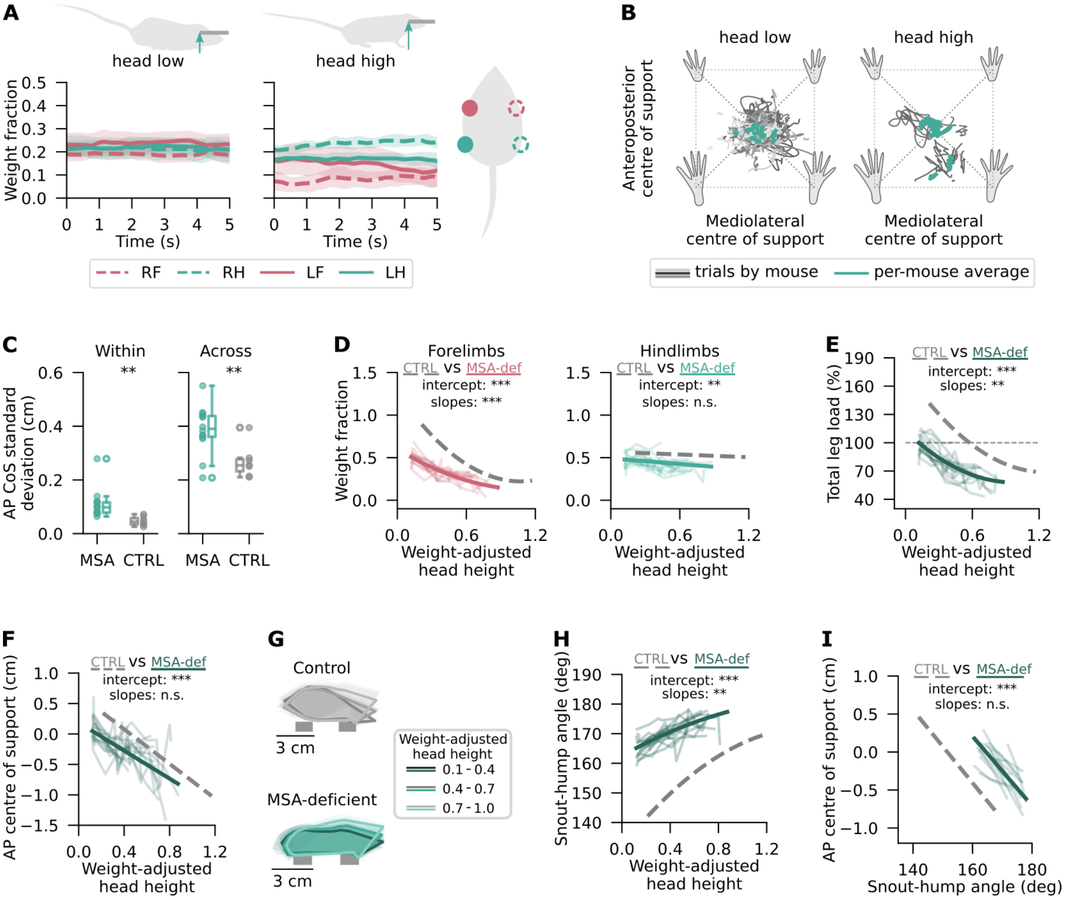

Figure 5.4: Posture-dependence of weight distribution is altered in MSA-deficient mice.

(A) Average body weight distribution on each limb by a representative MSA-deficient mouse during five-second standstills at two head heights 15 mm apart. Shaded areas show 95% confidence intervals across trials. **(B)** CoS along the anteroposterior axis of MSA-deficient mice at a low (*left*) and high (*right*) head positions. Grey traces show individual trials with shade indicative of mouse identity. Within-mouse means are shown in teal. **(C)** Standard deviation of anteroposterior CoS within (*left*) and across (*right*) trials at a given head height, shown as boxplots for MSA-deficient and control mice. Points represent individual mice. **(D)** Forelimb (*left*) and hindlimb (*right*) weight fractions as a function of weight-adjusted head height. Shown are averages of individual mice (n=14; thin lines) fitted with exponential decay (forelimb) and linear (hindlimb) models. Data from non-ataxic mice (*dashed; grey*) is reused from Chapter 3. **(E-F)** Same as (D), but showing the total detected load as a percentage of body weight (E) and anteroposterior CoS (F). **(G)** Silhouettes of MSA-deficient and control mice in three head height intervals. Lightly shaded shapes correspond to individual mice; solid outlines show the averages. **(H)** Same as (D), but showing the snout-hump angle. **(I)** Same as (F), but as a function of snout-hump angle.

Statistical significance refers to a comparison between MSA-deficient and control mice, using the following thresholds: * $p < 0.05$, ** $p < 0.01$, *** $p < 0.001$. For non-linear relationships, significance of only the first-order component is presented.

5.2.3 Muscle spindle afferents are important, but not solely responsible for homolateral phase modulation by leg load distribution

5.2.3.1 Muscle spindle feedback contributes to animal adaptability to changes in load distribution

To investigate the role of MSA signalling in homolateral phase dependence on anteroposterior leg load distribution, MSA-deficient mice were studied using the novel locomotor paradigm, specifically head height trials. Combined with existing insights on the sensory modality of muscle spindles, these experiments also aimed to clarify the potential causality between homolateral coordination and leg load distribution. For example, if MSAs were part of the sole pathway mediating the observed association between body biomechanics and homolateral phase, MSA-deficient mice would be expected coordinate their homolateral legs independently of leg load distribution, as quantified by the anteroposterior CoS position. Since MSAs are not considered the primary detectors of leg load, such a scenario would argue against a causal link between the variables of interest. Conversely, if MSA signalling played no role in this relationship, homolateral coordination in MSA-deficient mice should closely resemble that of their non-ataxic littermates. Alternatively, if MSAs were one of several mediators of the observed biomechanical influence, homolateral phase should still be modulated by leg load distribution, albeit to a lesser degree. Either of these latter outcomes would be consistent with a causal leg load-dependence of homolateral phase, although they would differ in the implied MSA contributions to load sensing in active muscles.

Data from MSA-deficient mice favoured the third outlined scenario, revealing a persistent, but significantly reduced, correlation between leg load distribution and homolateral phase in the absence of MSA signalling. In particular,

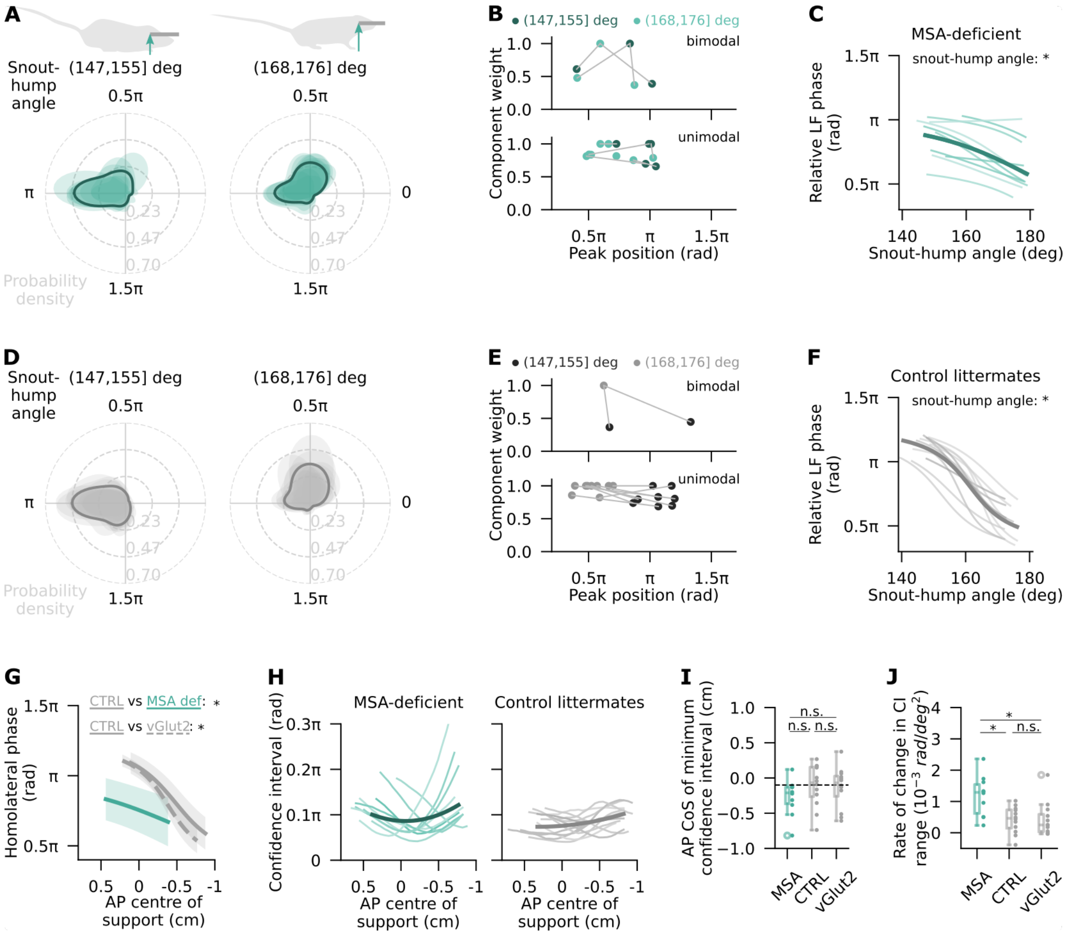

Figure 5.5: Leg load-dependent modulation of homolateral phase is disrupted but not eliminated in the absence of MSA signalling.
(A, D) Kernel density distributions of LF phase relative to LH in two snout-hump angle intervals of MSA-deficient mice (A; n=10 mice) and littermates (D; n=12 mice). Data include individual mice (*shaded*) and averages (*solid outlines*). **(B, E)** Component weights from Von Mises mixture model fits to homolateral phase in two snout-hump angle intervals of MSA-deficient mice (B) and littermates (E), plotted against the phase corresponding to peak of the respective component's probability distribution. Points are colour-coded by snout-hump angle interval and connected for the same mouse. Peak phase is shown on a linear scale. **(C, F)** Relative LF phase as a function of snout-hump angle in MSA-deficient mice (C) and littermates (F), with LH as reference. Shown are circular-linear mixed-effects regression fits to single mouse data (*light traces*) from head height trials, and the average (*dark trace*). **(G)** Homolateral phase as a function of anteroposterior CoS in MSA-deficient mice (*solid, teal*) and littermates (*solid, grey*). Data from vGlut2-Cre mice shown for reference (*dashed, grey*; Chapter 4). Statistics refer to slope comparisons between cohorts. **(H)** 95% confidence interval for homolateral phase as a function of anteroposterior CoS in MSA-deficient mice (*left*) and littermates (*right*) as individual animals (*thin traces*) and average (*thick*). **(I, J)** Boxplots of anteroposterior CoS position corresponding to minimum 95% confidence interval for homolateral phase (I) and rate of change in this confidence interval across CoS positions (J), quantified by the quadratic fit coefficient. Dashed line in (I) designates anteroposterior CoS at rest from Morina (2023). Statistical significance criterion (C, F): * HPD_{SSDO} interval does not include zero, n.s. otherwise. Thresholds (G, I, J): * $p < 0.05$, ** $p < 0.01$, *** $p < 0.001$.

the average homolateral phase of MSA-deficient mice shifted from 0.9±0.2 π rad at hunched postures (147-155 deg snout-hump angles) to 0.7±0.3 π rad when the hump-snout vector was more upward oriented (168-176 deg; **Figure 5.5 A**). Circular-linear regression of homolateral phase against snout-hump angle, speed, and their interaction confirmed snout-hump angle as a significant predictor of phase (HPD_{SSDO}=(0.53,0.84); **Figure 5.5 C**). As in littermate controls (**Figure 5.5 F**), its effect was bilaterally symmetrical (HPD_{SSDO}=(-0.01,0.17)), independent of speed (HPD_{SSDO}=(-0.85,0.81)), and significant even after accounting for mouse-specific variability (HPD_{SSDO}=(0.52,0.82)). Conversely, the effect of speed, although significant on average, was rendered statistically insignificant after allowing for mouse-specific variation, which suggests that its influence on phase varied considerably across animals. Thus, the primary features of homolateral phase modulation by snout-hump angle and speed were qualitatively conserved in MSA-deficient animals, making it unlikely for MSAs to be the sole mediator of this relationship.

At the same time, the phase transition observed in MSA-deficient mice was 50% less pronounced than in non-ataxic littermates whose homolateral phase changed from 1.00±0.02 π rad to 0.6±0.2 π rad over the same snout-hump angle intervals (**Figure 5.5 D**). The smaller average effect of snout-hump angle in MSA-deficient animals was partly due to greater variability across mice. While most mice of either genotype showed unimodal homolateral phase distributions at both extremes of the examined snout-hump angle range (**Figure 5.5 B, E**), the phase transitions of MSA-deficient animals were less concentrated around the mean (mean resultant length, MSA: 0.89, littermates: 0.94) and displayed a wider variety of slopes ($p=2 \times 10^{-5}$; **Figure 5.5 C, F**). Still, the maximum phase shift seen in any MSA-deficient mouse corresponded to only the 17th percentile of the phase shift distribution in littermate controls, indicating that the magnitude of biomechanical modulation was also reduced at the level of individual mice. Another explanation for the apparent difference in snout-hump angle effect on homolateral phase could be the anteriorward shift in the relationship between CoS position and snout-hump angle seen on the force sensors (see Figure 5.4). However, the reduced biomechanical influence was also present when homolateral phase was examined directly as a function of anteroposterior CoS position by leveraging force sensor data (p=0.006; **Figure 5.5 G**). Assuming consistent posture-load relationship across setups, these findings suggest that the more fore-biased load distribution of MSA-deficient animals could not, on its own, account for the differences in homolateral phase coordination between the ataxic mice and their littermates. Finally, looking at within-mouse variability, the width of 95% confidence intervals for homolateral phase typically followed a concave function of anteroposterior CoS position such that the lowest homolateral phase uncertainty mapped onto a single CoS position in most mice (**Figure 5.5 H**). This CoS position did not differ significantly between genotypes (MSA: -0.27±0.08 cm, littermates: -0.12±0.08 cm, p=0.2) and, on average, matched the CoS position of mice at rest (MSA: p=0.07, littermates: p=0.86; **Figure 5.5 I**). However, despite coordinating homolateral limbs with similar precision at the baseline weight distribution, phase variability of MSA-deficient mice increased 182% more rapidly as the CoS position shifted towards either extreme (p=0.003; **Figure 5.5 J**). Overall, these results suggest that MSA signalling plays a significant role in mediating the biomechanical influence on homolateral phase, and reinforce the anteroposterior weight distribution as the key variable in this relationship.

5.2.3.2 Muscle spindle signalling modulates prevalence of diagonal leg support

In 4.2.1.2, the shift from strict homolateral alternation to a quarter-of-phase more synchronised coordination was found to correlate with a decrease in diagonal support, which was partly compensated for by greater single-leg support. To investigate whether this relationship was preserved in MSA-deficient mice, I analysed their limb support data by projecting it onto the principal component axes of variance derived from non-ataxic animals and regressing the most heavily loaded projections against speed and snout-hump angle. As in control animals, changes in speed, snout-hump angle, and their interaction significantly influenced the projection of MSA-deficient animal data along the third PC (p between 3×10^{-6} and 8×10^{-31}), which reflects the prevalence of diagonal leg support (see Figure 4.4 D). However, the effect of snout-hump angle was smaller in MSA-deficient mice such that a reorientation of their hump-snout vector reduced the within-stride fraction of diagonal support by 35% less than in littermate controls (p=0.02). Although MSA-deficient mice performed only head height trials, the consistent effects on PC3 in both head height and slope trials of non-ataxic animals allowed for the relationship between PC3 and snout-hump angle to be mapped to the anteroposterior CoS space using force sensor recordings. This analysis confirmed that the effect of anteroposterior CoS position on the fraction of diagonal support captured by PC3 is statistically significant, but smaller than in control mice ($p=3 \times 10^{-6}$; **Figure 5.6 A**), consistent with these animals' reduced adaptability to changes in load distribution, as described earlier. Conversely, no association was found between anteroposterior CoS position and the within-stride fraction of single-leg leg support captured by PC4 (p=0.15; **Figure 5.6 B**). This result aligned with findings from control animals, whose limb support projection along PC4 was influenced by an interaction effect between snout-hump angle and slope (see Figure 4.4 F), but not by snout-hump angle alone. Likewise, speed was a significant predictor of the variance captured by PC4 irrespective of animal genotype ($p=4 \times 10^{-48}$; strain comparison: p=0.88). Considering the speed-dependence of load-related effects on diagonal support and the absence of a direct snout-hump angle effect on single-leg support, these results corroborate the hypothesis proposed in 4.2.1.2 that changes in limb support patterns are a secondary effect of load redistribution, likely driven by changes in homolateral phase.

To explore whether the absence of MSA signalling affects the relationship between homolateral coordination and limb support patterns independently of biomechanical modulation, I regressed the PC projections against the sine and cosine components of homolateral phase. Interestingly, the sensitivity of both diagonal (p=0.02) and single-leg (p=0.04) support patterns to changes in homolateral phase was slightly reduced in MSA-deficient mice compared to their non-ataxic littermates (**Figure 5.6 C, D**). In particular, MSA-deficient animals were 31% less likely to use a diagonal support pattern during strict homolateral alternation and 28% less likely to rely on single-leg support during synchronised homolateral motion. Altogether, these findings demonstrate that MSA deficiency disrupts animal adaptability to changes in load distribution, as well as the relationship between homolateral phase and the overall limb support pattern (**Figure 5.6 C, E**).

5.2.3.3 Non-restrained locomotion corroborates impaired phase adaptability due to altered muscle spindle feedback

To examine how MSA signalling influences homolateral phase during freely moving locomotion, MSA-deficient mice were recorded on the motorised treadmill. Under these conditions, the average homolateral phase shifted from $0.83\pm0.06\pi$ rad to $0.71\pm0.09\pi$ rad as the snout-hump angle increased by 20 degrees (**Figure 5.7 A**). As before, I quantified the relationship between homolateral phase, snout-hump angle, and speed using circular-linear mixed-effects regression. This analysis revealed that homolateral phase of MSA-deficient mice was significantly influenced by both predictors, as well as their interac-

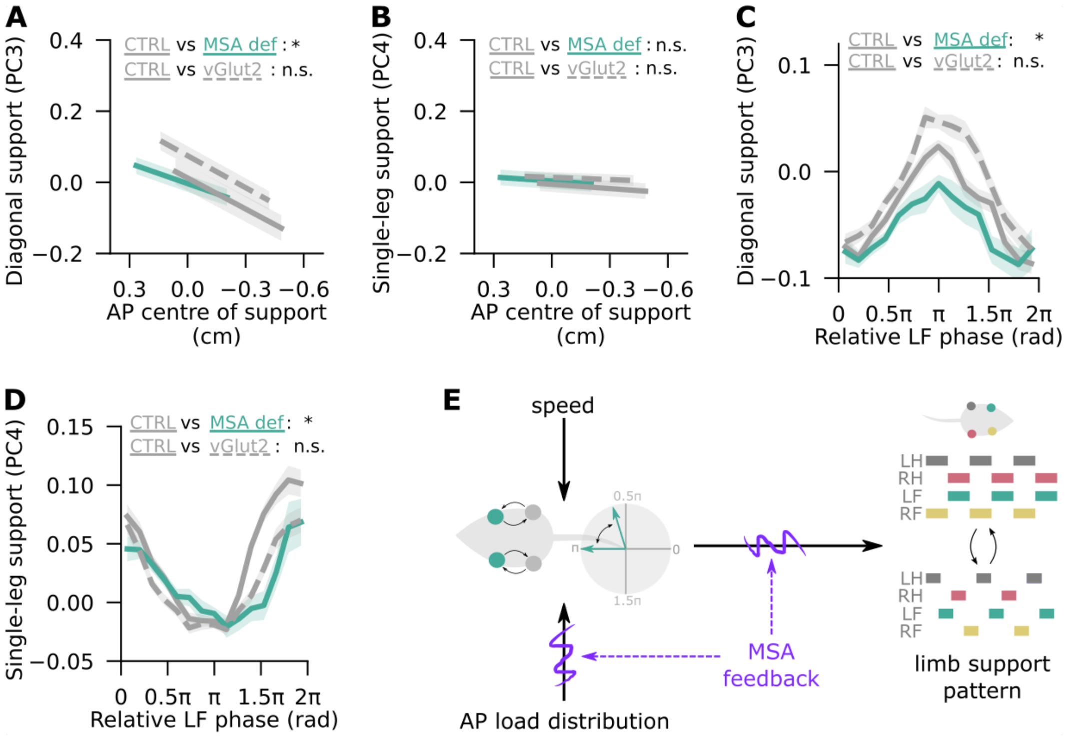

Figure 5.6: Absence of MSA signalling disrupts the relationship between diagonal limb support prevalence, load distribution, and homolateral phase.
(A, B) Projections of limb support data along PC3 (A) and PC4 (B) as a function of anteroposterior centre of support position in MSA-deficient mice (*solid, teal*) and littermate controls (*solid, grey*). Also shown for reference are data from vGlut2-Cre mice (*dashed, grey*) from Chapter 4. Statistics refer to slope comparisons between animal cohorts. **(C, D)** Same as (A), but showing the projections of limb support data along PC3 (C) and PC4 (D) as a function of left forelimb phase relative to left hindlimb phase. The horizontal axis presents a circular variable on a linear scale for convenience. **(E)** Schematic representation of the hypothesised homolateral limb control pathways, highlighting the components affected by MSA feedback.
Data in all panels are only from head height trials.
Statistical significance thresholds: * $p < 0.05$, ** $p < 0.01$, *** $p < 0.001$.

tion, consistent with non-ataxic littermates (**Figure 5.7 B**; see Table 2.9 for statistics). Although the average homolateral phase of MSA-deficient mice was 0.12π rad more synchronised than that of their non-ataxic littermates, the average slopes of homolateral phase plotted against snout-hump angle were similar across genotypes (HPD_{SSDO}=(-1.98,1.98); **Figure 5.7 C**), suggesting no difference in homolateral sensitivity to changes in leg load distribution. This was the case despite significantly greater homolateral phase volatility of MSA-deficient mice within the range of observed snout-hump angles ($p=5 \times 10^{-6}$; **Figure 5.7 D, E**). At a glance, this result contradicts the findings from head-fixed locomotion on the passive treadmill, where disrupted MSA signalling impaired animal adaptability to changes in anteroposterior CoS position, as reflected in snout-hump angle (see Figure 5.5). However, it is worth noting that individual MSA-deficient mice showed greater variability in the relationship between snout-hump angle and homolateral phase compared to controls (13-fold difference between standard deviations of slopes; see Figure 5.7 B), indicating that the apparent similarity in group-level effects may largely be an artifact of averaging. In addition, as evidenced by the reduced effect of snout-hump angle on the homolateral phase of littermate controls, it is plausible that non-restrained locomotion without experimental control over leg load distribution severely constrains the ability to observe pronounced changes in homolateral coordination. In Chapter 4.2.1.3, this limitation was hypothesised to arise in part from head pitch variability diluting the leg load correspondence of a given snout-hump angle, and in part because the observed range of load distributions likely fell within the low load-sensitivity region near homolateral alternation, characteristic of relatively anterior CoS positions. If the unaltered load sensitivity of homolateral phase following MSA ablation was due to differences in head pitch angle variability, MSA-deficient mice would be expected to show significantly less variability in head pitch at a given snout-hump angle. Indeed, this was the case ($p=7 \times 10^{-10}$, *Levene test*; **Figure 5.7 F, G**), supporting the idea that the blurred correspondence between snout-hump angle and load distribution seen in the absence of head restraint contributed to the apparent lack of an MSA-mediated effect on homolateral coordination. Moreover, since the non-restrained head of the animal was mostly pitched downward compared to its fixed orientation on the passive treadmill, it seems reasonable to infer that a given snout-hump angle on the motorised treadmill corresponded to a more anterior CoS position than on the passive treadmill. Consequently, a tendency of animals to maintain their CoS near the load-insensitive saturation region, which does not require substantial adaptations in homolateral phase, may have also contributed to the absence of an MSA-dependent effect on homolateral phase. Altogether, data from the motorised treadmill supports the hypothesis that MSA feedback is important for mice to adapt to changes in anteroposterior load distribution. The lack of an MSA-dependent effect on the cohort-averaged homolateral phase is likely attributable to a combination of factors, including population averaging, lower head tilt variability, and maintenance of CoS near a load-insensitive extreme.

5.2.4 Muscle spindle feedback influences hindlimb phase modulation by speed and descending input

5.2.4.1 Disrupted muscle spindle signalling weakens the association between homologous limb coordination and cuneiform nucleus stimulation

In 4.2.2.1, the stepping order of left and right homologous limbs was shown to correlate with the side of unilateral glutamatergic neuron stimulation in the cuneiform nucleus (CnF). Given the reliable and rapid induction of forward locomotion by such stimulation, its influence on homologous coordination was not necessarily expected to be altered by disruptions to MSA feedback. However, the stimulation side-dependence of out-of-phase forelimb movement was completely eliminated in MSA-deficient mice (p=0.3; **Figure 5.8 A-*left***). Although their hindlimb phase retained a statistically significant lateral bias (p=0.01), it was 14% less pronounced compared to non-ataxic littermates who had undergone identical experimental procedures (**Figure 5.8 A-*middle***). In fact, a binary classifier trained to predict the side of opsin expression and optic fibre implantation based on the homologous phase of MSA-deficient mice per-

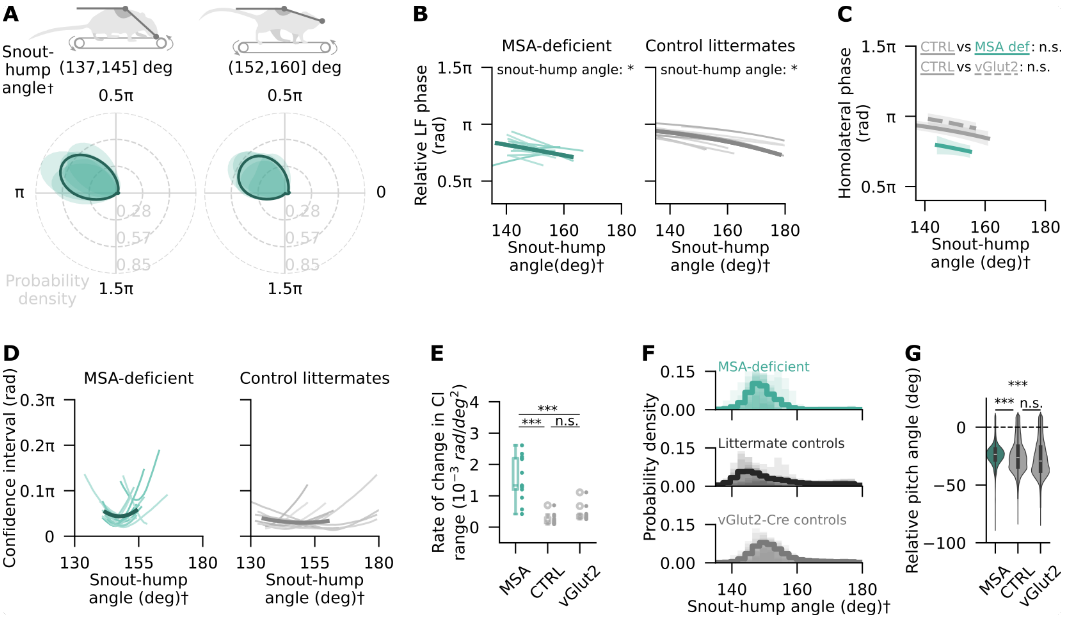

Figure 5.7: Non-restrained locomotion shows no evidence of impaired phase adaptability due to altered muscle spindle feedback.
(A) Kernel density distributions of LF relative to LH in two snout-hump angle intervals of MSA-deficient mice (n=13 mice) during non-restrained locomotion on the motorised treadmill. Individual animal (*shaded regions*) and average (*solid outlines*) data are shown. **(B)** Relative LF phase as a function of snout-hump angle in MSA-deficient mice (*left*) and littermate controls (*right*), with LH as the reference limb. Shown are circular-linear mixed-effects regression fits to single mouse data (*light traces*) from level trials and the average (*dark trace*) computed across snout-hump angles adopted by any mouse. **(C)** Homolateral phase as a function of snout-hump angle in MSA-deficient mice (*solid, teal*) and littermate controls (*solid, grey*), reflecting the range of angles adopted by all mice in the cohort. Also shown for reference are data from vGlut2-Cre mice (*dashed, grey*) from Chapter 4. Statistics refer to slope comparisons across genotypes **(D)** 95% confidence interval for homolateral phase as a function of snout-hump angle in MSA-deficient mice (*left*) and littermate controls (*right*). Shown are data from individual mice (*thin traces*) and the average (*thick*). **(E)** Boxplots showing the rate of change in 95% confidence interval for homolateral phase across snout-hump angles, quantified by the quadratic fit coefficient. Data from MSA-deficient mice, littermate controls, and vGlut2-Cre mice are shown with points representing individual mice. **(F)** Histograms of snout-hump angles observed in MSA-deficient mice (*top*), littermate controls (*middle*), and controls from the vGlut2-Cre cohort (*bottom*; same as top panel in Figure 3.9) during non-restrained locomotion on the motorised treadmill. Shaded histograms represent individual mice, the thick line is the average. **(G)** Distribution of head pitch angles recorded during non-restrained locomotion relative to the head tilt during head fixation. Statistics are based on a Levene test on bootstrapped distributions of interquartile ranges.
Data in all panels are only from level trials.
† indicates that snout-hump angle is measured in non-restrained conditions and is not necessarily directly comparable to the snout-hump angle from head-fixed experiments.
Statistical significance criterion (B, C): * HPD_{SSDO} interval does not include zero, n.s. otherwise. Statistical significance thresholds (E, G): * $p < 0.05$, ** $p < 0.01$, *** $p < 0.001$.

formed just slightly above chance (58.0±0.1% accuracy) and no better than a classifier trained on non-stimulated locomotor data from the motorised treadmill (60.2±0.1% accuracy; p=0.98, *one-sided t-test*; **Figure 5.8 A-*right*, B**). Conversely, a classifier trained on littermates' data performed with 68.9±0.1% accuracy ($p=3 \times 10^{-8}$; **Figure 5.8 C**). No differences were observed in the distributions of optogenetic stimulation frequency between cohorts (p=0.29). These results indicate that left-right coordination might be slightly biased by the side of surgical intervention alone, but its dependence on bilaterally asymmetrical descending inputs from the CnF has been significantly diminished by the absence of MSA signalling.

The greater propensity for a particular left-right stepping order seen in control animals could be expected to correlate with a transverse gallop-like footfall sequence. Similarly, the diminished lateral bias in mice lacking MSA feedback could arise from, or result in, more frequent adoption of a rotary gallop-like sequence. Indeed, the probability of using a transverse stepping sequence was reduced in MSA-deficient mice (p=0.003; **Figure 5.8 D**). However, with an average of 0.974±0.004, this probability remained significantly higher than chance ($p=7 \times 10^{-23}$), and was even higher on the motorised treadmill (0.998±0.001; $p=p=3 \times 10^{-6}$), despite mice showing no significant preference for either left-right stepping order. Chi-square analysis comparing observed and expected probabilities under the assumption of independence found no evidence of interdependence between the probabilities of transverse gallop and a specific stepping order in any animal cohort ($p>0.2$). Thus, the diminished association between the side of CnF activation and left-right stepping bias in MSA-deficient mice is unlikely to be driven by a change in gallop type preference and might instead reflect impaired supraspinal access to the circuits coordinating homologous limbs.

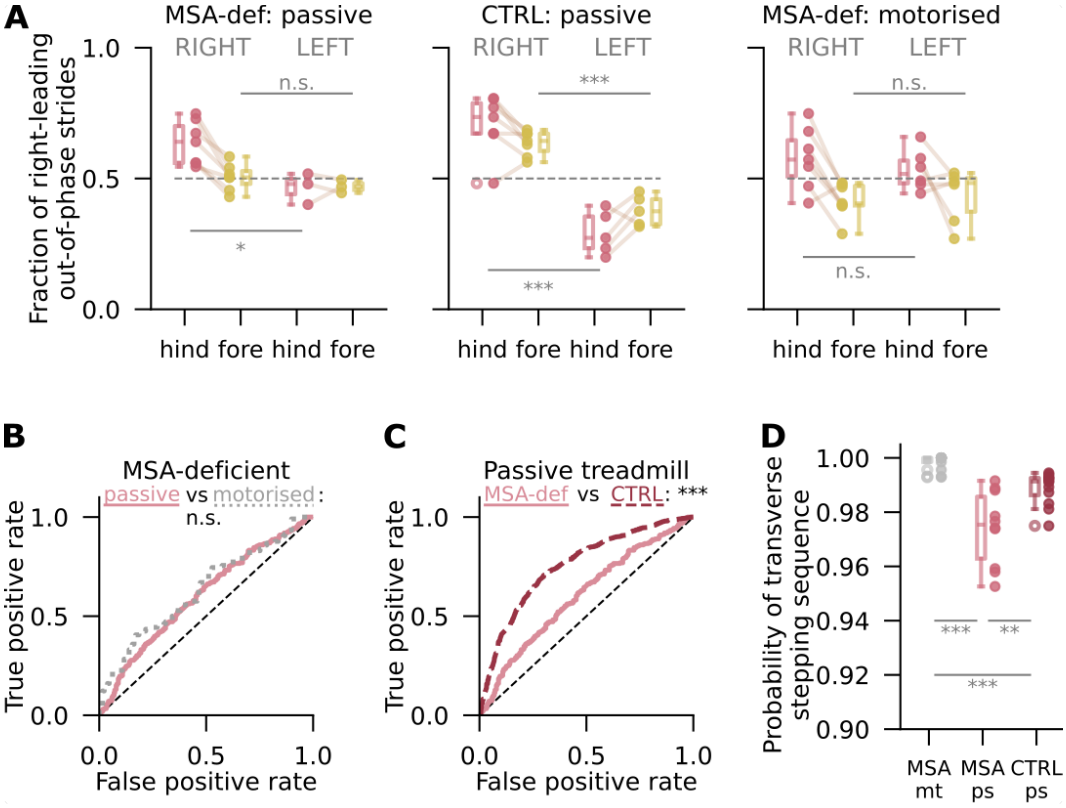

Figure 5.8: Non-restrained locomotion shows no evidence of impaired phase adaptability due to altered muscle spindle feedback.
(A) The fraction of right-leading steps between hindlimbs (*pink*) and forelimbs (*yellow*) during optogenetically induced locomotion on the passive treadmill in MSA-deficient mice (*left*) and littermate controls (*middle*). Also shown are data from MSA-deficient mice during non-stimulated locomotion on the motorised treadmill (*right*). Dots represent individual mice, connected by lines and plotted separately depending on the side of optogenetic stimulation. Near-alternating ($1 \pm 0.2\ \pi$ rad) or near-synchronised ($0 \pm 0.2\ \pi$ rad) steps are excluded. **(B-C)** Receiver operating characteristic curve of a binary classifier trained to predict the side of virus injection and optic fibre implantation. In (B), the classifier was trained on a combination of hindlimb and forelimb homologous phase data during stimulated locomotion on the passive treadmill (*pink, solid*) and non-stimulated locomotion on the motorised treadmill (*grey, dotted*). In (C), a similar classifier was trained on homologous phase data from MSA-deficient mice (*pink, solid*) and their non-ataxic littermates (*dark red, dashed*). **(D)** Boxplots showing the probability of a transverse gallop-like stepping sequence in MSA-deficient mice on the motorised (mt) and passive (ps) treadmill, and control littermates.
Statistical significance thresholds (E, G): * $p < 0.05$, ** $p < 0.01$, *** $p < 0.001$.

5.2.4.2 Muscle spindle feedback shapes the speed-dependence of hindlimb coordination

As discussed in 4.2.2.2, load-related variables have no direct effect on hindlimb coordination, but can modulate the relationship between hindlimb phase and speed. In particular, an increase in the total leg load, resulting from low head heights or upsloping surfaces, was found to heighten hindlimb phase sensitivity to speed, such that the stance onset delay of the leg ipsilateral to CnF stimulation decreased with growing speed. Conversely, a snout-hump angle-related variable qualitatively altered the relationship between homologous phase and speed, potentially reflecting a postural influence. To explore the role of MSA feedback in mediating these biomechanical effects, I analysed the hindlimb coordination of MSA-deficient mice during head height trials on the passive treadmill. In response to stimulation of the right CnF, the average hindlimb phase of MSA-deficient animals was $0.14 \pm 0.46\pi$ rad at smaller snout-hump angles (147-155 deg) and $0.07 \pm 0.08\pi$ when the hump-snout vector was more upward oriented (168-176 deg; **Figure 5.9 A**). Thus, similar to mice with intact MSA feedback (see Figure 4.9), hindlimb coordination of MSA-deficient mice during stimulation-induced locomotion was nearly synchronous on average, with a slight delay of the leg ipsilateral to stimulation side. A minority of mice (30%) displayed significantly bimodal phase distributions at one or both of the studied snout-hump angle intervals, showing a second peak at $0.99 \pm 0.01\pi$ rad, characteristic of strict hindlimb alternation (**Figure 5.9 B**). Thus, the overall distribution of hindlimb coordination patterns was similar in animals with and without MSA feedback.

Next, I regressed the relative hindlimb phase against speed and snout-hump angle as before (see 2.2.3.4). Neither predictor had a significant main effect individually, but their interaction was significant (HPD_{SSDO}=(0.42,1.03); **Fig-**

ure 5.9 C). Compared to non-ataxic littermates and the vGlut2-Cre cohort analysed in 4.2.2.2, hindlimb phase of MSA-deficient mice was equally unaffected by snout-hump angle alone and displayed diminished modulation by speed, being most sensitive to it at small snout-hump angles (**Figure 5.9 D, E**). However, whereas in control animals, the relative hindlimb phase shifted towards strict alternation at low speeds (<40 cm/s), MSA-deficient animals showed a similar desynchronisation of hindlimb stepping by $\sim 0.7\pi$ rad as the speed increased beyond 50 cm/s. These results suggest that MSA feedback might naturally support the shift from hindlimb alternation to synchrony upon acceleration.

Analysis of control animal locomotion in Chapter 4 showed that the snout-hump angle effect in head height trials could be attributed to two distinct factors: total leg load and an unspecified posture-related variable. These factors were reflected in head height and in the residuals of snout-hump angle regressed on head height, respectively. When the relative hindlimb phase of MSA-deficient mice was regressed against the same set of variables, acceleration from 50 to 100 cm/s was associated with a progressive increase in hindlimb phase lag by $0.5\text{-}0.6\pi$ rad specifically at low head heights (higher total load; see Figure 5.4 D) and negative snout-hump angle residuals (**Figure 5.9 F, G**). Although these relationships contrasted with the hindlimb desynchronisation observed at low speeds in control mice (see Figure 4.10), hindlimb coordination became less sensitive to changes in speed at higher head positions, which correspond to a decrease in total load, similar to animals with intact MSA feedback. Thus, the effects of MSA feedback appear to be limited to the nature of speed-dependent modulation of hindlimb phase under specific biomechanical conditions, without influencing the overall sensitivity of hindlimb phase to changes in speed. When the hump-snout vector is in a relatively natural downward oriented state, MSA signalling seems indispensable for the shift

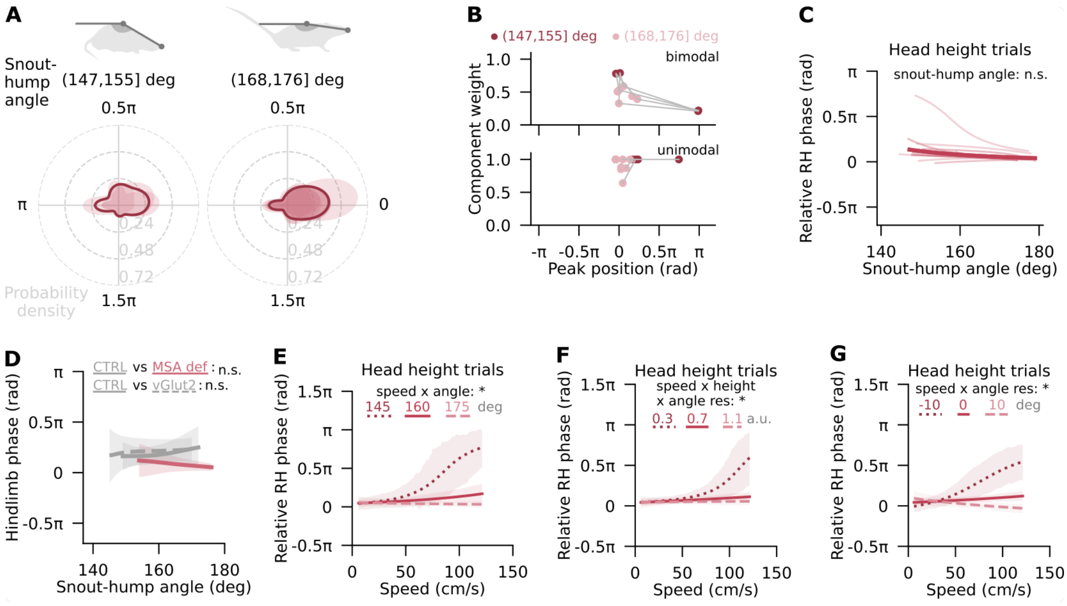

Figure 5.9: Absence of MSA feedback affects the pattern of speed-dependent hindlimb modulation, but not its overall sensitivity to speed changes.
(A) Kernel density distributions of RH relative to LH in two snout-hump angle intervals, shown for individual MSA-deficient mice (shaded regions; n=7 mice) and as averages across mice (solid outlines). Limb phase values of 0 and π rad reflect limb synchrony and alternation respectively. Data from mice with bimodal distributions (as defined in 2.2.3.3) or fewer than 40 strides per category were excluded. **(B)** Component weights from optimal Von Mises mixture model fits to hindleg phase data in two snout-hump angle intervals, plotted against the phase corresponding to the peak of the respective component's probability distribution. Points are colour-coded by snout-hump angle interval and connected for the same mouse. Peak phase is shown on a linear scale. **(C)** Relative RH phase as a function of snout-hump angle at median speed with LH as the reference. Shown are circular-linear mixed-effects regression fits to single mouse data from head height trials (*light traces*) and the average (*dark trace*). **(D)** Hindlimb phase as a function of snout-hump angle in MSA-deficient mice (*solid, red*) and littermates (*solid, grey*). For reference shown are data from vGlut2-Cre mice (*dashed, grey*; Chapter 4). Statistics refer to slope comparisons between cohorts. **(E-G)** Relative hindlimb phase as a function of speed at three representative snout-hump angles (E), weight-adjusted head heights (F), and residuals from snout-hump angle regression against the weight-adjusted head height (G). Shown are the fixed effects from circular-linear mixed-effects regression. Shaded regions are 95% highest posterior density intervals. In (G), positive residuals reflect snout-hump angles that exceed the angles predicted by the weight-adjusted head height.
Statistical significance criterion (C-G): * HPD_{SSDO} interval does not include zero, n.s. otherwise.

from hindlimb alternation to synchrony as speed increases.

Finally, to verify that the observed differences in biomechanical contributions to hindlimb phase in MSA-deficient and control mice were not an artifact of head fixation or optogenetic stimulation, I examined MSA-deficient animals' locomotion on the motorised treadmill. Since total load remained unchanged under these non-restrained conditions, the speed-dependent effect of snout-hump angle on hindlimb phase was expected to be limited to that associated with snout-hump angle residuals from the previous analyses. However, although smaller snout-hump angles tended towards delaying movement of the right hindlimb at higher speeds as expected, neither predictor nor their interaction was found to have a significant effect on hindlimb coordination in MSA-deficient mice (**Figure 5.10 A**; see Table 2.9 for statistics). In fact, over the entire observed range of speeds and snout-hump angles, left-right phase changed by only $\sim 0.03\pi$ rad on average. While the lack of snout-hump angle effect at low speeds was consistent with MSA-deficient animal locomotion on the passive treadmill, the absence of speed-dependent modulation at higher speeds was puzzling. It could not be attributed to insufficient variability in hindlimb phase: the dominance of left-right alternation was even more pronounced in control mice, yet a speed-dependent influence of snout-hump angle could still be detected (**Figure 5.10 B**, see also Figure 4.11 A). Likewise, the lack of effect could not be explained by the ambiguity of snout-hump angle as a metric under non-restrained conditions, since the range of head tilt variability associated with a given snout-hump angle was comparable across genotypes (see Figure 5.7 G). Instead, it seems plausible that MSA-deficient mice have at best weak intrinsic interdependence between speed and snout-hump angle, and that its apparent influence on the passive treadmill was largely related to optogenetic CnF stimulation. Therefore, MSA signalling can be considered necessary for biomechanical modulation of hindlimb coordination at low speeds, but the distinct effects observed in MSA-deficient and control mice at high speeds may reflect an experimental artifact. Figure 5.10 C provides a summary of MSA feedback effects within the context of the previously hypothesised hindlimb control pathways.

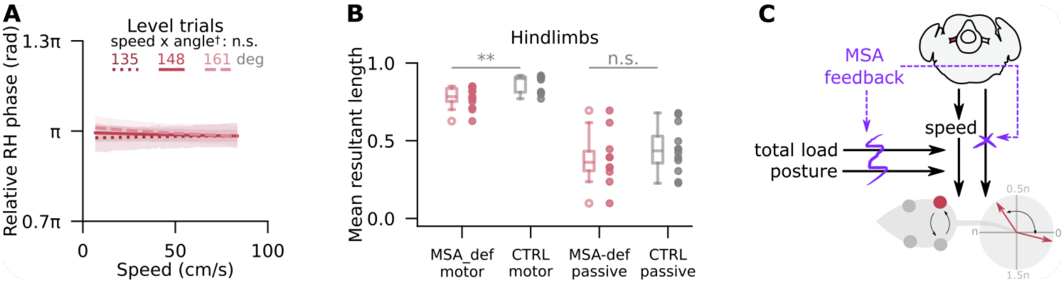

Figure 5.10: Biomechanical modulation of hindlimb phase is lost during non-restrained locomotion without MSA feedback.
(A) Relative phase of the right hindleg as a function of speed at three representative snout-hump angles during level trials on the motorised treadmill, with left hindlimb as the reference leg. Shown are the fixed effects from circular-linear mixed-effects regression analysis. Shaded regions represent 95% highest posterior density intervals. **(B)** Mean resultant length of MSA-deficient and control animal hindlimb phase distributions on motorised and passive treadmill setups. For reference, mean resultant length is an inverse measure of variability that varies between 0 and 1, with these extremes representing a uniform and a degenerate distribution respectively.
† indicates that snout-hump angle is measured in non-restrained conditions and is not necessarily directly comparable to the snout-hump angle from head-fixed experiments. **(C)** Schematic representation of the hypothesised hindlimb control pathways, highlighting the components affected by MSA feedback.
Statistical significance criterion: * HPD_{SSDO} interval does not include zero, n.s. otherwise.

5.3 Discussion

Here I have shown that the homolateral phase adaptability to changes in anteroposterior load distribution, described in the previous chapter, is reduced in Egr3-knockout mice that lack muscle spindle afferent feedback. In particular, deviations from the resting centre of support appear to disproportionately increase these animals' homolateral phase variability, suggesting that MSA signalling is necessary, even if not solely responsible, for the ability to regulate homolateral phase under altered load conditions. Additionally, I have provided evidence that MSA feedback supports hindlimb phase control through asymmetrical input from the cuneiform nucleus and a biomechanics-dependent mechanism at low speeds. Lastly, I have demonstrated that, even in absence of all proprioceptive feedback, unilateral optogenetic stimulation of the CnF reliably triggers forward locomotion, although the resulting movement is highly inefficient.

By conducting experiments in mice without MSA or any proprioceptive afferent feedback, I sought to determine whether the associations between biomechanical variables and interlimb coordination observed in Chapter 4 were causal or driven by an unidentified confounding variable. Regrettably, this question could not be fully addressed, as PA-deficient mice proved unsuitable for experiments in the novel paradigm, and the role of MSA in load detection remains unclear. The traditional view on muscle spindles, shaped significantly by experiments on passive muscle, has largely limited the function of these proprioceptors to detection of muscle length and its rate of change (Proske & Gandevia, 2012; Tuthill & Azim, 2018). However, recent findings have demonstrated that many MSA units additionally encode non-kinematic variables, including force, and are capable of regulating the strength of muscle activity (Blum et al., 2017; Mayer et al., 2018; Olson et al., 2024). While biophysical modelling suggests that the force-related MSA activity does not directly represent external load but instead reflects intrafusal force generated through interactions between activities of alpha and gamma motor neurons (Blum et al., 2020), it does not necessarily diminish the potential relevance of these representations to the animal. Until the behavioural relevance of MSA feedback in force sensing is fully understood, it remains to be determined whether the MSA-dependent features of the relationship between interlimb coordination, speed, and biomechanical variables identified in this thesis truly reflect a role for MSAs in load detection.

Alternatively, changes in leg load or its distribution might not be solely responsible for the observed mechanical dependence of interlimb phase, especially in the case of homolateral coordination. Indeed, although the results suggest contributions from somatosensory systems that were left intact in MSA-deficient mice, such as the load-sensing Golgi tendon organs or cutaneous mechanoreceptors, homolateral limbs could be controlled by a complex interplay of load- and posture-related inputs. In favour of this hypothesis, the observed transitions in homolateral phase, while consistent with modulation by load distribution, were more pronounced in relation to changes in snout-hump angle than to changes in slope (see Figure 4.2). It is therefore plausible that the partial attenuation of homolateral phase dependence on snout-hump angle seen in the absence of MSA signalling might reflect full elimination of the posture-related component, while leaving the load-related component intact. Experimental manipulation of surface slope, as previously conducted in non-ataxic mice (Chapter 4), could help contextualise the precise impact of muscle spindle feedback on homolateral phase.

There is also a third possibility, one that aligns with load redistribution being the primary trigger of homolateral phase transitions while maintaining that muscle spindles have no direct role in load detection. By studying response to saphenous nerve stimulation during hindlimb swing in MSA-deficient and intact mice, Mayer and Akay (2021) have shown that the animals' stumbling corrective reaction includes an MSA-independent posteriorward displacement of the forelimb that guides an adjustment of hindlimb position in an MSA-dependent manner. This work suggests a potential interplay between an intralimb mechanism triggered by changes in load and a homolateral limb coordination mechanism mediated by muscle spindles, which could help explain the effects on homolateral phase described in this thesis.

Previous studies also support a role for muscle spindles in ensuring locomotor adaptability and robustness, having linked MSA deficiency with increased variability in foot placement, limb phase, and several kinematic variables (Mayer et al., 2018; Santuz & Akay, 2023; Takeoka et al., 2014). The rise in homolateral phase variability observed in the present study aligns with these findings and is specifically associated with deviations from baseline load distribution. While it is tempting to link this increased phase variability of MSA-deficient mice to the reduced average effect of load distribution on homolateral phase, the two patterns were decoupled during non-restrained locomotion on the motorised treadmill. To an extent, this discrepancy could relate to the differences in homolateral phase modulation that are seen across experimental setups even in non-ataxic control mice. However, it must also be acknowledged that the MSA-deficient mice used in this thesis lose muscle spindles soon after birth, potentially allowing for long-term compensatory mechanisms to mask or modify the true function of MSAs. Consequently, it seems plausible that the reduced phase variability near the baseline load distribution might reflect an adaptation to the loss of MSA feedback rather than naturally lower MSA involvement at smaller deviations from baseline. Future experiments with acute muscle spindle removal (Mayer et al., 2018) or spatially restricted ablation of all proprioceptors (Takeoka et al., 2014) could help clarify the load-dependence of muscle spindle contribution to homolateral coordination.

In contrast to the partial effects of MSA signalling on homolateral phase, the influence of load and postural variables on hindlimb coordination was completely abolished at low speeds in the absence of MSA feedback. Speed-dependent effects of MSA input have been shown before, albeit highlighting its role in modulating extensor muscle activity and setting a limit for sustained locomotor speed (Mayer et al., 2018). Although the present focus on instantaneous, rather than sustained, speeds does not allow direct for comparison of the speed limits, the observed effects on hindlimb coordination are consistent with the hypothesis that sensory feedback is of particular relevance at low speeds and under greater mechanical instability (Ijspeert & Daley, 2023). In addition, mice lacking MSA feedback were found to have lost the propensity to lead locomotion with the leg ipsilateral to the the side of unilateral CnF stimulation. These findings relate to a previously reported interaction between descending stimulation and the effectiveness of feedback-mediated gait entrainment (Kriellaars et al., 1994), underscoring the important interplay between descending and feedback influences on hindlimb coordination.

Chapter 6

General discussion

Recent advancements in murine transgenic technology and markerless motion capture have enabled remarkable progress towards unravelling the computational logic and neural circuits at the core of locomotor behaviour (Arber & Costa, 2022; Ferreira-Pinto et al., 2018; Kiehn, 2016). These tools have opened new avenues for addressing complex and compelling questions, such as the interplay of sensory feedback, spinal pattern generation, and supraspinal modulation in controlling locomotion (Ijspeert & Daley, 2023). In this thesis, I argue that this interplay is particularly pertinent to understanding the stereotyped yet adaptable nature of interlimb coordination, or gait, and that this locomotor feature has remained comparatively underexplored specifically due to a disconnect between mechanical and neural experimental techniques. To address this challenge, I have presented a novel locomotor paradigm in mice that leverages these animals' experimental tractability to decouple the influences of descending, speed-related commands and biomechanical feedback on interlimb coordination (Chapter 3). Using this paradigm, I have studied locomotion of both intact mice (Chapter 4) and mice lacking proprioceptive feedback from muscle spindles (Chapter 5), gaining insight into the mechanical and neural bases of homolateral and hindlimb coordination. While the influence of back curvature-related factors could not be ruled out, I have been able to demonstrate that anteroposterior leg load distribution contributes to homolateral phase modulation in a speed-independent manner, with the resulting phase change primarily calibrating the prevalence of diagonal limb support. From these results, I have proposed that the baseline load distribution of mice supports strict homolateral alternation with dominance of diagonal support, similar to most quadrupeds, and that the circular direction of phase deviation from this pattern is governed by whether the baseline load distribution is fore-heavy or hind-heavy. In addition, I have found that muscle spindle feedback plays a significant role in homolateral phase adaptability to biomechanical perturbations, but further experiments are needed to clarify how this contribution relates to changes in load distribution. Finally, I have shown that hindlimb coordination can be biased by asymmetrical descending activation from the cuneiform nucleus and modulated in a speed-dependent manner by total leg load and an unspecified posture-related variable, with both functions critically reliant on muscle spindle feedback. What follows is a discussion of the implications and limitations of the present study, as well as potential avenues for future research.

6.1 Future directions and limitations of the novel locomotor paradigm

Among the primary contributions of this thesis is the development of a novel behavioural paradigm for studying mouse locomotion. However, it has certain inherent shortcomings that limit its potential for future applications. Most notably, since the observed interlimb effects primarily emerge through trial averaging of single mouse data, each experimental animal must perform a sufficient number of coordinated strides in response to CnF stimulation. While the required minimum number of strides could be slightly lower than the 1000 strides used in the present study, DTX-inducible ablation of all proprioceptive afferents in Chapter 5 showed that mice with pronounced ataxia cannot reach this threshold within a reasonable experimental time frame. Moreover, the need for CnF stimulation to induce high-speed locomotion not only brings into question the ethological relevance of the observed behaviour, but also limits the kind of neural activity manipulations and recordings that could be performed during movement. This is due to both limited spatial access to the regions near CnF and the challenges associated with integration of neural recording and optogenetics, such as photoelectric artifacts and network effects (Buzsáki et al., 2015). These factors put fundamental constraints on the kind of neural insight that could be gleaned through the new locomotor paradigm.

In addition to these inherent limitations, the present implementation of the passive treadmill paradigm has several shortcomings that could be addressed through refinement. First, future experiments with transgenic animals must incorporate manipulation of both head height and surface slope modulation, as it is through comparison of effects related to slope and snout-hump angle that the roles of total load, load distribution, and posture can be disentangled. Second, tracking leg joints and spine curvature, in addition to the positions of feet and the hump, would add valuable dimensions to the data that could yield further understanding of the mechanism linking biomechanical changes to the shift in limb phase. It could also enhance the appreciation of the caveats associated with the paradigm's reductionist approach when compared to non-restrained, volitional movement, as has been demonstrated through comparison of motorised treadmill and overground locomotion (Blaszczyk & Loeb, 1993; Buchner et al., 1994). Third, the study would benefit from varying not only the frequency but also the intensity of optogenetic CnF stimulation to temper the prevalence of left-right synchronised coordination and thereby enable more uniform coverage of plausible homologous limb phases. Finally, it would be useful to improve the design of the passive treadmill by enabling load measurement directly on the setup and along all three force dimensions. Current inferences have been drawn by relating force sensor and treadmill data based on slope or postural variables, but the impact of setup-specific adaptations, such as differences in foot placement, on the load borne by the legs remains unaccounted for. Leg load is also known to vary throughout the step cycle, showing qualitatively distinct dynamics across gaits and a speed-dependent magnitude (Clayton & Hobbs, 2019), so the standstill forces recorded here fail to capture the full complexity of the relationship between load, speed, and interlimb coordination. Taken together, these refinements could allow the novel behavioural paradigm to more effectively represent the nuances of quadrupedal locomotion and how internal and environmental factors interact to shape its expression.

Despite the aforementioned limitations, the new locomotor paradigm already provides an unparalleled opportunity to study the interplay between biomechanical and descending influences on interlimb coordination by allowing systematic and independent manipulation of the total leg load, its anteroposterior distribution, and speed-related control pathways from the brain. Previous approaches to modulation of leg load have had several major limitations: swim tests or changes in surface texture support only binary or discrete adjustments in load (Akay et al., 2014; Gruner & Altman, 1980; Pocratsky et al., 2020), while application of extra load is incompatible with small animals like mice (Farley & Taylor, 1991; Lee et al., 1999; Lee et al., 2004). Similarly, manipulation of surface slope during non-restrained locomotion, commonly used across quadrupedal species (Dutto et al., 2004; Lammers et al., 2006; Lee et al., 2008), allows for substantial postural adaptations that counter slope-imposed load redistribution and likely diminish the interlimb phase adjustments needed for biomechanically stable locomotion. As a result, load-related changes mediated by these methods have typically revealed minor, if any, effects on interlimb coordination, and have not distinguished between the influences of total load and load distribution (Farley & Taylor, 1991; Lammers et al., 2006; Lee, 2011; Lee et al., 2004; Wickler et al., 2003). Furthermore, without precise control over biomechanical feedback, it has been challenging to dissociate primary effects on interlimb phase from secondary effects driven by changes in locomotor speed (Batka et al., 2014). In this thesis, the integration of head restraint with head height or surface slope modulation has addressed these limitations, offering a linear handle on load distribution and expanding its observable range. Owing to CnF stimulation, the new locomotor paradigm has also been more effective than the traditionally used motorised treadmill at evoking a wide range of interlimb coordination patterns, which is necessary for studying changes in gait. Collectively, these factors have likely been pivotal in enabling the passive treadmill experiments to both reveal a significantly stronger association between homolateral phase preference and load distribution than detectable during non-restrained locomotion, and to statistically dissociate the expression of speed and gait. These advances pave the way towards investigation of quadrupedal gait that is driven by behaviour and does not rely on loss-of-function interventions to reveal gait-specific effects.

Future prospects for this behavioural paradigm primarily relate to the strong appeal of the mouse as a model system, which stems from its amenability to experimental constraints and the ever growing set of techniques to monitor and manipulate its neural activity (International Brain Laboratory et al., 2023; Navabpour et al., 2020). Building on the results from chronically muscle spindle-deficient mice presented in this thesis, an important next step would be spatially restricted and acute ablation of muscle spindle feedback to dissect their involvement in load-dependent homolateral limb coordination without potentially confounding long-term adaptations (Mayer et al., 2018). Similarly, spatially and temporally confined elimination of all proprioceptive afferents would help deduce the role of Golgi tendon organs (Takeoka & Arber, 2019). Subsequently, the paradigm could be used to explore the descending and feedback influences on locomotion of mice lacking genetically and spatially defined types of spinal interneurons. Potential neural targets include the propriospinal neurons that connect the cervical and lumbar segments of the spinal cord and have been shown to contribute to both context- and speed-dependent locomotion (Pocratsky et al., 2020; Ruder et al., 2016). While propriospinal neurons encompass a diverse array of genetic profiles, an especially appealing subset for further investigation includes neurons of V2a and V2b identities that have been found to collaboratively shape homolateral limb coupling and might be involved in processing balance-related information (Hayashi et al., 2023). Likewise, it would be interesting to explore the role of another recently described population of spinal interneurons that is involved in homolateral coordination, namely parvalbumin-expressing neurons in the deep dorsal horn, which receive proprioceptive, cutaneous, and descending input (Gradwell et al., 2024). Although there is likely redundancy in the system, acute manipulation of any neuron population involved in mediating the biomechanics-dependent effects on interlimb coordination presented in this thesis is likely to be captured by the passive treadmill paradigm.

6.2 Interplay between descending commands and biomechanical feedback in shaping various aspects of interlimb coordination

Central pattern generators, sensory feedback, and descending modulation from the brainstem have all been established as critical building blocks of basic adaptable locomotion in vertebrates (Grillner & El Manira, 2019). Now, research attention is shifting towards exploring the interplay between these fundamental components, with emerging hypotheses assigning distinct roles to spinal, supraspinal, and peripheral networks depending on factors like movement speed, animal size, mechanical stability, and time to locomotor maturity (Frigon et al., 2021; Ijspeert & Daley, 2023; Molkov et al., 2024; Rybak et al., 2024; Ryczko et al., 2020). The present study contributes to that discussion in two significant ways. First, it demonstrates scope for speed-independent control of homolateral coordination mediated, in part, by receptors other than muscle spindles. Previous studies across various legged animals (Cabelguen et al., 2003; Caggiano et al., 2018; Dautan et al., 2021; Shik & Orlovsky, 1976) have shown that stimulation of the mesencephalic locomotor region (MLR), which includes the CnF, evokes coordinated changes in both speed and gait, and certain gaits are typically expressed within a limited speed range in absence of stimulation as well (Griffin et al., 2004; Hoyt & Taylor, 1981; Lemieux et al., 2016; Maes & Abourachid, 2013; Wickler et al., 2003). The present observation of independent homolateral phase modulation by speed and biomechanical variables suggests that the organisation of the rhythm-generating and pattern-forming functions of the gait control system is not strictly hierarchical. At least under the mechanically restrained conditions of the passive treadmill paradigm, biomechanical feedback appears to have a speed-independent route to the homolateral control module. Downstream in the control pathway, this influence may be combined with speed-related input to modulate limb support periods, consistent with the dominant effect of speed on support patterns (Frigon et al., 2014). Curiously, the homolateral phase and limb support patterns seen at hind-heavy load distributions also closely resemble those observed upon degeneration of cerebellar Purkinje cells, suggesting a role for these cells in biomechanics-dependent gait regulation (Machado et al., 2015). This parallel highlights a potential interaction between biomechanical feedback pathways and cerebellar control that warrants further investigation.

Second, the work presented in this thesis shows that hindlimb coordination is influenced by asymmetrical commands from the brainstem, with muscle spindle feedback playing an enabling role irrespective of whether hindlimbs were, on average, alternating or synchronised. These findings are consistent with prior empirical reports of an interaction between intensity of descending stimulation and the ability of muscle afferent-mediated mechanical perturbations to entrain locomotor rhythm in decerebrate cats (Kriellaars et al., 1994). That the effects of top-down commands are critically dependent on sensory feedback has also been shown in *Drosophila* after leg amputation (Berendes et al., 2016) and through neuromechanical modelling that has demonstrated emergence of MLR-driven gait transitions specifically in the presence of sensory feedback (Harischandra et al., 2011; Owaki & Ishiguro, 2017). Collectively, these results indicate that, akin to many highly conserved features of locomotion, the observed interdependence of descending and sensory signals is likely a general feature of left-right coordination, applicable beyond the hindlimbs of a quadruped.

However, while this thesis has offered a fresh perspective on the empirical study of the interplay between descending and feedback influences on interlimb coordination, its focus on homolateral and hindlimb coordination separately has meant that the generated insights remain fragmented. Achieving an integrated understanding of the gait control system will require continued collaboration between experimentalists and theorists to iteratively test and refine hypotheses about the neural circuits underlying observed behaviours and link those to higher-level objectives of the animal (Dickinson et al., 2000; Ijspeert & Daley, 2023). With development of increasingly realistic neuro-musculoskeletal models (DeWolf et al., 2024; Merel, Aldarondo, et al., 2019; Tata Ramalingasetty et al., 2021; Tata Ramalingasetty et al., 2024) and a growing focus on posture, balance, and fall avoidance as the key triggers of gait transitions (Molkov et al., 2024; Shafiee et al., 2024), it will be interesting to see future work identify network implementations that reproduce the distinct interactions between top-down input and sensor feedback observed in the present work. Such models could serve as predictive tools, pinpointing the most plausible sources of relevant muscle spindle feedback, and assessing whether they likely differ for homolateral and hindlimb coordination. Prior work has highlighted the role of hip proprioceptors in enabling the emergence of walk in an otherwise trotting quadrupedal system (Harischandra et al., 2011), which may apply to the present observations as well. Furthermore, modelling of this new data could illuminate the extent to which intralimb and interlimb mechanisms interact to shape coordination patterns under varying biomechanical conditions. Previous computational simulations have shown that the same locomotor output can arise from network configurations with varying degrees of inter-CPG connectivity and centrally or feedback-driven dynamics (Harischandra et al., 2011; Molkov et al., 2024; Owaki & Ishiguro, 2017), but it is the ability of a model to reconcile diverse experimental findings without major circuit reorganisation that offers the most valuable frameworks for understanding biological systems.

6.3 Close coupling of load distribution, posture, and homolateral coordination

As shown in Chapter 4, the strong correlation of homolateral coordination with both snout-hump angle and surface slope is consistent with limb phase modulation by anteroposterior load distribution. However, it is plausible that the posture of neck and trunk contributes to this limb phase transition not only through their effect on leg load distribution, but also through direct coupling of the axial and limb mechanics. For example, trotting dogs have been shown to actively redistribute their body weight along the anteroposterior body axis in order to counteract an upward pitching moment during acceleration or, conversely, generate one to resist an externally imposed load, with load placement governing changes in homolateral limb phase (Lee et al., 1999; Lee et al., 2004). Likewise, bending of the spine has been linked to the emergence of high-speed gaits, like gallop and bound, which are asymmetrical along the anteroposterior axis and offer the benefit of brief elastic strain energy storage in the back musculature (Alexander et al., 1985; Alexander, 1988; Khoramshahi et al., 2013; Yesilevskiy et al., 2018). Integrating these ideas with the results of this thesis, it seems likely that leg load distribution and articulation of the back are tightly coupled, exerting complementary and partly redundant effects on homolateral phase, mediated through both muscle spindles and primarily force-sensitive receptors. In addition, seeing this relationship between interlimb coordination and body biomechanics during head-fixed locomotion suggests that the need to avoid a fall, conceptualised as gait viability (Shafiee et al., 2024), might not be the immediate trigger for changes in gait. Instead, these results support a mechanical trigger for gait transitions and align with the idea that such a trigger may have evolved at least partly in response to the need for energetically efficient locomotion (Bertram, 2013). As with questions regarding the interplay between top-down and feedback influences on locomotion, understanding the teleology of gait control and the complementary roles of load and posture will likely require more than just comparative biology; theoretical models and robotics will be crucial for progress.

6.4 Implications for other quadrupeds

At the end of Chapter 4, I have put forth a hypothesis that whether a posteriorward redistribution of load delays or advances the movement of a forelimb relative to the homolateral hindlimb depends on the animal's baseline load distribution being fore-heavy or hind-heavy respectively. This difference could account for the opposite effects of load redistribution on homolateral phase observed in fore-heavy quadrupreds, such as dogs, goats, and opossums (Bertram et al., 2000; Lammers et al., 2006; Lee, 2011; Lee et al., 2004), compared to mice, whose resting centre of support is closer to the hindlimbs (Morina, 2023). The discrepancy between opossums and mice is particularly interesting since both species share a similar non-cursorial body build with comparatively horizontal limb orientation, despite the differences in their centre of support position (Alexander & Jayes, 1983; Lammers et al., 2006; Stein & Casinos, 1997). If the baseline distribution is indeed the relevant factor determining homolateral phase in response load redistribution, other hind-heavy quadrupeds that primarily use trot should display similar locomotor behaviour to that of mice. Notably, this expectation applies to other small rodents, including rats, gerbils, and voles (Eilam, 1997), but most quadrupeds with hind-biased baseline load distributions, such as ring-tailed lemurs and rabbits, do not normally trot at all (Dagg, 1973). In line with the presented hypothesis, these animals would be expected to adopt a trotting gait upon a sufficient anteriorward redistribution of load, but demonstrating this empirically would likely require physical restraints, like head-fixation, that might be too extreme to be feasible in these species. Perhaps a more practical way to test this hypothesis empirically would be to investigate the effects of more pronounced fore-biased load distributions in large, fore-heavy animals like dogs, which are amenable to carrying additional, strategically placed loads. It would also be interesting to explore how redistribution of load affects the homolateral coordination of quadrupeds whose primary gait at moderate or high speeds is pace, such as camels and greyhounds (Dagg, 1973; Hildebrand, 1980). In any case, the current study has presented a hypothesis that could be explored in multiple species. Even if the simplicity of this hypothesis may ultimately fail to capture the complexity of quadrupedal locomotor strategies and constraints, I hope it will inspire further research into the fascinating nature of interlimb coordination.

Bibliography

Abourachid, A. (2003). A new way of analysing symmetrical and asymmetrical gaits in quadrupeds. *Comptes Rendus. Biologies*, **326**(7), 625–630.

Abourachid, A., Herbin, M., Hackert, R., Maes, L., & Martin, V. (2007). Experimental study of coordination patterns during unsteady locomotion in mammals. *Journal of Experimental Biology*, **210**(2), 366–372.

Akay, T., & Murray, A. J. (2021). Relative contribution of proprioceptive and vestibular sensory systems to locomotion: Opportunities for discovery in the age of molecular science. *International Journal of Molecular Sciences*, **22**(3), 1467.

Akay, T., Tourtellotte, W. G., Arber, S., & Jessell, T. M. (2014). Degradation of mouse locomotor pattern in the absence of proprioceptive sensory feedback. *Proceedings of the National Academy of Sciences*, **111**(47), 16877–16882.

Alexander, R. M. (1984). The gaits of bipedal and quadrupedal animals. *The International Journal of Robotics Research*, **3**(2), 49–59.

Alexander, R. M. (1989). Optimization and gaits in the locomotion of vertebrates. *Physiological Reviews*, **69**(4), 1199–1227.

Alexander, R. M., Dimery, N. J., & Ker, R. (1985). Elastic structures in the back and their role in galloping in some mammals. *Journal of Zoology*, **207**(4), 467–482.

Alexander, R. M., & Jayes, A. (1983). A dynamic similarity hypothesis for the gaits of quadrupedal mammals. *Journal of Zoology*, **201**(1), 135–152.

Alexander, R. M. (1988). Why mammals gallop. *American zoologist*, **28**(1), 237–245.

Andersson, L. S., Larhammar, M., Memic, F., Wootz, H., Schwochow, D., Rubin, C.-J., Patra, K., Arnason, T., Wellbring, L., Hjälm, G., Imsland, F., Petersen, J. L., McCue, M. E., Mickelson, J. R., Cothran, G., Ahituv, N., Roepstorff, L., Mikko, S., Vallstedt, A., Lindgren, G., Andersson, L., & Kullander, K. (2012). Mutations in DMRT3 affect locomotion in horses and spinal circuit function in mice. *Nature*, **488**(7413), 642–646.

Aoi, S., Katayama, D., Fujiki, S., Tomita, N., Funato, T., Yamashita, T., Senda, K., & Tsuchiya, K. (2013). A stability-based mechanism for hysteresis in the walk–trot transition in quadruped locomotion. *Journal of The Royal Society Interface*, **10**(81), 20120908.

Aoi, S., Yamashita, T., & Tsuchiya, K. (2011). Hysteresis in the gait transition of a quadruped investigated using simple body mechanical and oscillator network models. *Physical Review E*, **83**(6), 061909.

Arber, S., & Costa, R. M. (2022). Networking brainstem and basal ganglia circuits for movement. *Nature Reviews Neuroscience*, **23**(6), 342–360.

The art of horseback riding. (1895). *Scientific American*, **73**(10), 373–374.

Ausborn, J., Shevtsova, N. A., Caggiano, V., Danner, S. M., & Rybak, I. A. (2019). Computational modeling of brainstem circuits controlling locomotor frequency and gait. *eLife*, **8**, e43587.

Ballion, B., Morin, D., & Viala, D. (2001). Forelimb locomotor generators and quadrupedal locomotion in the neonatal rat. *European Journal of Neuroscience*, **14**(10), 1727–1738.

Bankhead, P., Loughrey, M. B., Fernández, J. A., Dombrowski, Y., McArt, D. G., Dunne, P. D., McQuaid, S., Gray, R. T., Murray, L. J., Coleman, H. G., James, J. A., Salto-Tellez, M., & Hamilton, P. W. (2017). Qupath: Open source software for digital pathology image analysis. *Scientific Reports*, **7**(1), 1–7.

Barbeau, H., & Rossignol, S. (1987). Recovery of locomotion after chronic spinalization in the adult cat. *Brain Research*, **412**(1), 84–95.

Basu, C., Wilson, A. M., & Hutchinson, J. R. (2019). The locomotor kinematics and ground reaction forces of walking giraffes. *Journal of Experimental Biology*, **222**(2), jeb159277.

Bates, D., Mächler, M., Bolker, B., & Walker, S. (2014). Fitting linear mixed-effects models using lme4. *arXiv:1406.5823*.

Batka, R. J., Brown, T. J., Mcmillan, K. P., Meadows, R. M., Jones, K. J., & Haulcomb, M. M. (2014). The need for speed in rodent locomotion analyses. *The Anatomical Record*, **297**(10), 1839–1864.

Bay, J. S., & Hemami, H. (1987). Modeling of a neural pattern generator with coupled nonlinear oscillators. *IEEE Transactions on Biomedical Engineering*, (4), 297–306.

Bellardita, C., & Kiehn, O. (2015). Phenotypic characterization of speed-associated gait changes in mice reveals modular organization of locomotor networks. *Current Biology*, **25**(11), 1426–1436.

Bellegarda, G., & Ijspeert, A. (2022). CPG-RL: Learning central pattern generators for quadruped locomotion. *IEEE Robotics and Automation Letters*, **7**(4), 12547–12554.

Berendes, V., Zill, S. N., Büschges, A., & Bockemühl, T. (2016). Speed-dependent interplay between local pattern-generating activity and sensory signals during walking in drosophila. *Journal of Experimental Biology*, **219**(23), 3781–3793.

Bertram, J. E. (2013). Gait as solution, but what is the problem? Exploring cost, economy and compromise in locomotion. *The Veterinary Journal*, **198**, e3–e8.

Bertram, J. E., Lee, D. V., Case, H. N., & Todhunter, R. J. (2000). Comparison of the trotting gaits of labrador retrievers and greyhounds. *American journal of veterinary research*, **61**(7), 832–838.

Biancardi, C. M., & Minetti, A. E. (2012). Biomechanical determinants of transverse and rotary gallop in cursorial mammals. *Journal of Experimental Biology*, **215**(23), 4144–4156.

Biewener, A. A. (1983). Allometry of quadrupedal locomotion: The scaling of duty factor, bonecurvature and limb orientation to body size. *Journal of Experimental Biology*, **105**(1), 147–171.

Biewener, A. A., & Taylor, C. R. (1986). Bone strain: A determinant of gait and speed? *Journal of Experimental Biology*, **123**(1), 383–400.

Blaszczyk, J., & Loeb, G. E. (1993). Why cats pace on the treadmill. *Physiology & Behavior*, **53**(3), 501–507.

Blum, K. P., Campbell, K. S., Horslen, B. C., Nardelli, P., Housley, S. N., Cope, T. C., & Ting, L. H. (2020). Diverse and complex muscle spindle afferent firing properties emerge from multiscale muscle mechanics. *eLife*, **9**, e55177.

Blum, K. P., Lamotte D'Incamps, B., Zytnicki, D., & Ting, L. H. (2017). Force encoding in muscle spindles during stretch of passive muscle. *PLoS Computational Biology*, **13**(9), e1005767.

Borowska, J., Jones, C., Deska-Gauthier, D., & Zhang, Y. (2015). V3 interneuron subpopulations in the mouse spinal cord undergo distinctive postnatal maturation processes. *Neuroscience*, **295**, 221–228.

Borowska, J., Jones, C. T., Zhang, H., Blacklaws, J., Goulding, M., & Zhang, Y. (2013). Functional subpopulations of V3 interneurons in the mature mouse spinal cord. *Journal of Neuroscience*, **33**(47), 18553–18565.

Bosco, G., & Poppele, R. (2001). Proprioception from a spinocerebellar perspective. *Physiological Reviews*, **81**(2), 539–568.

Bouman, A., Ginting, M. F., Alatur, N., Palieri, M., Fan, D. D., Touma, T., Pailevanian, T., Kim, S.-K., Otsu, K., Burdick, J., & Agha-mohammadi, A.-a. (2020). Autonomous spot: Long-range autonomous exploration of extreme environments with legged locomotion. *2020 IEEE/RSJ International Conference on Intelligent Robots and Systems (IROS)*, 2518–2525.

Bouyer, L., & Rossignol, S. (2003a). Contribution of cutaneous inputs from the hindpaw to the control of locomotion. I. Intact cats. *Journal of Neurophysiology*, **90**(6), 3625–3639.

Bouyer, L., & Rossignol, S. (2003b). Contribution of cutaneous inputs from the hindpaw to the control of locomotion. II. Spinal cats. *Journal of Neurophysiology*, **90**(6), 3640–3653.

Britz, O., Zhang, J., Grossmann, K. S., Dyck, J., Kim, J. C., Dymecki, S., Gosgnach, S., & Goulding, M. (2015). A genetically defined asymmetry underlies the inhibitory control of flexor–extensor locomotor movements. *eLife*, **4**, e04718.

Brockett, E., Seenan, P., Bannatyne, B., & Maxwell, D. (2013). Ascending and descending propriospinal pathways between lumbar and cervical segments in the rat: Evidence for a substantial ascending excitatory pathway. *Neuroscience*, **240**, 83–97.

Brown, T. G. (1911). The intrinsic factors in the act of progression in the mammal. *Proceedings of the Royal Society of London. Series B, containing papers of a biological character*, **84**(572), 308–319.

Buchli, J., & Ijspeert, A. J. (2008). Self-organized adaptive legged locomotion in a compliant quadruped robot. *Autonomous Robots*, **25**, 331–347.

Buchner, H., Savelberg, H., Schamhardt, H., Merkens, H., & Barneveld, A. (1994). Kinematics of treadmill versus overground locomotion in horses. *Veterinary Quarterly*, **16**(sup2), 87–90.

Buono, P.-L., & Golubitsky, M. (2001). Models of central pattern generators for quadruped locomotion I. Primary gaits. *Journal of mathematical biology*, **42**, 291–326.

Butt, S. J., & Kiehn, O. (2003). Functional identification of interneurons responsible for left-right coordination of hindlimbs in mammals. *Neuron*, **38**(6), 953–963.

Buzsáki, G., Stark, E., Berényi, A., Khodagholy, D., Kipke, D. R., Yoon, E., & Wise, K. D. (2015). Tools for probing local circuits: High-density silicon probes combined with optogenetics. *Neuron*, **86**(1), 92–105.

Cabelguen, J.-M., Bourcier-Lucas, C., & Dubuc, R. (2003). Bimodal locomotion elicited by electrical stimulation of the midbrain in the salamander notophthalmus viridescens. *Journal of neuroscience*, **23**(6), 2434–2439.

Caggiano, V., Leiras, R., Goñi-Erro, H., Masini, D., Bellardita, C., Bouvier, J., Caldeira, V., Fisone, G., & Kiehn, O. (2018). Midbrain circuits that set locomotor speed and gait selection. *Nature*, **553**(7689), 455–460.

Canavier, C. C., Butera, R. J., Dror, R., Baxter, D. A., Clark, J., & Byrne, J. H. (1997). Phase response characteristics of model neurons determine which patterns are expressed in a ring circuit model of gait generation. *Biological Cybernetics*, **77**, 367–380.

Capelli, P., Pivetta, C., Soledad Esposito, M., & Arber, S. (2017). Locomotor speed control circuits in the caudal brainstem. *Nature*, **551**(7680), 373–377.

Carlson-Kuhta, P., Trank, T. V., & Smith, J. L. (1998). Forms of forward quadrupedal locomotion. ii. a comparison of posture, hindlimb kinematics, and motor patterns for upslope and level walking. *Journal of Neurophysiology*, **79**(4), 1687–1701.

Cartmill, M., Lemelin, P., & Schmitt, D. (2002). Support polygons and symmetrical gaits in mammals. *Zoological Journal of the Linnean Society*, **136**(3), 401–420.

Carvalho, M. M., Tanke, N., Kropff, E., Witter, M. P., Moser, M.-B., & Moser, E. I. (2020). A brainstem locomotor circuit drives the activity of speed cells in the medial entorhinal cortex. *Cell Reports*, **32**(10).

Castiglioni, A., Gallaway, M., & Coulter, J. (1978). Spinal projections from the midbrain in monkey. *Journal of Comparative Neurology*, **178**(2), 329–345.

Cavagna, G. A., Heglund, N. C., & Taylor, C. R. (1977). Mechanical work in terrestrial locomotion: Two basic mechanisms for minimizing energy expenditure. *American Journal of Physiology-Regulatory, Integrative and Comparative Physiology*, **233**(5), R243–R261.

Chakraborty, S., & Wong, S. W. (2021). Bambi: An r package for fitting bivariate angular mixture models. *Journal of Statistical Software*, **99**, 1–69.

Chang, S. J., Santamaria, A. J., Sanchez, F. J., Villamil, L. M., Saraiva, P. P., Benavides, F., Nunez-Gomez, Y., Solano, J. P., Opris, I., Guest, J. D., & Noga, B. R. (2021). Deep brain stimulation of midbrain locomotor circuits in the freely moving pig. *Brain Stimulation*, **14**(3), 467–476.

Choi, S., Ji, G., Park, J., Kim, H., Mun, J., Lee, J. H., & Hwangbo, J. (2023). Learning quadrupedal locomotion on deformable terrain. *Science Robotics*, **8**(74), eade2256.

Claudi, F., Tyson, A. L., Petrucco, L., Margrie, T. W., Portugues, R., & Branco, T. (2021). Visualizing anatomically registered data with brainrender. *eLife*, **10**, e65751.

Clayton, H. M., & Hobbs, S. J. (2019). Ground reaction forces: The sine qua non of legged locomotion. *Journal of Equine Veterinary Science*, **76**, 25–35.

Collins, J. J., & Richmond, S. A. (1994). Hard-wired central pattern generators for quadrupedal locomotion. *Biological Cybernetics*, **71**(5), 375–385.

Conway, B., Hultborn, H., & Kiehn, O. (1987). Proprioceptive input resets central locomotor rhythm in the spinal cat. *Experimental Brain Research*, **68**, 643–656.

Cowley, K., & Schmidt, B. (1997). Regional distribution of the locomotor pattern-generating network in the neonatal rat spinal cord. *Journal of Neurophysiology*, **77**(1), 247–259.

Cregg, J. M., Leiras, R., Montalant, A., Wanken, P., Wickersham, I. R., & Kiehn, O. (2020). Brainstem neurons that command mammalian locomotor asymmetries. *Nature Neuroscience*, **23**(6), 730–740.

Cregg, J. M., Sidhu, S. K., Leiras, R., & Kiehn, O. (2024). Basal ganglia–spinal cord pathway that commands locomotor gait asymmetries in mice. *Nature Neuroscience*, 1–12.

Cremers, J., & Klugkist, I. (2018). One direction? A tutorial for circular data analysis using R with examples in cognitive psychology. *Frontiers in Psychology*, **9**.

Cremers, J., Mulder, K. T., & Klugkist, I. (2018). Circular interpretation of regression coefficients. *British Journal of Mathematical and Statistical Psychology*, **71**(1), 75–95.

Cresswell, T., & Ott, J. (2022). *Muybridge and mobility* (Vol. 6). Univ of California Press.

Crone, S. A., Quinlan, K. A., Zagoraiou, L., Droho, S., Restrepo, C. E., Lundfald, L., Endo, T., Setlak, J., Jessell, T. M., Kiehn, O., & Sharma, K. (2008). Genetic ablation of V2a ipsilateral interneurons disrupts left-right locomotor coordination in mammalian spinal cord. *Neuron*, **60**(1), 70–83.

Crone, S. A., Zhong, G., Harris-Warrick, R., & Sharma, K. (2009). In mice lacking V2a interneurons, gait depends on speed of locomotion. *Journal of Neuroscience*, **29**(21), 7098–7109.

Dagg, A. I. (1973). Gaits in mammals. *Mammal Review*, **3**(4), 135–154.

Dagg, A. I., & Vos, A. d. (1968a). Fast gaits of pecoran species. *Journal of Zoology*, **155**(4), 499–506.

Dagg, A. I., & Vos, A. d. (1968b). The walking gaits of some species of pecora. *Journal of Zoology*, **155**(1), 103–110.

Danner, S. M., Shevtsova, N. A., Frigon, A., & Rybak, I. A. (2017). Computational modeling of spinal circuits controlling limb coordination and gaits in quadrupeds. *eLife*, **6**, e31050.

Danner, S. M., Wilshin, S. D., Shevtsova, N. A., & Rybak, I. A. (2016). Central control of interlimb coordination and speed-dependent gait expression in quadrupeds. *The Journal of Physiology*, **594**(23), 6947–6967.

Dautan, D., Kovács, A., Bayasgalan, T., Diaz-Acevedo, M. A., Pal, B., & Mena-Segovia, J. (2021). Modulation of motor behavior by the mesencephalic locomotor region. *Cell Reports*, **36**(8).

Demes, B., Larson, S., Stern Jr, J., Jungers, W., Biknevicius, A., & Schmitt, D. (1994). The kinetics of primate quadrupedalism: "hindlimb drive" reconsidered. *Journal of Human Evolution*, **26**(5-6), 353–374.

DeWolf, T., Schneider, S., Soubiran, P., Roggenbach, A., & Mathis, M. (2024). Neuro-musculoskeletal modeling reveals muscle-level neural dynamics of adaptive learning in sensorimotor cortex. *bioRxiv*, 2024–09.

Dickinson, M. H., Farley, C. T., Full, R. J., Koehl, M., Kram, R., & Lehman, S. (2000). How animals move: An integrative view. *Science*, **288**(5463), 100–106.

Diedrich, F. J., & Warren, W. H. (1995). Why change gaits? Dynamics of the walk-run transition. *Journal of Experimental Psychology: Human Perception and Performance*, **21**(1), 183.

Donelan, J. M., McVea, D. A., & Pearson, K. G. (2009). Force regulation of ankle extensor muscle activity in freely walking cats. *Journal of Neurophysiology*, **101**(1), 360–371.

Drew, T., & Marigold, D. S. (2015). Taking the next step: Cortical contributions to the control of locomotion. *Current Opinion in Neurobiology*, **33**, 25–33.

Dutto, D. J., Hoyt, D. F., Cogger, E. A., & Wickler, S. J. (2004). Ground reaction forces in horses trotting up an incline and on the level over a range of speeds. *Journal of Experimental Biology*, **207**(20), 3507–3514.

Duysens, J., & Pearson, K. (1980). Inhibition of flexor burst generation by loading ankle extensor muscles in walking cats. *Brain Research*, **187**(2), 321–332.

Duysens, J., & Stein, R. (1978). Reflexes induced by nerve stimulation in walking cats with implanted cuff electrodes. *Experimental Brain Research*, **32**, 213–224.

Duysens, J., Clarac, F., & Cruse, H. (2000). Load-regulating mechanisms in gait and posture: Comparative aspects. *Physiological Reviews*, **80**(1), 83–133.

Eidelberg, E., Story, J., Meyer, B., & Nystel, J. (1980). Stepping by chronic spinal cats. *Experimental Brain Research*, **40**, 241–246.

Eilam, D. (1997). Postnatal development of body architecture and gait in several rodent species. *Journal of Experimental Biology*, **200**(9), 1339–1350.

Eisenstein, B. L., Postillion, F. G., Norgren, K. S., & Wetzel, M. C. (1977). Kinematics of treadmill galloping by cats: II. Steady-state coordination under positive reinforcement control. *Behavioral Biology*, **21**(1), 89–106.

Evans, D. A., Stempel, A. V., Vale, R., Ruehle, S., Lefler, Y., & Branco, T. (2018). A synaptic threshold mechanism for computing escape decisions. *Nature*, **558**(7711), 590–594.

Farley, C. T., & Taylor, C. R. (1991). A mechanical trigger for the trot-gallop transition in horses. *Science*, **253**(5017), 306–308.

Ferreira-Pinto, M. J., Kanodia, H., Falasconi, A., Sigrist, M., Esposito, M. S., & Arber, S. (2021). Functional diversity for body actions in the mesencephalic locomotor region. *Cell*, **184**(17), 4564–4578.

Ferreira-Pinto, M. J., Ruder, L., Capelli, P., & Arber, S. (2018). Connecting circuits for supraspinal control of locomotion. *Neuron*, **100**(2), 361–374.

Flynn, J. R., Conn, V. L., Boyle, K. A., Hughes, D. I., Watanabe, M., Velasquez, T., Goulding, M. D., Callister, R. J., & Graham, B. A. (2017). Anatomical and molecular properties of long descending propriospinal neurons in mice. *Frontiers in Neuroanatomy*, **11**, 5.

Forssberg, H., Grillner, S., Halbertsma, J., & Rossignol, S. (1980). The locomotion of the low spinal cat. ii. interlimb coordination. *Acta Physiologica Scandinavica*, **108**(3), 283–295.

Frigon, A. (2017). The neural control of interlimb coordination during mammalian locomotion. *Journal of Neurophysiology*, **117**(6), 2224–2241.

Frigon, A., Akay, T., & Prilutsky, B. I. (2021). Control of mammalian locomotion by somatosensory feedback. *Comprehensive Physiology*, **12**(1), 2877.

Frigon, A., D'Angelo, G., Thibaudier, Y., Hurteau, M.-F., Telonio, A., Kuczynski, V., & Dambreville, C. (2014). Speed-dependent modulation of phase variations on a step-by-step basis and its impact on the consistency of interlimb coordination during quadrupedal locomotion in intact adult cats. *Journal of Neurophysiology*, **111**(9), 1885–1902.

Fukuoka, Y., Habu, Y., & Fukui, T. (2015). A simple rule for quadrupedal gait generation determined by leg loading feedback: A modeling study. *Scientific Reports*, **5**(1), 8169.

Full, R. J., & Koditschek, D. E. (1999). Templates and anchors: Neuromechanical hypotheses of legged locomotion on land. *Journal of Experimental Biology*, **202**(23), 3325–3332.

Gariépy, J.-F., Missaghi, K., Chevallier, S., Chartré, S., Robert, M., Auclair, F., Lund, J. P., & Dubuc, R. (2012). Specific neural substrate linking respiration to locomotion. *Proceedings of the National Academy of Sciences*, **109**(2), E84–E92.

Gatto, G., & Goulding, M. (2018). Locomotion control: Brainstem circuits satisfy the need for speed. *Current Biology*, **28**(6), R256–R259.

Gay, S., Santos-Victor, J., & Ijspeert, A. (2013). Learning robot gait stability using neural networks as sensory feedback function for central pattern generators. *2013 IEEE/RSJ international conference on intelligent robots and systems*, 194–201.

Gonçalves, A. I., Zavatone-Veth, J. A., Carey, M. R., & Clark, D. A. (2022). Parallel locomotor control strategies in mice and flies. *Current Opinion in Neurobiology*, **73**, 102516.

Goñi-Erro, H., Selvan, R., Caggiano, V., Leiras, R., & Kiehn, O. (2023). Pedunculopontine Chx10+ neurons control global motor arrest in mice. *Nature Neuroscience*, **26**(9), 1516–1528.

Gottschall, J. S., & Nichols, T. R. (2007). Head pitch affects muscle activity in the decerebrate cat hindlimb during walking. *Experimental Brain Research*, **182**, 131–135.

Goulding, M. (2009). Circuits controlling vertebrate locomotion: Moving in a new direction. *Nature Reviews Neuroscience*, **10**(7), 507–518.

Gradwell, M. A., Ozeri-Engelhard, N., Eisdorfer, J. T., Laflamme, O. D., Gonzalez, M., Upadhyay, A., Medlock, L., Shrier, T., Patel, K. R., Aoki, A., Gandhi, M., Abbas-Zadeh, G., Oputa, O., Thackray, J. K., Ricci, M., George, A., Yusuf, N., Keating, J., Imtiaz, Z., Alomary, S. A., Bohic, M., Haas, M., Hernandez, Y., Prescott, S. A., Akay, T., & Abraira, V. E. (2024). Multimodal sensory control of motor performance by glycinergic interneurons of the mouse spinal cord deep dorsal horn. *Neuron*, **112**(8), 1302–1327.

Granatosky, M. C., Bryce, C. M., Hanna, J., Fitzsimons, A., Laird, M. F., Stilson, K., Wall, C. E., & Ross, C. F. (2018). Inter-stride variability triggers gait transitions in mammals and birds. *Proceedings of the Royal Society B*, **285**(1893), 20181766.

Gray, J. (1944). Studies in the mechanics of the tetrapod skeleton. *Journal of Experimental Biology*, **20**(2), 88–116.

Gregor, R. J., Smith, D. W., & Prilutsky, B. I. (2006). Mechanics of slope walking in the cat: Quantification of muscle load, length change, and ankle extensor emg patterns. *Journal of Neurophysiology*, **95**(3), 1397–1409.

Griffin, T. M., Kram, R., Wickler, S. J., & Hoyt, D. F. (2004). Biomechanical and energetic determinants of the walk–trot transition in horses. *Journal of Experimental Biology*, **207**(24), 4215–4223.

Grillner, S. (1981). Control of locomotion in bipeds, tetrapods, and fish. In V. Brooks (Ed.), *Handbook of physiology, the nervous system, motor control* (Volume II). American Physiological Society.

Grillner, S., & Zangger, P. (1975). How detailed is the central pattern generation for locomotion? *Brain Research*, **88**(2), 367–371.

Grillner, S., & Zangger, P. (1979). On the central generation of locomotion in the low spinal cat. *Experimental Brain Research*, **34**, 241–261.

Grillner, S. (2003). The motor infrastructure: From ion channels to neuronal networks. *Nature Reviews Neuroscience*, **4**(7), 573–586.

Grillner, S., & El Manira, A. (2019). Current principles of motor control, with special reference to vertebrate locomotion. *Physiological Reviews*.

Gruner, J., & Altman, J. (1980). Swimming in the rat: Analysis of locomotor performance in comparison to stepping. *Experimental Brain Research*, **40**, 374–382.

Harischandra, N., Knuesel, J., Kozlov, A., Bicanski, A., Cabelguen, J.-M., Ijspeert, A., & Ekeberg, Ö. (2011). Sensory feedback plays a significant role in generating walking gait and in gait transition in salamanders: A simulation study. *Frontiers in Neurorobotics*, **5**, 3.

Hayashi, M., Gullo, M., Senturk, G., Di Costanzo, S., Nagasaki, S. C., Kageyama, R., Imayoshi, I., Goulding, M., Pfaff, S. L., & Gatto, G. (2023). A spinal synergy of excitatory and inhibitory neurons coordinates ipsilateral body movements. *eLife*, **12**, RP89362.

Heglund, N., Fedak, M., Taylor, C., & Cavagna, G. (1982). Energetics and mechanics of terrestrial locomotion. iv. total mechanical energy changes as a function of speed and body size in birds and mammals. *Journal of Experimental Biology*, **97**(1), 57–66.

Heglund, N. C., Cavagna, G. A., & Taylor, C. R. (1982). Energetics and mechanics of terrestrial locomotion. iii. energy changes of the centre of mass as a function of speed and body size in birds and mammals. *Journal of Experimental Biology*, **97**(1), 41–56.

Heglund, N. C., & Taylor, C. R. (1988). Speed, stride frequency and energy cost per stride: How do they change with body size and gait? *Journal of Experimental Biology*, **138**(1), 301–318.

Heglund, N. C., Taylor, C. R., & McMahon, T. A. (1974). Scaling stride frequency and gait to animal size: Mice to horses. *Science*, **186**(4169), 1112–1113.

Hérent, C., Diem, S., Usseglio, G., Fortin, G., & Bouvier, J. (2023). Upregulation of breathing rate during running exercise by central locomotor circuits in mice. *Nature Communications*, **14**(1), 2939.

Hiebert, G. W., Whelan, P. J., Prochazka, A., & Pearson, K. G. (1996). Contribution of hind limb flexor muscle afferents to the timing of phase transitions in the cat step cycle. *Journal of Neurophysiology*, **75**(3), 1126–1137.

Hildebrand, M. (1959). Motions of the running cheetah and horse. *Journal of Mammalogy*, **40**(4), 481–495.

Hildebrand, M. (1960). How animals run. *Scientific American*, **202**(5), 148–160.

Hildebrand, M. (1961). Further studies on locomotion of the cheetah. *Journal of Mammalogy*, **42**(1), 84–91.

Hildebrand, M. (1965). Symmetrical gaits of horses: Gaits can be expressed numerically and analyzed graphically to reveal their nature and relationships. *Science*, **150**(3697), 701–708.

Hildebrand, M. (1967). Symmetrical gaits of primates. *American Journal of Physical Anthropology*, **26**(2), 119–130.

Hildebrand, M. (1977). Analysis of asymmetrical gaits. *Journal of Mammalogy*, **58**(2), 131–156.

Hildebrand, M. (1980). The adaptive significance of tetrapod gait selection. *American Zoologist*, **20**(1), 255–267.

Hildebrand, M. (1989). The quadrupedal gaits of vertebrates. *BioScience*, **39**(11), 766.

Hoyt, D. F., & Taylor, C. R. (1981). Gait and the energetics of locomotion in horses. *Nature*, **292**(5820), 239–240.

Hreljac, A. (1993). Preferred and energetically optimal gait transition speeds in human locomotion. *Medicine and Science in Sports and Exercise*, **25**(10), 1158–1162.

Hsu, L.-J., Bertho, M., & Kiehn, O. (2023). Deconstructing the modular organization and real-time dynamics of mammalian spinal locomotor networks. *Nature Communications*, **14**(1), 873.

Hurteau, M.-F., Thibaudier, Y., Dambreville, C., Danner, S. M., Rybak, I. A., & Frigon, A. (2018). Intralimb and interlimb cutaneous reflexes during locomotion in the intact cat. *Journal of Neuroscience*, **38**(17), 4104–4122.

Ijspeert, A. J., & Daley, M. A. (2023). Integration of feedforward and feedback control in the neuromechanics of vertebrate locomotion: A review of experimental, simulation and robotic studies. *Journal of Experimental Biology*, **226**(15), jeb245784.

Ijspeert, A. J., Crespi, A., & Cabelguen, J.-M. (2005). Simulation and robotics studies of salamander locomotion: Applying neurobiological principles to the control of locomotion in robots. *Neuroinformatics*, **3**, 171–195.

Improvement in the gait of trotting horses. (1882). *Scientific American*, **47**(10), 151.

International Brain Laboratory, Benson, B., Benson, J., Birman, D., Bonacchi, N., Bougrova, K., Bruijns, S. A., Carandini, M., Catarino, J. A., Chapuis, G. A., Churchland, A. K., Dan, Y., Davatolhagh, F., Dayan, P., Dewitt, E. E., Engel, T. A., Fabbri, M., Faulkner, M., Fiete, I. R., Findling, C., Freitas-Silva, L., Gercek, B., Harris, K. D., Hausser, M., Hofer, S. B., Hu, F., Hubert, F., Huntenburg, J. M., Khanal, A., Krasniak, C., Langdon, C., Lau, P. Y., Mainen, Z. F., Meijer, G. T., Miska, N. J., Mrsic-Flogel, T. D., Noel, J.-P., Nylund, K., Pan-Vazquez, A., Paninski, L., Pouget, A., Rossant, C., Roth, N., Schaeffer, R., Schartner, M., Shi, Y., Socha, K. Z., Steinmetz, N. A., Svoboda, K., Urai, A. E., Wells, M. J., West, S. J., Whiteway, M. R., Winter, O., & Witten, I. B. (2023). A brain-wide map of neural activity during complex behaviour. *BioRxiv*, 2023–07.

Iriarte-Diaz, J., Bozinovic, F., & Vasquez, R. A. (2006). What explains the trot–gallop transition in small mammals? *Journal of Experimental Biology*, **209**(20), 4061–4066.

Jackson, J., Karnani, M. M., Zemelman, B. V., Burdakov, D., & Lee, A. K. (2018). Inhibitory control of prefrontal cortex by the claustrum. *Neuron*, **99**(5), 1029–1039.

Josset, N., Roussel, M., Lemieux, M., Lafrance-Zoubga, D., Rastqar, A., & Bretzner, F. (2018). Distinct contributions of mesencephalic locomotor region nuclei to locomotor control in the freely behaving mouse. *Current Biology*, **28**(6), 884–901.

Juvin, L., Simmers, J., & Morin, D. (2005). Propriospinal circuitry underlying interlimb coordination in mammalian quadrupedal locomotion. *Journal of Neuroscience*, **25**(25), 6025–6035.

Kasper, J., Schor, R., & Wilson, V. (1988). Response of vestibular neurons to head rotations in vertical planes. ii. response to neck stimulation and vestibular-neck interaction. *Journal of Neurophysiology*, **60**(5), 1765–1778.

Kelso, J. S., & Schöner, G. (1988). Self-organization of coordinative movement patterns. *Human Movement Science*, **7**(1), 27–46.

Khona, M., & Fiete, I. R. (2022). Attractor and integrator networks in the brain. *Nature Reviews Neuroscience*, **23**(12), 744–766.

Khoramshahi, M., Spröwitz, A., Tuleu, A., Ahmadabadi, M. N., & Ijspeert, A. J. (2013). Benefits of an active spine supported bounding locomotion with a small compliant quadruped robot. *2013 IEEE international conference on robotics and automation*, 3329–3334.

Kiehn, O. (2006). Locomotor circuits in the mammalian spinal cord. *Annual Review of Neuroscience*, **29**, 279–306.

Kiehn, O. (2016). Decoding the organization of spinal circuits that control locomotion. *Nature Reviews Neuroscience*, **17**(4), 224–238.

Kimura, H., Akiyama, S., & Sakurama, K. (1999). Realization of dynamic walking and running of the quadruped using neural oscillator. *Autonomous Robots*, **7**, 247–258.

Koch, S. C., Del Barrio, M. G., Dalet, A., Gatto, G., Günther, T., Zhang, J., Seidler, B., Saur, D., Schuele, R., & Goulding, M. (2017). Rorβ spinal interneurons gate sensory transmission during locomotion to secure a fluid walking gait. *Neuron*, **96**(6), 1419–1431.

Krakauer, J. W., Ghazanfar, A. A., Gomez-Marin, A., MacIver, M. A., & Poeppel, D. (2017). Neuroscience needs behavior: Correcting a reductionist bias. *Neuron*, **93**(3), 480–490.

Kram, R., & Taylor, C. R. (1990). Energetics of running: A new perspective. *Nature*, **346**(6281), 265–267.

Kriellaars, D., Brownstone, R., Noga, B., & Jordan, L. (1994). Mechanical entrainment of fictive locomotion in the decerebrate cat. *Journal of Neurophysiology*, **71**(6), 2074–2086.

Laflamme, O. D., Markin, S. N., Deska-Gauthier, D., Banks, R., Zhang, Y., Danner, S. M., & Akay, T. (2023). Distinct roles of spinal commissural interneurons in transmission of contralateral sensory information. *Current Biology*, **33**(16), 3452–3464.

Lammers, A. R., Earls, K. D., & Biknevicius, A. R. (2006). Locomotor kinetics and kinematics on inclines and declines in the gray short-tailed opossum monodelphis domestica. *Journal of Experimental Biology*, **209**(20), 4154–4166.

Lanuza, G. M., Gosgnach, S., Pierani, A., Jessell, T. M., & Goulding, M. (2004). Genetic identification of spinal interneurons that coordinate left-right locomotor activity necessary for walking movements. *Neuron*, **42**(3), 375–386.

Lauer, J., Zhou, M., Ye, S., Menegas, W., Schneider, S., Nath, T., Rahman, M., Di Santo, V., Soberanes, D., Feng, G., Murthy, V., Lauder, G., Dulac, C., Mathis, M., & Mathis, A. (2022). Multi-animal pose estimation, identification and tracking with deeplabcut. *Nature Methods*, **19**, 496–504.

Lee, D. V. (2011). Effects of grade and mass distribution on the mechanics of trotting in dogs. *Journal of Experimental Biology*, **214**(3), 402–411.

Lee, D. V., Bertram, J. E., & Todhunter, R. J. (1999). Acceleration and balance in trotting dogs. *Journal of Experimental Biology*, **202**(24), 3565–3573.

Lee, D. V., McGuigan, M. P., Yoo, E. H., & Biewener, A. A. (2008). Compliance, actuation, and work characteristics of the goat foreleg and hindleg during level, uphill, and downhill running. *Journal of Applied Physiology*, **104**(1), 130–141.

Lee, D. V., Stakebake, E. F., Walter, R. M., & Carrier, D. R. (2004). Effects of mass distribution on the mechanics of level trotting in dogs. *Journal of Experimental Biology*, **207**(10), 1715–1728.

Leiras, R., Cregg, J. M., & Kiehn, O. (2022). Brainstem circuits for locomotion. *Annual Review of Neuroscience*, **45**, 63–85.

Lemelin, P., Schmitt, D., & Cartmill, M. (2003). Footfall patterns and interlimb co-ordination in opossums (family didelphidae): Evidence for the evolution of diagonal-sequence walking gaits in primates. *Journal of Zoology*, **260**(4), 423–429.

Lemieux, M., Josset, N., Roussel, M., Couraud, S., & Bretzner, F. (2016). Speed-dependent modulation of the locomotor behavior in adult mice reveals attractor and transitional gaits. *Frontiers in Neuroscience*, **10**, 42.

Lopes, G., Bonacchi, N., Frazao, J., Neto, J. P., Atallah, B. V., Soares, S., Moreira, L., Matias, S., Itskov, P. M., Correia, P. A., Medina, R. E., Calcaterra, L., Dreosti, E., Paton, J. J., & Kampff, A. R. (2015). Bonsai: An event-based framework for processing and controlling data streams. *Frontiers in Neuroinformatics*, **9**, 1662–5196.

Lundberg, A. (1981). Half-centres revisited. In *Regulatory functions of the CNS Principles of Motion and Organization* (pp. 155–167). Elsevier.

Machado, A. S., Darmohray, D. M., Fayad, J., Marques, H. G., & Carey, M. R. (2015). A quantitative framework for whole-body coordination reveals specific deficits in freely walking ataxic mice. *eLife*, **4**, e07892.

Maes, L., & Abourachid, A. (2013). Gait transitions and modular organization of mammal locomotion. *Journal of Experimental Biology*, **216**(12), 2257–2265.

Mathis, A., Mamidanna, P., Cury, K. M., Abe, T., Murthy, V. N., Mathis, M. W., & Bethge, M. (2018). Deeplabcut: Markerless pose estimation of user-defined body parts with deep learning. *Nature Neuroscience*, **21**(9), 1281–1289.

Mayer, A. (2020). *The science of walking: Investigations into locomotion in the long nineteenth century*. University of Chicago Press.

Mayer, W. P., & Akay, T. (2021). The role of muscle spindle feedback in the guidance of hindlimb movement by the ipsilateral forelimb during locomotion in mice. *eNeuro*, **8**(6).

Mayer, W. P., Murray, A. J., Brenner-Morton, S., Jessell, T. M., Tourtellotte, W. G., & Akay, T. (2018). Role of muscle spindle feedback in regulating muscle activity strength during walking at different speed in mice. *Journal of Neurophysiology*, **120**(5), 2484–2497.

McClearn, D. (1992). Locomotion, posture, and feeding behavior of kinkajous, coatis, and raccoons. *Journal of Mammalogy*, **73**(2), 245–261.

McCrea, D. A., & Rybak, I. A. (2008). Organization of mammalian locomotor rhythm and pattern generation. *Brain Research Reviews*, **57**(1), 134–146.

McGhee, R., & Jain, A. (1972). Some properties of regularly realizable gait matrices. *Mathematical Biosciences*, **13**(1-2), 179–193.

McLaughlin, R. M., Gaughan, E. M., Roush, J. K., & Skaggs, C. L. (1996). Effects of subject velocity on ground reaction force measurements and stance times in clinically normal horses at the walk and trot. *American Journal of Veterinary Research*, **57**(1), 7–11.

McMahon, T. A. (1985). The role of compliance in mammalian running gaits. *Journal of Experimental Biology*, **115**(1), 263–282.

McVea, D. A., Donelan, J. M., Tachibana, A., & Pearson, K. G. (2005). A role for hip position in initiating the swing-to-stance transition in walking cats. *Journal of Neurophysiology*, **94**(5), 3497–3508.

Merel, J., Aldarondo, D., Marshall, J., Tassa, Y., Wayne, G., & Ölveczky, B. (2019). Deep neuroethology of a virtual rodent. *arXiv:1911.09451*.

Merel, J., Botvinick, M., & Wayne, G. (2019). Hierarchical motor control in mammals and machines. *Nature Communications*, **10**(1), 1–12.

Miller, S., Van Der Burg, J., & Van Der Meche, F. (1975). Locomotion in the cat: Basic programmes of movement. *Brain Research*, **91**(2), 239–253.

Miller, S., & Van der Meche, F. (1976). Coordinated stepping of all four limbs in the high spinal cat. *Brain Research*.

Mitrevica, Z., & Murray, A. J. (2023). Speed-independent modulation of locomotor gait preference by sensory feedback in mice. *bioRxiv*, 2023–03.

Molkov, Y. I., Yu, G., Ausborn, J., Bouvier, J., Danner, S. M., & Rybak, I. A. (2024). Sensory feedback and central neuronal interactions in mouse locomotion. *Royal Society Open Science*, **11**(8), 240207.

Morina, E. (2023). *A novel behavioural paradigm for characterising anticipatory postural adjustments in mice* (Doctoral dissertation). University College London.

Muybridge, E. (2012). *Animals in motion*. Courier Corporation.

Nath, T., Mathis, A., Chen, A. C., Patel, A., Bethge, M., & Mathis, M. W. (2019). Using deeplabcut for 3D markerless pose estimation across species and behaviors. *Nature protocols*, **14**(7), 2152–2176.

Nauwelaerts, S., Aerts, P., & Clayton, H. (2013). Spatio-temporal gait characteristics during transitions from trot to canter in horses. *Zoology*, **116**(4), 197–204.

Navabpour, S., Kwapis, J. L., & Jarome, T. J. (2020). A neuroscientist's guide to transgenic mice and other genetic tools. *Neuroscience & Biobehavioral Reviews*, **108**, 732–748.

Ni, Y., Nawabi, H., Liu, X., Yang, L., Miyamichi, K., Tedeschi, A., Xu, B., Wall, N. R., Callaway, E. M., & He, Z. (2014). Characterization of long descending premotor propriospinal neurons in the spinal cord. *Journal of Neuroscience*, **34**(28), 9404–9417.

Noga, B. R., & Whelan, P. J. (2022). The mesencephalic locomotor region: Beyond locomotor control. *Frontiers in Neural Circuits*, **16**, 884785.

Olson, W. P., Chokshi, V. B., Kim, J. J., Cowan, N., & O'Connor, D. H. (2024). Muscle spindles provide flexible sensory feedback for movement sequences. *bioRxiv*, 2024–09.

O'Neill, M. C., & Schmitt, D. (2012). The gaits of primates: Center of mass mechanics in walking, cantering and galloping ring-tailed lemurs, lemur catta. *Journal of Experimental Biology*, **215**(10), 1728–1739.

Owaki, D., & Ishiguro, A. (2017). A quadruped robot exhibiting spontaneous gait transitions from walking to trotting to galloping. *Scientific Reports*, **7**(1), 277.

Owaki, D., Kano, T., Nagasawa, K., Tero, A., & Ishiguro, A. (2013). Simple robot suggests physical interlimb communication is essential for quadruped walking. *Journal of The Royal Society Interface*, **10**(78), 20120669.

Pearson, K. G. (1995). Proprioceptive regulation of locomotion. *Current opinion in neurobiology*, **5**(6), 786–791.

Pennycuick, C. (1975). On the running of the gnu (connochaetes taurinus) and other animals. *Journal of Experimental Biology*, **63**(3), 775–799.

Perry, S., Larhammar, M., Vieillard, J., Nagaraja, C., Hilscher, M. M., Tafreshiha, A., Rofo, F., Caixeta, F. V., & Kullander, K. (2019). Characterization of dmrt3-derived neurons suggest a role within locomotor circuits. *Journal of Neuroscience*, **39**(10), 1771–1782.

Pocratsky, A. M., Shepard, C. T., Morehouse, J. R., Burke, D. A., Riegler, A. S., Hardin, J. T., Beare, J. E., Hainline, C., Brown, B. L., Whittemore, S. R., & Magnuson, D. S. K. (2020). Long ascending propriospinal neurons provide flexible, context-specific control of interlimb coordination. *eLife*, **9**, e53565.

Polet, D. T., & Bertram, J. E. (2019). An inelastic quadrupedal model discovers four-beat walking, two-beat running, and pseudo-elastic actuation as energetically optimal. *PLoS Computational Biology*, **15**(11), e1007444.

Prochazka, A., Gillard, D., & Bennett, D. J. (1997). Implications of positive feedback in the control of movement. *Journal of Neurophysiology*, **77**(6), 3237–3251.

Proske, U., & Gandevia, S. C. (2012). The proprioceptive senses: Their roles in signaling body shape, body position and movement, and muscle force. *Physiological Reviews*.

Prost, J. (1969). A replication study on monkey gaits. *American Journal of Physical Anthropology*, **30**(2), 203–208.

Quinlan, K. A., & Kiehn, O. (2007). Segmental, synaptic actions of commissural interneurons in the mouse spinal cord. *Journal of Neuroscience*, **27**(24), 6521–6530.

Robilliard, J. J., Pfau, T., & Wilson, A. M. (2007). Gait characterisation and classification in horses. *Journal of Experimental Biology*, **210**(2), 187–197.

Roseberry, T. K., Lee, A. M., Lalive, A. L., Wilbrecht, L., Bonci, A., & Kreitzer, A. C. (2016). Cell-type-specific control of brainstem locomotor circuits by basal ganglia. *Cell*, **164**(3), 526–537.

Rossignol, S., Dubuc, R., & Gossard, J.-P. (2006). Dynamic sensorimotor interactions in locomotion. *Physiological Reviews*, **86**(1), 89–154.

Rubin, C. T., & Lanyon, L. E. (1982). Limb mechanics as a function of speed and gait: A study of functional strains in the radius and tibia of horse and dog. *Journal of Experimental Biology*, **101**(1), 187–211.

Ruder, L., Takeoka, A., & Arber, S. (2016). Long-distance descending spinal neurons ensure quadrupedal locomotor stability. *Neuron*, **92**(5), 1063–1078.

Ruina, A., Bertram, J. E., & Srinivasan, M. (2005). A collisional model of the energetic cost of support work qualitatively explains leg sequencing in walking and galloping, pseudo-elastic leg behavior in running and the walk-to-run transition. *Journal of theoretical biology*, **237**(2), 170–192.

Rybak, I. A., Dougherty, K. J., & Shevtsova, N. A. (2015). Organization of the mammalian locomotor CPG: Review of computational model and circuit architectures based on genetically identified spinal interneurons. *eNeuro*, **2**(5).

Rybak, I. A., Shevtsova, N. A., Lafreniere-Roula, M., & McCrea, D. A. (2006). Modelling spinal circuitry involved in locomotor pattern generation: Insights from deletions during fictive locomotion. *The Journal of Physiology*, **577**(2), 617–639.

Rybak, I. A., Shevtsova, N. A., Markin, S. N., Prilutsky, B. I., & Frigon, A. (2024). Operation regimes of spinal circuits controlling locomotion and role of supraspinal drives and sensory feedback. *bioRxiv*, 2024–03.

Rybak, I. A., Stecina, K., Shevtsova, N. A., & McCrea, D. A. (2006). Modelling spinal circuitry involved in locomotor pattern generation: Insights from the effects of afferent stimulation. *The Journal of Physiology*, **577**(2), 641–658.

Ryczko, D. (2022). The mesencephalic locomotor region: Multiple cell types, multiple behavioral roles, and multiple implications for disease. *The Neuroscientist*, 10738584221139136.

Ryczko, D., Simon, A., & Ijspeert, A. J. (2020). Walking with salamanders: From molecules to biorobotics. *Trends in Neurosciences*, **43**(11), 916–930.

Santuz, A., & Akay, T. (2023). Muscle spindles and their role in maintaining robust locomotion. *The Journal of Physiology*, **601**(2), 275–285.

Santuz, A., Akay, T., Mayer, W. P., Wells, T. L., Schroll, A., & Arampatzis, A. (2019). Modular organization of murine locomotor pattern in the presence and absence of sensory feedback from muscle spindles. *The Journal of Physiology*, **597**(12), 3147–3165.

Santuz, A., Laflamme, O. D., & Akay, T. (2022). The brain integrates proprioceptive information to ensure robust locomotion. *The Journal of Physiology*, **600**(24), 5267–5294.

Satoda, T., Matsumoto, H., Zhou, L., Rose, P., & Richmond, F. (2002). Mesencephalic projections to the first cervical segment in the cat. *Experimental Brain Research*, **144**, 397–413.

Satoh, D., Pudenz, C., & Arber, S. (2016). Context-dependent gait choice elicited by epha4 mutation in lbx1 spinal interneurons. *Neuron*, **89**(5), 1046–1058.

Schmitt, D., & Lemelin, P. (2004). Locomotor mechanics of the slender loris (loris tardigradus). *Journal of Human Evolution*, **47**(1-2), 85–94.

Schöner, G., Jiang, W. Y., & Kelso, J. S. (1990). A synergetic theory of quadrupedal gaits and gait transitions. *Journal of theoretical Biology*, **142**(3), 359–391.

Serra Bragança, F., Broomé, S., Rhodin, M., Björnsdóttir, S., Gunnarsson, V., Voskamp, J., Persson-Sjodin, E., Back, W., Lindgren, G., Novoa-Bravo, M., Gmel, A., Roepstorff, C., van der Zwaag, B., Van Weeren, P., & Hernlund, E. (2020). Improving gait classification in horses by using inertial measurement unit (IMU) generated data and machine learning. *Scientific Reports*, **10**(1), 17785.

Shafiee, M., Bellegarda, G., & Ijspeert, A. (2024). Viability leads to the emergence of gait transitions in learning agile quadrupedal locomotion on challenging terrains. *Nature Communications*, **15**(1), 3073.

Shao, Y., Jin, Y., Liu, X., He, W., Wang, H., & Yang, W. (2021). Learning free gait transition for quadruped robots via phase-guided controller. *IEEE Robotics and Automation Letters*, **7**(2), 1230–1237.

Shik, M. L., & Orlovsky, G. N. (1976). Neurophysiology of locomotor automatism. *Physiological Reviews*, **56**(3), 465–501.

Shik, M., Severin, F., & Orlovsky, G. (1966). Control of walking and running by means of electrical stimulation of the mid-brain. *Biofizika*, **11**(4), 659–666.

Smetana, R., Juvin, L., Dubuc, R., & Alford, S. (2010). A parallel cholinergic brainstem pathway for enhancing locomotor drive. *Nature Neuroscience*, **13**(6), 731–738.

Smith, J. L., Carlson-Kuhta, P., & Trank, T. V. (1998). Forms of forward quadrupedal locomotion. III. A comparison of posture, hindlimb kinematics, and motor patterns for downslope and level walking. *Journal of Neurophysiology*, **79**(4), 1702–1716.

Stafford, F., & Barnwell, G. (1985). Mathematical models of central pattern generators in locomotion: Iii. interlimb model for the cat. *Journal of motor behavior*, **17**(1), 61–76.

Stantcheva, K. K., Iovino, L., Dhandapani, R., Martinez, C., Castaldi, L., Nocchi, L., Perlas, E., Portulano, C., Pesaresi, M., Shirlekar, K. S., de Castro Reis, F., Paparountas, T., Bilbao, D., & Heppenstall, P. A. (2016). A subpopulation of itch-sensing neurons marked by ret and somatostatin expression. *EMBO Reports*, **17**(4), 585–600.

Starke, S. D., Robilliard, J. J., Weller, R., Wilson, A. M., & Pfau, T. (2009). Walk–run classification of symmetrical gaits in the horse: A multidimensional approach. *Journal of the Royal Society Interface*, **6**(33), 335–342.

Stein, B., & Casinos, A. (1997). What is a cursorial mammal? *Journal of Zoology*, **242**(1), 185–192.

Takeoka, A., & Arber, S. (2019). Functional local proprioceptive feedback circuits initiate and maintain locomotor recovery after spinal cord injury. *Cell Reports*, **27**(1), 71–85.

Takeoka, A., Vollenweider, I., Courtine, G., & Arber, S. (2014). Muscle spindle feedback directs locomotor recovery and circuit reorganization after spinal cord injury. *Cell*, **159**(7), 1626–1639.

Talpalar, A. E., Bouvier, J., Borgius, L., Fortin, G., Pierani, A., & Kiehn, O. (2013). Dual-mode operation of neuronal networks involved in left–right alternation. *Nature*, **500**(7460), 85–88.

Tata Ramalingasetty, S., Danner, S. M., Arreguit, J., Markin, S. N., Rodarie, D., Kathe, C., Courtine, G., Rybak, I. A., & Ijspeert, A. J. (2021). A whole-body musculoskeletal model of the mouse. *IEEE Access*, **9**, 163861–163881.

Tata Ramalingasetty, S., Markin, S. N., Lockhart, A. B., Arreguit, J., Shevtsova, N. A., Ijspeert, A. J., Rybak, I. A., & Danner, S. M. (2024). On all fours: A 3D framework to study closed-loop control of quadrupedal mouse locomotion. *ALIFE 2024: Proceedings of the 2024 Artificial Life Conference.*

Tello, A. J., van der Zouwen, C. I., Dejas, L., Duque-Yate, J., Boutin, J., Medina-Ortiz, K., Suresh, J. S., Swiegers, J., Sarret, P., & Ryczko, D. (2024). Dopamine-sensitive neurons in the mesencephalic locomotor region control locomotion initiation, stop, and turns. *Cell Reports*, **43**(5).

Tomita, M. (1967). A study on the movement pattern of four limbs in walking. *Journal of the Anthropological Society of Nippon*, **75**(3), 120–146.

Tourtellotte, W. G., Keller-Peck, C., Milbrandt, J., & Kucera, J. (2001). The transcription factor egr3 modulates sensory axon–myotube interactions during muscle spindle morphogenesis. *Developmental Biology*, **232**(2), 388–399.

Tourtellotte, W. G., & Milbrandt, J. (1998). Sensory ataxia and muscle spindle agenesis in mice lacking the transcription factor egr3. *Nature Genetics*, **20**(1), 87–91.

Tuthill, J. C., & Azim, E. (2018). Proprioception. *Current Biology*, **28**(5), R194–R203.

Usherwood, J. R. (2020). An extension to the collisional model of the energetic cost of support qualitatively explains trotting and the trot–canter transition. *Journal of Experimental Zoology Part A: Ecological and Integrative Physiology*, **333**(1), 9–19.

Usseglio, G., Gatier, E., Heuzé, A., Hérent, C., & Bouvier, J. (2020). Control of orienting movements and locomotion by projection-defined subsets of brainstem V2a neurons. *Current Biology*, **30**(23), 4665–4681.

Vallstedt, A., & Kullander, K. (2013). Dorsally derived spinal interneurons in locomotor circuits. *Annals of the New York Academy of Sciences*, **1279**(1), 32–42.

Van der Zouwen, C. I., Boutin, J., Fougère, M., Flaive, A., Vivancos, M., Santuz, A., Akay, T., Sarret, P., & Ryczko, D. (2021). Freely behaving mice can brake and turn during optogenetic stimulation of the mesencephalic locomotor region. *Frontiers in Neural Circuits*, **15**, 639900.

Vilensky, J. A., & Larson, S. G. (1989). Primate locomotion: Utilization and control of symmetrical gaits. *Annual Review of Anthropology*, **18**(1), 17–35.

Vincelette, A. (2023). The characteristics, distribution, function, and origin of alternative lateral horse gaits. *Animals*, **13**(16), 2557.

Wang, Q., Ding, S. L., Li, Y., Royall, J., Feng, D., Lesnar, P., Graddis, N., Naeemi, M., Facer, B., Ho, A., Dolbeare, T., Blanchard, B., Dee, N., Wakeman, W., Hirokawa, K. E., Szafer, A., Sunkin, S. M., Oh, S. W., Bernard, A., Phillips, J. W., Hawrylycz, M., Koch, C., Zeng, H., Harris, J. A., & Ng, L. (2020). The Allen mouse brain common coordinate framework: A 3D reference atlas. *Cell*, **181**(4), 936–953.

Warren, R. A., Zhang, Q., Hoffman, J. R., Li, E. Y., Hong, Y. K., Bruno, R. M., & Sawtell, N. B. (2021). A rapid whisker-based decision underlying skilled locomotion in mice. *eLife*, **10**, e63596.

Wei, J. Y., Simon, J., Randic, M., & Burgess, P. (1986). Joint angle signaling by muscle spindle receptors. *Brain Research*, **370**(1), 108–118.

Weihmann, T., Brun, P. G., & Pycroft, E. (2017). Speed dependent phase shifts and gait changes in cockroaches running on substrates of different slipperiness. *Frontiers in Zoology*, **14**(1), 1–15.

Wickler, S. J., Hoyt, D. F., Cogger, E. A., & Myers, G. (2003). The energetics of the trot–gallop transition. *Journal of Experimental Biology*, **206**(9), 1557–1564.

Wutke, S., Andersson, L., Benecke, N., Sandoval-Castellanos, E., Gonzalez, J., Hallsson, J. H., Lougas, L., Magnell, O., Morales-Muniz, A., Orlando, L., Hulda Pálsdóttir, A., Reissmann, M., Muñoz-Rodríguez, M. B., Ruttkay, M., Trinks, A., Hofreiter, M., & Ludwig, A. (2016). The origin of ambling horses. *Current Biology*, **26**(15), R697–R699.

Xi, W., Yesilevskiy, Y., & Remy, C. D. (2016). Selecting gaits for economical locomotion of legged robots. *The International Journal of Robotics Research*, **35**(9), 1140–1154.

Xiao, C., Cho, J. R., Zhou, C., Treweek, J. B., Chan, K., McKinney, S. L., Yang, B., & Gradinaru, V. (2016). Cholinergic mesopontine signals govern locomotion and reward through dissociable midbrain pathways. *Neuron*, **90**(2), 333–347.

Yesilevskiy, Y., Yang, W., & Remy, C. D. (2018). Spine morphology and energetics: How principles from nature apply to robotics. *Bioinspiration & biomimetics*, **13**(3), 036002.

Yu, W., Yang, C., McGreavy, C., Triantafyllidis, E., Bellegarda, G., Shafiee, M., Ijspeert, A. J., & Li, Z. (2023). Identifying important sensory feedback for learning locomotion skills. *Nature Machine Intelligence*, **5**(8), 919–932.

Yuasa, H., & Ito, M. (1990). Coordination of many oscillators and generation of locomotory patterns. *Biological Cybernetics*, **63**(3), 177–184.

Zador, A., Escola, S., Richards, B., Olveczky, B., Bengio, Y., Boahen, K., Botvinick, M., Chklovskii, D., Churchland, A., Clopath, C., DiCarlo, J., Ganguli, S., Hawkins, J., Körding, K., Koulakov, A., LeChun, Y., Lillicrap, T., Marblestone, A., Olshausen, B., Pouget, A., Savin, C., Sejnowski, T., Simoncelli, E., Solla, S., Sussillo, D., Tolias, A. S., & Tsao, D. (2023). Catalyzing next-generation artificial intelligence through neuroai. *Nature Communications*, **14**(1), 1597.

Zhang, H., Deska-Gauthier, D., MacKay, C. S., Hari, K., Lucas-Osma, A. M., Borowska-Fielding, J., Letawsky, R. L., Akay, T., Fenrich, K. K., Bennett, D. J., & Zhang, Y. (2024). Widespread innervation of motoneurons by spinal V3 neurons globally amplifies locomotor output in mice. *bioRxiv*, 2024–03.

Zhang, H., Shevtsova, N. A., Deska-Gauthier, D., Mackay, C., Dougherty, K. J., Danner, S. M., Zhang, Y., & Rybak, I. A. (2022). The role of V3 neurons in speed-dependent interlimb coordination during locomotion in mice. *eLife*, **11**, e73424.

Zhang, Y., Narayan, S., Geiman, E., Lanuza, G. M., Velasquez, T., Shanks, B., Akay, T., Dyck, J., Pearson, K., Gosgnach, S., et al. (2008). V3 spinal neurons establish a robust and balanced locomotor rhythm during walking. *Neuron*, **60**(1), 84–96.

Zug, G. R. (1972). A critique of the walk pattern analysis of symmetrical quadrupedal gaits. *Animal Behaviour*, **20**(3), 436–438.

Author contribution statement

Most aspects of the project were carried out by the author of this thesis.

In **Chapter 2**, the ataxic scoring strategy for *Egr3-/-* and *PV-Cre;Avil-iDTR* mice (see Table 2.1) was initially devised by the Named Animal Care and Welfare Officer Tina O'Mahony, and refined by the author of this thesis in consultation with the Named Veterinary Surgeon Olga Woolmer. The ataxic scoring of *Egr3-/-* animals between weaning and 7-8 weeks of age was performed by Ben Foster, Rosie Keenan, Amy Veness, and Sian Murphy with valuable support from the rest of the Neurobiological Research Facility team. This data is included in **Chapter 5**, specifically Figure 5.1.